DISS. ETH NO. 21013

ENVIRONMENTAL APPLICATIONS OF LOW-ENERGY ACCELERATOR MASS SPECTROMETRY

A dissertation submitted to

ETH ZURICH

for the degree of

Doctor of Sciences

presented by

JOHANNES RAIMUND LACHNER

Diplom-Physiker Univ., Technische Universität München

born June 7, 1983

citizen of the Federal Republic of Germany

accepted on the recommendation of

Prof. Dr. Hans-Arno Synal, examiner
Prof. Dr. Günther Dissertori, co-examiner
Prof. Dr. Walter Henning, co-examiner

2013

Contents

Abstract

Since the beginnings of accelerator mass spectrometry (AMS) this method has been employed to investigate environmental processes via the detection of rare radionuclides. Highly sensitive and selective analysis as well as a high sample throughput are key parameters that make AMS attractive for large scale studies in the environmental sciences, not only as a powerful dating method. In this context, the reduction in size and complexity and easier handling are not the sole arguments in favour of compact and dedicated AMS facilities. In particular, the efficient beam transport with high transmission from the source of the negative ions to the detection of the charge reversed positive ions is an enormous advantage compared to larger accelerator systems as it allows reducing the amount of required sample material. Major developments in this direction have been performed at ETH Zurich with the construction of the compact 0.5 MV Pelletron system Tandy and the smaller (0.2 MV) ^{14}C-dedicated MICADAS. The installation of an additional magnet on the high-energy side of the Tandy system raised the selectivity of this setup for measurements of other radionuclides that previously were not accessible with low-energy AMS. Following the findings at the MICADAS, in the course of this work the stripper gas at the Tandy was changed from Argon to Helium, which further improved the beam transport efficiency of this facility. Amongst others, these modifications led to a major transformation of the existing system. A number of tests were conducted to specify the system's new performance parameters and established it as a versatile and competitive AMS facility. Compared to the original setup, ^{10}Be and ^{236}U, for example, are now determined with a selectivity that is higher by up to two and three orders of magnitude, respectively. The transmission of actinide beams through the accelerator is increased by a factor of three when changing to Helium as stripper gas and choosing the charge state 3^+. With this enhanced efficiency, measurements down to low concentration levels are possible. At the low levels now reachable with the Tandy, special effort has to be made to fully eliminate surviving molecules in the 3^+ charge state. The observed triply charged molecules were identified as previously unknown states of actinide-hydrides. The remaining background originates from neighbouring abundant nuclides (^{235}U, ^{238}U) to the isotopes of interest (^{236}U, ^{239}Pu). The installation of an absorber in front of the gas ionization chamber was tested and promises to rise the overall efficiency for the detection of ^{10}Be and ^{26}Al. In this

setup, background nuclides are suppressed by completely stopping them in a passive absorber volume while the desired radionuclides can enter the detector.

The recently completed technical improvements already facilitate routine measurements of ^{10}Be and rare actinide isotopes. They triggered the development of novel applications: New chemical methods were designed to separate Be, U, or Pu from water and sediment samples. Natural ^{10}Be/^{9}Be ratios of environmental samples were determined without addition of ^{9}Be carrier. This carrier-free technique simplifies the measurement and the analysis of the results, but requires a special treatment of the samples and a sensitive quantification of low ^{9}Be currents. Comparison studies were conducted between the carrier-free method and the conventional technique. These tests verified that the new method produces reliable ^{10}Be/^{9}Be ratios and supplied new data on sedimentation rates in the Arctic Ocean and ages of river terraces. In a first larger project, the ^{10}Be/^{9}Be ratio during the Brunhes-Matuyama geomagnetic field reversal ($\approx$780 ka BP) was investigated in five marine drill cores from the different world oceans and the potential of this isotope system for reconstruction of past magnetic field changes was demonstrated.

The high selectivity of the Tandy facility concerning the suppression of neighbouring nuclides in the actinide mass range permits for the first time the analysis of samples with ^{236}U/^{235}U ratios of 10^{-10} by means of low-energy AMS. ^{236}U, Pu isotopes, ^{10}Be, ^{14}C, and ^{41}Ca were applied to diagnose sources of anthropogenic radionuclide releases. In addition, ^{236}U was determined in several North Sea and Atlantic Ocean water samples and will be explored as a new conservative tracer of water mass transport.

Zusammenfassung

Seit den Anfängen der Beschleunigermassenspektrometrie (AMS) wurde diese Mess-methode zur Untersuchung von Umweltprozessen mithilfe seltener Radionuklide verwen-det. Hochempfindliche und äußerst selektive Messungen im Zusammenspiel mit einem großen Probendurchsatz sind die ausschlaggebenden Faktoren, durch die AMS attraktiv für umfangreiche Studien in den Umweltwissenschaften wird, nicht nur als eine wichtige Datierungsmethode. In diesem Zusammenhang sind die Reduktion der Maße und der Komplexität nicht die einzigen Argumente, die für kompakte und AMS-spezifische Anla-gen sprechen. Insbesondere ihr effizienter Strahltransport, der durch eine hohe Trans-mission von der Quelle negativer Ionen bis zur Detektion der umgeladenen positiven Io-nen gekennzeichnet ist, bietet einen enormer Vorteil im Vergleich zu größeren Beschleu-nigersystemen, da die zur Messung benötigte Probenmenge verringert werden kann. An der ETH Zürich sind die Hauptentwicklungen in dieser Richtung durchgeführt wor-den, unter anderem die Konstruktion der kompakten Pelletron-basierten Anlage Tandy und des kleineren ^{14}C-spezifischen MICADAS. Die Installation eines zusätzlichen Mag-neten auf der Hochenergieseite der Tandy-Anlage hat die Selektivität dieses Aufbaus für den Nachweis von Radionukliden erhöht, die bislang für die Niederenergie-AMS nicht zugänglich waren. Ausgehend von Erkenntnissen am MICADAS wurde im Rahmen dieser Arbeit ein Wechsel des Strippergases am Tandy von Argon auf Helium vollzogen, was die Effizienz des Strahltransportes weiter erhöhte. Diese Änderungen hatten eine weit-reichende Umgestaltung des existierenden Systems zur Folge. Eine Vielzahl von Tests wurde zur Charakterisierung des modifizierten Systems ausgeführt und konnten es als vielseitige und wettbewerbsfähige AMS-Anlage etablieren.

Im Vergleich zum ursprünglichen Aufbau können nun beispielsweise ^{10}Be und ^{236}U mit um zwei beziehungsweise drei Größenordnungen verringertem Untergrund bestimmt werden. Die Transmission von Actinoiden durch den Beschleuniger ist mit Helium als Strippergas um einen Faktor drei erhöht, wenn man den Ladungszustand 3$^+$ wählt. Mit dieser gesteigerten Effizienz sind Messungen bei niedrigen Konzentrationen im Proben-material möglich. Die verbesserte Separation im Massenbereich der Actinoiden verlangt nun besonderen Aufwand zur vollständigen Unterdrückung von molekularem Untergrund. Dreifach geladene Moleküle wurden am Tandy nachgewiesen und konnten als zuvor un-bekannte Zustände von Actinoid-Hydriden identifiziert werden. Der übrige Untergrund

stammt von häufigen Nukliden auf den Nachbarmassen (^{235}U, ^{238}U) der zu messenden Isotope (^{236}U, ^{239}Pu).

Desweiteren wurde die Installation eines Absorbers vor dem zum Nuklidnachweis benutzten Gasionisationsdetektor getestet. Diese Technik stellt eine weitere Verbesserung der Nachweisempfindlichkeit für ^{10}Be und ^{26}Al in Aussicht. In diesem Aufbau werden störende Nuklide unterdrückt, indem sie in einem passiven Absorbervolumen komplett abgestoppt werden, wohingegen die seltenen Radionuklide bis zum empfindlichen Detektor gelangen können.

Die fertiggestellten technischen Neuerungen erlauben schon jetzt Routineanalysen von ^{10}Be und seltenen Actinoid-Isotopen. Neue Anwendungen wurden daraufhin ausgeführt: Für die Extraktion von Be, U, oder Pu aus Wasser- oder Sedimentproben wurden chemische Aufbereitungsrezepte entwickelt. Natürliche ^{10}Be/^{9}Be Verhältnisse in Umweltproben wurden ohne Zugabe von ^{9}Be-Trägermaterial bestimmt. Diese trägerfreie Methode erleichtert die Messungen und Analyse der Ergebnisse. Jedoch ist eine besondere Probenaufbereitung notwendig, sowie eine empfindliche Messung der niedrigen ^{9}Be Ströme. Mehrere Vergleichsstudien zwischen der trägerfreien und der konventionellen Methode wurden durchgeführt. Diese Tests bewiesen, dass die neue Methode gute und verlässliche Resultate für die ^{10}Be/^{9}Be Verhältnisse liefert, und erbrachten auch neue Daten zu Sedimentationsraten im Arktischen Ozean und zu geologischen Altern von Flussterassen. Im Rahmen eines ersten größeren Projekts wurde das ^{10}Be/^{9}Be Verhältnis während der Brunhes-Matuyama-Umkehr des Erdmagnetfelds ($\approx$780 ka vor heute) in fünf marinen Bohrkernen aus den verschiedenen Ozeanen untersucht. Damit konnte das Potential dieses Isotopenverhältnisses für die Rekonstruktion von Änderungen des Erdmagnetfelds in der Vergangenheit gezeigt werden.

Die hohe Selektivität des Tandy bezüglich der Unterdrückung von Nukliden mit benachbarten Massen im Bereich der Actinoiden ermöglicht es zum ersten Mal Proben mit ^{236}U/^{235}U Verhältnissen im Bereich von 10^{-10} mittels Niederenergie-AMS zu messen. ^{236}U, Pu Isotope, ^{10}Be, ^{14}C und ^{41}Ca wurden verwendet um Quellen von anthropogenen Radionukliden zu identifizieren. Weiterhin wurde ^{236}U in mehreren Wasserproben aus der Nordsee und dem Atlantischen Ozean nachgewiesen. Dieses Isotop eignet sich als neuartiger konservativer Tracer von Wassermassen.

Chapter 1

Introduction

1.1 Overview: Across the world and to the ends of the nuclide chart

The detection of long-lived rare radionuclides in natural samples is one of the main application areas of accelerator mass spectrometry (AMS). This method is usually applied to identify radioactive isotopes abundant in the range of 10^{-10} to 10^{-16} relative to stable isotopes of the same element. Elimination of background is achieved using magnetic and electric mass filters for ions in combination with the acceleration of these ions to energies ranging from several hundred keV to several hundred MeV. In the filtering units, ions with neighbouring masses are rejected and the high energies of the ions and their charge reversal in a stripper medium allow for suppression of molecular and isobaric background. Apart from some special cases, the half-lives of the studied nuclides via AMS range from few 1000 a to 100 Ma, so that determining the number of atoms by counting their decays would be rather sample- and time-consuming.

One way to expand the use of AMS as a versatile and powerful method in the environmental sciences is to simplify the setup so that a large number of measurements of various radionuclides in different sample materials can be performed. Compact AMS systems with acceleration voltages below 1 MeV were pioneered by the installation of the 0.5 MV NEC pelletron system (Tandy) at ETH Zurich and have become very popular for radiocarbon determinations in the past 15 years. In order to broaden the practicality of AMS at low beam energies beyond the use of ^{14}C, several modifications of the existing Tandy setup were undertaken, the recent installation of a third magnet being the most prominent. Several technical advancements were carried out in the course of this thesis, such as the usage of He as stripper gas and the test of an absorber cell for background suppression at low beam energies. These modifications resulted in a major transformation of the Tandy AMS system. A number of test studies was conducted in order to characterize this modified system for different nuclides in diverse configurations. At the same time,

measurements on real samples were performed to establish new applications in the field of environmental sciences.

The methods and applications presented here are mainly related to the nuclides ^{10}Be, ^{26}Al, ^{236}U, and the Pu isotopes. Examples of applications for these isotopes are dating of natural archives (^{10}Be) or indicating sources of anthropogenic radioactivity and using their input to trace environmental transport processes (actinides). In this context, for the first time ^{236}U and ^{244}Pu were determined in natural samples at a compact AMS system. Additionally, the carrier-free method for ^{10}Be/^{9}Be ratios was established in first studies processing about hundred samples. Further important AMS isotopes analysed at this facility include ^{129}I for environmental and ^{41}Ca for medical applications, but these were not part of this thesis and therefore are not discussed in detail.

A number of sample materials were used to explore the potential of low-energy AMS for environmental sciences: The carrier-free method was tested on sediments from the Arctic Ocean and from a fossil find spot in Bulgarian River terraces. The main study related to ^{10}Be/^{9}Be ratios was carried out on five sediment drill cores from the three world oceans. The projects concerning the actinides were conducted on water flushing U-rich mines, on samples from the North Sea and the Atlantic Ocean, and on coral $CaCO_3$ from the Bikini atoll.

In the following, an outline of this thesis is given by describing the general content of the single chapters. The introduction continues with an overview of the development of AMS and the application of rare radionuclides as environmental tracers.

Subsequently, the basics of the compact Tandy AMS system and its technical advancements are presented. A description of the main parameters limiting the efficiency of an AMS measurement will provide an overview of the challenges involved in improving this method. One of the main technical developments to enhance the efficiency of radioisotope detection at the Tandy was the application of He as stripper gas.

In the third chapter the AMS measurement of the light isotopes ^{10}Be and ^{26}Al is covered. ^{10}Be AMS at low energies is already competitive with larger facilities with respect to efficiency and sensitivity, while the efficiency for ^{26}Al measurements still has to be improved. A detector concept previously not applied for compact AMS is presented employing a passive absorber to suppress the background, which might lead to a gain in the overall yield of ^{10}Be and ^{26}Al.

The fourth chapter covers the study of AMS at low energies for actinides, i.e. ^{236}U, ^{237}Np and Pu isotopes. Here, the separation of the rare isotopes from the abundant nuclides ^{235}U and ^{238}U is critical as well as the suppression of molecular background. The sensitivity studies performed for the individual isotopes and the experiments that led to the discovery of triply charged actinide-hydride molecules are discussed.

Afterwards, the focus is moved towards environmental applications: In the fifth chapter the carrier-free ^{10}Be/^{9}Be technique is examined. The special technical and chemical prerequisites for ^{10}Be AMS without carrier are discussed and several projects are presented. These include comparison studies with conventional AMS in fluvial and marine sediments and the reconstruction of the ^{10}Be/^{9}Be signature during the Brunhes-Matuyama field reversal.

The sixth chapter deals with the potential of actinides as evidence of an anthropogenic contamination with radioactivity and as tracer of natural transport processes.

In the conclusion the main achievements are summarized and an overview of the present performance of the Tandy system is given for the various radionuclides and setups.

1.2 Environmental applications in the development of AMS

A hundred years ago the potential of radioactive tracers was discovered for chemistry by Hevesy and Paneth [1913]. The decay product Ra D (Radium D) could not be separated from Pb by chemical means - as it actually is ^{210}Pb - and was used to define the solubilities of PbS and PbCrO$_4$. The application of radioisotopes in environmental sciences started later, e.g. limits were set on mixing times of atmosphere and ocean with the cosmic-ray produced ^{14}C [Anderson and Libby, 1951]. Furthermore, via radiocarbon dating the ages of water masses were identified [Stuiver et al., 1983] and thereby our current knowledge of oceanic water transport in the so-called conveyor belt was created. It is not only radioactivity from natural sources (cosmogenic or nucleogenic) that has been studied in the environment but also anthropogenic radionuclides have proven to be valuable tracers. With the rise of AMS even more nuclides have become available as tracers. After the potential of AMS for the determination of long-lived radionuclides such as ^{14}C and ^{10}Be was recognized [Muller, 1977], a number of facilities quickly started to implement the presented methods. The application of negative ions for isobar suppression opened the way for radiocarbon AMS with Tandem van-de-Graaff accelerators [Nelson et al., 1977; Bennett et al., 1977, 1978]. Still, in the late 70s also cyclotrons and positive ions were used, e.g. the primary experiments of ^{10}Be and ^{14}C [Raisbeck et al., 1978b; Muller et al., 1978] and even the first applications of ^{10}Be in Antarctic ice were carried out with a cyclotron [Raisbeck et al., 1978a]. Tandem AMS became the favoured method for this isotope as well and was first applied to determine ^{10}Be concentrations in Manganese nodules [Turekian et al., 1979] in order to date these slowly growing marine archives. Detection methods have been established for further isotopes, for example ^{26}Al [Kilius et al., 1979], ^{36}Cl [Elmore et al., 1979], and ^{129}I [Elmore et al., 1980], that today are important nuclides

in geology or hydrology. Other radioisotopes proved to be more demanding, such as ^{41}Ca [Fink et al., 1984, 1991] or the actinides [Zhao et al., 1994, 1997; Fifield et al., 1996, 1997] In general, the radionuclides interesting for AMS originate from essentially every possible source of radioactivity on Earth: They are

- primordial: present on Earth since its formation (e.g. ^{244}Pu, Superheavies)

- radiogenic/fissiogenic: decay products of the primordial nuclides (e.g. ^{129}I)

- nucleogenic: produced via nuclear reactions induced by radiogenic nuclides (e.g. ^{36}Cl, ^{236}U, ^{239}Pu)

- cosmogenic: created in nuclear reactions induced by the primary cosmic radiation and its secondary products (e.g. ^{10}Be, ^{14}C, ^{26}Al, ^{36}Cl)

- extraterrestrial: collected in space or introduced via meteorites or dust and produced in cosmogenic reactions or in recent and nearby nucleosynthesis events (e.g. ^{10}Be, ^{26}Al, ^{53}Mn, ^{60}Fe)

- anthropogenic: produced in nuclear reactors or weapons and released via accidents, reprocessing plants or atmospheric and underwater explosions (e.g. ^{14}C, ^{36}Cl, ^{41}Ca, ^{63}Ni, ^{129}I, ^{236}U, Pu)

In the past thirty years AMS has been applied to study radionuclides in every conceivable environmental sample material, for example organic, water, ice, air, dust, meteorites, sand, sediment, rocks and lava. This variety illustrates the broad range of applications available with AMS, which makes this method an important tool in environmental sciences.

Chapter 2

AMS at a compact facility

In the following, the design and development of the low-energy AMS system Tandy is described. The setup is introduced and the improvements and upgrades undertaken in the past four years are summarized. In addition, the general limitations of the yields during an AMS measurement are discussed in special relation to the current Tandy setup. An overview of possible background contributions is given, again with special focus on their occurrence in compact AMS systems.

2.1   Overview of the Tandy setup

The compact Tandy AMS setup (Fig. 2.1) was originally designed in collaboration with the company NEC for ^{14}C analysis at low energies using the 1^+ charge state [Suter et al., 1999; Synal et al., 2000a,b; Jacob, 2001]. Later, the system was adapted for measurements of a number of other radioisotopes [Stocker et al., 2004, 2005]. Some have been studied in more detail, such as ^{41}Ca^{3+} [Schulze-König et al., 2010], ^{129}I^{3+} [Alfimov and Synal, 2010], actinides in 3^+ charge state [Fifield et al., 2004; Wacker et al., 2005; Christl et al., 2010a] and ^{10}Be^{1+} [Grajcar et al., 2004; Müller et al., 2010b; Christl et al., 2010c]. Several modifications have been made to the original setup since its construction, the most prominent new feature being the second HE magnet with a bending angle of $130°$ [Müller et al., 2010b]. The additional magnet was designed for further suppression of ^{9}Be during ^{10}Be measurements [Müller, 2009]. Furthermore, the energy focusing effect of the magnetic sector field enhances the beam transport efficiency on the HE side. It also should provide a better suppression of neighbouring nuclides in actinide AMS.

On the next pages, the general setup of the system is explained and for each instrumental section the main technical changes performed during this thesis are summarized. The details of performances for the single radionuclides are discussed later.
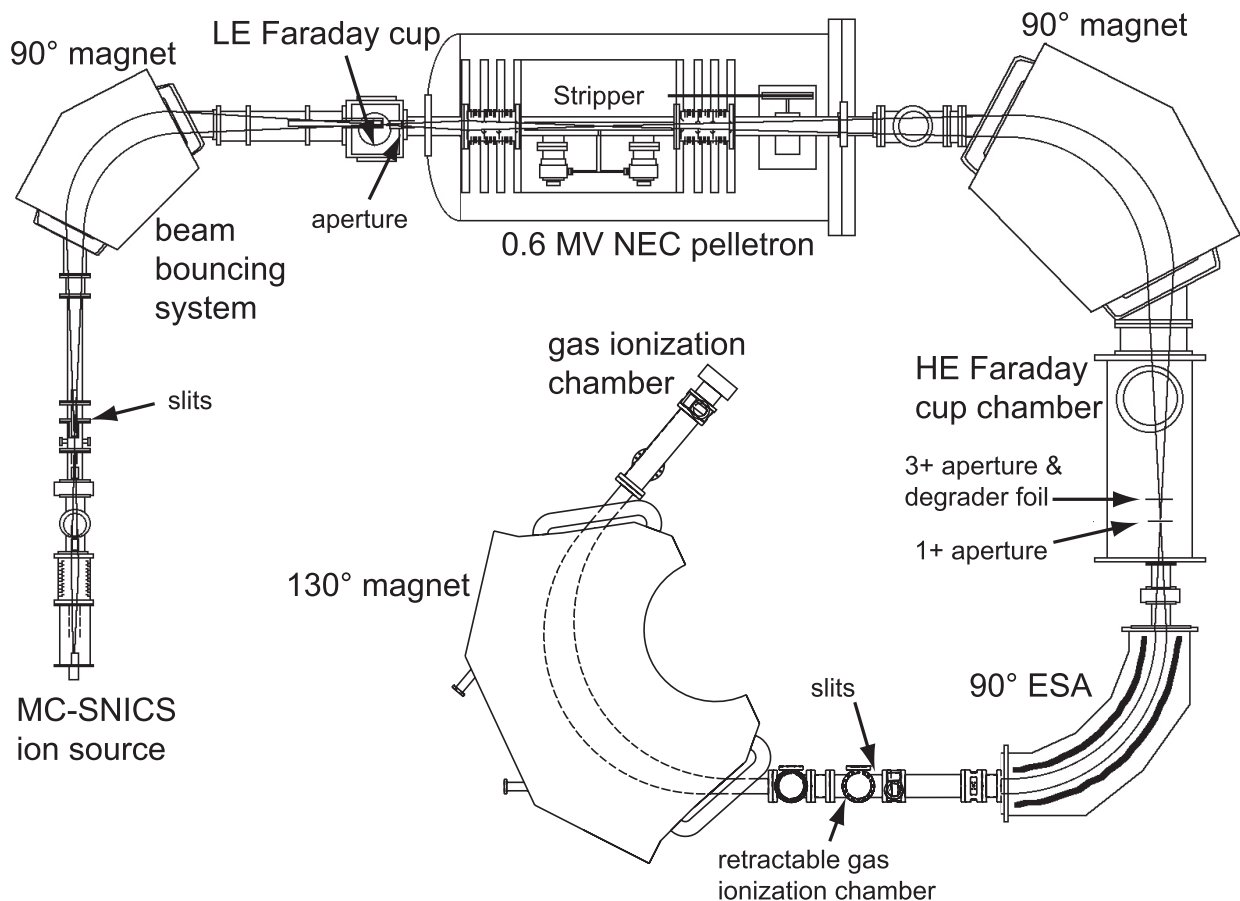
Figure 2.1: The upgraded TANDY AMS setup, modified from Müller et al. [2010b]

Ion source - formation of negative ions and molecules

In the NEC 40 MC-SNICS (Multi Cathode Source of Negative Ions by Caesium Sputtering) negative atomic and molecular ions of the desired isotopes are produced and accelerated to an energy of up to 65 keV. Al and Ti wheels are used that carry up to 40 sample cathodes made of Al, Ti, and Cu. The cathodes have sample holes with a diameter of 1 mm.

Modifications: The ion source was rebuilt following changes implemented by Southon and Santos [2007] and Priller et al. [2007]. A controllable lens focusing the Cs^+ beam onto the target was removed and replaced by an immersion lens, which is at the same potential as the target. The previous conical ionizer was substituted for a spherical Spectramat® ionizer. During operation of the ion source the target can be positioned via three lucite rods connected to the positioning screws of the sample wheel. The positions and the measures of the lenses were optimized for best Cs^+ focusing to the target and a minimal divergent negative ion beam at the extractor (Fig. 2.2) using the SIMION ion optics program [Simion, 2010]. The present beam output can be monitored simultaneously on a
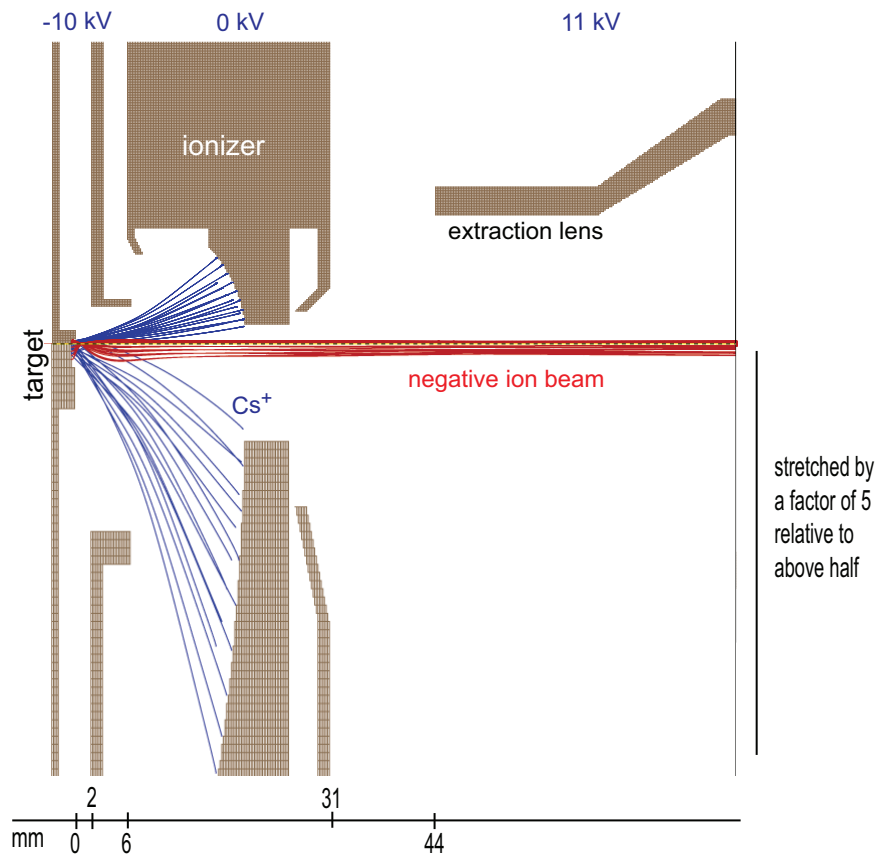
Figure 2.2: The SIMION simulation of the new ion source geometry as presented in Müller et al. [2010b] shows the good focusing of the Cs⁺ beam onto the target and the low divergence of the extracted beam. The numbers written above give the electrostatic potentials used in this simulation and the numbers below give the length scale. For better visibility of the Cs⁺ and the ion paths the lower half of the figure shows only a section of the radial symmetric setup that is magnified by a factor of five.

multimeter. However, positioning the target on the optical axis proved to result in higher currents on longer time scales than only optimizing for the momentary output during the tuning process. The positioning can be checked via an IP camera mounted behind the telescope focusing through the low-energy magnet.

Low-energy side - first magnetic separation and bouncing system

Electrostatic steerers on the low-energy (LE) side of the system direct the beam to the focus of the LE magnet, the first mass selective element in the beam transport. The LE magnet is equipped with a beam bouncing system enabling for fast switching between different masses. The bouncing system adjusts the beam energy of the different isotopes during their passage through the magnet so that they can be inserted sequentially into the pelletron or the LE Faraday cup. One pulse can be used to send the abundant isotope to

the LE Faraday cup and a second pulse to send the abundant isotope to the accelerator and subsequently to a cup on the high-energy (HE) side. With an appropriate positioning of the LE Faraday cup a quasi-simultaneous injection of a rare isotope into the accelerator and of an abundant isotope into the cup is possible, allowing for continuous monitoring of the beam output. A set of differently dimensioned apertures is used to adjust the resolution of the magnetic filter. With a set of steerers the injection to the pelletron is optimized.

Modifications: The coils of the LE magnet were replaced with a new set with more windings. Thereby, the maximal magnetic field was increased to 750 mT and the maximal deflection ability $(B_{max} \cdot r)^2$ now amounts to ca. 6800 amu·keV·e^{-2*}. A new power supply for the bouncing system was installed [Christl et al., 2013a]. The TREK 10/40A power supply can operate with a sequence of three pulsation voltages (max. ± 10 kV) to the chamber of the LE magnet. The capacity of the chamber amounts to 5.7 nF. The average loading current of the TREK power supply is 40 mA, but on short time scales < 1 ms higher loading currents can be provided. In this way, voltage changes of up to 4 kV can be reliably applied in ca. 1 ms. In addition to the pulsing of the abundant isotopes into the Faraday cups an offset bias can be employed to the rare isotope. By changing this voltage the sequential analysis of the abundant isotope on the LE and HE side is possible. Besides, more than one rare isotope can be sent to the detector (e.g. ^{233}U and ^{236}U) by switching the offset bias. The offset voltage facilitates the tuning process as the LE magnetic field can be kept stable at all times and only the pulsation voltages have to be changed to optimize the beam transport. As another new feature, the set of steerers at the entrance of the accelerator („ANA steerers ") now has a new maximal voltage of ± 400 V instead of ± 300 V.

Pelletron - acceleration, charge exchange and elimination of molecules

In the pelletron the beam can be accelerated by voltages of up to 600 kV. Long-time stable conditions can be reached with terminal voltages < 530 kV. In a gas stripper medium on the high voltage terminal, molecules are destroyed and positive charge states of the beam ions are populated. These positively charged ions are accelerated once more on the HE side of the pelletron. The transmission denotes the fraction of ions in the respective charge state measured as current on the HE side relative to the ion current on the LE side. At a given energy the yield of the charge states after the stripper depends on the density of the stripper medium (Fig. 2.3). At low stripper density the charge exchange processes between beam and stripper are not complete and thus the charge state distribution of the beam ions after the passage may not be in equilibrium. When the thickness d_{eq} is reached, the relative yields of the charge states stay constant if the thickness is increased further, but may be reduced by scattering processes of the beam ions with the stripper

---

*amu denotes one atomic mass unit
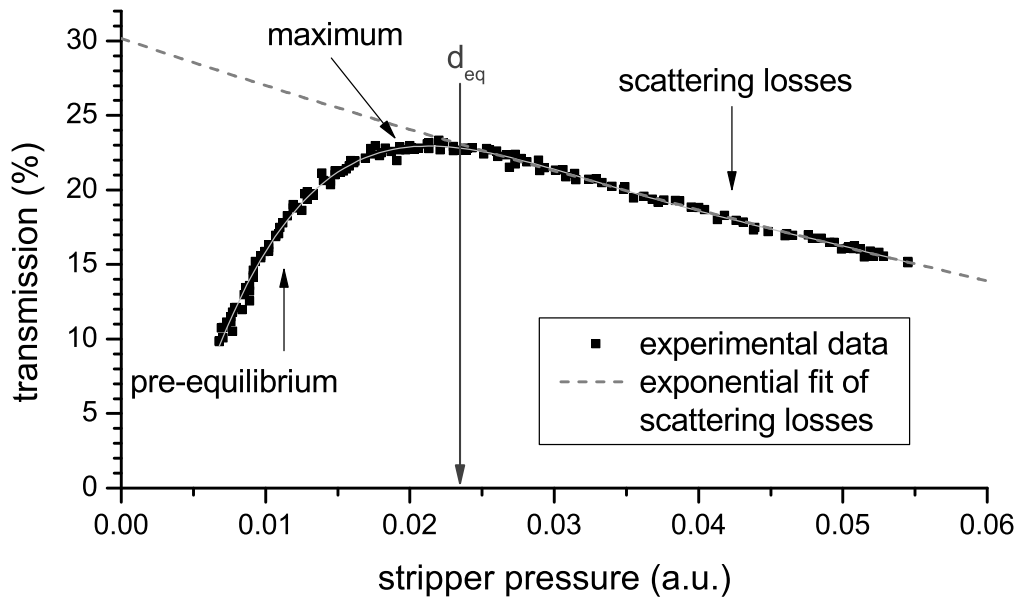
Figure 2.3: Stripper pressure dependent transmission of a positive charge state including an exponential fit that describes the beam losses caused by scattering at higher target densities.

medium. A detailed description of these processes is given in Jacob [2001]. A higher stripper density than d_{eq} may be required for full destruction of isobaric molecules. For routine measurements the transmission of the beam may be reduced compared to the maximal available value because of the scattering processes.

Modifications: Tests showed that high charge state yields through the Tandy accelerator can be achieved when using He as stripper gas [Vockenhuber et al., 2011, 2013] and will be discussed in detail in section 2.4. Repeated problems caused by sparks from the accelerator tubes to the PEEK capillary supplying the He gas were solved by mounting a He bottle on the terminal. The gas capillary leading from ground potential to the terminal was removed. The SF_6 gas handling system was replaced by a dedicated SF_6 system from the company DILO that had previously been used in the High Voltage Laboratory of ETH Zurich.

High-energy side - magnetic and electrostatic filters, current measurement

One charge state - usually the most populated one - is chosen by the first HE magnet following the accelerator. The focus position of the beam after the HE magnet is different for the various nuclides and charge states. The accelerator acts as a lens, whose focusing strength depends on the fraction of the energy gained on the HE side of the accelerator relative to the energy gained on the LE side [Jacob, 2001; Stocker, 2006]. The first main parameter for the focus position hence is the HE side charge state. Second, it is important whether the desired ion is extracted as a negative molecule from the ion source, because

then it carries on only the part of the LE side energy corresponding to its mass fraction of the total molecule. Faraday cups and extractable stacks of apertures are positioned in the cup chamber to allow for measurements in the 1^+ and the 3^+ charge state (Fig. 2.1). A thin degrader foil can be inserted close to the 3^+ focus [Müller, 2009]. As will be described later, this foil is used for $^{10}Be/^{10}B$ separation. Due to the molecular breakup of BeO^- in the terminal the focus of the Be^{1+} ions is closer to the 3^+ focus than to the 1^+ focus. An energy separation of the ions is achieved in the electrostatic analyser (ESA). Via adjustable slits the resolution of this device can be chosen in order to optimize the transmission of the desired ions relative to the background.

Modifications: The positions of the Faraday cups were altered. Now, in the one cup on the plane of the 3^+ focus position the isotopes ^{27}Al or ^{238}U can be collected when ^{26}Al or ^{233}U are counted. The analysis of ^{127}I and ^{40}Ca is performed in the other cup in the same plane, which also can be positioned on the beam axis. Another cup is placed closer to the first HE magnet and is used for ^9Be read out.

Detection system - counting of single radionuclides

The final detector in routine operation is a gas ionization chamber (GIC) [Müller et al., 2010a, 2012] with a split anode. In this setup, a two-dimensional energy signal can be recorded with the information on the energy loss ΔE from the first and on the deposition of the residual beam energy E_{res} from the second anode. After entering through a thin SiN window (dimensions range from $4 \times 4\,mm^2$ to $10 \times 8\,mm^2$ with thicknesses between 30 nm and 75 nm) the ions lose their energy in collisions with the isobutane detector gas (10-20 mbar). Depending on the stopping power of the incoming ion and its energy, a signal from both anodes or only from the first anode can be recorded. Two extractable GIC [Grajcar, 2005] are positioned at the ESA focal points for the 1^+ and the 3^+ charge state, respectively.

Modifications: For sensitivity tests or detector development the GIC was altered or replaced, which is explained in sections 3.3 and 4.2.1.

2.2   Efficiency of low-energy AMS

The following section discusses different processes that limit the efficiency of an AMS analysis with some special respects to the Tandy facility. For a highly sensitive AMS determination an optimized efficiency of the setup is crucial.

Several parameters provide information on the efficiency of an AMS setup: In routine operation one can control the **transmission** through the accelerator via the particle currents on the LE side and the HE side. The rare isotope events are eventually measured in the detector relative to the intensity of the abundant isotope in the HE cup. This ratio

is affected by the quality of the beam transport through the HE side of the spectrometer and by the detection efficiency. When examining a standard material and comparing the result to the nominal value, one gets the **HE side yield**. The transmission through the accelerator multiplied with the HE side yield results in the **overall transmission** through the system.

The measurement's **overall yield** additionally includes the efficiency for producing the desired negative ion in the sputter source. It is quantified by preparing targets containing a known amount of the rare isotope and counting the number of events of this isotope in the detector until the target is fully exhausted. With a well-known overall transmission through the system the yield for the formation of negative ions can therefore be calculated in such a sample. The overall yield of an AMS measurement is governed by several parameters, which are summarized below.

Negative ion yield: The extraction of negative ions or molecules provides the opportunity to suppress isobaric background but even with the appropriate choice of the extracted ion or molecule generally only small yields $< 1\%$ are achieved. The performance can be improved using metallic matrizes (Cu, Nb) for better thermal and electric conductivity of the target [Hunt et al., 2006]. In other cases, Fe_2O_3 as part of the matrix is thought to facilitate the formation of negative oxide-molecules, e.g. during BeO^- [Christl and Kubik, 2013] or UO^- extraction because of the enhanced availability of O in the matrix.

Charge state yield: At present, for LE-AMS charge states up to the 3^+ are used on the HE side of the accelerator. The transmission of the beam through the accelerator usually amounts to 10-60%. The yield of the positive charge states in the stripping process is determined by the charge exchange cross sections for electron capture and ionization processes. The cross sections strongly depend on both the proton number of the beam nuclide and the velocity of the beam nuclide when interacting with the stripper gas, which is possibly lowered by the initial use of molecular negative ions. They also depend on the ionization potential of the applied stripper gas. The mass of the stripper gas defines the maximal scattering angle in a single collision.

The transmission for a given charge state is decreased below the actual charge state yield because of these scattering processes, in particular if a high thickness of the stripper is necessary for full destruction of molecular background via multiple collisions (Fig. 2.3). The intensity of the beam is roughly described by $I = I_0 \cdot e^{-\sigma_{scat} \cdot \delta}$, i.e. it decreases exponentially with increasing stripper density (Fig. 2.3). In addition, the breakup of molecules in the stripping process (Coulomb explosion) causes a broadening of the beam because of the Coulomb repulsion between the two breakup partners.

Ion optical losses: The ion optical acceptance is mainly given by the dimensions of the beam and the system. It is limited by parameters such as size and position of slits and apertures or the acceptance angle of the stripper (e.g. 14 mrad at the Tandy).

At the Tandy system no lenses are installed after the ion source. Furthermore, electrostatic steerers are used for beam guidance only on the LE side. For the Tandy, the given geometry on the HE side is critical because a further adjustment of the position of the focal points via lenses is not possible. As a result, the detector position is adjusted to the final focal point of the magnets and the ESA on the HE side for the charge state 1^+ from the breakup of a BeO^- molecule. As stated in the previous section, the HE accelerator tube has a strong lens effect, so that the focus position after the HE magnet depends on the ratio between the energy gained on the LE side relative to the energy on the HE side. The focal position of Be^{1+} originating from the breakup of a BeO^- molecule is close to the focus for the 3^+ charge state if negative atomic ions are used or if the breakup is only of minor importance as in the case of actinide-oxides. Ion optical losses are reduced for these configurations compared to the 2^+ or higher charge states than the 3^+. Furthermore, losses in the beam transport may occur in the detection system, e.g. after the interaction with the degrader foil, but they are listed below in the part on the detection efficiency.

Detection efficiency: The efficiency of detecting the ions is given by the geometric acceptance of the detector and its ability to convert charge created by the beam ions into an electronic signal. For the GIC in the routine Tandy setup the efficiency of the detector amounts to almost 100%, but can be reduced by effects such as pile-up, dead time or wide-angle scattering in the entrance foil.

The term detection efficiency denotes the factor of a sample's measured ratio relative to its nominal or real value and includes ion optical losses between the HE cup measuring the abundant isotope and the detector counting the rare isotope. Because of these ion optical losses on the HE side, in practice at most 90% of the ions leaving the accelerator in the right charge state can be guided to the detector. However, this value is further lowered to ca. 18% when applying the degrader foil technique in the case of ^{10}Be AMS. Scattering in this foil leads to angular and energy broadening of the beam and to losses in the ESA and the HE2 magnet. Similarly, with a time-of-flight detector installed in this setup, the detection efficiency is reduced to ca. 30% [Vockenhuber et al., 2011]. Because of beam broadening after scattering in the start-foil only a fraction of the initial particles reach the stop detector. Geometric losses on grids integrated in the start and stop detectors can additionally lower the efficiency of the time-of-flight detector. In the new absorber setup, with foils and a gas volume preceding the GIC, 2^+ ions were used. The detection efficiency then is reduced to at most 60% because of straggling and ion optical losses.

2.3   AMS background counting rates

Background counting rates in AMS can occur for a number of reasons. The following discussion focuses on the kinds of background that mimic the radioisotope so that it cannot

be distinguished in a simple GIC detector. This excludes e.g. pile-up originating from high counting rates caused by interferences of other isotopes with the same m/q ratio than the desired one. One major source of such mimicking background in mass spectrometry is isobaric and molecular interferences. In the Tandy setup, scattering or charge exchange processes of the abundant isotopes on the residual gas in the accelerator tubes, in the degrader, or in the magnets and the ESA also can give rise to background. The destruction of molecular isobaric background in AMS takes place in a foil or a gas target in the so-called stripper. In the charge exchange process positively charged beam ions are created and molecules are broken up after multiple collisions with the stripper medium [Suter et al., 1997; Synal et al., 2007] or in a Coulomb explosion if they reach higher positive charge states.

At the low incident beam energies used at compact AMS facilities the efficient destruction of molecules in multiple collisions is the dominant process. The number of collisions with the stripper gas depends on the target density. Therefore, on the one hand a thicker stripper medium results in a better suppression of molecular background. But on the other hand the gas density in the stripper affects the amount of residual gas in the accelerator tubes and thus the number of background events due to scattered or recharged abundant isotopes.

In the following equation the single background contributions are identified. The measured ratio R_{tot} of a counting rate at the mass of a rare isotope (e.g. ^{236}U) relative to the intensity of an abundant isotope (N_{ab}, e.g. ^{235}U, ^{238}U) is given depending on the stripper areal density δ.

$$
\begin{aligned}
R_{tot} &= R_{real} + R_{isobar} + R_{mol,HE}(\delta) + R_{scat}(\delta^*) \\
&= \frac{N_{real}}{N_{ab}} + \frac{N_{isobar}}{N_{ab}} + \frac{N_{mol,LE}}{N_{ab}} \cdot e^{-\sigma_{mol} \cdot \delta} + \frac{N_{mol,LE}}{N_{ab}} \cdot (1 - e^{-\sigma_{scat} \cdot \delta^*})
\end{aligned}
\tag{2.1}
$$

It is presumed that the rare and the abundant nuclide have the same phase space after the interaction with the stripper medium. In the following, the various background contributions are listed:

R_{real} & R_{isobar}:   Depending on the sample a component of real radionuclides may be available (N_{real}, e.g. ^{236}U). Furthermore, the material may contain atomic isobars (N_{isobar}, e.g. ^{236}Np to ^{236}U) that cannot be separated in this setup. If these rates N_{real} and N_{isobar} are normalized to the rate of the abundant isotope N_{ab}, the deduced ratios R_{isobar} and R_{real} are independent of the stripper pressure.

$R_{mol,HE}$:   The counting rate of surviving molecules relative to the beam intensity ($R_{mol,HE}$) depends on the initial number of molecules ($N_{mol,LE}$) before interaction with the stripper medium, the cross section for molecular destruction σ_{mol}, and the areal density δ. The intensity of molecules decreases exponentially with increasing stripper thickness (Fig. 2.4).
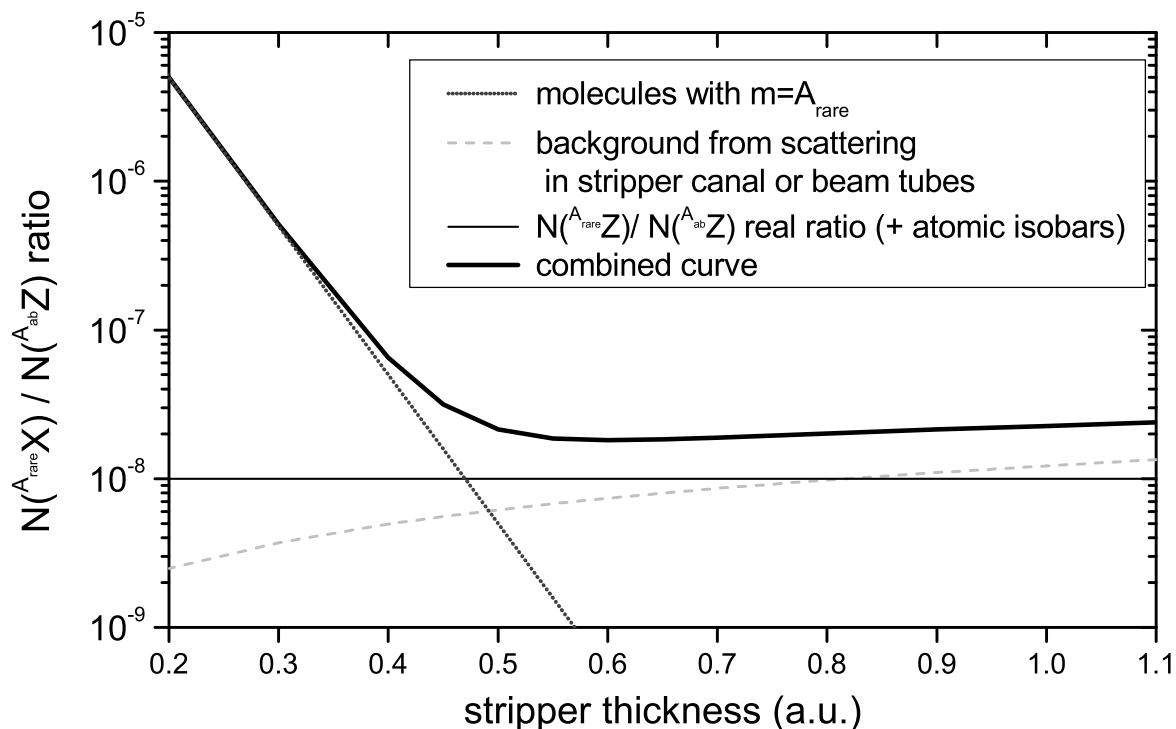
Figure 2.4: The theoretical curve for the stripper dependent ratio of the target mass A_{rare} relative to a stable (or abundant) isotope $N_{ab} = N(^{A_{ab}}Z)$ is influenced by molecular survival. Background from scattering processes and counting rates of a nuclide or its atomic or molecular isobars are summarized under $N(^{A_{rare}}X)$.

Thus, if molecular isobars exist, the exponential trend of the molecular destruction dominates at lower stripper densities.

R_{scat}:   On the other hand, the relative number of scattering processes (R_{scat}) increases with the number of projectiles $N_{mol,LE}$ (usually molecules of the abundant isotopes) available for such processes, the areal density δ^* in the accelerator tubes, and the respective cross section σ_{scat}. With higher areal stripper density δ, the vacuum in the accelerator beam tubes might be reduced and more background events may occur by scattering and charge exchange reactions with the residual gas (δ^*). However, the appearance of this effect may depend strongly on the general vacuum quality of the system. This background contribution is linear with δ^* for small values of $\sigma_{scat} \cdot \delta^*$ but should approach a maximal value for high areal densities, which is represented by the negative exponential growth function. In addition, energy and angular straggling of the ions in the stripper increase with the number of collisions.

2.4   Effects of He stripping

Experiments at the MICADAS AMS facility with He as stripper gas revealed very high charge state yields for C^{1+} at beam energies below $100\,keV$ [Schulze-König et al., 2011], which might even facilitate mass-spectrometric radiocarbon measurements without an accelerator stage [Synal et al., 2013]. Furthermore, scattering of beam nuclides on He to large angles also is reduced due to its lower mass compared to N or Ar. Following these successful developments, the effects of He stripping were investigated at the higher energies of the Tandy system for different radionuclides. Generally, an enhanced yield of the mean charge state is observed compared to other stripper media. This would mean that after the interaction with the He stripper the distribution of charge states is narrower than in other gases. At certain beam energies hence very high yields for the preferred charge state can be gained.

By choosing He and an appropriate charge state the efficiency for all isotopes measured at the Tandy can be improved compared to Ar, which had been used before [Vocken-huber et al., 2013]. Here, the results for actinides, Be, and Al are discussed. The pressures p given in mbar can be converted to areal He densities d by means of the formula $d = 2.96 \cdot p^2 + 2.90 \cdot p - 8.3 \cdot 10^{-4}$ with d resulting in $[\mu g/cm^2]$ and the pressure p [mbar] quantified in the stripper gas supply line on the terminal [Maxeiner, 2012].

2.4.1   Transmission improvements for actinides

Wittkower and Betz [1973a] already found that charge state fractions of U ions with energies of few MeV can be unexpectedly high with He as stripper gas. They explained this by the high electron binding energy of He compared to other gases, which reduces the occurrence of electron transfer from He to beam nuclides with low energies. For the actinides several tests were performed at the Tandy using the abundant and long-lived isotopes ^{238}U and ^{232}Th [Vockenhuber et al., 2011]. In Fig. 2.5 the transmission of U is depicted for various beam energies at the terminal. The charge states $< 3^+$ cannot be recorded over the full energy range accessible with the Tandy pelletron. The bending strength of the HE magnet ($33\,000\,amu{\cdot}keV{\cdot}q^{-2}$) defines the maximal value of the terminal voltage for heavy ions in low charge states (e.g. Fig. 2.5).

The ion source voltage was adjusted for the ion optical properties of the system, i.e. in order to obtain a beam waist in the middle of the stripper canal the energy of the beam after the source has to be about 10% of the energy gained in the acceleration on the LE side of the pelletron [Jacob, 2001].

In order to guarantee a full suppression of molecular isobars such as $^{235}UH^{3+}$ and $^{232}ThH^{3+}$ (section 4.3), the stripper pressure has to be increased above the value for maximal transmission. Still, in regular measurements of U samples a transmission of 40% can
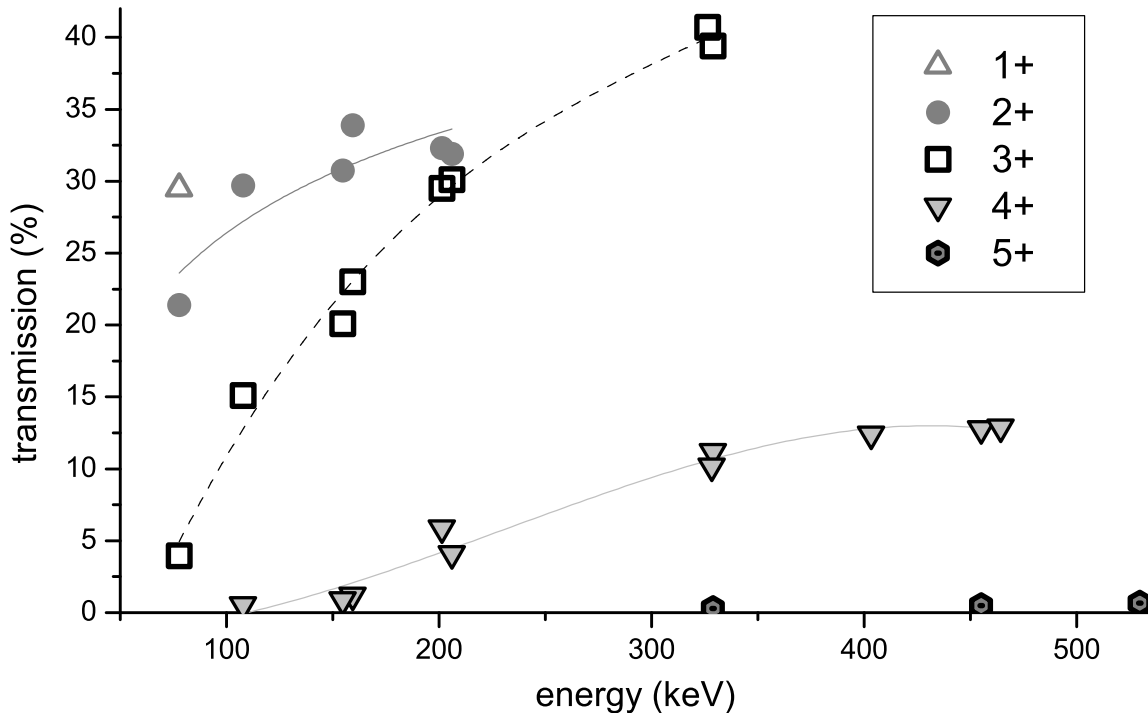
Figure 2.5: Transmission of ^{238}U from UO$^-$ molecules to different positive charge states at stripper pressures of 0.02-0.03 mbar (corresponding to a thickness d=0.07 μg/cm^2) for various energies of U at the terminal. At this value of the stripper thickness the charge state distribution is in equilibrium. The bending strength of the first HE magnet limits the record for low charge states to low terminal voltages. For the charge states 2$^+$, 3$^+$ and 4$^+$ fits are included to guide the eye.

be reached. This is an enormous improvement as with Ar at full suppression of molecular background a maximal transmission of 15% had been achieved [Wacker et al., 2005]. Furthermore, even in the 4$^+$ charge state a transmission above 10% at a terminal beam energy of 460 keV can be attained, which triggered tests for ^{236}U^{4+} measurements (section 4.2.1).

2.4.2   Transmissions for lighter elements

Be and B stripping with He

The Be transmission with Ar amounts to at most 55% for the 1$^+$ charge state and to 13% for the 2$^+$ charge state at stripping energies of 240 keV [Grajcar, 2005]. After the installation of the He gas bottle on the terminal detailed studies of Be and B transmissions in He were performed (Fig. 2.6). For both, Be and B, the 1$^+$ charge state provides high transmissions through the pelletron reaching up to 60%. Thus, the yield during routine Be AMS is improved by the transition from Ar to He, too.
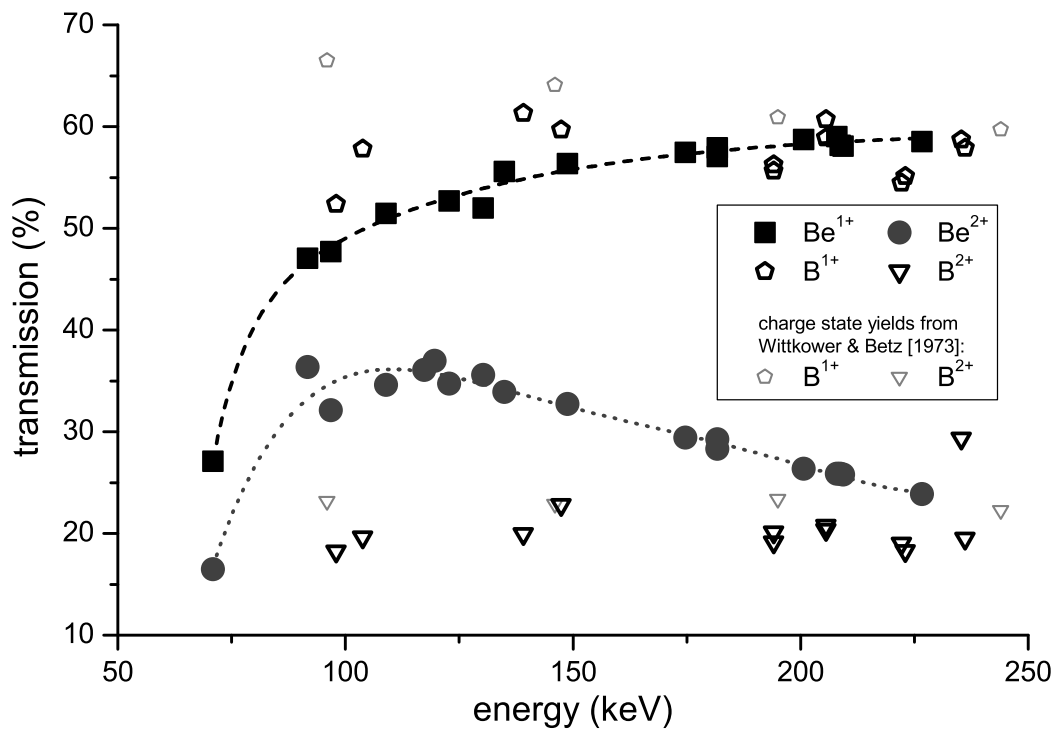
Figure 2.6: Transmissions through the Tandy accelerator equipped with a He stripper (p= 0.035 mbar or d=0.10 μg/cm^2, pressure adjusted for optimal transmission) were recorded for Be and B at terminal voltages ranging from 220 kV to 525 kV. Be and B carry only the fraction of the kinetic energy reached at the terminal corresponding to their mass fraction of the original BeO$^-$ or BO$^-$ molecule. Fits for Be^{1+} and Be^{2+} are included to guide the eye. Charge state yields of B in He from Wittkower and Betz [1973b] are included for comparison.

A surprising effect was found for low terminal voltages. Usually, the charge state yield maxima follow one another with increasing terminal voltage. The charge state 2$^+$ of Be exhibits a local maximum (37%) at a stripping energy of ca. 120 keV, while the 1$^+$ maximum (60%) is at a stripping energy above 200 keV. Such an increase for a higher charge state at lower energies has not been observed yet. It is possibly related to electron shell effects in the interaction of the beam with the He gas. Be^{2+} carries two electrons and thereby has a He-like closed 1s-shell. There are several examples for the atomic shell structure affecting the charge state yield, e.g. in C foils for I and Br [Moak et al., 1967] or Sr [Kumar et al., 2011]. Shima et al. [1992] also report on enhanced mean charge states when stripping ions to electron configurations of noble gases via a C foil. Increased mean charge states compared to preceding noble gases also were observed for B, Na, Mg, and Al when stripping with He gas by Hvelplund et al. [1972], pointing at an easier ionization of those elements.

Apart from the high yield at low energies the selection of the 2$^+$ charge state would give the advantage of additional B suppression because the B^{2+} yield is nearly a factor of two lower than the Be^{2+} yield. The Be^{2+} yield increases to ca. 37% while the B^{2+} yield

stays relatively constant at ca. 22% over the energy range accessible with the Tandy. In contrast, the Be and B transmissions are similar in the 1^+ charge state over the same energy range.

The available data for B charge state yields in interaction with He show slightly higher percentages [Hvelplund et al., 1972; Wittkower and Betz, 1973b] than the transmission data observed at the Tandy. This is consistent because the transmission data observed at the Tandy setup are not corrected for scattering and ion optical losses, which would be necessary in order to calculate the charge state yields.

The high charge state yields of Be^{2+} at energies < 150 keV imply that with a compact AMS system working at 300 kV and equipped with an ESA and two magnets on the HE side a competitive determination of ^{10}Be is possible. In this configuration the same final beam energy of ca. 750 keV can be gained in the 2^+ state as in the current routine setup with the Tandy working at 525 kV terminal voltage in the 1^+ charge state. Hence, the Be-B separation in the detection system is the same, too. As stated above, using the 2^+ charge state at low energies the ^{10}B counting rate is reduced by an additional factor of two. However, due to the lower maximal transmission compared to the 1^+ state a reduction of the overall efficiency of $\frac{37}{60}$ compared to the optimal 1^+ conditions has to be accepted in a compact 300 kV AMS system applying the 2^+ charge state and the degrader foil technique. Such a setup shall be competitive to the current Tandy setup concerning the ^{10}B suppression with the degrader and the ion detection efficiency.

Al stripping with He

He stripping provides higher yields for the charge states 2^+ and 3^+ of Al (Fig. 2.7). In previous operation with Ar at the Tandy maximal transmissions of 44% and 9%, respectively, had been achieved for a beam energy of 600 keV [Stocker et al., 2004; Stocker, 2006].

Equilibrium charge states for Al in He were reported by Hvelplund et al. [1972] in the energy range from 100 keV to 400 keV. They also found a dominant 2^+ charge state (ca. 60%) and rising yields for the 3^+ (<15%) and 1^+ fractions between 20% and 30%. For the charge state 4^+ a yield of 0.8% is given at the highest beam energy of 400 keV. At the Tandy, the charge states 4^+ and 5^+ only have yields in the sub-percent level after passing the He stripper, too.

In the 2^+ charge state the m/q interference of $^{13}C^{1+}$ complicates the measurement of ^{26}Al in the current setup. With the He stripper the transmission for the 1^+ charge state is 25%, lower than the maximal value of nearly 50% with Ar, which had been recorded at a beam energy of ca. 300 keV. The transmission in the 1^+ charge state is dramatically reduced for both, He and Ar, if full suppression of molecular background is required. Then only a transmission of 20-25% is reached with Ar and less than 15% with He. N_2 shows similar charge state yields as Ar [Ryding et al., 1970; Suter, 1998], also regarding that mostly the
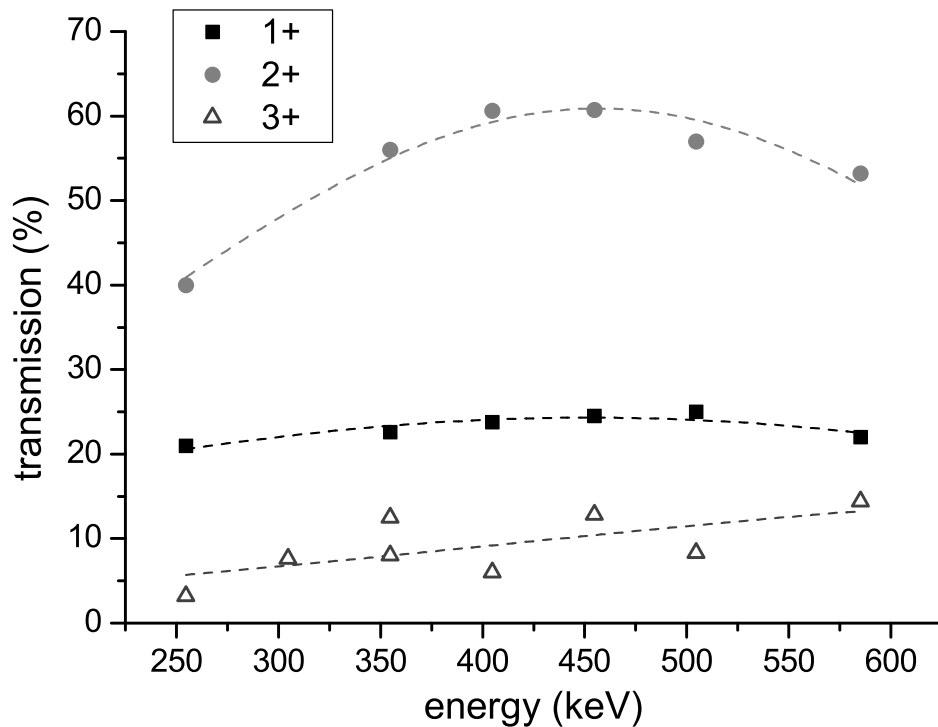
Figure 2.7: Al transmissions for the Tandy using He stripping at 0.04 mbar gas pressure (d=0.12 µg/cm²). Fits are included to guide the eye.

1⁺ charge state is populated at beam energies below 500 keV and higher yields for the 2⁺ charge state are observed above this energy.

In general, He as stripper gas improves the yields for the charge states 2⁺ and 3⁺ at the beam energies available with the Tandy. These states were further investigated.

However, for Al the advantage of LE-AMS compared to larger facilities in terms of beam transport efficiency is not as pronounced as for other nuclides. At other AMS systems using higher charge states overall transmissions of 15% (7⁺, E≈110 MeV, Fifield et al. [2007]) or 48% (3⁺, E≈12 MeV, Auer et al. [2007]) can be reached, too, but beam handling is more complex and special detection systems may be required.

Chapter 3

Low-energy AMS of light radionuclides

3.1 ^{10}Be AMS

Techniques

The first detection of natural ^{10}Be in deep-sea sediments used decay counting [Goel et al., 1957] and a total run time of 1400 h was necessary to determine the activities of four samples. Due to the long half-life of ^{10}Be of (1.387$\pm$0.012) Ma [Korschinek et al., 2010; Chmeleff et al., 2010] mass-spectrometric methods are clearly favourable for its detection. The mass-spectrometric determination of ^{10}Be is interfered by the stable isobar ^{10}B. Unlike ^{14}N in AMS of ^{14}C, the isobar ^{10}B readily forms negative ions while Be$^-$ yields are only poor. The optimal extraction of Be from a Cs sputter ion source is accomplished by generating BeO$^-$ from a BeO target, but B forms BO$^-$, too. Consequently, ^{10}B has to be suppressed on the HE side of the AMS system by six to ten orders of magnitude. Generally, this is done by taking advantage of the higher proton number of B, which results in a higher stopping power compared to Be.

In the first AMS measurement with a cyclotron [Raisbeck et al., 1978b] the problem was circumvented by extracting positive ions (2$^+$), which were accelerated to 30 MeV. Afterwards the ^{10}B was completely absorbed in an Al foil. Even during normal AMS operation the ^{10}B beam is too intense for a direct detection in a GIC, which can handle counting rates of few 1000 events per second. For this reason, ^{10}B has to be suppressed by several orders of magnitude before the beam enters the sensitive detector volume. At tandem accelerators the method of absorbing ^{10}B directly in front of the detector was applied, too [Turekian et al., 1979; Klein et al., 1982; Kubik and Christl, 2010].

An alternative method, the so-called degrader method, realizes the separation of the two isobars partially already at an earlier point in the beamline: The ^{10}Be-^{10}B beam passes a thin foil on the HE side. There, the isobars lose a different amount of energy corresponding to their stopping power. By applying an electric or magnetic sector field the ions are filtered according to their energy and momentum and the isobars are separated. At the

Tandy the ^{10}B interference can be suppressed by ca. ten orders of magnitude in total [Müller, 2009]. However, losses of ^{10}Be are caused by energy and angular straggling in the degrader foil. Additionally, like in the situation after the stripper medium, a distribution of charge states (mainly 1$^+$ and 2$^+$) is present and leads to a further reduction of the beam intensity by about a factor of two. The advantage of this method is its easy practicality at lower total beam energies because range straggling in an absorber increases when lowering the beam energy. Therefore, the degrader method is more readily available at compact AMS systems, e.g. it was early used for measuring ^{10}Be at a tandetron running at 2 MV [Raisbeck et al., 1984].

There are manifold applications of cosmogenic ^{10}Be: Meteoric (or atmospheric) ^{10}Be designates ^{10}Be originally produced in the atmosphere and in-situ produced ^{10}Be means the one created by reactions in rocks on the Earth's surface. Natural archives (Manganese crusts, sediments) store the meteoric ^{10}Be and can be dated via the ^{10}Be decay curve. In rocks, ^{10}Be is continuously produced in nuclear reactions, e.g. on the O in SiO_2. This can be used for dating: From the concentration of ^{10}Be the time span can be calculated, during which the sample has been exposed to the cosmic rays. Other examples of ^{10}Be applications will be discussed below in chapter 5. Typical ^{10}Be/^{9}Be ratios in environmental samples are relatively high, ca. 10^{-11} to 10^{-8}. Usually, in the chemical preparation samples are spiked with a larger amount of ^{9}Be than present in the original material. This way, the concentration of ^{10}Be can be determined in the final AMS samples, which then have ratios in the order of 10^{-15} to 10^{-11}.

^{10}**Be at a beam energy < 1 MeV**

In order to facilitate the suppression of ^{10}B in LE-AMS the suppression of the isobar in the ion source was tested in previous studies [Grajcar, 2005; Müller, 2009]. After extracting fluoride ions from targets prepared as BeF_2 or $BaBeF_4$, the ^{10}B can be easily suppressed in the GIC because BF$^-$ is only metastable and thus the ^{10}B is reduced already by five orders of magnitude [Zhao et al., 2004; Grajcar et al., 2007]. But with maximal currents of 300 nA the negative ion yield for BeF$^-$ is lower than for BeO$^-$, which would require measurement times that are ca. a factor of 10 longer. Additionally, either the handling of the sample material is difficult (BeF_2) or the material shows bad performance characteristics in the ion source ($BaBeF_4$). Hence, also for LE-AMS BeO$^-$ is preferable, although it requires more elaborate ways of suppressing the B isobar, e.g. the application of the degrader foil method in combination with a sensitive GIC. For this reason, a GIC with very low noise-level was constructed [Müller, 2009; Müller et al., 2010a, 2012]. During routine operation with the present ion source setup maximal BeO$^-$ currents of 4.5 μA are extracted from BeO targets mixed with Nb powder (325 mesh), which is added to improve the Be output [Müller et al., 2010b].

For the degrader foil method at the Tandy [Müller et al., 2010b] a thin $Si_3N_{3.1}$[*] foil (75 nm thickness, $10 \times 8 \, mm^2$) is installed close to the focus of Be^{1+} between the first HE magnet and the ESA. In this foil, surviving ^9BeH molecules are destroyed and, as the primary effect, ^{10}B loses more energy than ^{10}Be. ^{10}B is stronger deflected in the following ESA. With asymmetric slits at the ESA focal point, ^{10}B is suppressed by ca. four orders of magnitude. The final HE2 magnet refocuses the beam to the detector and removes background originating from ^9Be ions. The counting rate of an AMS sample is typically reduced to a maximum of 3000 events per second, which can be handled in a GIC. The detector is equipped with a split anode: The energy loss in the first part can be recorded as ΔE signal, while the residual beam energy (E_{res}) can be measured with the second anode.
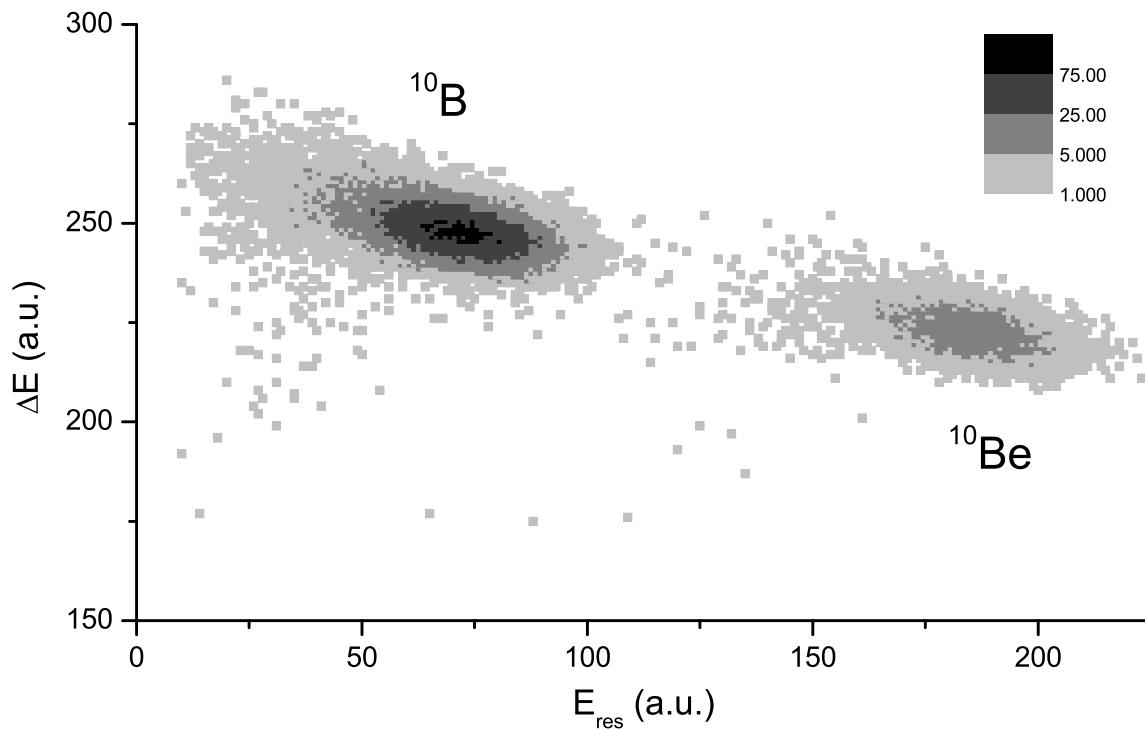
Figure 3.1: ^{10}Be and ^{10}B are separated on the split anode of the GIC due to their different energy loss behaviour. The spectrum was recorded in the degrader foil setup, so ^{10}B already entered the detector with a lower energy than ^{10}Be ($E_{^{10}Be} \approx 700 \, keV$). As the channel number in the spectrum corresponds to the deposited energy for this and all other spectra, the axis values are given as energy in arbitrary units (a.u.). Electronic amplification factors are the same for both anodes.

The ^{10}Be and ^{10}B beams are separated as a result of their different energy loss in the GIC (Fig. 3.1). The HE side yield of the beam, i.e. the ^{10}Be transmission through the foil to the detector, amounts to nearly 20%. This reduction in detection efficiency results from energy- and angular straggling as well as from post-stripping and is the major drawback

---

[*]In the following, the material $Si_3N_{3.1}$ is written as SiN

of this method. Still, with a value of ca. 11% the overall transmission through the system is competitive to the larger Tandem facility at ETH Zurich, which reaches the same value.

3.2 ^{26}Al AMS

Techniques

The analysis of ^{26}Al ($T_{1/2}$=(715±20) ka, weighted average from Wallner et al. [2000]) is interfered by the stable isobar ^{26}Mg. Because Mg does not form negative ions, the extraction of Al$^-$ from a Cs sputter ion source is an easy way to suppress the isobar. This method finds application at most AMS facilities measuring this isotope. The yield of Al$^-$, however, is relatively low. Typically, Al$_2$O$_3$ is prepared for AMS targets and Al$^-$ currents up to several hundred nA can be extracted. Hence, for a sample with an ^{26}Al/^{27}Al ratio of 10^{-13} one has to count for nearly one hour in order to achieve a 5% statistical uncertainty at a HE side particle current of 200 nA. Examples for environmental ^{26}Al/^{27}Al ratios are 10^{-14} in marine sediments [Wang et al., 1996] and 10^{-12} in sand and silcrete samples [Fifield et al., 2007]. The highest reported overall efficiency for Al from environmental samples is achieved with Al$^-$ extraction and amounts to $2.2 \cdot 10^{-4}$ [Auer et al., 2007]. The extraction of AlO$^-$ results in a much higher negative ion yield and currents of up to 3 μA. Thereby, the yield in the ion source can be increased by factors 10-20 [Fifield et al., 2007]. But the isobar separation methods, e.g. a gas filled magnet [Arazi et al., 2004; Fifield et al., 2007], that are necessary to suppress ^{26}Mg, require high beam energies and are available only at few facilities.

^{26}Al^{3+} at the Tandy

First tests at the novel Tandy setup were performed with the GIC detector equipped with a 30 nm thin SiN entrance foil and demonstrated that the 3$^+$ charge state is the most uncomplicated way to measure ^{26}Al. For Al, molecular background is completely eliminated when using the charge state 3$^+$. The spectrum for ^{26}Al^{3+} hence is very clean and only shows ^{26}Al (Fig. 3.2).
The beam transport from the HE cup to the detector is very efficient in this charge state. Standards are measured close to their nominal value. However, the maximal transmission through the accelerator is only 15%. This reduces the overall efficiency and makes it difficult to determine samples with very low ^{26}Al/^{27}Al levels. Already single counts lead to blank values in the order of 10^{-14} at a run time of 900 s with the currents available at the Tandy (I(Al$^-$) < 200 nA).
In the 1$^+$ charge state the yield would be much higher, peaking at 25%. But the suppression of surviving 1$^+$ molecules requires a large increase of the stripper pressure. This
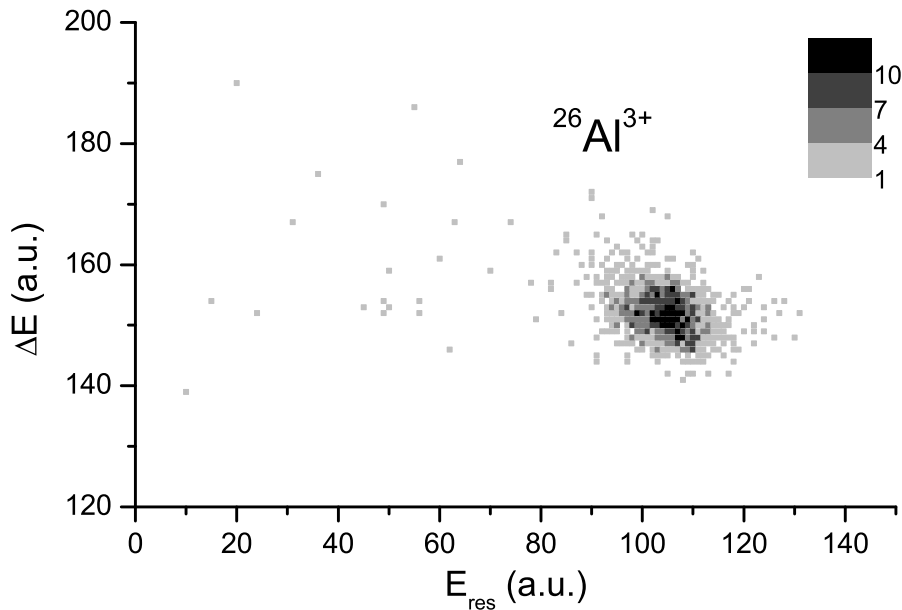
Figure 3.2: No interferences of other nuclides are visible in the two-dimensional spectrum (ΔE-$E_{res.}$) of a $^{26}Al^{3+}$ standard. The total energy of the beam was $E_{^{26}Al} = 2.17\,MeV$

entails major beam losses and transmission for the 1^+ eventually is reduced to ca. 12% and is lower than for the 3^+ under real measurement conditions. The usage of this charge state was not pursued, also because the 1^+ charge state yield with He is about a factor of two lower compared to the use of Ar or N_2 as stripper gas (section 2.4.2).

In the 2^+ charge state the background of the m/q interference $^{13}C^{1+}$ hampered analysis with the routine detector. In the following section a method to suppress this interference will be described.

3.3   Passive absorber method in low-energy AMS

3.3.1   Introduction and setup

Similar to the usage of a degrader foil for background suppression, a passive absorber takes advantage of the different energy loss characteristics of isobars. Absorbers were early applied in AMS for ^{10}B rejection at energies above $20\,MeV$ [Turekian et al., 1979; Klein et al., 1982]. More exotic applications of AMS at large facilities include the separation of ^{182}W from ^{182}Hf [Vockenhuber et al., 2007; Winkler et al., 2007]. Also in the current setup for ^{10}Be AMS at the EN Tandem in Zurich this method is used [Kubik and Christl, 2010]. But the absorber method was thought to fail at beam energies $< 10\,MeV$ as the straggling ranges of ^{10}Be and ^{10}B were estimated to be too large for sufficient isobar separation. However, Sun et al. [2007] found that very thin and homogeneous SiN foils can be produced that show little energy loss straggling at beam energies of few MeV and

below, which was critical for the development of LE-AMS gas ionization detectors [Müller et al., 2010a, 2012]. With the low straggling ranges in SiN foils, the good ^{10}Be-^{10}B separation achieved in the novel detector, and the low ^{10}B counting rates observed during some carrier-free ^{10}Be measurements, the absorber method promised to be an alternative to the degrader setup. As described in section 2.2, about 80% of the ^{10}Be beam are lost in the HE spectrometer when using the degrader foil method. If a suppression of ^{10}B in an absorber were possible, the detection efficiency could be increased. The passive absorber constructed to test this method at the Tandy consists of a modified entrance window holder for the routine GIC (Fig. 3.3). The volume preceding the normal entrance window is connected to the detector volume via two 1 mm holes. So, in this setup the absorber and the detector volume can only be filled with the same gas at equal pressure.
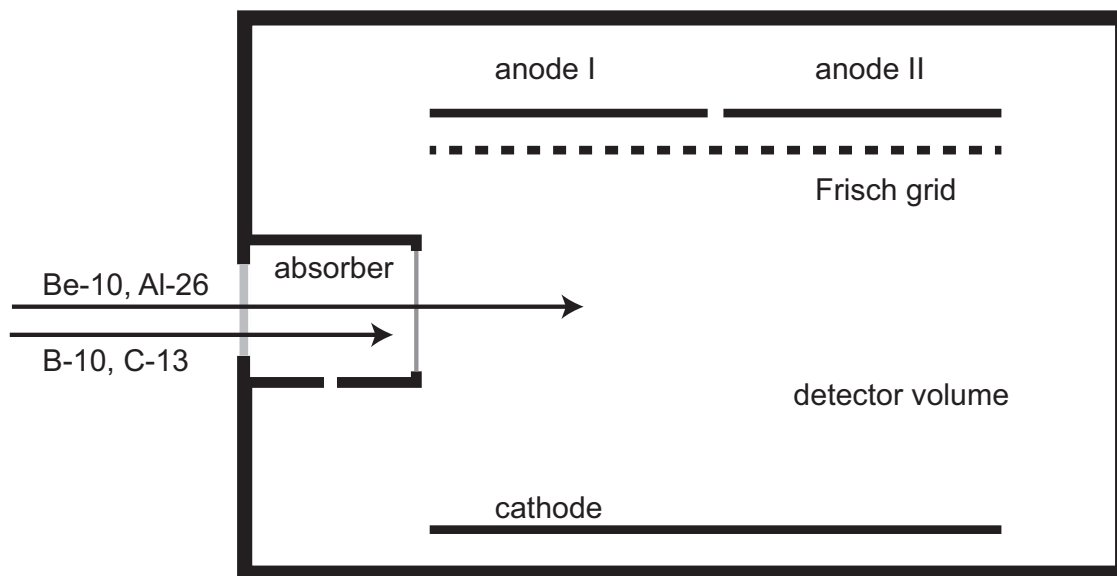
Figure 3.3: Sketch of the absorber setup mounted to the GIC.

The absorber volume has a length of 16 mm. It is sealed off from the beam tube by an initial 5×5 mm^2 SiN foil with a thickness of 500 nm. A second SiN window (10×8 mm^2, 75 nm thickness) is mounted at the normal position of the entrance window. It prevents the large amounts of charge created by the intense beams, which are stopped in the absorber, from entering the charge-sensitive detector area. Because of its larger area, the second window provides better angular acceptance for nuclides scattered in the first foil and the absorber volume. By changing the overall pressure in the setup, the stopping power of the absorber can be adjusted such that the intense interfering beams are stopped, while the rare isotopes still may enter the detector volume.

3.3.2   Separation of ^{10}Be from ^{10}B

Test measurements

An advantage of the degrader foil setup is that besides the ^{10}B also molecular background is suppressed. If the molecules are not yet destroyed in the stripper canal they break up in the degrader foil and can be rejected by the ESA and the HE2 magnet.

In the absorber setup, if the beam at 10 amu extracted from a blank sample is guided directly into the detector, ^{9}BeH that survived the stripper breaks up in the entrance foil and ^{9}Be appears as additional shoulder to the ^{10}B tail (Fig. 3.4a). The ^{9}Be energy corresponds to 90% of the ^{10}Be energy because the H partner carries away $\frac{1}{10}$ of the ^{9}Be^{1}H energy. The ^{9}Be is stopped prior to the ^{10}Be and deposits less energy in the detector. With increasing He stripper pressures the molecular background from ^{9}Be^{1}H survival decreases exponentially (Fig. 3.4b). The counting rate in the ^{10}B +^{9}Be gate is fitted by a function according to equation 2.1 and results in an R^2=0.99 and a destruction cross section of BeH^{2+} molecules in He of σ_{mol}=(2.5$\pm$0.1)$\cdot$10^{-16}cm^2. By applying a He stripper pressure larger than 0.13 mbar (d=0.43 μg/cm^2), the molecular background can be suppressed so that no ^{9}Be^{1}H reaches the detector. The high-energy background is not influenced by the stripper gas pressure.
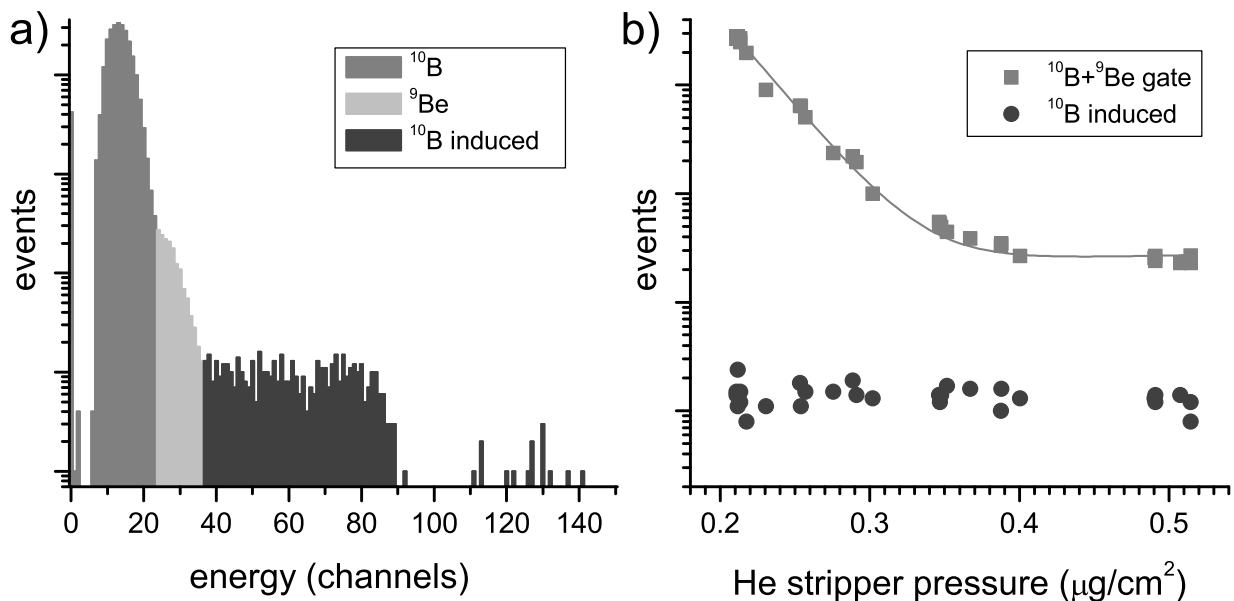
Figure 3.4: An energy spectrum of a blank was recorded at a beam energy of 1280 keV while varying the stripper pressure: a) The contributions of ^{10}B, ^{9}Be from the breakup of a ^{9}BeH molecule and a ^{10}B induced high-energy background are identified in the spectrum. b) Counting rates are shown dependent on the applied He stripper pressure. Because of their poor separation in the GIC, the counting rates of ^{10}B and ^{9}Be from the ^{9}BeH breakup were combined in this graph.

Experiments with the test setup were conducted in the 2^+ charge state at various terminal voltages, resulting in beam energies ranging from 750 keV to 1270 keV. In the following, only results recorded at the minimal and maximal beam energy are discussed. A ^{10}B-^{10}Be separation is visible for both beam energies (Fig. 3.5). Gas pressures necessary to suppress ^{10}B in the absorber to an extent that could be handled with the GIC amounted to 25 mbar for 750 keV ions and to 45 mbar for 1270 keV ions.
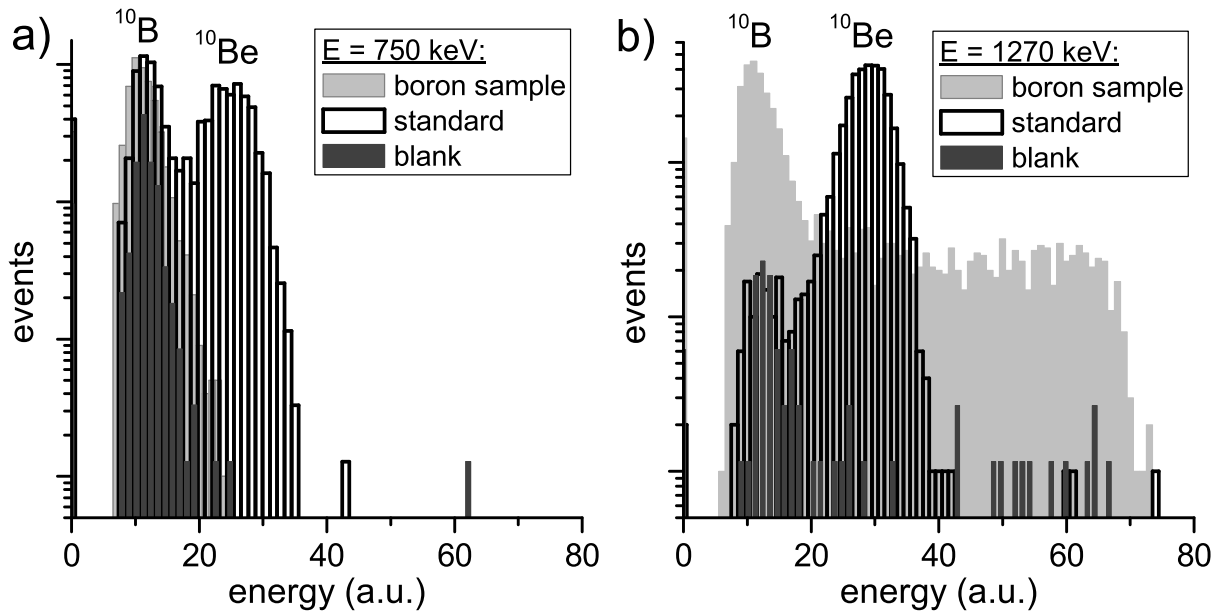
Figure 3.5: Energy spectra were recorded at beam energies of a) 750 keV and b) 1270 keV for a standard, a blank and a boron sample: a) At 750 keV the separation of ^{10}Be from the background is only poor, even the standard material shows a high background counting rate. b) At 1270 keV the ^{10}B background can be well suppressed by increasing the detector and absorber pressure. The energy, which the ^{10}Be deposits in the detector after passing the absorber, amounts to only ca. 100-200 keV.

When measuring a standard material at a beam energy of 1270 keV, a separation of ^{10}B and ^{10}Be is observed, but also a partial overlap of the ^{10}B tail in the blank and the ^{10}Be peak in the standard. At lower beam energies wide angle scattering gets more significant and in particular the relative separation of ^{10}Be from the background is worse. This requires cuts to the energy signal, also reducing the acceptance of ^{10}Be events. The detection efficiency is lowered because of this restriction to the higher energetic ^{10}Be events and for a beam energy of 750 keV it amounts to only ca. 25%. Taking into account the transmission through the accelerator in the 2^+ charge state (26%), the overall transmission is 5%. This value could be doubled if applying the 1^+ charge state at a terminal voltage of 525 kV. Then the same final energy is reached at much higher transmission through the accelerator.

At the higher energy of 1270 keV the detection efficiency is maximal 60%. If the detection efficiency is multiplied with the transmission for the 2$^+$ charge state at this energy (ca. 23%), a maximal overall transmission of 13% results for the current setup. Still, already in this proof-of-principle setup this value would improve the overall efficiency compared to the degrader foil method by 10-15%.

But not only the ^{10}B-^{10}Be separation is critical, as an additional background appears at higher energies (Figs. 3.4, 3.5b). This is discussed in the following.

Continuous high-energy background

Background events are recorded that create a higher signal than the intruding ^{10}B and ^{9}Be in Fig. 3.4. In typical blank samples they result in ^{10}Be/^{9}Be levels in the order of 10^{-14}. A first idea to explain the origin of this background was the nuclear reaction ^{10}B(p,α)^{7}Be. Because the Q-value of this reaction is 1.1 MeV, the products of this reaction have higher maximal energies in forward direction than the initial ^{10}B nuclides. The rate R [1/s] of events induced by a nuclear reaction is given by the number of available targets N_T, the irradiated area A [m^2], the beam intensity I [1/s] and the cross section σ [m^2] for the nuclear reaction:

$$R = I \cdot \frac{N_T}{A} \cdot \sigma \tag{3.1}$$

Several experimental observations indicated the occurrence of this reaction: First, the reaction is ^{10}B induced and the background rate scales with the B beam intensity (Fig. 3.6). In order to demonstrate this, targets were produced with different amounts of B content and not containing significant amounts of Be.

The ^{11}BO$^-$ current was measured in the LE cup and the detector counting rate was evaluated only from the gate set for the high-energy background. The material had been pressed into Ti cathodes and the measurements were performed at very low Cs supply to the ion source to limit the ^{10}B counting rate. Thus, no contribution of ^{27}Al$^-$ to the ^{11}BO$^-$ current is expected. A linear fit gives an R^2=0.99 for the correlation of ^{11}BO$^-$ current and background rate.

Second, target protons are abundant both in the silicon nitride foils (Si$_3$N$_{3.1}$H$_{0.06}$, Sun et al. [2007]) and in isobutane (C$_4$H$_{10}$). Due to the high abundance of H in the isobutane an enhancement of this reaction by using this gas was supposed. However, tests with Ar as detector and absorber gas instead of isobutane showed the same continuous high-energy background. It is concluded that the reactions primarily occur in the foil and not in the absorber volume.

Third, the cross section decreases drastically for lower beam energies (Fig. 3.7), explaining why the background is not observed at a beam energy of 750 keV.
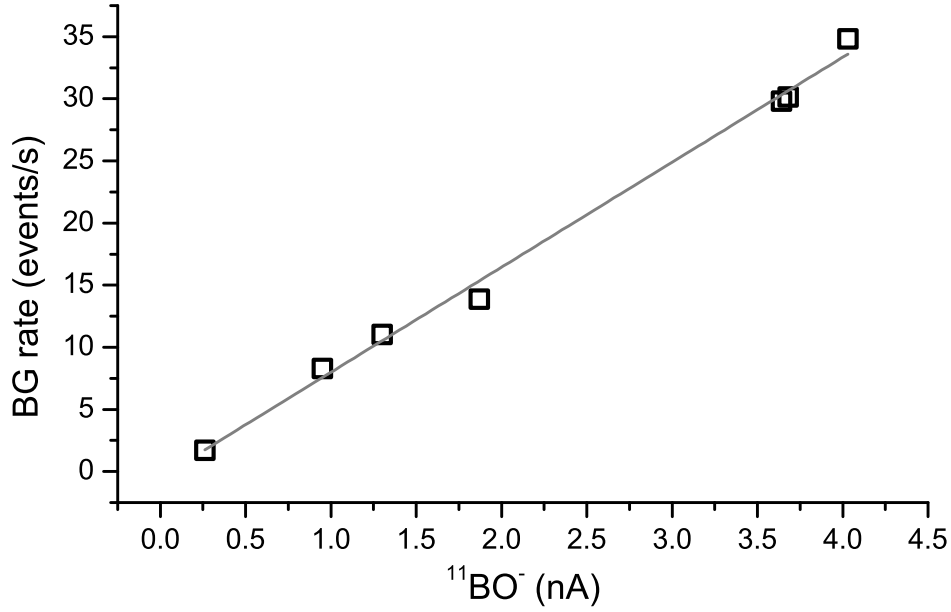
Figure 3.6: In samples with varying B content the counting rate in the gate for the high-energy background and the $^{11}BO^-$ current were determined. Both parameters show a linear correlation.

Finally, a continuous energy spectrum with a sharp maximal energy is observed matching the expectations of a nuclear reaction as origin of the background. However, two high-energy products ^7Be (E_{max}=2.36 MeV) and α (E_{max}=2.39 MeV) are created after an interaction of a 1.3 MeV ^{10}B ion with H. One therefore would expect a much higher signal and not only one continuous background, but a superposition of two different energy loss spectra.

The most important argument against the occurrence of this reaction is that the H target density in the foil and the cross section for the reaction (< 0.3 mb*, Fig. 3.7) are by three orders of magnitude too low to explain the observed background rates. The background induced via the $^{10}B(p,\alpha)^7Be$ reaction is not significant for LE-AMS ^{10}Be measurements.

A more promising explanation for the background events is Rutherford scattering of ^{10}B on protons. Depending on the angle θ of the recoil nucleus relative to the incoming particle, the scattering cross section can be calculated in the following way [Kottler, 2005]:

$$\frac{d\sigma}{d\Omega} = \left(\frac{z_H Z_B e^2}{4\pi\epsilon_0 \cdot 2E} \right)^2 \left(1 + \frac{M_B}{m_H} \right)^2 \frac{1}{\cos^3\theta} \tag{3.2}$$

$$\sigma = \int_0^{0.3} \frac{d\sigma}{d\Omega} \cdot 2\pi\sin\theta \cdot d\theta \approx 3\,b \tag{3.3}$$

The angular integration assumes a ^{10}B beam hitting the entrance window in the centre. The maximal scattering angle θ_{max}=0.3 is given by the length of the absorber and the width of the second SiN window.

$^*1\,b = 10^{-24}\,cm^2$
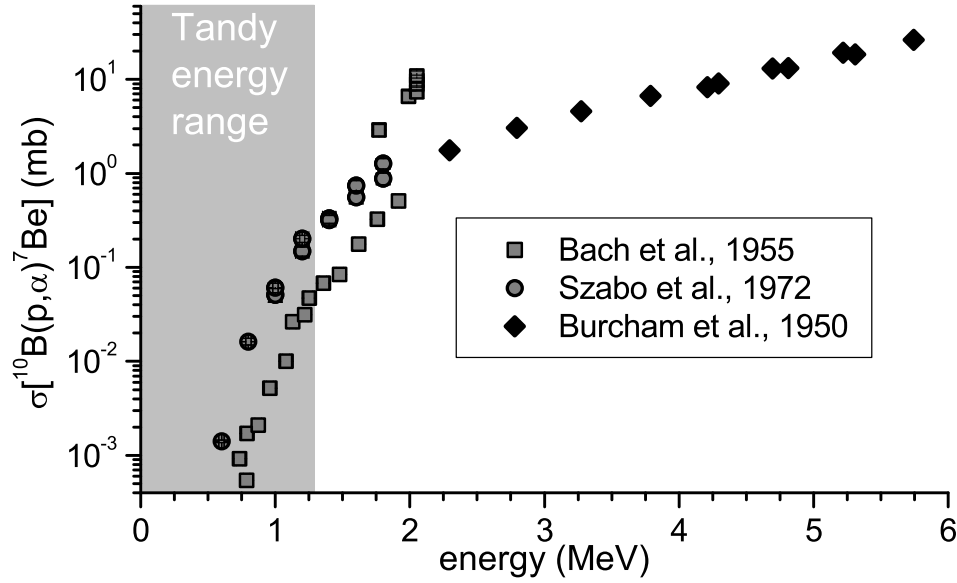
Figure 3.7: Cross section data for $^{10}B(p,\alpha)^7Be$ from Burcham and Freeman [1950]; Bach and Livesey [1955]; Szabó et al. [1972].

The maximal energy of the protons is defined by the beam energy E_B and the masses of the colliding partners (m_H, m_B).

$$E_{H,max} = \frac{4m_H m_B}{(m_H + m_B)^2} \cdot E_B = \frac{40}{121} \cdot E_B \approx \frac{E_B}{3} \qquad (3.4)$$

Simulations with the SRIM program [Ziegler et al., 2008] showed that the energy loss of ^{10}B in the 500 nm SiN entrance foil is so high that the maximal energy transferred to the protons in the isobutane via elastic scattering is too low for them to pass the absorber and enter the detector. That is why for this reaction no dependence on the absorber gas was observed as only protons scattered in the SiN entrance foil get enough energy in the Rutherford scattering to reach the detector volume. However, to rule out the possibility of background creation in the absorber, in particular with respect to future experiments with thinner entrance foils, another H depleted absorber gas would be more convenient.

Using the cross section $\sigma=3$ b the expected counting rate in the background region is overestimated by a factor of three. At least part of this factor can be explained by the fact that the $Si_3N_{3.1}H_{0.06}$ stoichiometry had been determined in a much thinner 35 nm foil. If H is enriched in the surface of the foil and is not uniformly distributed over the total foil thickness, the H concentration in the 500 nm foil will be overestimated.

Regarding the cross sections for the $^{10}B(p,\alpha)^7Be$ reaction ($3 \cdot 10^{-4}$ b) and the Rutherford scattering (3 b) it can be deduced that the scattered protons probably are the reason for the uniform and continuous high-energy background observed with the absorber setup. This is confirmed by simulations of the energy losses of different nuclides involved (^1H,

^{10}B, ^{10}Be) at the various measurement settings that were conducted for the absorber setup described above. They are discussed in the following section.

Comparison to SRIM calculations

The simulated detector consists of an initial 500 nm SiN foil followed by 16 mm of absorber and a second 70 nm SiN foil. The detector and absorber volumes are filled with butane gas at pressures of 25 mbar (750 keV beams) and 45 mbar (1270 keV beams). Although the SRIM program is not very accurate at low energies due to the lack of experimental input data, the results match the experimental data surprisingly well.

Ionization losses of the incoming beam via energy transfer to electrons account for more than 90% of the total energy loss. The energies directly transferred from the incoming ions to target electrons and to target atoms are returned separately by SRIM, but are combined in the following to a total energy loss.

For 1.273 MeV ^{10}B ions the maximal energy transferred to H is 423 keV. The continuous spectrum below this maximal energy stems from two effects: First, energy losses of the ^{10}B in the SiN and interactions with H in greater foil depths lead to a lower initial energy and a shorter range of the scattered H. Second, H scattered to larger angles retrieves less energy than in the central collision. The geometry of the setup limits the scattering angles in forward direction. Assuming that the scattering reactions only occur in the top layer of the foil, where the energy of ^{10}B still equals the initial 1273 keV, the geometry also defines a minimal energy of the scattered protons (300 keV). These 300 keV protons would still pass the absorber but would only deposit very little energy in the detector. Protons that are scattered to angles between the forward direction and the maximal energy defined by the absorber geometry have intermediate energies ($300 \text{ keV} < E_p < 423 \text{ keV}$) and cause a continuous distribution of the background.

For initial 1270 keV Be and B ions in this setup, the energy deposited in the detector volume creating free electrons amounts to negligible 1 keV for ^{10}B, ca. 170 keV for ^{10}Be and ca. 250 keV for protons starting with 423 keV.

At a lower beam energy of 750 keV the maximal H energy is only 249 keV, but the Rutherford scattering cross section is nearly a factor of 3 higher. The relative separation of ^{10}Be and the scattered protons increases if the beam energy is lowered: After passing the absorber only ca. 60 keV are left over for the protons according to the SRIM simulation. The energy deposited by ^{10}Be in the detector and transferred to ionization amounts to ca. 110 keV while ^{10}B is stopped (1 keV). From these calculations one would conclude that the low-energy background in Fig. 3.5a) is due to protons with an energy of 60 keV and not due to insufficient ^{10}B separation. Even better separation of the scattered protons and ^{10}Be shall be achieved when further lowering the beam energy.

The general characteristics of the absorber/detector setup is well reproduced by the SRIM simulations. Yet, in this case it is not easily possible to scale the experimentally recorded
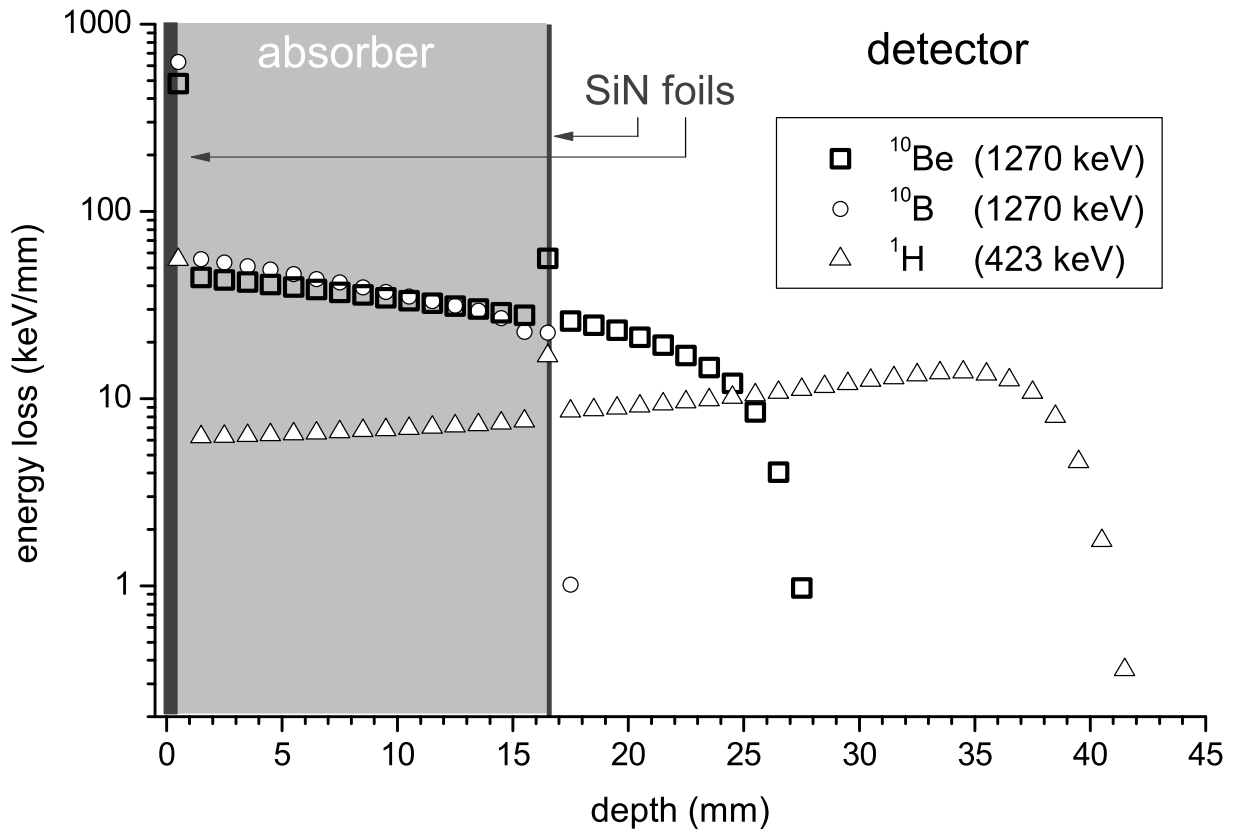
Figure 3.8: The SRIM simulation results for the energy loss in the different detector compartments are depicted for an initial beam energy of 1270 keV. The ^{10}B ions are nearly completely stopped in the absorber ($E_{^{10}B,det}$=1 keV) when setting the detector and absorber pressure to 45 mbar. The energy available for creating ions in the detector gas is $E_{^{10}Be,det}$=170 keV for ^{10}Be and for the maximal H energy it is $E_{H,det}$=250 keV.

signals to ion energies in order to compare them with the values received from the SRIM simulations as the electronic minimum signal thresholds were varied and no energy calibration of the absorber setup is available. The experimentally determined pressures for good ^{10}B suppression in the absorber/detector setup match those in the simulation: For both beam energies, 750 keV and 1270 keV, at the respective experimental pressures a simulated ^{10}B ion can only deposit little energy in the detector, whereas ^{10}Be can enter the sensitive detector area. In addition, the characteristics of the scattered protons are reproduced: At 1270 keV beam energy the protons are expected to produce a higher signal than ^{10}Be, at 750 keV the situation is inverted.
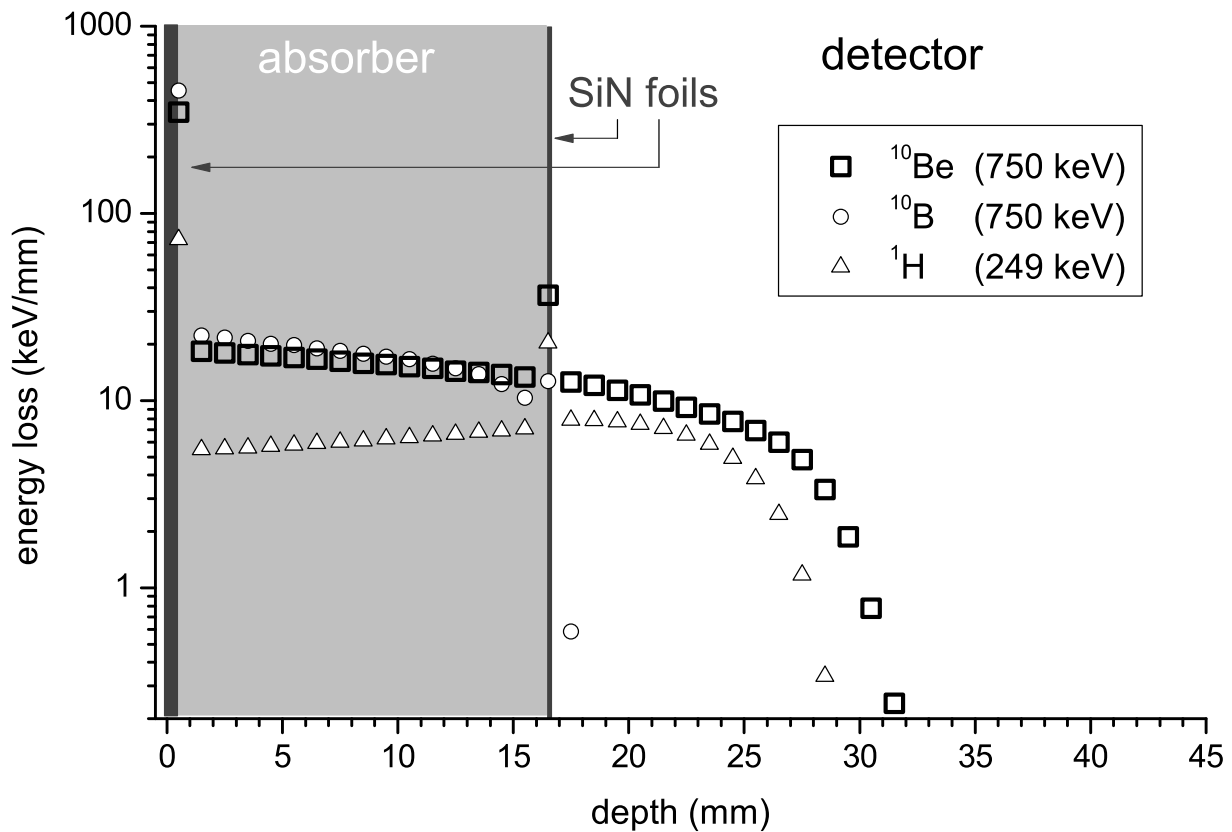
Figure 3.9: The SRIM simulation results for the energy loss in the different detector compartments are depicted for an initial beam energy of 750 keV. The ^{10}B is stopped in the absorber ($E_{^{10}B,det}$=1 keV) implementing butane at a pressure of 25 mbar. Incoming protons from Rutherford scattering are estimated to deposit a similar energy for ionization ($E_{H,det}$=60 keV) as ^{10}Be ($E_{^{10}Be,det}$=110 keV).

3.3.3 Separation of $^{26}Al^{2+}$ and $^{13}C^{1+}$

The positive results for the ^{10}B-^{10}Be separation motivated to apply the absorber technique also for other difficult isotope systems in LE-AMS. The high maximal transmission for Al in the 2$^+$ charge state (ca. 60%) makes it very interesting for AMS at low energies. However, in contrast to the 3$^+$ charge state one has to handle molecular background and the m/q interference of $^{13}C^{1+}$. The m/q interference is very intense because it is present on the LE side and the HE side and is not separated with the mass filtering devices: On the LE side both $^{26}Al^-$ and $^{13}C_2^-$ have mass 26 and on the HE side the m/q ratio is the same for $^{13}C^{1+}$ and $^{26}Al^{2+}$.

Molecules of mass 26 on the HE side may consist of combinations such as $^{13}C_2^{2+}$, $^{14}N^{12}C^{2+}$, $^{10}B^{16}O^{2+}$, $^{1}H_2{}^{24}Mg^{2+}$ or $^{1}H^{25}Mg^{2+}$. This molecular background can be suppressed by increasing the He stripper pressure to values >0.14 mbar (Fig. 3.10). The
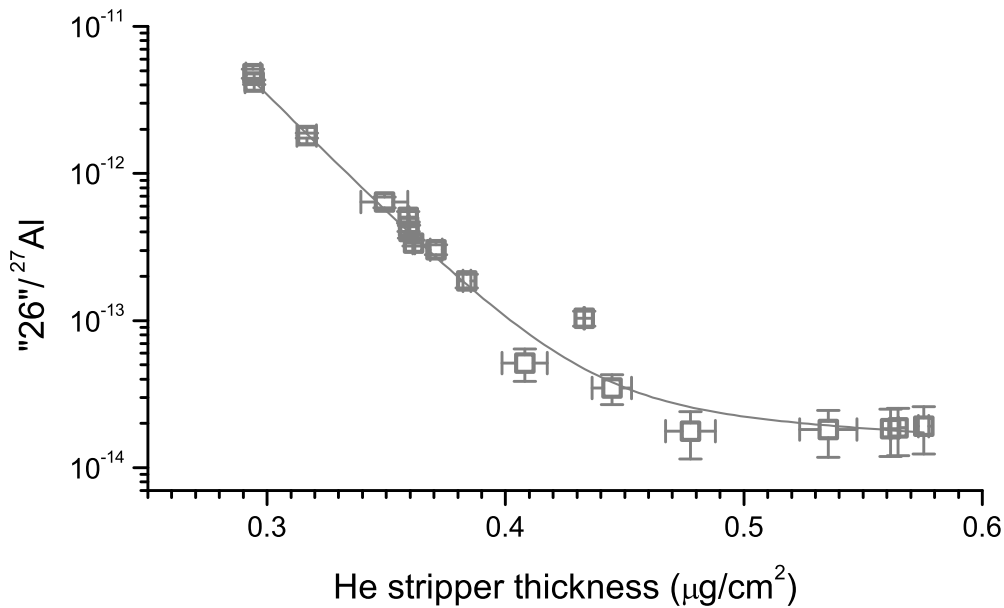
Figure 3.10: A scan over the stripper pressure at a terminal voltage of 500 kV shows that suppression of 2$^+$ molecules at mass 26 in the absorber setup is only possible at stripper pressures larger than 0.14 mbar (d=0.46 μg/cm^2).

fit according to equation 2.1 yields an R^2=0.98 and a destruction cross section for 2$^+$ molecules at 26 amu in He of σ_{mol}=(2.5$\pm$0.1)$\cdot$10^{-16}cm^2.

With the pressure of isobutane in the absorber and the detector adjusted for almost full ^{13}C^{1+} rejection, the ^{26}Al ions only reach the first anode in the existing geometry (Fig. 3.11). Previous experiments at the Tandy [Stocker, 2006] demonstrated that in two-dimensional spectra the molecule breakup particles can be separated from the ^{26}Al ions because of their different energy loss behaviour. Although good separation of ^{13}C^{1+} and ^{26}Al^{2+} can be achieved in the absorber, some background counts were collected in the ^{26}Al gate, resulting in ^{26}Al/^{27}Al blank ratios ranging from (5$\pm$4)$\cdot$10^{-15} to (1.0$\pm$0.4)$\cdot$10^{-13}. One explanation for this is cross talk in the ion source, as a high standard (ZAL94 N: ^{26}Al/^{27}Al=4.8$\cdot$10^{-10}) was used during the experiment. Cross talk in the order of 10^{-4} is realistic for a Cs sputter ion source. For normal Al targets and using an absorber/detector pressure of 22 mbar it is possible to decelerate the ^{13}C^{1+} beam in the absorber to energies below the signal threshold of the detector. Still, very intense ^{13}C^{1+} beams may deposit enough energy in the detector to create a signal via pile-up. This can be solved by increasing the pressure in the absorber.

Molecules surviving the stripper are expected to break up in the entrance foil of the absorber cell. Light molecular breakup products (^{14}N, ^{12}C, ^{13}C) carry energies similar to ^{13}C^{1+} and should be stopped in the absorber. Only Mg, e.g. from ^{1}H^{25}Mg^{2+}, might carry enough energy (1490 keV) to pass through the absorber volume. Because the proton number Z of Mg is one less than that of Al, the energy loss of the breakup Mg can be ex-
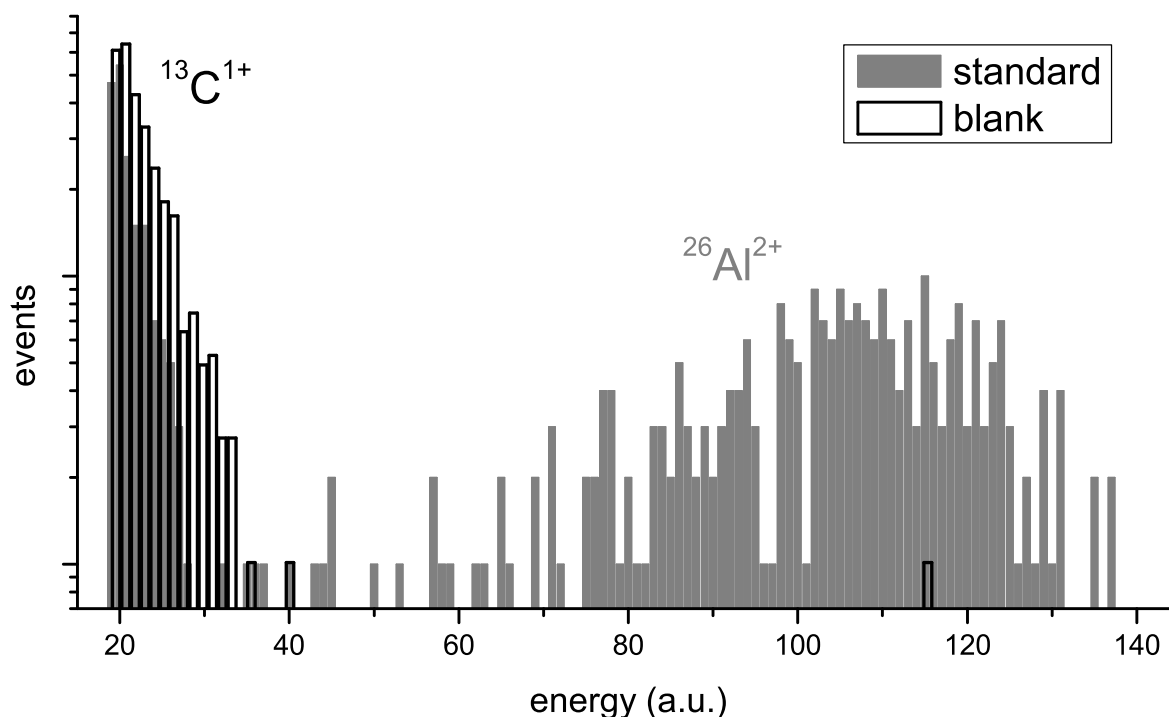
Figure 3.11: Spectra of a ^{26}Al standard and a blank sample recorded in the GIC preceded by a simple absorber cell. For this experiment the terminal voltage was set to 500 kV, so ^{26}Al ions that passed the absorber have only an energy of ca. 250 keV.

pected to be similar to the one of Al. This also was reproduced by a SRIM simulation of C, Al and Mg in the absorber/detector setup for the ^{26}Al measurements (Fig. 3.12). Because Mg can give rise to severe background in the Al gate, the ^{1}H^{25}Mg^{2+} molecules need to be broken up already in the stripper canal. Then Mg can be filtered out in the magnets and the ESA.

A high stripper pressure is required for molecule elimination (Fig 3.10). This reduces the maximal transmission into the 2$^+$ charge state by ca. 20% to 52% when running the accelerator at 460 kV. The standards are measured at 58% of their nominal value because beam losses occur at the slits in front of ESA, HE2 magnet and detector as the ion optics is not optimized for the 2$^+$ charge state. The overall transmission of the setup is 29%. Regarding the efficiency this means an improvement over the previous state at the Tandy: With Al^{1+} and Ar as stripper gas 22% overall transmission were achieved [Stocker, 2006].

The relatively large loss of beam on the HE side is probably related to the fact that ion optics and slit positions are not optimized for the 2$^+$ charge state. As the position of the detector is not in the focus of the 2$^+$ charge state, the beam diameter might have a similar size as the first window of the absorber or even be larger. From SRIM calculations it can be concluded that scattering processes of an Al beam centrally entering the absorber cell
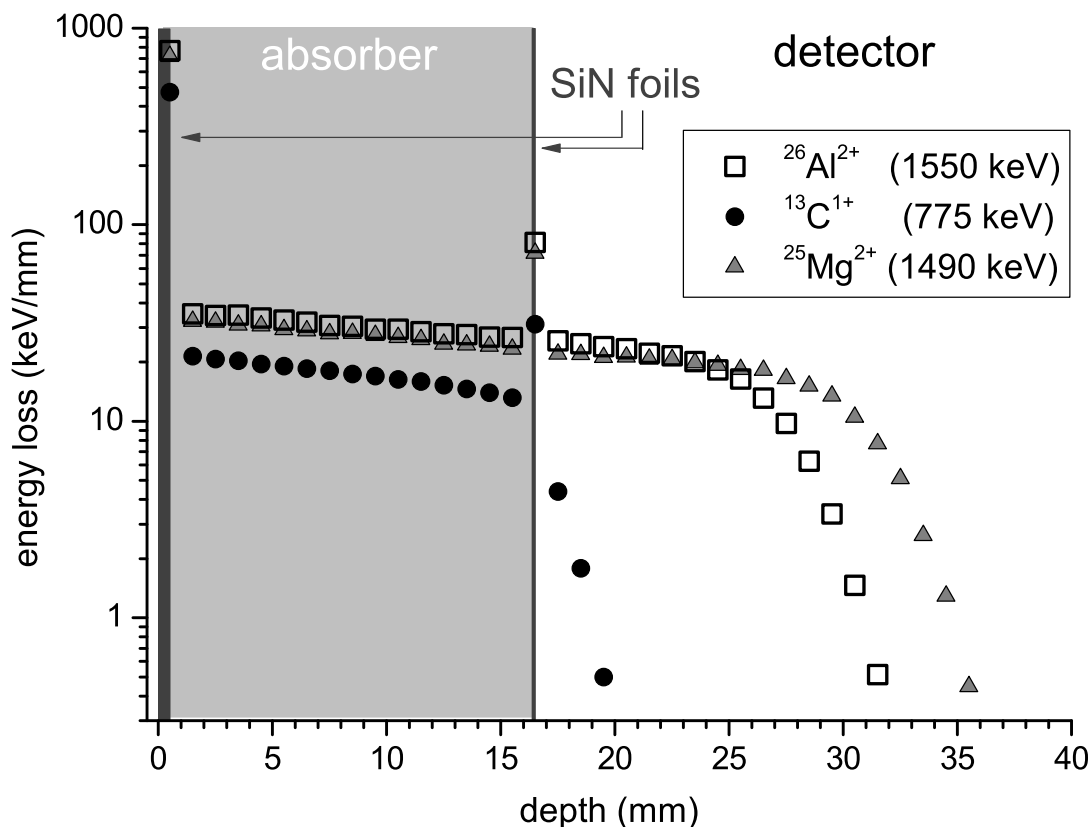
Figure 3.12: Simulation of the energy loss of 1550 keV ^{26}Al ions, 1490 keV ^{25}Mg ions and 775 keV ^{13}C ions in a detector with absorber cell as described above. The gas pressure is set to 22 mbar. The energies deposited for ionization processes amount to $E_{^{13}C,det}$=7 keV, $E_{^{25}Mg,det}$=280 keV, and $E_{^{26}Al,det}$=230 keV, respectively.

only marginally reduce its intensity until it reaches the detector. A spread beam, however, might be affected by geometric losses from the limited entrance window size and also the angular scattering of nuclides entering at the window edges might decrease the detection efficiency.

At higher terminal voltages the beam losses on the HE side are reduced. The standards are measured to 63% of their nominal value at a terminal voltage of 525 kV. However, the transmission through the accelerator is lowered to 44% and thus the overall transmission for ^{26}Al is slightly reduced to 28%.

3.3.4   Conclusion

This first simple setup for a GIC equipped with a passive absorber indicates the potential of this detection method for LE-AMS. The thin and homogeneous SiN foils in combination with the high-resolving and sensitive GIC now enables the usage of this background

suppression technique, which had previously been limited to large AMS facilities. So far, standards have been measured only at maximal 60% of their nominal value for Be-B and Al-C separation. Blank ratios in the order of 10^{-14} have been achieved for ^{10}Be/^{9}Be and ^{26}Al/^{27}Al.

In the first tests the separation of Be and B was possible, but for routine measurements the Be-B isobar system requires a more elaborate absorber. High-energy events in the detector occur depending on the beam energy. This background limits the sensitivity of the setup for energies > 750 keV. SRIM calculations show that the protons originating from Rutherford scattering of ^{10}B on H in the initial SiN absorber foil have enough energy to enter the detector creating a continuous background. In order to remove this source of background other foils with lower H content have to be used as initial absorbing material. More tests thus are essential.

At a beam energy of 1270 keV (2^+, 525 kV) the overall transmission of the Tandy can be improved to 13%, but blanks are influenced by the high-energy background. With a lower beam energy of 750 keV (1^+, 525 kV), an overall transmission of 10% is realistic in the current setup. The source of the background at 750 keV beam energy is not yet clearly identified. If it is ^{10}B, then measurements will only possible at higher beam energies. But if the background were produced by scattered protons from the incident ^{10}B, as suggested by the simulations, the suppression could even be improved by further lowering the beam energy. Then, also the low-energy ^{10}Be counts that are not distinguishable from the background at 750 keV could be accepted in the electronic detector gate and the detection efficiency might be improved. The transmission through the accelerator is relatively stable for the 1^+ in this energy range (Fig. 2.6) and therefore the overall transmission could be increased. However, more losses due to enhanced wide angle scattering have to be anticipated if the energy is further decreased. Hence, it is questionable whether the performance can actually be improved by choosing a final beam energy lower than 750 keV. The first results of ^{26}Al in the absorber/detector setup are already very promising for an establishment of this method towards routine operation. In general, the ^{13}C^{1+} can be suppressed. ^{26}Al^{2+} overall transmissions of 30% are realistic with an absorber cell, making it the most efficient way of determining this isotope via LE-AMS. However, the method has to be tested with real prepared samples where the ^{13}C content might be higher.

Chapter 4

Actinide AMS[*]

Following the many technical modifications of the Tandy setup the new performance for actinides was systematically investigated. Tests, parameters, and technical developments for the measurement of actinides are described in the following chapter.

4.1   Actinide detection methods

AMS of actinides is mainly used for determinations of rare isotopes of Pa, U, Np and Pu. In contrast to many other radioisotopes, which in their natural abundance can only be detected with AMS, for actinide nuclides other techniques such as counting of α-, β-, or γ-decays or classical mass spectrometry are alternatives. Below, the different techniques shall be compared for those nuclides that are usually analysed via AMS. The important parameters in doing so are the sensitivity and the selectivity, which are mutually dependent: The **sensitivity** denominates the minimum amount of nuclides necessary for detection and thus is related to the overall efficiency. The **selectivity** is given by the suppression of background via separation of isobars or scattered neighbouring nuclides. For mass-spectrometric methods higher selectivity can be reached by narrower slits restraining the acceptance of the filters and the detectors. This in turn causes a reduction of the sensitivity as thereby also the overall transmission is affected. A very good overall efficiency and therefore a high sensitivity of a setup alone may not be sufficient for the detection of low natural concentrations of the desired radionuclides. If the method has only little selectivity, it may not be able to suppress naturally occurring background nuclides. On the other hand, a too large selectivity is not adequate if the overall efficiency is so low that large amounts of sample are necessary in order to detect enough events for good counting statistics. Optimal results can be achieved with the right combination of the two parameters.

---

[*]Parts of this chapter are based on Lachner et al. [2013b] and Lachner et al. [2012a].

Pu isotopes and ^{236}U are the most common actinides for AMS and will be discussed in more detail. First, the practicability of decay counting is discussed, afterwards common mass spectrometry techniques are compared to AMS.

The α-counting of ^{236}U is hampered by the long half-life ($T_{1/2}$=(23.42$\pm$0.04) Ma, Holden [1989]) and the much higher α-counting rates from ^{234}U, ^{235}U and ^{238}U in natural samples. The counting technique is interesting for actinides with short half-lives such as the β-decaying ^{241}Pu. However, it is not always isotope selective. For example, the α-decay energies of the isotopes ^{239}Pu and ^{240}Pu with half-lives of 24.1 ka and 6560 a [Holden, 1989], respectively, are very similar and generally cannot be distinguished. Hence, usually only the overall activity of $^{239+240}$Pu is examined, but not the ^{240}Pu/^{239}Pu ratio. So, although the sensitivity of ^{240}Pu decay counting is relatively good (ca. 1 pg is required for 2% statistical uncertainty at a detection efficiency of 30% and a counting time of ten days), this method does not allow evaluating a concentration of this isotope in a natural sample because of the insufficient selectivity, which does not enable to separate the ^{239}Pu. Only in special cases the ratio can be deduced by means of activity measurements: León Vintró et al. [1996] were successful with a high-resolution setup and algorithms to deconvolute the $^{240+239}$Pu peak. Else, the determination of ^{240}Pu/^{239}Pu ratios via α-counting requires supplementary information, e.g. the Lx-ray activity [Komura et al., 1984].

On the other hand, mass-spectrometric (MS) methods can easily distinguish ^{239}Pu and ^{240}Pu. Techniques such as Inductively Coupled Plasma Mass Spectrometry (ICP-MS) or Thermal Ionization Mass Spectrometry (TIMS), that use positive ions from the source, have similar efficiency in detecting actinides than AMS [Boulyga, 2011] and enable to analyse amounts of 100 ag (corresponding to few 10^5 atoms). Therefore, even for relatively short-lived isotopes good results can be achieved: In the above example with 1 pg ^{240}Pu a mass-spectrometric technique counting the atoms instead of the decays will reach a statistical error of 2% if it has an overall efficiency of 10^{-6}. At the Tandy, this statistical uncertainty can be accomplished in a Pu AMS run lasting about one minute.

Besides the atomic isobars, which are problematic for all methods, ICP-MS, TIMS, or LE-AMS utilizing charge states $<4^+$ may suffer from background of molecular isobars. In particular this molecular background has to be taken care of and will be discussed in section 4.3. Mass spectrometry in the actinide region fails to resolve background from atomic isobars because the relative differences of the proton numbers of the nuclei are small and thus the stopping power in the detector is too similar. Small isobaric effects can be observed at high beam energies above 100 MeV, but still are not sufficient to obtain a good separation [Lachner et al., 2012b]. So, chemical separation is the only way to suppress isobars, but it is limited to systems where the abundance of the isobar is in the same magnitude as the desired isotope, e.g. in the case of ^{241}Pu, which can be influenced by its decay product ^{241}Am. For the most common Pu AMS isotopes ^{239}Pu, ^{240}Pu and ^{242}Pu there are no isobars with half-lives longer than 1 a. In contrast, the long-lived and

abundant isobar ^{238}U makes the mass-spectrometric analysis of ^{238}Pu impracticable and hence for this nuclide the α-decays are counted.

The high selectivity of AMS in the measurement of minor isotopes such as ^{236}U facilitates the determination of low concentrations in presence of ^{235}U and ^{238}U [Boulyga, 2011], which are not accessible with conventional MS techniques. Atomic isobars for ^{236}U are ^{236}Pu ($T_{1/2}$=2.86 a) and ^{236}Np ($T_{1/2}$=154 ka). They also have to be separated by chemical means prior to the AMS analysis (section A.2). However, the abundance of both isotopes is low compared to ^{236}U and especially the short half-life of ^{236}Pu additionally decreases its occurrence.

So far, most AMS measurements have been performed at accelerators with terminal voltages > 3 MV in high charge states. The 5$^+$ charge state is most commonly used [Zhao et al., 1994; Hotchkis et al., 2000; Steier et al., 2008; Fifield et al., 2010; De Cesare et al., 2013], other charge states, for example 7$^+$ [Fifield et al., 1996], 11$^+$ [Berkovits et al., 2000], or 3$^+$ [Fifield et al., 2004; Chamizo et al., 2008], are rarely applied. However, more new facilities with terminal voltages < 1 MV are built and also will be active in the AMS of heavy isotopes. This increasing number of available facilities and the high yield with He as stripper gas at low beam energies [Vockenhuber et al., 2013] will support actinide AMS in the 3$^+$ charge state, so that it might become the standard method in future.

The measurement procedure for actinides at the Tandy is similar to other AMS nuclides: The magnetic filters are kept at constant values and the voltages of the LE bouncer, the pelletron and the ESA are switched to select the different nuclides. Another similarity, at least for U isotopes, is that one abundant isotope (^{238}U) is measured in Faraday cups. However, the actinide yield tracers generally are rare isotopes and therefore also are counted in the detector. The yield tracers (e.g. ^{233}U) and the sample isotopes (e.g. ^{236}U and ^{238}U) are injected sequentially into the accelerator. The Faraday cup on the HE side can be positioned such that the measurement of the ^{238}U^{3+} current can be performed at the pelletron voltage used during the ^{233}U^{3+} counting in the detector. These two isotopes thus are quantified quasi-parallel, as only the fast pulsation on the LE side is changed.

Table 4.1: Actinide standards used at the ETH Zurich. Values are taken from Christl et al. [2013a] (ZUTRI), Steier et al. [2008] (Vienna-KkU, LOT2061), and Christl et al. [2013b] (CNA)

Uranium			Plutonium:	CNA	
material	^{236}U/^{238}U [10^{-12}]	err	isotopes	value	err
ZUTRI	4055	5%	^{240}Pu/^{239}Pu	0.530	2.1%
Vienna-KkU	69.8	4.6%	^{240}Pu/^{242}Pu	0.281	2.1%
LOT2061	6.05	7.3%	^{239}Pu/^{242}Pu	0.534	2.4%

During Pu and Np measurements no isotope is present in quantities that could be read out from a Faraday cup, but all nuclides are counted in the final detector.

4.2 Tandy performance parameters for the actinides

The upgrade of the Tandy facility by the installation of an additional magnet on the HE side [Müller et al., 2010b] improved the separation of neighbouring masses. This becomes important if the more abundant actinides ^{232}Th, ^{235}U and ^{238}U are present in the sample material. When measuring the isotopes ^{231,233}Pa, ^{233}U, ^{237}Np and ^{239}Pu, previous chemical separation can already suppress the neighbouring masses. In the Tandy setup, ^{236}U is more demanding as the neighbouring ^{235}U can only be suppressed in the beam transport and cannot be distinguished in the final gas ionization chamber. The critical parameter in such a determination is the suppression of the neighbouring mass nuclide, the so-called selectivity of the setup.

In most AMS laboratories the extraction of negative oxide ions is used for all actinides, but also fluoride compounds were tested and promise high yields for PuF_4^- and UF_5^- [Zhao et al., 2013]. The relative yields for the formation of UO^-, PuO^-, etc. vary compared to values at other Cs sputter ion sources [Fifield et al., 1997] and additionally with time: The data in Fig. 4.1 demonstrates that in the beginning of the measurement, when counting rates are rising, PuO^- gets more readily ionized than UO^-. After ca. 60 minutes maximal counting rates and nearly equal ionization efficiency for both elements are reached. UO^-
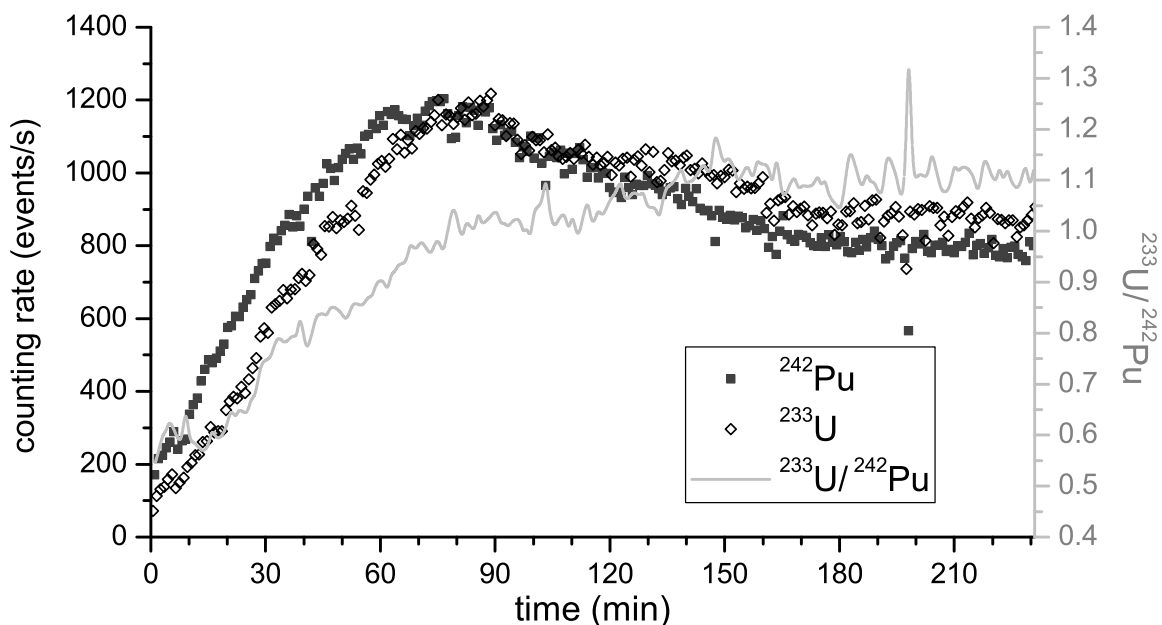
Figure 4.1: Material with a nominal ratio ^{233}U$/^{242}$Pu $= 1$ was measured for several hours. On the left axis the counting rates for the two nuclides are depicted and on the right axis their ratio.

is slightly dominant in the further course, but this difference is small and potentially could be attributed to effects from different tuning. In this test the overall efficiency over the whole time span amounted to the same value of $2 \cdot 10^{-4}$ for both nuclides. Time dependent effects may be related to geometric effects of the target such as cratering or to the development of a Cs implanted layer at the top of the target.

4.2.1 ^{236}U

Several possible setups were checked for their practicability concerning routine measurements of ^{236}U. The charge states 3^+ and 4^+ were tested. Besides, in the 3^+ setup the gas ionization chamber was replaced by a time-of-flight detector to gain another mass filter. Finally, the 3^+ charge state in the setup with the standard gas ionization chamber turned out to be the most efficient technique and also allows measuring ^{236}U/^{238}U ratios in most natural samples. The applications related to ^{236}U are discussed in section 6.3.

^{236}U^{3+} detection in the gas ionization chamber

In the previous Tandy setup with the detector mounted after the ESA the lowest detectable ^{236}U/^{238}U ratios were in the order of 10^{-9} [Wacker et al., 2005]. With the new magnet an improvement over the previous setup of ca. three orders of magnitude is achieved and the experiments and data defining the new background are described in the following.
In the energy spectra for ^{233}U^{3+} and ^{236}U^{3+} recorded with the gas ionization chamber (Fig. 4.2) only m/q interferences with other charge states are discriminated. The meas-
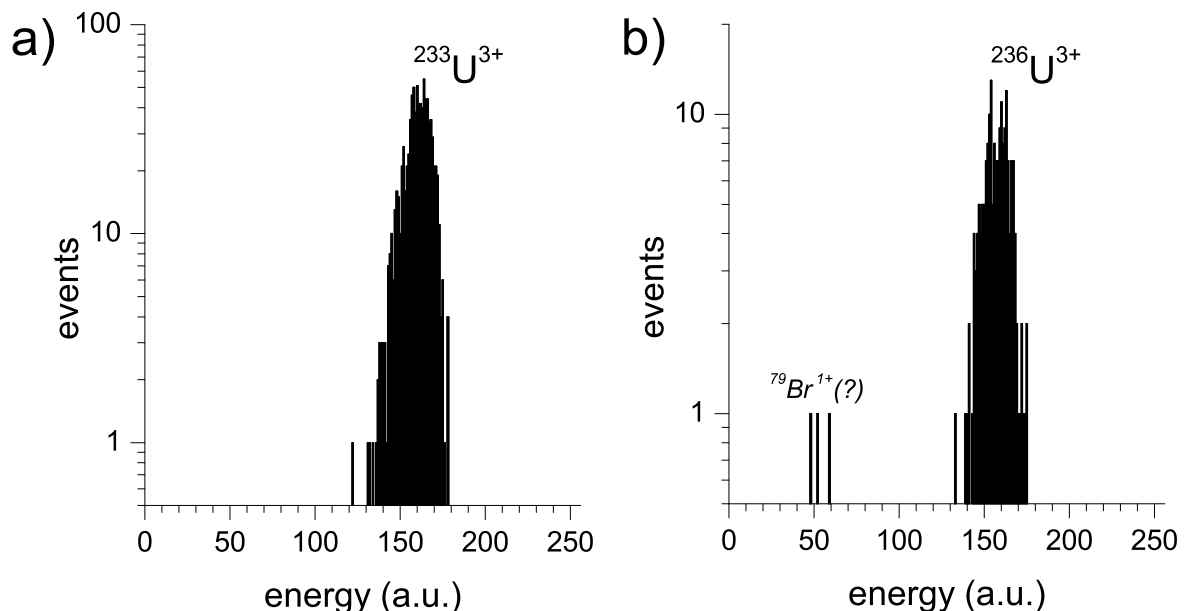
Figure 4.2: ZUTRI standard spectra were recorded with the Tandy tuned to a) ^{233}U^{3+} and b) ^{236}U^{3+}

urements in the 3^+ charge state result in very clean spectra for both isotopes. However, as stated above, background from other actinides entering the detector cannot be resolved. In this setup, neighbouring isotopes are only identified if one varies the settings of the E/q or p/q sensitive devices such that their masses are filtered and the different isotopes are injected into the detector. This is done during the scans when searching the optimal settings for the beam transport. Figure 4.3 shows the ^{235}U suppression in the ESA and the HE2 magnet for the sample material Vienna-KkU (table 4.1). When scanning the fields of these devices, flat tops rather than Gaussian peaks are observed for the counting rates of ^{235}U and ^{236}U. This is due to the smaller beam diameter (< 3 mm) compared to the size of the slits, which are typically 4-5 mm wide, or compared to the detector window, which is used in sizes of 4×4 mm^2 or 5×5 mm^2.
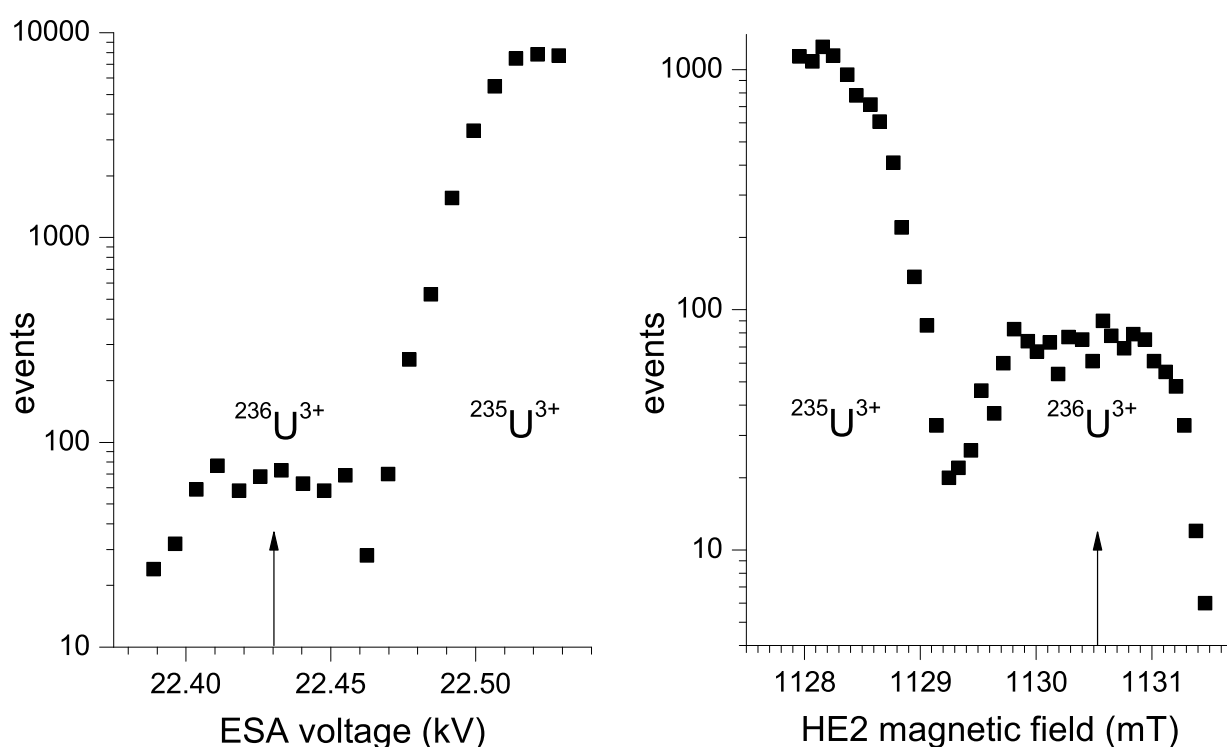
Figure 4.3: Scans in charge state 3^+ over the electric field of the ESA (with the HE2 field at 1130.5 mT) and the magnetic field of the HE2 magnet (with ESA voltage at ± 22.43 kV) for the ^{236}U standard Vienna-KkU (nominal ratio of ^{236}U/^{238}U$=69.8 \cdot 10^{-12}$) show the good separation of masses at this low level.

For all samples and standards in this work it can be assumed that the natural ratio of 0.0073 between the major U isotopes ^{235}U and ^{238}U is present. On account of this, a measurement of a Vienna-KkU sample with a ^{236}U/^{238}U ratio of $69.8 \cdot 10^{-12}$ requires a selectivity of better than ($<$) 10^{-8}. From extrapolations of the ^{235}U tail to the settings loaded for the ^{236}U measurements in the scans over the ESA and HE2 magnet (Fig. 4.3) it can be derived that the ^{236}U/^{238}U background, which originates from the tailing of ^{235}U, should

only be in the order of 10^{-13}. However, these fits do not include the possibilities of secondary scattering processes and therefore the real background level cannot be evaluated. With this method the selectivity on mass 236 could be better assigned in a sample containing only ^{235}U and no ^{236}U. So far, no material has been found that contains no traces of ^{236}U detectable via AMS, thus there is no true blank material. Samples with the lowest nominal ratios (LOT2061: ^{236}U/^{238}U=(6.05±0.44)·10^{-12}, Steier et al. [2008]) were measured along in a standard dilution series with other standards of known ^{236}U/^{238}U ratio. It revealed a background of ^{236}U/^{238}U $\approx 4 \cdot 10^{-12}$. This offset is higher than the one deduced from the scans over ESA and HE2 magnet, as multiple scattering processes in the HE side beam transport may lead to other tailing than derived from the scans.

In summary, ^{236}U/^{238}U ratios of ca. 10^{-12} can be determined corresponding to a selectivity in the order of 10^{-10}. Such a blank level is sufficient for the measurement of most environmental samples.

Installation of a time-of-flight detector

By replacing the gas ionization chamber with a time-of-flight (TOF) detection system an additional suppression of other U isotopes could be achieved. Thereby, the origin of the background was investigated. These experiments are described in more detail elsewhere [Hofmann, 2010; Vockenhuber et al., 2011].

The energy-loss straggling in the start foil reduces the timing resolution to about 1 ns and in particular gives rise to the low-energy tail in the TOF spectrum. One can assume that ^{235}U arriving at the detector has the same E/q or p/q than ^{236}U^{3+}, probably due to charge exchange reactions in the HE tube of the accelerator or due to scattering processes in the filtering devices. With either the same momentum or the same energy as ^{236}U^{3+}, the ^{235}U^{3+} has a different velocity and can be distinguished in the TOF detector. The ^{236}U/^{238}U background ratio of 4·10^{-12} that had been observed in the U standard series with the gas ionization chamber thus could be assigned to an E/q interference of ^{235}U^{3+} (Fig. 4.4). Besides background from scattered U isotopes, another background in charge state 3$^+$ with a mass of 236 amu was observed, which was at first attributed to a contamination with ^{236}U. Further experiments (section 4.3) could demonstrate that surviving molecules were the cause of this background.

U in charge state 4$^+$

The yield for the 4$^+$ charge state of U is relatively high with He as stripper gas, at a terminal voltage of 500 kV a maximal transmission of 12% can be achieved. Tests were performed to explore the background and the overall efficiency for ^{236}U measurements in this charge state [Diebold, 2012]. The survival of molecules becomes even more unlikely than in the 3$^+$ charge state and the higher beam energy also would offer the opportunity
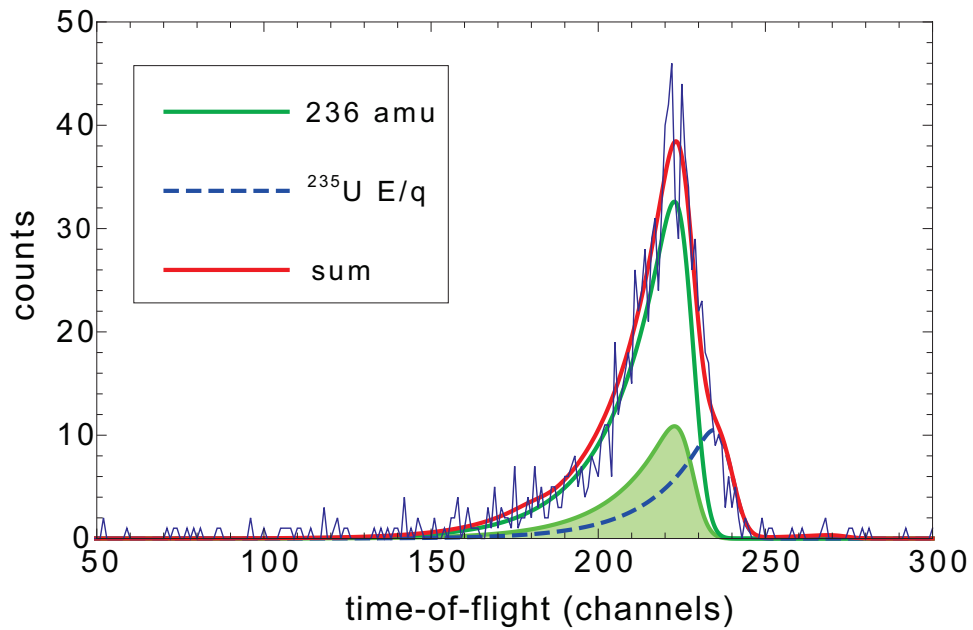
Figure 4.4: The TOF-spectrum is taken from Vockenhuber et al. [2011] and shows small contributions of $^{235}U^{3+}$ with the same E/q ratio as $^{236}U^{3+}$ in the sample material LOT2061. The coloured area corresponds to the expected peak size for the nominal value of the sample (i.e. $6 \cdot 10^{-12}$). This indicates that the increased background is a result of ions at mass 236 reaching the detector, which eventually were identified as surviving $^{235}UH^{3+}$ molecules (section 4.3).
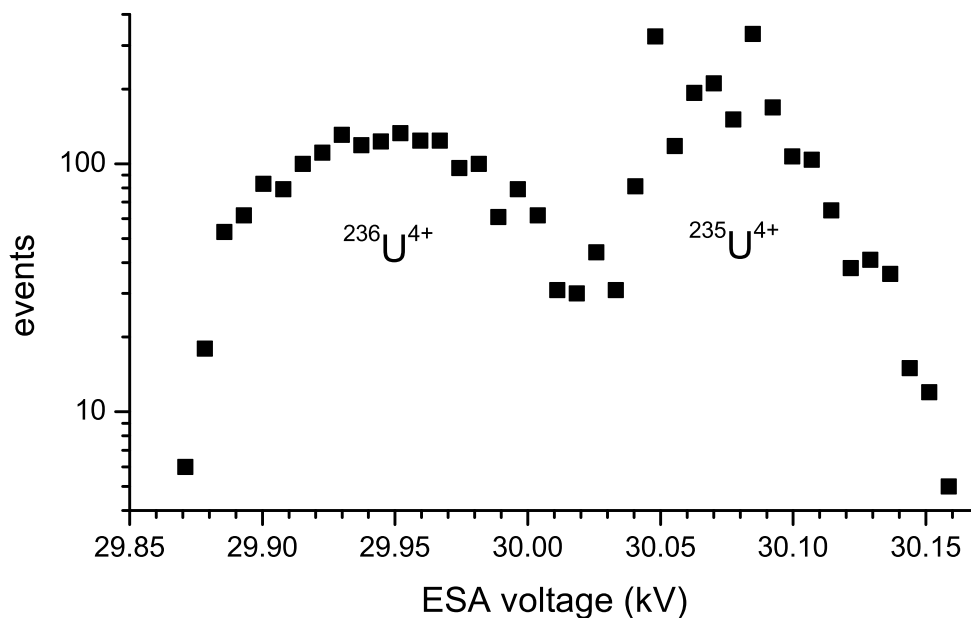
Figure 4.5: The scan in charge state 4^+ over the electric field of the ESA for the high-level ^{236}U standard ZUTRI (nominal ratio of $^{236}U/^{238}U=4.06\cdot10^{-9}$) illustrates the worse suppression of the neighbouring mass compared to the 3^+ charge state (Fig. 4.3).
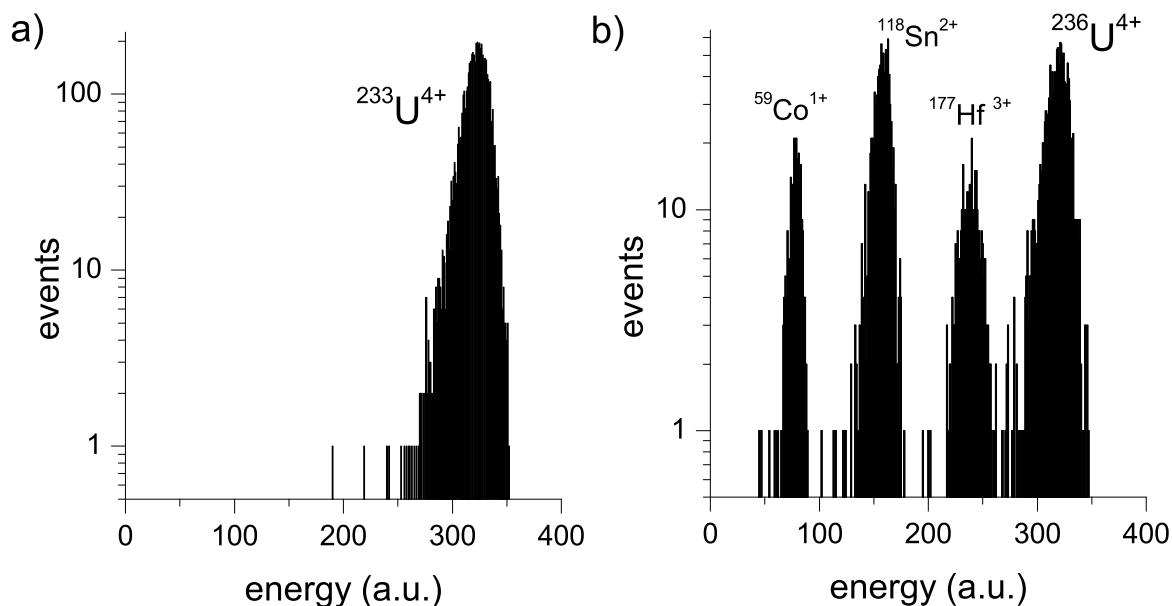
Figure 4.6: ZUTRI standard spectra were recorded with the Tandy tuned to a) $^{233}U^{4+}$ and b) $^{236}U^{4+}$.

to record two-dimensional spectra. Although the ratio of the ZUTRI standard used for the scans is much higher than for the Vienna-KkU material used for the 3^+ tests, the $^{235}U^{4+}$ counting rate is not reduced to the same extent. The separation of neighbouring nuclides is worse because the positions of the slits and the detector on the HE side are not aligned to the focal points of the ESA and the magnets (Fig. 4.5).

The $^{233}U^{4+}$ spectrum is very clean, for $^{236}U^{4+}$ ions the m/q interferences ($^{59}Co^{1+}$, $^{118}Sn^{2+}$, and $^{177}Hf^{3+}$) can be separated (Fig. 4.6), but also may cause a serious background via pile-up.

Because of this background and the three times lower transmission through the accelerator, the setup for U^{4+} is not competitive with the 3^+ in terms of selectivity and yield, which will leave the 3^+ as the favourite charge state for routine measurements.

4.2.2 ^{237}Np

The isotope ^{237}Np ($T_{1/2}$=2.1 Ma) originates from the β-decay of the short-lived ^{237}U ($T_{1/2}$=6.8 d), which is created by thermal neutron capture on ^{236}U or in a (n_{fast},2n) reaction on ^{238}U. In spent nuclear fuel the α-decay of ^{241}Am directly creates ^{237}Np. This radionuclide is interesting for environmental applications [Keith-Roach et al., 2001] but also for dosimetry in nuclear facilities. Among the actinides ^{237}Np shows a high risk for induction of bone cancer [Taylor, 1989]. Because of the long half-life of ^{237}Np, α-decay counting requires large amounts of sample material. On the other hand, MS detection may be complicated by the abundant neighbouring isotope ^{238}U. In a project together with DTU Risø measurements of ^{237}Np were performed for possible future use of AMS

to determine low ^{237}Np concentrations in urine samples. These tests intended to investigate the background level on mass 237, in particular the separation of the neighbouring isotope ^{238}U, the efficiency for Np in AMS and possible ways of standard normalization. The quantification of the overall yield of ^{237}Np in the chemical preparation and the physical measurement of samples is a critical point. The standard procedure would be to add another Np isotope to the sample as spike to determine the overall yield. ^{236}Np (T$_{1/2}$=154 ka) could be an appropriate Np carrier isotope. As this isotope is difficult to produce, it is not easily available. Besides, the amounts needed (typically 0.5 pg per sample) may cause cross contaminations in the laboratory or the ion source with ^{236}Np and might affect the highly sensitive ^{236}U measurements. The alternative is a method already carried out at other AMS laboratories [Fifield et al., 1997; Brown et al., 2004], which used ^{242}Pu as carrier. The prerequisite for such an approach is that both isotopes behave similarly during the chemical separation and the measurement. In the AMS measurement the charge state yield in the stripper should be the same or at least constant for both nuclides. The extraction of ^{237}NpO$^-$ relative to ^{242}PuO$^-$ from the ion source is expected to be more problematic. Not only that the general yield may be different for NpO$^-$ and PuO$^-$, also time (e.g. Fig. 4.1) and matrix dependent ion formation rates can affect the stability and reproducibility of the measurement. The comparability between standards, blanks, and samples thus has to be ensured in each particular preparation and for each beam time. In the chemical extraction of Np from a real sample, the consistent behaviour with the added Pu spike has to be guaranteed. For environmental samples a reliable chemical extraction of both elements (Np, Pu) can be conducted [Qiao et al., 2011], for urine samples this still has to be proven.

So far, two dilution series of targets containing ^{237}Np and ^{242}Pu were prepared by our collaborators at DTU Risø.

In a first set of tests a measurement of ^{237}Np down to very low levels was not possible. All samples with a nominal Np concentration of 10 fg or lower were influenced by a background counting rate at 237 amu. This background was real mass 237 amu and not originating from a surviving molecule or from scattered ^{238}U. Also the blank samples prepared from the Fe solution used for the precipitation showed a ^{237}Np counting rate. Press blanks produced from the Nb, which is added to the samples, were clean and showed no ^{237}Np counting rate. This points out that possibly the ^{237}Np contamination was transported via the Fe or the chemicals used for the precipitation. An inconsistency was observed in the detection of ^{237}Np relative to ^{242}Pu between tuning standards and the samples from the dilution series. Standards for tuning had been prepared with a relatively large amount of 500 fg of each isotope and showed a ^{237}Np/^{242}Pu ratio of 0.87. The higher concentrated dilution series samples also were not influenced by the above discussed background and showed ^{237}Np/^{242}Pu ratios that were only 0.2-0.25 of their nominal ^{237}Np/^{242}Pu value. Hence, it has to be assumed that the Fe matrix has an influence on the NpO$^-$ formation

rate. The Fe of the tuning standards had been precipitated as a larger amount (4-5 mg) and was red and flaked when pressed into the targets. In contrast, only 1 mg of Fe had been precipitated for the samples in the dilution series and the resulting powder was black and harder. A similar matrix effect is known for the formation of PuO$^-$ [Child et al., 2010]. In our experiment, however, Np seems to be the nuclide most affected by the matrix. Comparable amounts of ^{242}Pu were present in all targets and the counting rates of ^{242}Pu also were similar. However, so far it cannot be excluded that the observed matrix effect is in fact by pH sensitive precipitation efficiencies of the two elements in the chemical processing.
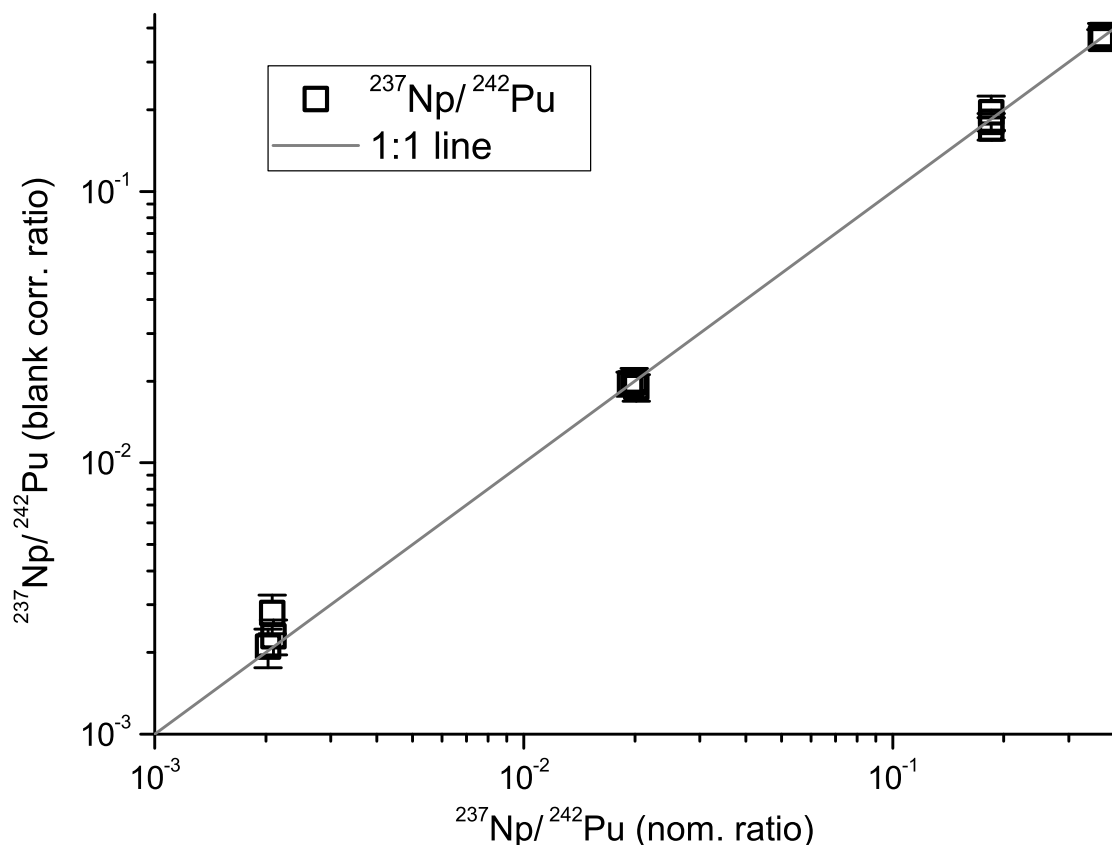
Figure 4.7: A standard series with different ^{237}Np concentrations relative to a fixed amount of ^{242}Pu was measured with AMS and is compared to the nominal ratios. The results from the second set of tests are shown.

A second set of tests was performed on targets containing 0-180 fg ^{237}Np and 500 fg ^{242}Pu each. The preparation was only slightly changed compared to the previous test. A Np cleaned Fe solution was employed and another washing step with pH 8 water was performed after the final precipitation and prior to the oxidation. Surprisingly, in this test the overall efficiency for ^{237}Np and ^{242}Pu was the same (Fig. 4.7). This time, a minor contamination of the Fe matrix with ^{242}Pu was observed showing the need for the Fe

solution to be carefully cleaned from both isotopes in advance. The results of this study are corrected for the ^{242}Pu rate of the Fe blank.

From these first experiments the conclusion can be drawn that AMS is useful to determine ^{237}Np down to fg concentration levels. In all targets analysed the relative isotopic yields were stable over time, which is an important prerequisite for a stable ^{237}Np measurement. This is in contrast to the time-dependent ^{233}U/^{242}Pu ratio observed in tests with ^{233}U and ^{242}Pu spike material (Fig. 4.1). The relative efficiencies of Np and Pu were stable in the two individual preparations of standard dilution series, but the values differed strongly with a Np/Pu efficiency of 0.2 in the first test and 1 in the second test. In previous studies Np/Pu efficiencies varied from 0.65 [Brown et al., 2004] to 0.77 [Fifield et al., 1997]. Hence, the utilization of Pu as efficiency indicator for Np bares additional uncertainties, but possibly can be overcome by parallel preparation of standards, blanks and samples.

4.2.3   Pu isotopes

Five Pu isotopes are interesting for AMS: ^{239}Pu ($T_{1/2}$=24.1 ka), ^{240}Pu ($T_{1/2}$=6560 a), ^{241}Pu ($T_{1/2}$=14.4 a), ^{242}Pu ($T_{1/2}$=375 ka), and ^{244}Pu ($T_{1/2}$=81 Ma). Their applications in the course of this work are described in section 6.4. The measurements are performed in the 3$^+$ charge state with the gas ionization chamber as final detector (Fig. 4.8). Rates of the individual Pu isotopes are counted sequentially. Individual problems may occur related to isotope specific background and will be discussed in the following:

- ^{239}Pu measurements may be influenced by background from scattered ^{238}U or from ^{238}UH^{3+}. This requires good chemical separation of U prior to the analysis and/or a special U correction for the scattered U nuclides. Therefore, in the routine measurement of Pu isotopes also a U sample is included. Runs with the injection (i.e. the Pulse Base Line) set to the mass of ^{238}U^{16}O$^-$ are undertaken for all samples while the HE side of the spectrometer is tuned to ^{239}Pu^{3+}. For the U sample the counting rates in this setup ($R_{238LE,U}$) are scaled to the counting rate observed during normal operation at mass 239 amu ($R_{239,U}$). The ratio $r_U = \frac{R_{239,U}}{R_{238LE,U}}$ is deployed for U correction of the samples. The counting rate $R_{238LE,sample}$ observed during those runs of the samples, when ^{238}U^{16}O$^-$ is injected, is multiplied with the ratio r_U to estimate the sample specific correction, which is finally subtracted from the 239 amu counting rate ($R_{239,sample}$). The corrected ^{239}Pu rate is estimated as $R_{239,final} = R_{239,sample} - r_U \cdot R_{238LE,sample}$.

  The chemical U suppression, that is usually achieved in the extraction of Pu from environmental samples, is sufficient so that in the new Tandy setup this correction becomes negligible.
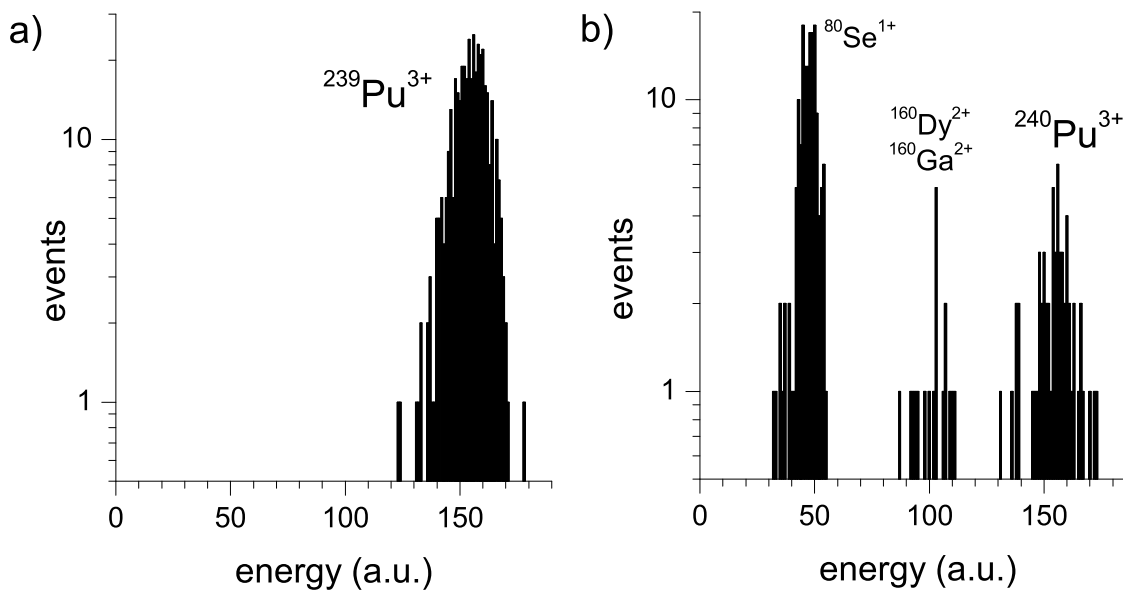
Figure 4.8: Spectra for the isotopes (a) $^{239}Pu^{3+}$ and (b) $^{240}Pu^{3+}$ from a natural sample.

- ^{240}Pu has possible m/q interferences from $^{160}Dy^{2+}$, $^{160}Ga^{2+}$ or $^{80}Se^{1+}$, which can be distinguished in the gas ionization chamber because of their lower energy (Fig. 4.8b). So far, pile-up problems due to intense stable beams of those isotopes have not been observed in samples.

- ^{241}Pu has the shortest half-life of those Pu isotopes that are determined via MS techniques. It decays via β^--emission to its isobar ^{241}Am. ^{241}Pu contaminated samples from the 60s now contain more ^{241}Am than ^{241}Pu. For reliable results of the original ^{241}Pu content, ^{241}Am has to be separated by chemical means so that only ^{241}Pu is counted. From its present concentration the original amount of ^{241}Pu then can be recalculated. Due to the unknown ionization efficiency of AmO^-, a rather immediate measurement of the samples after the chemical preparation is necessary in order to avoid an influence of the ingrowing ^{241}Am [Steier et al., 2013]. Because ^{241}Pu is relatively easy to include in the sequence for Pu isotopes, it is detected by AMS in those samples that have a sufficiently high ^{241}Pu content, although with decay counting lower concentrations of this isotope are measurable.

- In most MS (including AMS) measurements ^{242}Pu is used as spike to evaluate the efficiency of the chemical preparation and the physical analysis. Typically, 5 pg (or ca. 10^{10} atoms) of ^{242}Pu are sufficient to obtain good counting rates of this isotope even when run times at this mass are shortened compared to the unknown isotopes. The uncertainty from the determination of the efficiency via the counting of the ^{242}Pu then becomes negligible.

- For ^{244}Pu there is no isobar with a long half-life, ^{244}Cm ($T_{1/2}$=18.1 a) is the longest-lived. Due to its low abundance in the environment, the uncertainty of a ^{244}Pu AMS measurement is generally limited by the counting rate.

A standard dilution series for ^{239}Pu and ^{240}Pu was recorded in artificial urine samples and verified the sensitivity of the Tandy setup down to concentrations at the fg level [Dai et al., 2012]. However, it can be seen from Fig. 4.9, which was recorded for a second study, that background in spike materials also is a serious problem for Pu detection. In this double blind study, samples containing ^{239}Pu, ^{240}Pu, and ^{242}Pu were weighted in by the National Institute of Standards and Technology (NIST) in USA and the ratios were determined at the Tandy. Results were returned to NIST, which then handed out the original isotope ratios. Again, a good agreement down to fg concentrations of ^{239}Pu and ^{240}Pu could be proven, although major background corrections had been necessary for ^{240}Pu. It has to be emphasized that this was a background from a contamination in the preparation laboratory and is not typical for the AMS measurement of this isotope at the Tandy.
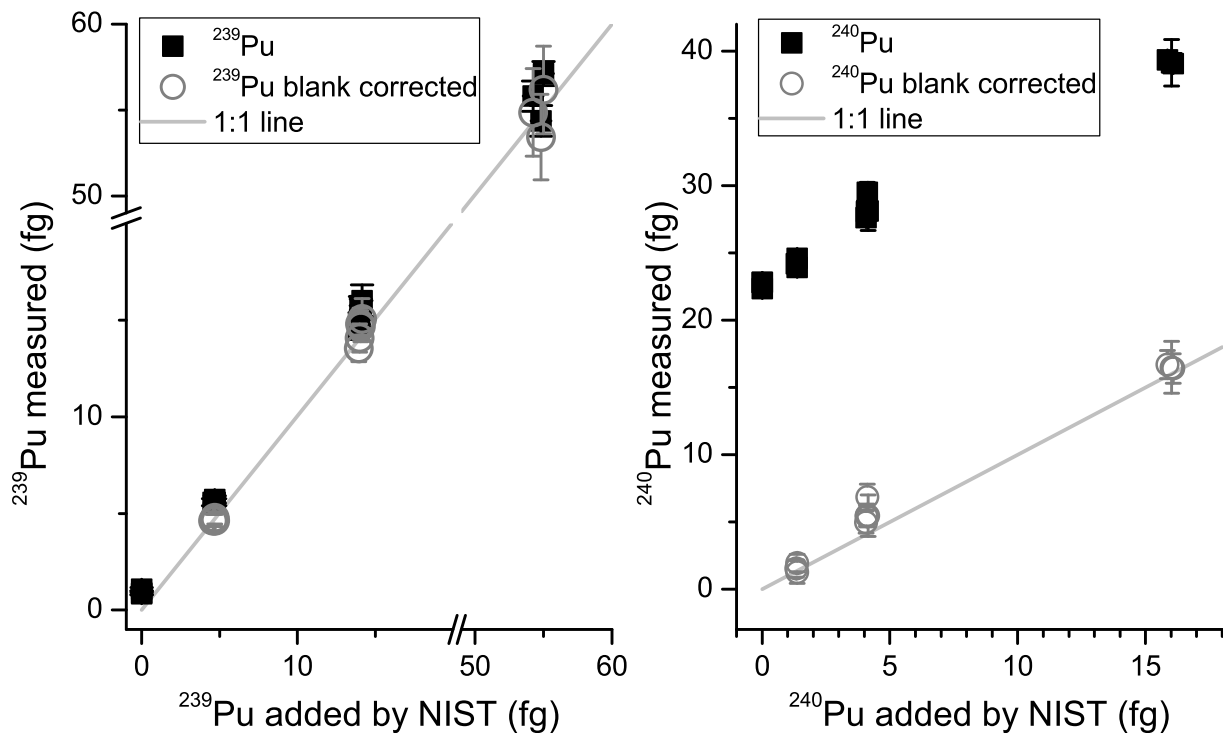
Figure 4.9: The standard dilution series for ^{239}Pu and ^{240}Pu prepared by NIST shows good linearity but for ^{240}Pu also a significant offset due to contaminated spike material. The offset can be corrected via the blank measurements.

4.3   Molecular background in charge state 3$^+$

The first sensitivity measurements with ^{236}U^{3+} in the new setup with the HE2 magnet revealed that the background level at mass 236 depends on the applied stripper pressure. Stripper density dependent counting rates usually indicate the survival of molecules at the mass of the desired radionuclide. Background from undestroyed molecules in charge state 3$^+$ has never been considered in AMS, although some diatomic trications were first observed at a tandem accelerator [Weathers et al., 1991; Anthony et al., 1991]. A catalogue of more than 70 exotic highly charged molecules was collected [Franzreb et al., 2004], but some of the listed candidates, e.g. CH^{3+}, seem to be dubious, because one would expect them to occur during routine AMS measurements. However, the selection of triply charged ions after the stripper has generally been thought to guarantee a beam free of molecules [Purser et al., 1979; Kutschera, 2005], because the amount of energy necessary to ionize molecules to the 3$^+$ is usually so large that a Coulomb explosion is considered to be energetically more favourable than a bound triply charged state.

From a series of observations and from dedicated experiments in the course of the background studies for actinides at the Tandy it could be concluded that surviving molecules are particularly relevant for AMS of ^{236}U^{3+} and ^{239}Pu^{3+}.

As already mentioned, a first hint at the existence of UH^{3+} and ThH^{3+} molecules was the detection of stripper density dependent counting rates one mass above all abundant actinide isotopes. In addition, the ThH^{3+} molecule was verified in an experiment breaking up the molecule and identifying the breakup product Th^{3+}. All the presented experiments were conducted with Ar as stripper gas before the setup was switched to the use of He. Measured Ar pressures in the stripper inlet are converted into areal densities following the empirical formula presented by Jacob [2001].

4.3.1   Experimental observation of stripper density dependent background

Dilution series measurements of ^{236}U standards were performed at various stripper pressures. During these experiments it was observed that the counting rate at 236 amu increases exponentially with decreasing stripper pressure (Fig. 4.10). Such a behaviour is well known from the incomplete destruction of molecules in the charge states 1$^+$ [Synal et al., 2007] and 2$^+$ [Lee et al., 1984]. In the previous TOF-measurement (section 4.2.1) of the standard dilution series a background at mass 236 had been identified (Fig. 4.4). From the results of the two experiments the background was assigned to molecules and its m/q ratio was matched to ^{236}U^{3+}. With the measurements performed in the gas ionization chamber, it was ascertained that the background deposited the energy of triply
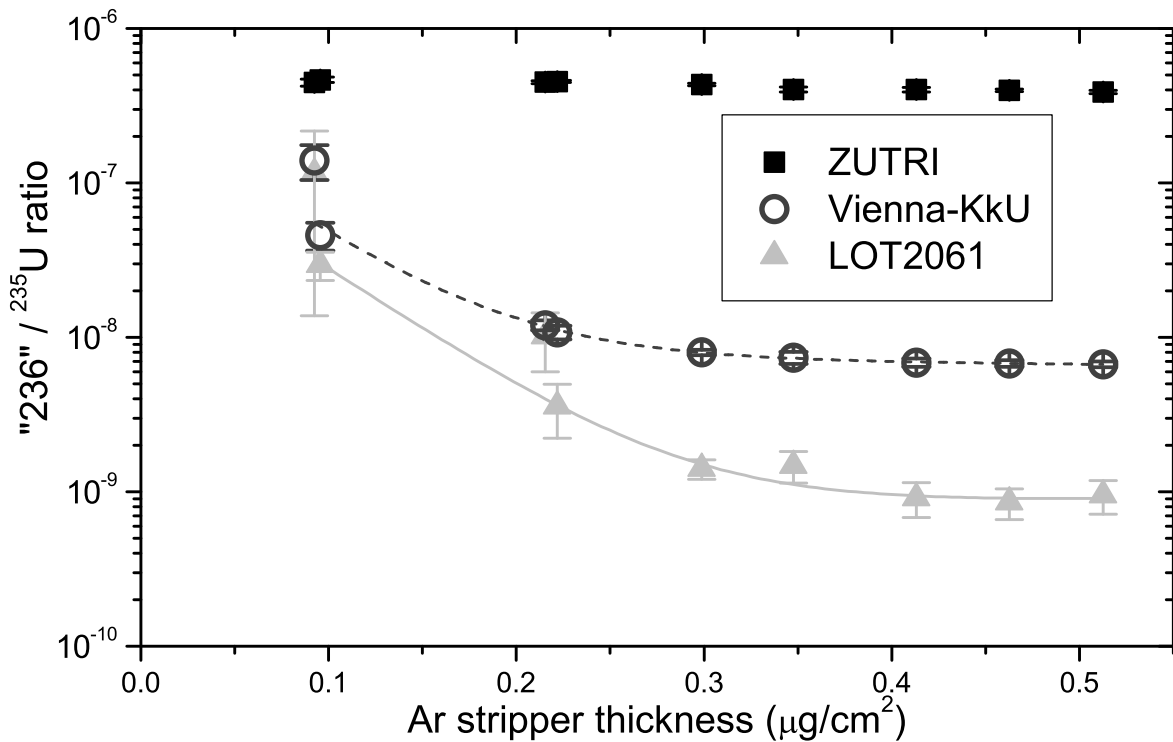
Figure 4.10: The exponential decrease of the counting rate at mass 236 is given relative to the ^{235}U intensity as a function of the Ar stripper density. The ^{235}U intensity is deduced from the ^{238}U current measured after the first HE magnet, assuming the natural ratio $\frac{^{235}U}{^{238}U} = 0.0073$.

charged ions. This way already the existence of triply charged molecules at mass 236 can be concluded.

The stripper pressure dependent counting rate appeared one mass unit above every abundant actinide isotope (^{232}Th, ^{235}U, ^{238}U, Figs. 4.10 and 4.11). Because of this regularity hydride molecules of Th and U were suspected to be the source of the background. When measuring one mass unit below the abundant isotopes (231, 237) the suppression of the neighbouring nuclides was better by up to 3 orders of magnitude and did not depend on the stripper gas pressure.

The fits to the data series Vienna-KkU and LOT2061 in Fig. 4.10 according to equation 2.1 give molecular destruction cross sections σ_{mol} of $(1.2\pm0.3)\cdot10^{-15}\,cm^2$ and $(1.3\pm0.2)\cdot10^{-15}\,cm^2$, respectively. In Fig. 4.11a only the data set of the ZUTRI standard is fitted relatively well with equation 2.1, for the other samples the uncertainties of the fit are too high to deduce a reliable value for the molecular destruction cross section. The ZUTRI fit returns a $\sigma_{mol}=(1.6\pm0.4)\cdot10^{-15}\,cm^2$. The cross section for ThH^{3+} destruction is estimated to $1.4\cdot10^{-15}\,cm^2$ (Fig. 4.11b).

There are two effects that can complicate the measurement of the stripper density dependent background:
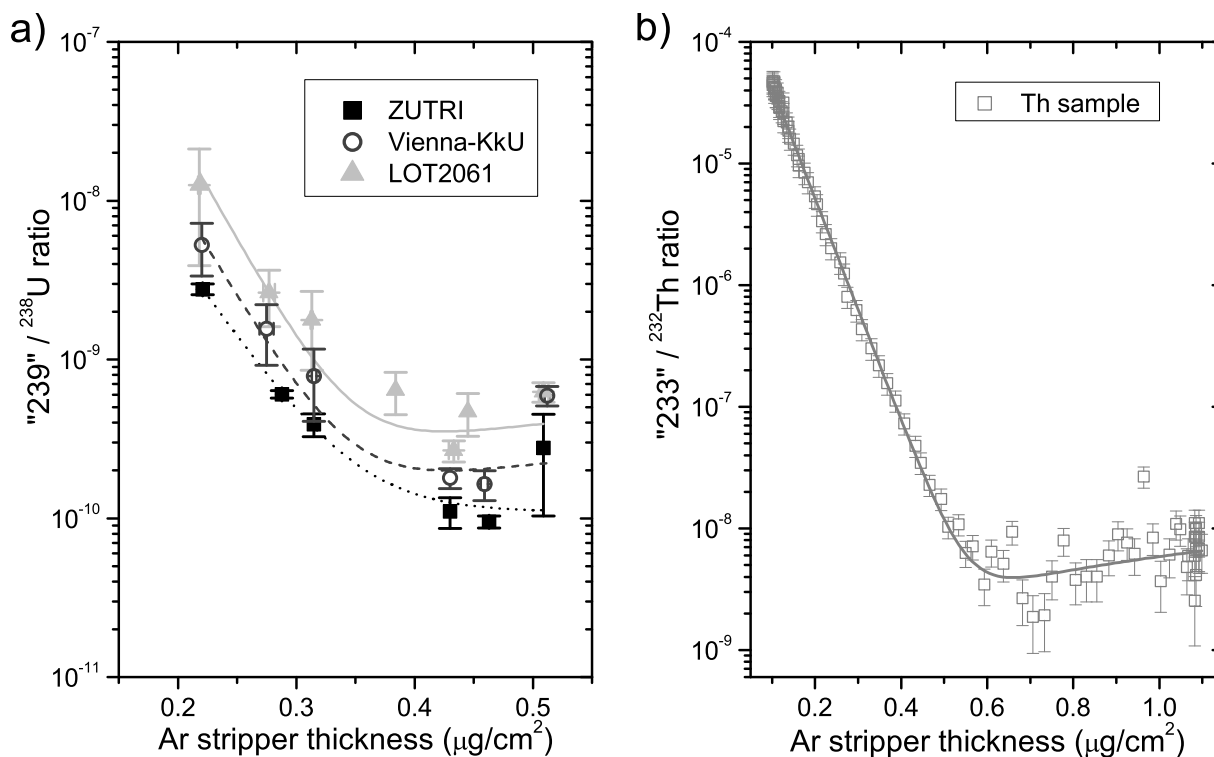
Figure 4.11: The exponential decrease of the counting rates as a function of the Ar stripper gas pressure are given for a) mass 239 relative to the ^{238}U intensity and for b) mass 233 relative to the ^{232}Th intensity.

As soon as the stripper gas thickness is changed, also the energy loss of the beam in this medium is varied. A stripper density dependent tuning might become relevant. This could be corrected by the measurement of a reference material. However, the acceptances of the energy related devices (pelletron terminal voltage and the ESA) are large enough to permit the same settings during all runs in which the stripper pressure was scanned.

Second, the observation of actinide-hydride molecules is overlayed by a time dependent behaviour of the samples in the ion source. During the sputtering process the target is heated by the ionizer and the formation of actinide-hydroxide molecules decreases. This process is partly reversible: H reaccumulates in the sample when it is removed from the focus of the ionizer so that the background counting rates are increased again when it is returned to the source. For this reason, the observed ratio of the actinide-hydride molecule relative to the regular actinide beam also depends on the time the single target had been measured before and even different targets of the same material cannot be easily compared.

This problem is overcome using two different approaches for Th and U. Relative to the Th^{3+} HE-current more ThH^{3+} molecules survive after the stripper than UH^{3+} molecules do relative to the U^{3+} HE-current. The higher ThH^{3+} counting rates quickly provide good statistics and permit fast scans over different stripper pressures on only one Th target

before the H is depleted. In addition, fast stripper scans from high to low stripper pressures and vice versa average the effect of H depletion during sputtering. For the U samples the stripper pressure was fixed and the whole standard dilution series was recorded. In this mode, the samples are in the source for few minutes only. During the time the targets are not in the Cs focus they may reaccumulate H. However, the H content varies anyhow between different targets. This would explain the slight offsets of the counting rates at 239 amu for the three U samples in Fig. 4.11a.

4.3.2 Detection of the breakup of ThH^{3+}

In addition to the observation of the stripper pressure dependent counting rates, an experiment was conducted to break up the molecules at mass 233 and to identify the breakup products ^{232}Th^{3+} and ^{1}H^{1+}. While previously only the molecular character of the background had been determined, this experiment was intended to prove that the molecules consist of the suspected actinide-hydride combination. Therefore, a foil was inserted on the HE side between the first magnet and the ESA. Post-stripping of the beam is a typical method of separating isobars in AMS, here it was used to destroy molecules surviving after the stripper canal. Because the breakup products are extremely asymmetric, the relative mass difference between the molecule and the heavy breakup particle is very small. Hence, energy and momentum of the heavy breakup particle are close to the values of the original molecule:

$$E_{233} = E_{232,\text{breakup}} + E_1; \qquad p_{233} = p_{232,\text{breakup}} + p_1$$
$$E_{232,\text{breakup}} = \frac{232}{233} \cdot E_{233}; \qquad p_{232,\text{breakup}} = \frac{232}{233} \cdot p_{233} \qquad (4.1)$$

^{232}Th from the breakup of ^{232}Th^{1}H, for example, will receive 232/233 parts (= 99.6%) of the primary energy and momentum. In order to be still able to resolve the breakup particle, very low energy and angular scattering are required during the breakup process. For this purpose a very thin (2 µg/cm^2) diamond-like carbon (DLC) foil was used.

In the interaction with the foil the beam energy was lowered, which required a new tuning for the ESA and the HE2 magnet. A beam of ^{233}U (Fig. 4.12) was used to determine the reference settings in the foil setup from which the new settings for Th from the breakup could be calculated. In Fig. 4.12 the ^{232}Th traces in the ^{233}U sample are separated in the HE2 magnet, as from the ESA one energy (E = E$_{233}$ = E$_{232}$) is defined, which results in a lower momentum for the ^{232}Th compared to the ^{233}U. The dashed line in this figure marks the expected magnetic field for ^{232}Th^{3+} from ^{232}ThH^{3+} breakup at the according ESA settings. Counting rates were normalized to facilitate the comparison between the two settings.
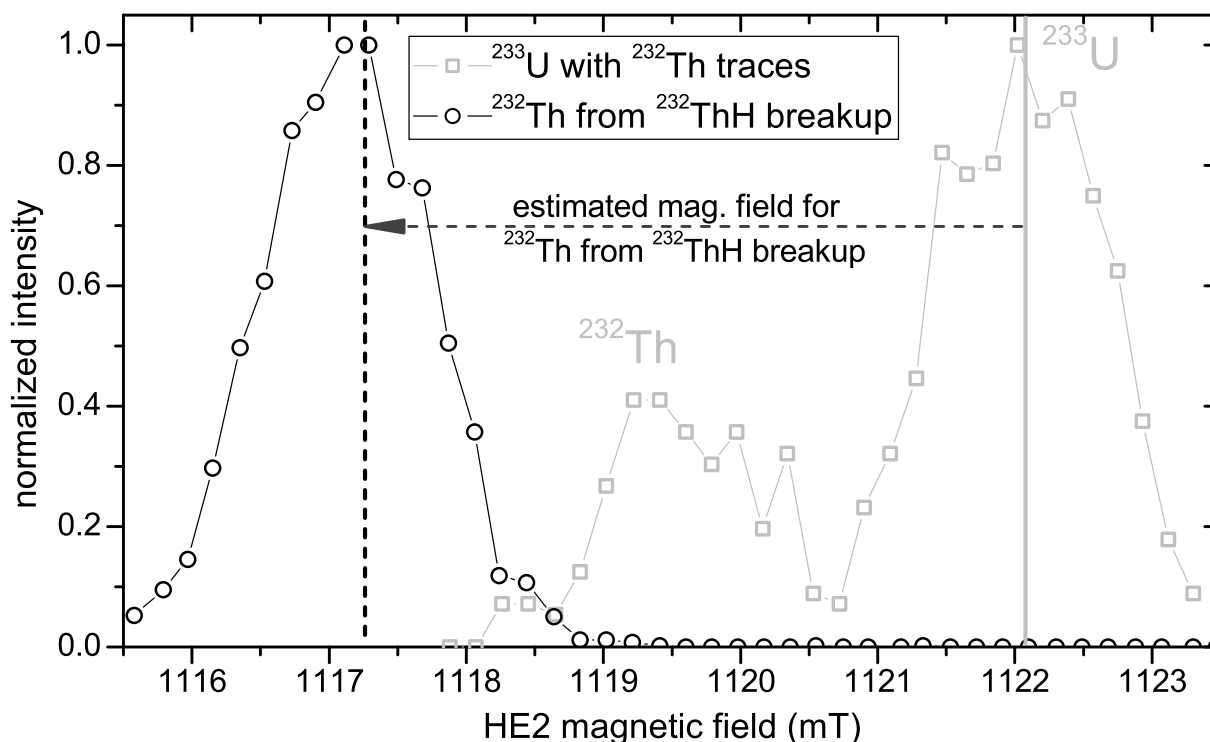
Figure 4.12: Scans of the HE2 magnet in the DLC foil setup on a ^{233}U (at ESA=$\pm$22.33 kV, open squares, the straight line marks the optimum value) and a ^{232}Th (at ESA=$\pm$22.23 kV, circles) sample are shown at a stripper thickness of 0.16 μg/cm^2.

The experiment determined the overall energy loss of ^{233}U to ca. 60 keV corresponding to about 5% of the initial beam energy. It is presumed that U and Th have a similar energy loss, which was confirmed by calculations with the SRIM program [Ziegler et al., 1985].

In the experiment a ThO$_2$ sample was used and a 233 amu beam of ThH^{3+} was sent to the DLC post-stripping foil. A beam was found at the ESA and the HE2 magnet settings calculated for ^{232}Th^{3+} from ^{232}ThH^{3+} breakup.

The counting rate at the breakup settings (circles in Fig. 4.13) showed a stripper pressure dependent behaviour. The exponential decrease of ^{232}Th^{3+} from the breakup is visible only up to a stripper areal density of 0.25 μg/cm^2, but the slope is comparable with the one of the molecular background (squares in Fig. 4.13). This proves that the 232 amu counting rate originates from the breakup of a 233 amu molecule and is not only produced by ^{232}Th scattered in the beam transport.

Because of the energy and angular straggling in the foil, the ^{232}Th^{3+} beam from the breakup has a larger divergence. The transmission of the beam from the foil through the ESA, the following slits and the HE2 magnet into the detector therefore is much lower than it is for the beam not interacting with the foil. It is further reduced by the charge state distribution after the post-stripping process. This results in a lower counting rate in the region where the exponential decrease dominates (Fig. 4.13, 0-0.3 μg/cm^2). How-
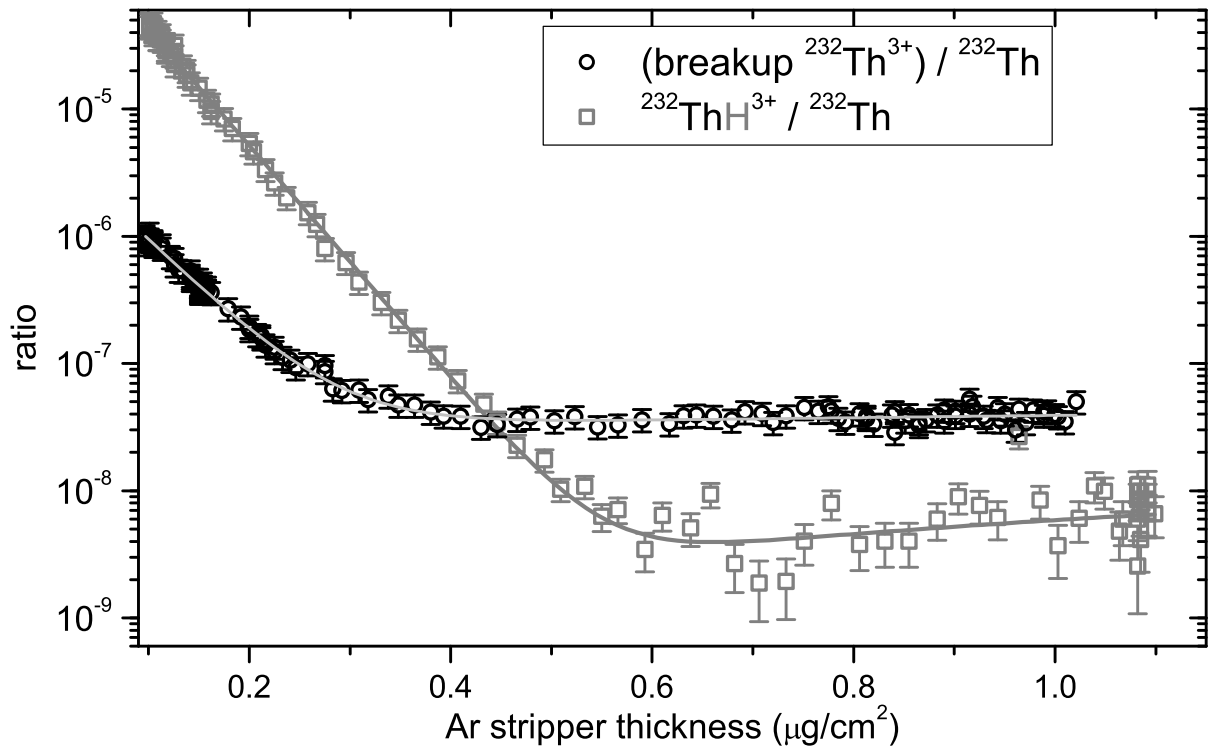
Figure 4.13: The counting rate at mass 233 relative to the ^{232}Th^{3+} current after the HE magnet (squares) decreases exponentially as a function of the Ar stripper gas thickness until the background level of the measurement is reached. In the setup with the post-stripping foil, ^{232}Th^{3+} from the breakup is detected and again normalized to the ^{232}Th^{3+} HE current (circles). For both cases, with and without foil, the raw measured isotopic ratios are shown without any correction for possible beam losses between the HE cup and the detector. The function 2.1 was used to fit the experimental data.

ever, with the foil inserted into the beam, the background level for higher areal densities is shifted upwards by a factor of 10 (Fig. 4.13, 0.3-1.0 μg/cm^2). The increased counting rate in the foil setup at higher stripper pressures is most probably caused by the scattering processes in the foil and the enhanced tailing of the more intense ^{232}Th^{3+} beam: The ^{232}Th^{3+} beam is not completely filtered out of the 233 amu beam by the HE1 magnet. In this setting, scattered ^{232}Th^{3+} ions that are not further suppressed by the ESA cannot be separated in the HE2 magnet. Consequently, they also will appear at the HE2 magnetic field marked by the dashed vertical line in Fig. 4.12.

An attempt to detect H$^+$ from the breakup using a Channeltron detector positioned after the ESA was not successful. The proton beam would have been expected at an energy of only 5.4 keV. No distinct peak was found at this energy when scanning the ESA. The angular divergence of the protons caused by the Coulomb dissociation in the foil might be too large. Furthermore, at these low beam energies a significant amount of H might be neutral after the breakup and the interaction with the foil.

4.3.3 Implications

The flight time of the ions starting from the stripper canal to the detector amounts to 10 μs. This gives a minimum estimate of the lifetime of the triply charged molecules.

The survival of ThH^{3+} and UH^{3+} after stripping the ThOH$^-$ and UOH$^-$ molecules gives information on the original structure of the negative precursor molecule. Obviously, the O of the negative molecules can be removed during the stripping to charge state 3$^+$ while at the same time the actinide-hydrogen bond is not destroyed. The H can be directly bound to the actinide ion and not only via the O in an OH molecule. The direct bonding of H to the actinide in the precursor molecule and the existence of ThH^{3+} and UH^{3+} are confirmed by quantum-theoretical calculations performed at the University of Cologne, which are described in Lachner et al. [2012a].

At areal stripper densities above ca. 0.3 μg/cm^2 for U and ca. 0.6 μg/cm^2 for Th the background levels are relatively constant, only a little trend of increasing background due to enhanced scattering in the beam tubes is observed. The minimum background level for the actinides most likely is influenced by scattered abundant isotopes that are injected into the accelerator as UOH$^-$ or ThOH$^-$ molecules and that are not filtered on the LE side. At high stripper pressure all of these molecules are broken up and only Th^{3+} and U^{3+}
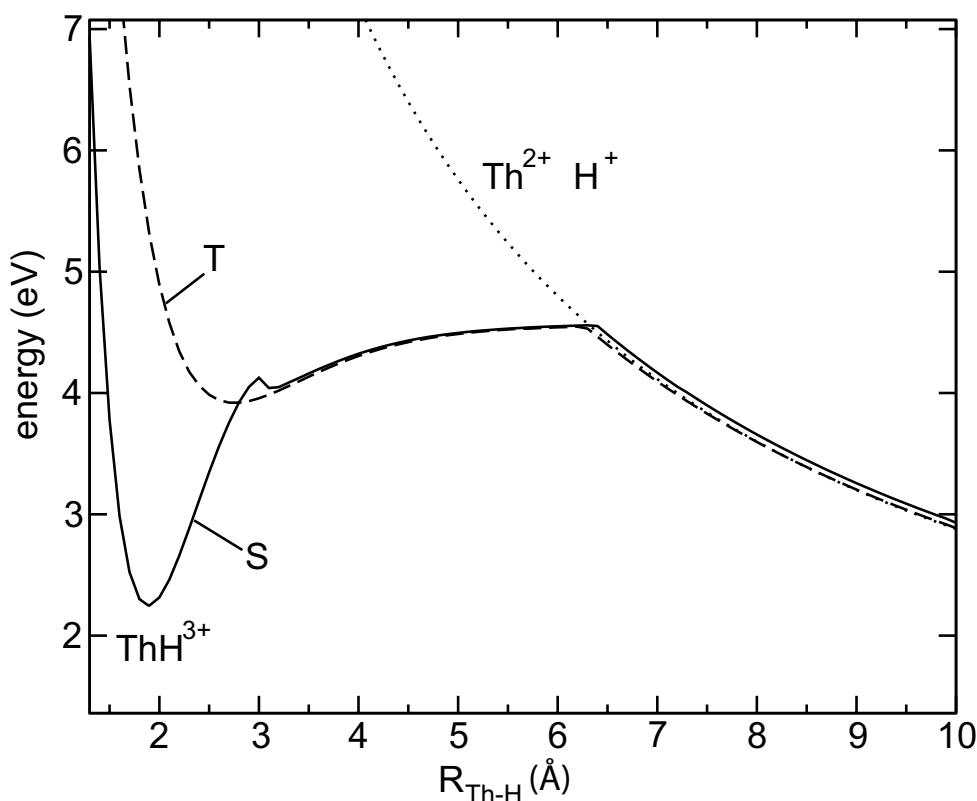
Figure 4.14: The potential energy for the lowest singlet (S) and triplet (T) ThH^{3+} states are depicted versus the binding length R$_{Th-H}$. The picture is taken from Lachner et al. [2012a].

leave the stripper tube, but may be scattered in the following. Assuming a similar formation rate of the precursor hydride molecules, the background levels are expected to be the same for $233/^{232}$Th, $236/^{235}$U and $239/^{238}$U. However, the absolute values of the background levels are not equal (Figs. 4.10 and 4.11). This has different reasons: In all measured U samples there are traces of real ^{236}U. Consequently, if one wants to show the consistency of the background levels at masses 236 and 239, the nominal ^{236}U$/^{235}$U ratio has to be subtracted from the measured one before comparing the $236/^{235}$U and the $239/^{238}$U background level. If this is done for the lowest sample LOT2061, the corrected background ratio $236/^{235}$U amounts to ca. $5 \cdot 10^{-10}$. This again is fairly consistent with the $239/^{238}$U level of ca. $3 \cdot 10^{-10}$. Still, the background for mass 233 relative to the ^{232}Th intensity is about a factor of 20 higher. Hence, one can conclude that Th more readily than U forms negative molecules containing O and H in the ion source. Such a difference in the formation rates would be in agreement with the higher ThH^{3+} rate observed at lower stripper thicknesses, the reason why the Th experiments could be more easily conducted in fast scans over the stripper pressure. Maybe the higher rate of ThH^{3+} is related to its stronger bonding compared to UH^{3+}. The quantum-theoretical calculations predict that only 0.60 eV are needed for the dissociation of the UH^{3+} molecule, whereas the barrier for Th-H separation is 2.26 eV.

4.4   Conclusion

The systematic tests of the new Tandy setup have demonstrated its gain in sensitivity of a factor of three caused by the switching to He as stripper gas and in selectivity of three orders of magnitude due to the installation of the second HE magnet. The overall efficiency for U and Pu amounts to $2 \cdot 10^{-4}$, the selectivity to $\approx 4 \cdot 10^{-12}$. Although the selectivity is not as high as for larger systems, e.g. at VERA [Steier et al., 2008] and ANU [Wilcken et al., 2008; Fifield et al., 2013], the Tandy setup is competitive regarding the determination of actinides in environmental samples because of its high sensitivity. The achieved selectivity of 10^{-10} for the suppression of a neighbouring mass isotope is sufficient for the measurement of most environmental samples (chapter 6). During the selectivity tests triply charged molecules were observed, which can be eliminated by increasing the areal density in the stripper. For this reason, transmission losses have to be accepted. In the further development of LE-AMS the possibility of molecular background even in charge state 3^{+} has to be considered.

Chapter 5

Carrier-free Be analysis[*]

5.1 Introduction

In most applications the investigation of ^{10}Be ($T_{1/2}$=(1.387$\pm$0.012) Ma, Korschinek et al.
[2010]; Chmeleff et al. [2010]) via AMS aims at the determination of this radioisotope's
concentration in a natural sample. This is achieved by spiking the sample with several
100 μg of the stable isotope ^{9}Be, an amount that by far exceeds the natural abundance of
^{9}Be in the original sample. The natural ^{9}Be concentration can be neglected in this case. In
the AMS measurement the ^{10}Be/^{9}Be ratio of the spiked sample is detected and thereby
the ^{10}Be concentration can be derived. Examples for important applications of the ^{10}Be
concentration are the dating of natural archives, e.g. Mn nodules [Segl et al., 1984], the
reconstruction of past cosmic ray flux, solar activity, or the geomagnetic field via the ^{10}Be
production [Raisbeck et al., 1981b; Beer et al., 1988; Steinhilber et al., 2012], e.g. from
ice cores or sediments. The disadvantage of examining only the ^{10}Be concentration is
that this value can be strongly affected by natural and environmental conditions, such
as the composition or the accumulation rate of the archive. To extract a ^{10}Be production
rate nonetheless, the assumption of constant environmental conditions has to be valid or
additional data have to be available, e.g. in the marine environment the Be flux from the
water column to the sediment can be explored via the ^{230}Th$_{excess}$ method [Francois et al.,
2004]. As an alternative, ^{9}Be can be used as tracer of all environmental and chemical
processes that might affect ^{10}Be. If it is assumed that no significant change occurred in
the ^{9}Be supply to the archive's environment, the ratio of the two isotopes can circumvent
the normalization problems.

The conventional method to determine the natural ^{10}Be/^{9}Be ratio is measuring the ^{10}Be
concentration with Accelerator Mass Spectrometry (AMS) and the ^{9}Be concentration with
an appropriate method for abundant stable isotopes. A main focus of this thesis was to

---

[*]Parts of this chapter are based on Lachner et al. [2013a].

demonstrate that the ^{10}Be/^{9}Be ratio also can be analysed directly with AMS in routine measurements.

In the following, the instrumental setup and its special requirements for the carrier-free ^{10}Be AMS operation at the Tandy are described. For the determination of the ^{10}Be/^{9}Be ratio in sediments the samples are not fully dissolved (appendix A.1): Be is only extracted from the sediment fraction that is built in at the position and during the formation of the archive, the so-called authigenic fraction. The authigenic ^{10}Be/^{9}Be ratio was suggested early to be used for applications such as dating marine archives [Bourlès et al., 1989] and studying geomagnetic field variations [Henken-Mellies et al., 1990].

In this work, the ^{10}Be/^{9}Be ratio was used for dating and to examine the ^{10}Be production changes during the last geomagnetic field reversal. The extraction of the authigenic Be fraction is very sensitive to the applied chemical treatment of the sample. For this reason, multiple processings of marine sediments were performed and documented the reproducibility of the chemical procedure, which is based on Gutjahr et al. [2007]. Comparison studies of the conventional and the carrier-free method with marine and terrestrial sediment samples proved the reliability of the new technique.

The remeasurement of four sediment samples from the Arctic Ocean examined if the results of the new carrier-free method are consistent with values found in a previous conventional ^{10}Be/^{9}Be measurement [Sellén et al., 2009]. The sedimentation rates in the Arctic Ocean calculated from the ^{10}Be/^{9}Be ratio are compared with values derived from biomarkers and from the ^{231}Pa/^{230}Th ratio.

In a second test, an archaeological site was dated using sediment samples from river terraces. This constituted the first successful comparison between the conventional and the carrier-free technique and further samples were prepared to expand the age model over a wider range of the stratigraphy.

In a larger project, the last geomagnetic field reversal, called Brunhes-Matuyama, was studied at five different deep ocean sites in marine sediment cores. The results are compared with the palaeomagnetic data, with ^{10}Be records at other marine sites and ice cores, and with present seawater ^{10}Be/^{9}Be ratios deduced from the top layers of Mn nodules or crusts found close to the core sites. A relative Virtual Dipole Moment (rVDM) record is derived from the best-resolved study site.

5.2   Be budget

In order to use the authigenic ^{10}Be/^{9}Be ratio for dating or to study past geomagnetic field variability, the supply and behaviour of both isotopes in the surrounding of the archive is critical. The main processes of the transport of ^{10}Be and ^{9}Be to the ocean are summarized by McHargue and Damon [1991]. In the following, the important differences of the input of ^{10}Be and ^{9}Be to the ocean are discussed.

^{10}Be

The isotope ^{10}Be is mainly produced via nuclear reactions in the atmosphere. High-energy galactic cosmic rays, primarily protons and α-particles, create a cascade of secondary particles in spallation reactions. In further spallation reactions on atmospheric N and O the secondary protons and neutrons produce cosmogenic nuclides such as ^{10}Be [Arnold, 1956; Lal and Peters, 1967; Masarik and Beer, 2009]. The geomagnetic field partially shields the atmosphere from the charged cosmic rays modulating the galactic cosmic ray intensity in the different latitudes. Particles enter more easily in the region of the magnetic poles. That is why the radionuclide production is higher in those regions. On global scale ^{10}Be is produced in troposphere and stratosphere in a relation of 1 : 2, but production shows a strong latitudinal dependence [Lal and Peters, 1967; Masarik and Beer, 1999]. At low latitudes the contribution of the troposphere is even higher than that of the stratosphere.

Cosmogenic Be quickly attaches to submicron particles, which are scavenged in clouds [Young and Silker, 1980]. The stratospheric residence time of Be is ca. 1 a, in the troposphere it is much shorter (ca. 35 d) [Raisbeck et al., 1981a].

From the comparably high ^{10}Be concentrations in the surface waters of North Atlantic and Pacific it was derived that the ^{10}Be input to the ocean is dominated by rather uniform precipitation from the atmosphere [Ku et al., 1990]. Nevertheless, there are local variations of the ^{10}Be flux to the Earth's surface [Field et al., 2006; Heikkilä, 2007]: In the mid-latitudes the ^{10}Be flux is highest due to the break in the tropopause, which eases the downward transport of stratospheric ^{10}Be. The "hot spots" of the ^{10}Be flux are in the oceans at latitudes 40° North and South [Willenbring and von Blanckenburg, 2010] and the main contribution is from wet precipitation.

^{9}Be

Compared to its abundance in the solar system [Anders and Grevesse, 1989] ^{9}Be is enriched in crustal rocks [Taylor, 1964], but depleted in rivers or sea water [Merrill et al., 1960; Measures and Edmond, 1982]. Input of non-terrigenic ^{9}Be to the ocean is limited to ridge-crest hydrothermal sources [Measures and Edmond, 1983], which provide very acidic solutions with high ^{9}Be content. However, Be is efficiently scavenged with particles in the hydrothermal plumes. This suggests that the input delivered to the overall oceanic ^{9}Be budget from these sources is negligible [Bourlès et al., 1994]. Dissolved ^{9}Be in the ocean hence generally is of terrigenic origin, but the contributions of the main transport processes are not yet fully resolved and will be discussed in the following.

The transport of dissolved ^{9}Be via rivers only gives little contribution to the oceanic budget. The concentration of dissolved ^{9}Be is higher in acidic rivers with pH < 6 than it is in alkaline carbonate rivers [Measures and Edmond, 1983; Brown et al., 1992a]. However, the Be

concentration is decreasing with increasing salinity [Kusakabe et al., 1991] when going from rivers to estuaries. Thereby, almost 90% of the riverine Be is removed in the mixing with ocean water in the estuary. The high particle flux and the increasing pH lead to scavenging of Be. This effect was observed at a number of sites [Measures and Edmond, 1983; Kusakabe et al., 1991; Frank et al., 2009], showing that the main input of ^{9}Be to the ocean is not via dissolved riverine transport. ^{10}Be/^{9}Be ratios have values 2-12·10^{-9} in rivers and estuaries [Kusakabe et al., 1991], being an order of magnitude lower than typical open ocean values. Hence, the estuaries may act as source of ^{9}Be to the ocean, but as sink for oceanic ^{10}Be.

Brown et al. [1992b] concluded from a study in the Mediterranean Sea that the main ^{9}Be flux to the oceans is via aeolian (i.e. wind transported) dust. If ^{10}Be is used as tracer, one can calculate the accumulation rate of lithogenic minerals via the aeolian dust input [Measures et al., 1996]. But it is demonstrated that dust alone is not sufficient to reproduce the lithogenic flux in the South Atlantic. So, riverine input could still play a role at locations with low supply of aeolian dust. According to von Blanckenburg et al. [1996b] the amount of ^{9}Be transported to the ocean via aeolian dust is sufficient in the North Atlantic but not in the Pacific. Furthermore, the overall ^{9}Be mass in the ocean could only be explained if a large fraction of the dust particles were dissolved. Redissolution of a small fraction ($\approx 2\%$) of the detrital Be deposited by the rivers in the coastal margins is suggested as additional source.

In any case, the sources for ^{10}Be and ^{9}Be to the water in rivers and oceans are different. Therefore, the ^{9}Be concentration and the ^{10}Be/^{9}Be ratio in sea water may have a strong local dependence.

Oceanic residence time

In a number of studies the residence time of Be in the ocean was investigated, e.g. by Raisbeck et al. [1980], Mangini et al. [1984], Bourlès et al. [1989], Anderson et al. [1990], Ku et al. [1990], Kusakabe et al. [1991], von Blanckenburg and Igel [1999], and Frank et al. [2009]. It was found that on regional scales the residence time of Be may vary from 100 a to 1000 a, depending on the effectiveness of scavenging Be from the water column. The scavenging is strongly related to the particle flux and composition and is increased for opal and lithogenics compared to carbonate [Chase et al., 2003]. The residence time, notably in coastal areas, can be lower than 100 a due to the high particle fluxes scavenging the Be, but also the difference between the open Atlantic ($\tau \approx 500$ a) and the open Pacific ocean ($\tau > 1000$ a) is related to this fact [Anderson et al., 1990; Ku et al., 1990; Kusakabe et al., 1990]. In the open ocean the particle fluxes are generally low. Correspondingly, there the Be residence time is high. Hence, Be scavenging is especially sensitive to the high particle flux areas at the margins, which act as a Be sink.

5.3   The AMS setup for carrier-free ^{10}Be/^{9}Be at the Tandy

5.3.1   Description of the setup

At ETH Zurich the first attempts to measure ^{10}Be/^{9}Be without addition of ^{9}Be carrier were performed applying a SIMS source [Maden et al., 2004] and low-energy AMS [Christl et al., 2010c]. Also in this work, the carrier-free Be samples were analysed at the compact Tandy AMS system. The lowest samples examined with this technique have ratios in the order of 10^{-11}. After the installation of a second magnet on the HE side the background level for ^{10}Be/^{9}Be measurements was reduced below 10^{-15} [Müller et al., 2010b]. Due to the limited amount of ^{9}Be in the samples ($< \mu$g) this number is not fully applicable to the carrier-free measurements as no commonly measured natural samples have such low ratios. For the carrier-free samples the precision of the determination is limited by their ^{10}Be counting rates or they might suffer from the general background that also is present during conventional AMS of ^{10}Be. Besides, the low ^{9}Be currents may complicate the detection of the natural ^{10}Be/^{9}Be ratio, which is discussed in more detail in the next section. The ^{10}Be/^{9}Be sample ratios are normalized via the in-house standard S1. This standard is brought to accordance with the new ^{10}Be half-life according to Kubik and Christl [2010] and its nominal ^{10}Be/^{9}Be ratio is $9.51 \cdot 10^{-8}$.

Suppression of the ^{10}B interference is achieved by the degrader foil method [Müller et al., 2010b], where the 1$^+$ charge state is selected after the accelerator and the 2$^+$ charge state after the degrader foil. Thereby, an overall transmission from the LE side to the detector of up to 11% can be reached. But this value and consequently the value of the standard strongly depend on the tuning and slit settings required for sufficient ^{10}B suppression. For carrier-free measurements the stability of the setup within a run is illustrated by the results of the reference material S1 during three beam times (Fig. 5.1).

5.3.2   Handling of low ^{9}Be currents

Because of the low ^{9}Be concentration in the samples, ^{9}Be currents are reduced compared to the conventional method. Reliable measurements in the range of few hundred pA have to be guaranteed. At the Tandy system this is achieved by long integration times and sensitive integrators of the ^{9}Be current. In doing so, the bouncing time of the stable ^{9}Be beam into the Faraday cup on the HE side has to be longer compared to a conventional Be measurement using ^{9}Be carrier. This reduces the run time available for ^{10}Be by $\approx 25\%$. Typical carrier-free samples prepared from 1 g sediment show ^{10}Be/^{9}Be ratios above 10^{-10} and develop currents of 0.5-1 nA. For such samples the determination of the ^{10}Be/^{9}Be ratio is more sensitive to background from stable ^{9}Be than it is to contamination with ^{10}Be. This is a special situation in AMS: A critical contamination can not only stem from the rare radionuclide but also from the abundant isotope. ^{9}Be can be present
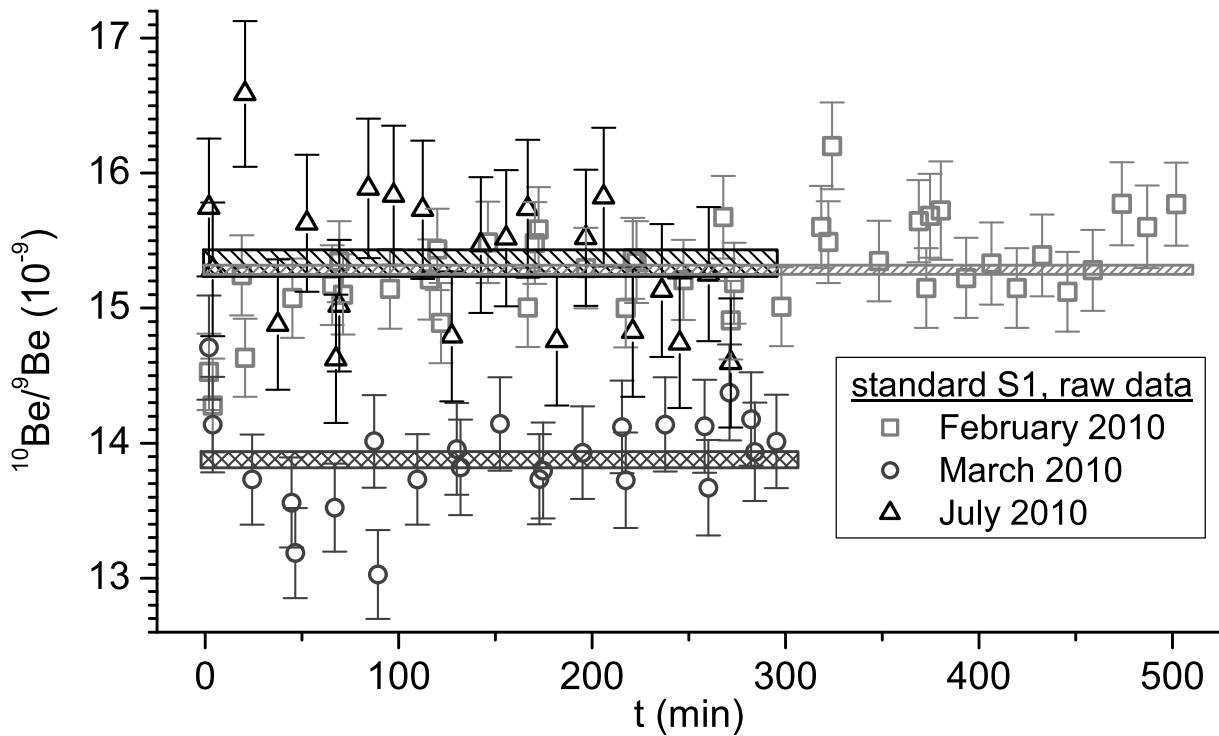
Figure 5.1: The results of the standard S1 are presented for the whole time span of the measurement during three different beam times. Due to varying ^{10}B separation in the chemical preparation of the samples and due to different tunings the slit settings had to be adjusted to achieve the required ^{10}B suppression. This led to different absolute standard values in the compared beam times. Shaded areas denote the mean standard value of the beam time, which typically has a 1σ uncertainty of $< 1\%$.

in any chemical that is used in the chemical preparation and accidental input cannot be monitored by processing a ^{9}Be-free natural sample because this isotope is present in any natural material. As it is described below, fully processed blank samples are used instead. Special attention is turned to the preparation of the samples and to the measurement of the low currents. It could be demonstrated that currents even below 100 pA can be reliably recorded in the new setup. The zero-level of the ^{9}Be current is checked in several ways: First, an instrumental offset is quantified by reading out the current at closed valves, i.e. no beam can reach the Faraday cups, corresponding to the offset in Fig. 5.2. This offset is automatically subtracted by the software. Second, targets solely containing Nb powder and no Be are used to control any cross contamination during the pressing of the sample material into the cathodes or during the sputtering process. The Nb targets usually give only few pA of ^{9}Be^{1+} on the HE side. Third, fully processed blank samples are produced starting from the leaching substance and by treating these blanks in the same way and with the same amount of chemicals as used for the normal samples. The fully processed blank samples should be free of ^{9}Be and ^{10}Be. Thereby, input of ^{9}Be or ^{10}Be by the chemicals used for the processing and cross contamination during
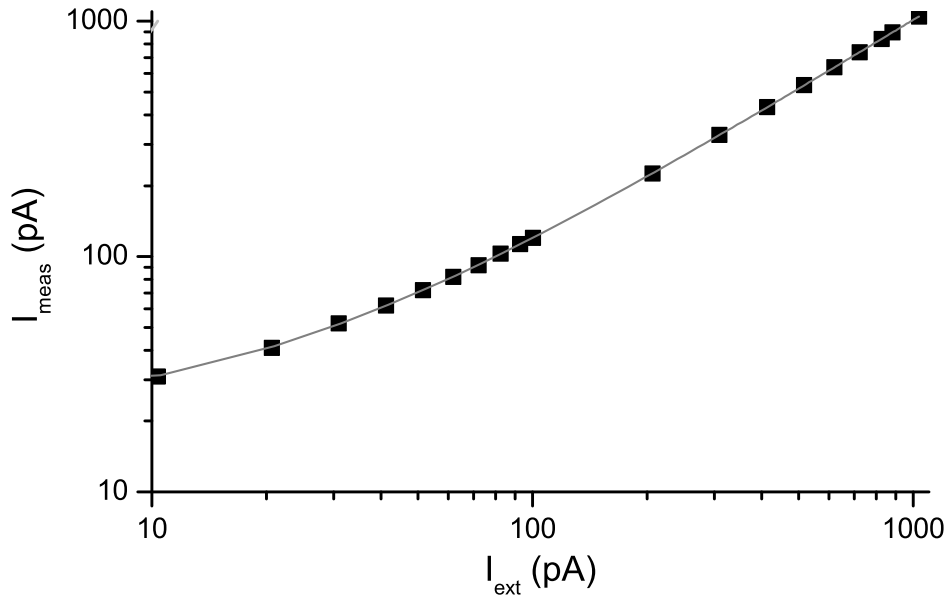
Figure 5.2: Measured currents I_{meas} are plotted against currents given by an external source I_{ext}. A linear fit $I_{meas}=a \cdot I_{ext}+b$ results in a slope $a=0.9940\pm0.0003$ and an offset $b=(20.79\pm0.12)\,pA$ ($R^2=1$).

sample preparation and in the ion source can be monitored. These blanks develop ^9Be HE currents of 10-15 pA and ^{10}Be rates of less than 2 counts per minute. Targets of the S1 standard with varying Be content are measured to identify a potential current dependence of the $^{10}Be/^9Be$ ratio. A correction for such a dependence may require an HE current offset of up to 15 pA. Usually, this offset correction on the current already accounts for the currents of the Nb press blanks and in some cases it is even larger than the current of the fully processed blanks. Either the offset correction or the HE current of the fully processed blanks determine the maximum HE current correction. The total HE current correction therefore is less than 15 pA and it has uncertainties lower than 5 pA, which are derived from the standard deviation of the uncorrected currents of the fully processed blank samples.

Burn-in processes in the target normally reduce the ^9Be background in all blank samples, which indicates that this background is introduced by a surface contamination of the targets. Therefore, a minimum burn-in time of 10 s is applied prior to the first run on each target. The blank corrections to samples with HE currents above 200 pA are negligible. Even for samples with lower currents, the uncorrected $^{10}Be/^9Be$ ratios are all in the $3\,\sigma$ uncertainty of the blank corrected values, while the uncertainty introduced by the blank correction for these samples is not larger than 4%.

5.4 Reproducibility of chemical processing and measurement

In the following, it will be described how the reproducibility of the chemistry was checked by multiple preparations of marine and terrestrial samples. Moreover, the reproducibility of the AMS measurement was investigated by multiple measurements of the same targets during different beam times. For tests on marine sediments, several samples from the Ocean Drilling Program Sites 769 in the Celebes Sea and 1021 at the California margin [Shipboard Scientific Party, 1997] were used. Four of the multiple preparations are discussed in detail. The Be content was extracted in independent preparations (A,B,C in Fig. 5.3) and two different targets were produced from each of the four samples. Some of the targets were repeatedly measured during different beam times with varying settings of the AMS devices. The differences in the Tandy settings and the chemistry yields are illustrated by the varying currents.
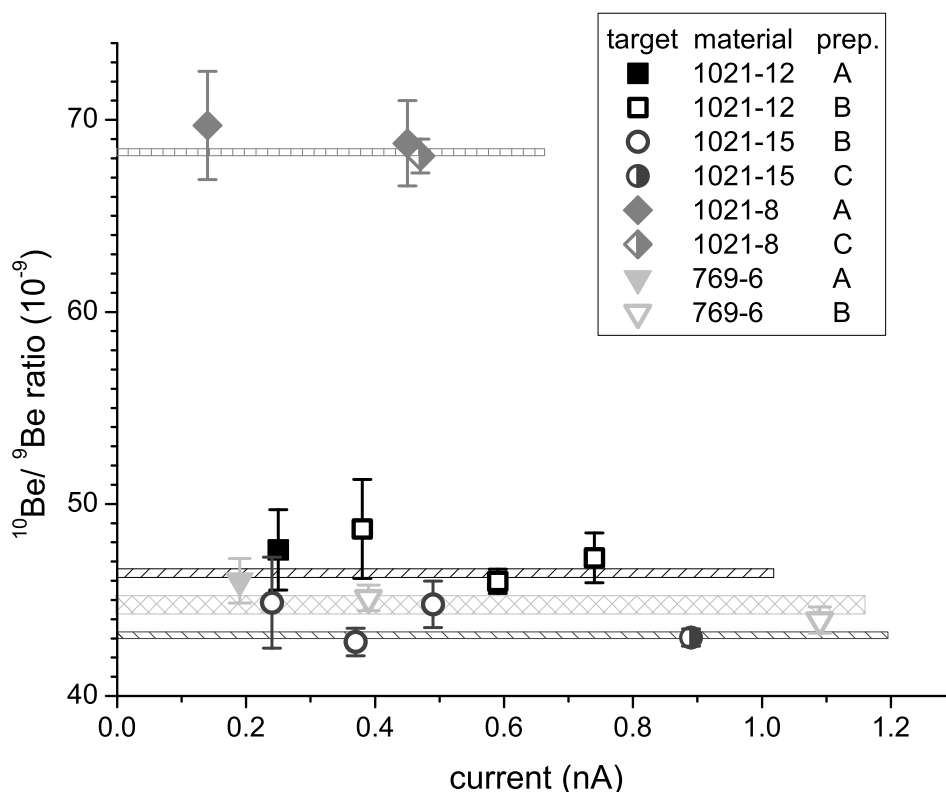
Figure 5.3: Sediment samples from different depths of the ODP Sites 769 and 1021 were processed in individual chemical treatments (A,B,C) and their ^{10}Be/^{9}Be ratios were measured in different tunings of the AMS system. These remeasurements of the same target during another beam time are depicted with the same symbol and resulted in differing ^{9}Be currents. The mean values of the samples and the according 1σ uncertainties are displayed as shaded areas.

The samples show $^{10}Be/^9Be$ ratios in the 10^{-8} range and the results are consistent. Uncertainties of the single measurements include measurement stability, counting rate, blank correction and the uncertainty of the standard. The overall internal 1σ uncertainty of a measurement on a single target typically is 1.5-3.5%. For the samples from ODP Site 1021 all but one of the single measurements (1021-15 B 3 in Fig. 5.3) include the mean value in their 1σ uncertainty. This indicates a possible overestimation of the uncertainty of a single measurement. A $\chi^2_{red} < 1$ is calculated for the three ODP Site 1021 datasets and a $\chi^2_{red} = 1.4$ for 769-6. Obviously, for the 1021 sediment samples no additional uncertainty is necessary to account for the variations from target to target and from tuning to tuning. In this case, the full reproducibility of the sample preparation and the measurement therefore is smaller than the uncertainty of a single measurement and may amount to a maximum of 2%.

However, in $CaCO_3$ and opaline silica rich sediments both in the marine environment (e.g. at ODP Site 1090) or in terrestrial samples (fluvial terraces) stronger variations of the $^{10}Be/^9Be$ ratios in different preparations and measurements were found. This is partially related to poor currents of the targets ($\lesssim 100\,pA$), which then are more strongly affected by blank corrections, but it might be related to the leaching of different fractions, too. This needs more study on the Be ratios of the different sediment fractions. Not only for sample 769-6, but also for other samples from ODP sites 769 and 1090 values of $\chi^2_{red} > 1$ are calculated. Values $\chi^2_{red} = 1$ can be generated by including an external uncertainty of 2%. This points out that the reproducibility of the preparation is depending on the sediment type and may be the limiting factor of the uncertainty if samples are measured to precisions $< 2.5\%$.

Results of single measurements can reach overall uncertainties of down to 1%. This clearly underestimates the errors caused by the variability of the leaching and separation procedure. Thus, even if samples are measured with very high precision, results are given with a minimum uncertainty of 2.5%. This is sufficient for all applications.

5.5 Sedimentation rates in the Arctic Ocean

5.5.1 Sample description

The water input to the Arctic Ocean carries quite different $^{10}Be/^9Be$ ratios [Frank et al., 2009]. Low ratios come from Siberian rivers ($< 3\cdot10^{-8}$), the Canadian Mackenzie river ($< 1\cdot10^{-8}$) and from river influenced Pacific Ocean water ($2-3\cdot10^{-8}$). The water from the Atlantic carries a $^{10}Be/^9Be$ ratio of ca. $7\cdot10^{-8}$ and in the Canadian Basin the melting of sea ice and direct atmospheric input can lead to ratios $> 10^{-7}$.

In the 2005 HOTRAX expedition, 29 piston cores were taken as a transect of the central Arctic Ocean to study stratigraphy and paleoclimate [Darby et al., 2005]. Two of the
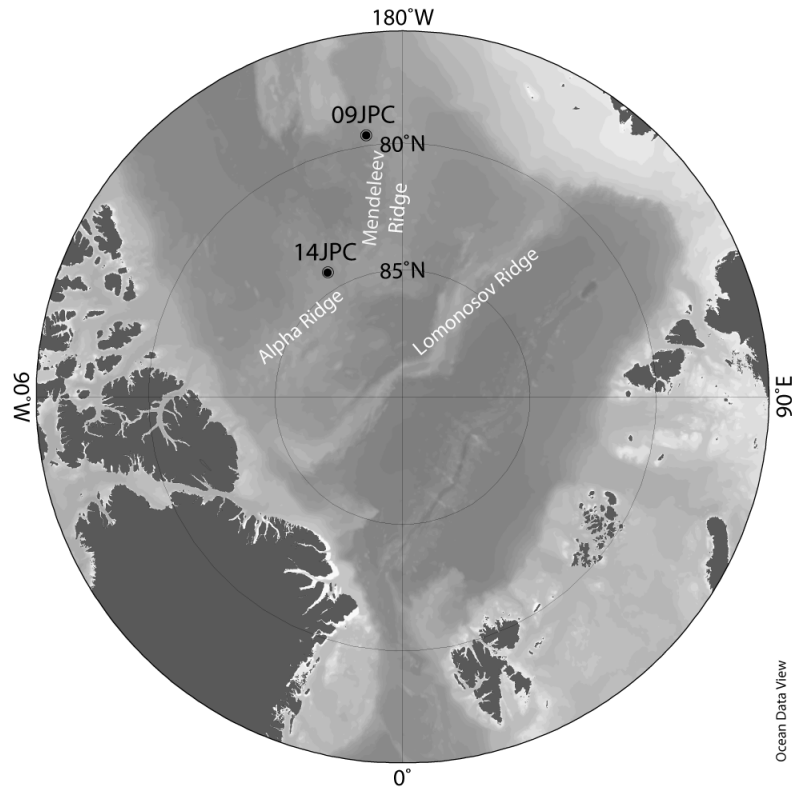
Figure 5.4: The two cores 09JPC and 14JPC were used to investigate sedimentation rates in the Arctic ocean.

sediment cores retrieved (Fig. 5.4), HLY0503-09JPC (09JPC) at the Mendeleev Ridge (2783 m water depth, 15.4 m core length) and HLY0503-14JPC (14JPC) at the Alpha Ridge (1856 m water depth, 11.2 m core length) had been analysed for their authigenic Be content and isotopic signature in a previous study [Sellén et al., 2009]. Average sedimentation rates of 0.27 cm/ka (09JPC) and 0.23 cm/ka (14JPC) had been estimated based on the decrease of ^{10}Be/^{9}Be in the core. These rates have to be newly calculated using the ^{10}Be half-life of 1.387 Ma resulting in values of 0.29 cm/ka (09JPC) and 0.25 cm/ka (14JPC), respectively. However, another study used dating via amino acid racemization [Adler et al., 2009] and revealed quite differing sedimentation rates at the Mendeleev Ridge, which will be discussed later.

5.5.2 Results

From each core (09JPC, 14JPC) two samples (close to top and bottom) were chosen to be remeasured with the carrier-free method. This remeasurement of the same material served both as a check of the sedimentation rates and as another test of the new method

in comparison with a conventional ^{10}Be/^{9}Be examination. Four carrier-free targets were prepared. In samples from the same sediment, the ^{10}Be concentration and the authigenic ^{10}Be/^{9}Be ratio had been examined with the conventional AMS + ICP-MS approach [Sellén et al., 2009]. The carrier-free ^{10}Be/^{9}Be values are compared with the corresponding results (table 5.1, Fig. 5.5) of this previous study in the next section. Here, only the four samples actually measured in both studies are taken into account for the calculation of sedimentation rates .

Table 5.1: Results for ^{10}Be/^{9}Be ratios (with $1\,\sigma$ uncertainty) and for sedimentation rates in the Arctic Ocean cores 09JPC and 14JPC are given. The carrier-free results are compared with values from selected samples that were measured with the conventional AMS + ICP-MS method [Sellén et al., 2009].

sample	depth [m]	current* [pA]	^{10}Be/^{9}Be [10^{-9}]	conv. ^{10}Be/^{9}Be [10^{-9}]
09JPC-1	0.02	249 ± 5	23.7 ± 0.6	12.1 ± 0.8
09JPC-11	15.30	718 ± 5	0.65 ± 0.03	0.35 ± 0.04
sedimentation rate			$0.215\,\frac{\text{cm}}{\text{ka}}$	$0.212\,\frac{\text{cm}}{\text{ka}}$
14JPC-1	0.60	35 ± 4	10.5 ± 1.3	5.72 ± 0.43
14JPC-8	11.01	1260 ± 5	0.24 ± 0.02	0.12 ± 0.02
sedimentation rate			$0.138\,\frac{\text{cm}}{\text{ka}}$	$0.135\,\frac{\text{cm}}{\text{ka}}$

* The current is given after correction for a stable current offset during the measurement, which is deduced from standard normalization.

In the chemical processing a behaviour differing from the usual was observed for the samples from the top of the core. Instead of the usual yellow colouration of the resin used for Fe separation, the resin was coloured green after processing the top samples of the Arctic sediment core. However, the processing of the bottom samples resulted in a light greenish colouration of the resin, too. This probably originates from specific geochemical compositions of the samples. Typically, the currents of parallel processed samples do not vary by more than a factor of five. The currents of the four Arctic sediment samples (table 5.1) show exceptionally large differences, which might be explained by these compound variations or by losses during the sample preparation.

5.5.3 Comparison of carrier-free and conventional determination

The sedimentation rates found by Sellén et al. [2009] are verified by the carrier-free method to a precision of $\pm\,2\%$ if the comparison is limited to the four samples measured in both studies (table 5.1). When the raw ^{10}Be/^{9}Be data are compared, a discrepancy
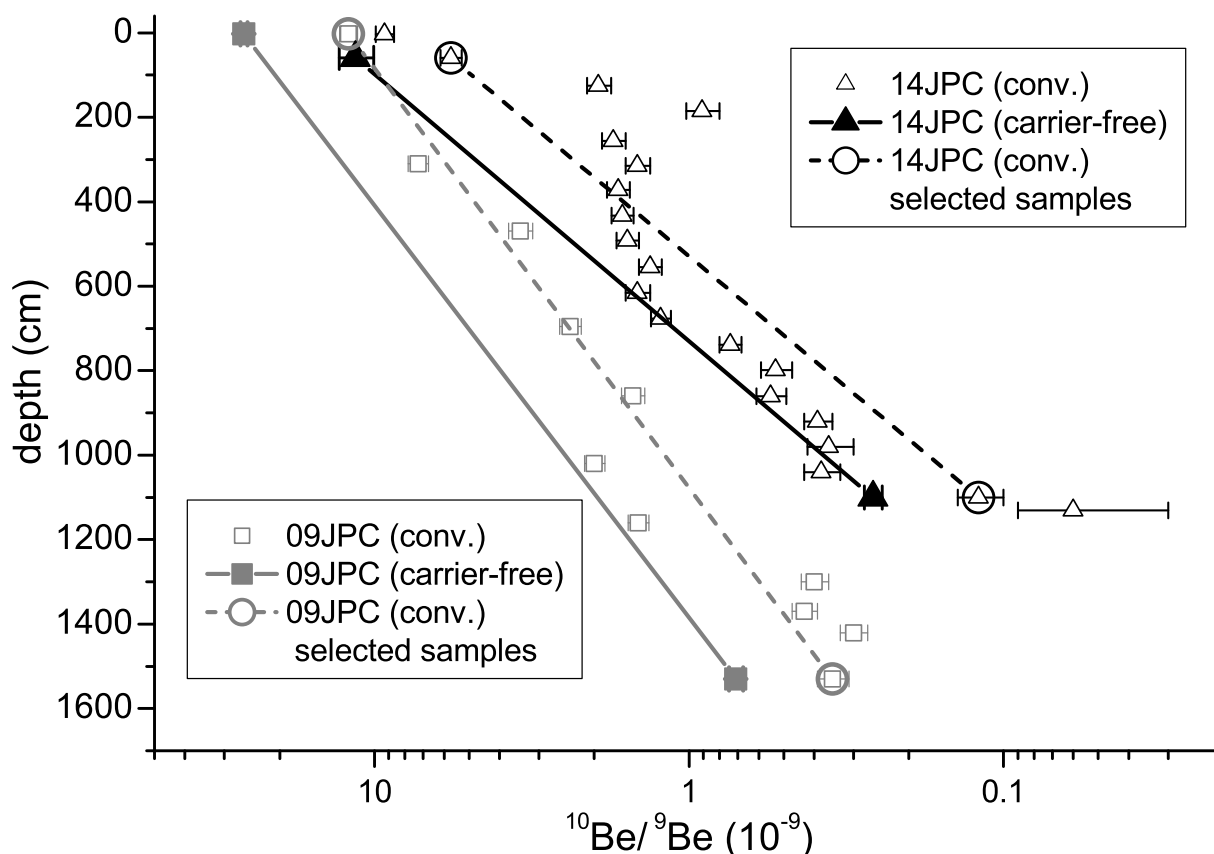
Figure 5.5: ^{10}Be/^{9}Be ratios from the cores 09JPC and 14JPC measured with carrier-free and conventional AMS [Sellén et al., 2009] show an exponential decrease with depth.

between the conventional and the carrier-free determination of this ratio appears. The results obtained with the carrier-free method are systematically higher by a factor of two. This deviation questions the compatibility of both Be methods. The fully processed blanks prove that no contamination with ^{10}Be or ^{9}Be has occurred during the preparation of the carrier-free samples. Accidental leaching of the detritus would cause an excess in ^{9}Be. Therefore, it might only explain the lower ratios derived from the conventional measurement. But in the extraction of Be for the conventional determination, the leach solution was used in the same concentration as in the carrier-free preparation. Assuming a possible failure during the carrier-free sample preparation, only a contamination with ^{10}Be would explain the higher ratios. However, for all samples a systematic difference by a factor of two would be required, which is unlikely to occur by accidental ^{10}Be input.

During the ICP-MS determination of ^{9}Be, matrix effects might account for the observed disagreement between the carrier-free and the conventional method. Progressive dimming of the signal during the ICP-MS standard addition measurements can cause results of too large ^{9}Be concentration. But this effect is strongly dependent on the measurement sequence and a substantiated discussion needs more experimental work.

The carrier-free ^{10}Be/^{9}Be ratios at the core tops ($\geq 10^{-8}$) match the values observed in another Arctic core top and in Arctic bottom waters [Frank et al., 2009]. This is an important control as the top of the core should represent the recent, seawater-derived ^{10}Be/^{9}Be ratio. Generally, if a contamination with ^{10}Be can be excluded, a high ^{10}Be/^{9}Be ratio is more plausible: The ^{10}Be is introduced from the atmosphere into the seawater where it mixes with the currently present amount of ^{9}Be. Any non-authigenic ^{9}Be from the sample material, for example released by leaching of the ^{10}Be free detritus, generates a lower ratio.

In summary, the carrier-free method seems to be robust concerning contaminations and its results for the authigenic ^{10}Be/^{9}Be ratio in the marine sediments also fit better to seawater values.

5.5.4   Comparison with other results for sedimentation rates

The low sedimentation rates in the order of few mm/ka assigned with authigenic ^{10}Be/^{9}Be at the Mendeleev Ridge are questioned by results from dating with biomarkers at a nearby site. A study on racemization rates for two different amino acids in planktonic foraminifera [Kaufman et al., 2008] resulted in a sedimentation rate at the site HLY0503-08JPC higher by more than a factor of five. Racemization denotes the transformation of fossil amino acids. The configuration of amino acids changes after the death of the organism. The rate of this process is constant under stable environmental conditions and allows for dating [Bada and Schroeder, 1975]. The site 08JPC studied via this method is located in a depth of 2792 m, very close to the site 09JPC at the Mendeleev Ridge. Additionally, the higher value observed at 08JPC site matches with the results of an authigenic ^{10}Be/^{9}Be measurement at another Arctic site: A study on the ACEX core from the Lomonosov Ridge in the central Arctic Ocean [Frank et al., 2008] quantified the average sedimentation rate for the last 11.3 Ma to (1.58±0.1) cm/ka. The time range was expanded by Backman et al. [2009], finding that 404.8 m of sediment were deposited at a rate of about 1.46 cm/ka over 27.8 Ma in the last 56.2 Ma. These values are revised for the new ^{10}Be half-life.

Recently, ^{231}Pa/^{230}Th measurements were used to generate an age model for two other cores from the Mendeleev Ridge [Not and Hillaire-Marcel, 2010]. The low sedimentation rates (0.15 cm/ka) detected with ^{231}Pa/^{230}Th agree well with the ^{10}Be/^{9}Be based values of Sellén et al. [2009] and this study. Generally, sedimentation rates in the Arctic Ocean range from 0.2 cm/ka to more than 30 cm/ka [Polyak et al., 2009]. These strong discrepancies between the different methods or sites are not resolved so far. However, the site 08JPC (2792 m water depth) used for racemization dating is situated slightly downslope of the site 09JPC (2783 m water depth), which was examined using authigenic ^{10}Be/^{9}Be. Therefore, it was suggested that enhanced deposition of fine grained material at the slope foot has led to the higher sedimentation rate determined with the amino acid racemization

technique [Adler et al., 2009]. The variations in sedimentation rates hence may be within the local natural variability and strongly depend on the regional setting.

5.6 Dating of fluvial sediments

5.6.1 Application of the ^{10}Be/^{9}Be ratio in terrestrial environments

The dating of sediments via the decay of ^{10}Be also is an interesting option on continents. The mobility of Be was thought to limit its applicability for dating [Monaghan et al., 1983]. However, first promising results of dating terraces of the Californian Merced river [Pavich et al., 1986] pointed out that the Be residence time in soils is long enough.

The combination of the in-situ produced radionuclides ^{10}Be and ^{26}Al in quartz can be used for dating buried sediments, because their production rates are similarly affected by site-specific parameters. A constant ^{10}Be/^{26}Al production rate is present as long as the material is exposed at the surface, but the ratio continuously decreases during burial due to the different half-lives. Ages in the range of 200 ka to 5 Ma can be investigated via the ^{10}Be/^{26}Al ratio [Granger and Muzikar, 2001; Shen et al., 2009]. The authigenic ^{10}Be/^{9}Be ratio in river sediments has the advantage over the ^{10}Be concentration that it does not depend on the grain size of the sediment [Wittmann et al., 2012]. Thus, the ^{10}Be/^{9}Be ratio in river water and sediments can be used to explore denudation rates [von Blanckenburg et al., 2012]. Again, the normalization with ^{9}Be might rule out environmental effects but only holds if both isotopes are in equilibrium prior to sedimentation and if the archive forms a closed system, i.e. once ^{10}Be and ^{9}Be are incorporated their ratio is not altered by later input or removal of Be. Because of the input from eroded ^{9}Be, rivers carry lower ^{10}Be/^{9}Be ratios (^{10}Be/^{9}Be $\approx 10^{-8}$, Kusakabe et al. [1991]) than ocean water ($(0.5\text{-}1)\cdot10^{-7}$, von Blanckenburg et al. [1996b]). Thus, also authigenic ^{10}Be/^{9}Be ratios of present riverine or lacustrine sediments ($(2.54\pm0.09)\cdot10^{-8}$, Lebatard et al. [2008]) are lower than in oceanic archives. Terrestrial ^{10}Be/^{9}Be ratios may strongly depend on the environmental setting. In order to guarantee a good normalization of the sediment data, one can try to identify the initial ratio via present-day ratios.

The first successful example of applying authigenic ^{10}Be/^{9}Be in soils was the dating of sediment layers in lacustrine sediments applied to detect the age of hominid fossils from the Mio-Pliocene in Chad [Lebatard et al., 2008, 2010].

5.6.2 Sample description

Clastic river terrace sediments from the Bulgarian Azmaka river were prepared by means of the new carrier-free method. A pre-human hominid tooth had been found in these de-

posits and by fossil assemblages the find was attributed to the second half of the Turolian, i.e. the tooth has an age of ca. 7 Ma [Spassov et al., 2012].

To obtain dates for the river terraces one has to know the initial ^{10}Be/^{9}Be ratio in the sediment at the time of deposition. Therefore, it has to be assumed that the present geological setting and ^{10}Be/^{9}Be input is the same as in the past 10 Ma. Active river channels are proposed as the suitable contemporary setting corresponding to the clastic sediments. Sediments from different positions in the active Azmaka river channel and a number of sediment samples from various depths of the terrace were studied. For each individual sampling site three subsamples were taken representing the same river channel or sediment layer. To reduce the number of analyses, in some cases these subsamples were combined and analysed as one sample.

5.6.3 Conventional ^{10}Be/^{9}Be determination

Following the problematic discrepancy observed between the conventional and the carrier-free results in the Arctic sediments, another comparison study was carried out. For the conventional technique four sediments were chosen. In this case, for each sample three subsamples were combined and mixed already prior to the preparation. ^{9}Be was measured at the Institute of Geochemistry and Petrology at ETH Zurich. Special care was taken to eliminate any matrix effects during the ICP-MS measurement of the ^{9}Be concentration by applying the method of standard addition. Thereby, the aliquot for the determination of the ^{9}Be concentration is split into several subsamples. These are mixed with different known amounts of ^{9}Be in the range of the expected ^{9}Be amount present in the sample. The original ^{9}Be concentration can be extrapolated via a linear fit to the results of the subsamples series.

5.6.4 Results

The carrier-free and the conventional method yield consistent results for the ^{10}Be/^{9}Be ratio and the ages of the sediment (Fig. 5.6). Apart from these comparison samples, targets were prepared from other sediments for the carrier-free method only.

Ratios in the present-day active river channels show a wide range of values from $5.5 \cdot 10^{-9}$ to $1.3 \cdot 10^{-8}$. Unfortunately, as mentioned in section 5.4, this strong variability is even reproduced for repreparations of the same sediment from an active river channel. The ^{10}Be/^{9}Be ratios seem to be very sensitive to the leaching of different fractions of the sediment. The highest ratios above $1 \cdot 10^{-8}$ are only found in samples containing a lot of $CaCO_3$. The other samples give results in the range of $(5\text{-}7) \cdot 10^{-9}$. However, in any case the ages of the sediment layers are consistent with the ages inferred from fossil assemblages, but more tests are necessary to resolve possible variations of the ^{10}Be/^{9}Be ratio
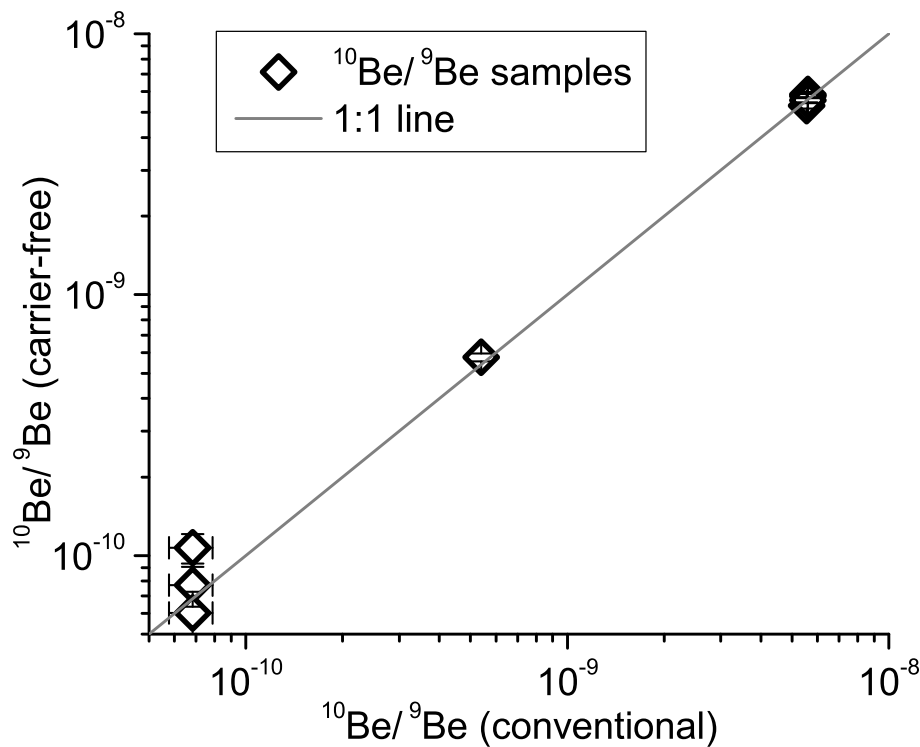
Figure 5.6: ^{10}Be/^{9}Be ratios from four sites were measured with carrier-free and conventional AMS. In the carrier-free determination the three subsamples were analysed for two of the four sites. Additional samples were analysed with the carrier-free technique only and are not included in this figure.

in different sediment fractions. Results for the sediments from greater depth show lowest ratios of $(7\pm1)\cdot10^{-11}$. Here, the uncertainties are already dominated by the counting statistics.

Because of the large scatter in the results of the present-day sediment, the chemical method of extracting Be from sediment probably has to be reevaluated before reliable dating with the authigenic ^{10}Be/^{9}Be ratio in terrestrial sediments can be conducted.

5.7 The Brunhes-Matuyama field reversal

5.7.1 General motivation

It was first suggested by Elsasser [1946] that the Earth's magnetic field is created by a geodynamo in the fluid outer core. Its polarity is not fixed but changes irregularly. One explanation proposed for this behaviour is that plate tectonics influence the thermal structure of the mantle and the convection of the fluid metallic core [Glatzmaier et al., 1999; Pétrélis et al., 2011]. This could generate a breakdown and reestablishment of the geodynamo. The energy stored in the dipole is partitioned to terms of higher order during magnetic

events such as excursions or field reversals. Furthermore, the intensity of the cosmic ray flux in the atmosphere increases, which causes a higher production of radionuclides [Elsasser et al., 1956; Masarik and Beer, 1999]. Hence, long-lived cosmogenic radionuclides such as ^{14}C, ^{10}Be, and ^{36}Cl can serve as a proxy indicator of past changes of the geomagnetic field.

Different time ranges can be studied with these radionuclides because of their unequal half-lives. With ^{14}C only the youngest excursions, the Mono Lake (≈ 33 ka) and the Laschamp-event (≈ 41 ka) are accessible [Hughen et al., 2004; Beck et al., 2001]. The Laschamp excursion also can be seen in marine and ice core records of ^{10}Be, e.g. [McHargue et al., 1995; Yiou et al., 1997; Carcaillet et al., 2004; Christl et al., 2010b; Ménabréaz et al., 2011], and ^{36}Cl [Baumgartner et al., 1997, 1998; Muscheler et al., 2005]. An increased ^{10}Be concentration was observed in ice cores, caused by the last geomagnetic reversal [Raisbeck et al., 1985, 2006]. It is called the Brunhes-Matuyama field reversal and designates the transition from the previous Matuyama period of magnetic field orientation to the present Brunhes period. An overview of the excursions during the Brunhes period is given in Lund et al. [2006]. In addition to the above mentioned Mono Lake and Laschamp excursions, several events were retrieved in ^{10}Be records (Iceland Basin event (ca. 190 ka), Frank et al. [1997]; Knudsen et al. [2008]; Christl et al. [2010b]; Jamaica event 190-200 ka, Christl et al. [2007a]; Blake, Jamaica/Pringle Falls, Calabrian Ridge, Carcaillet et al. [2004]; Delta excursion, Carcaillet et al. [2003]). Ages of sediments can be identified by fitting the temperature sensitive δ^{18}O data[*] of the archive to known δ^{18}O-age records. By measuring the excess ^{230}Th$_{excess}$, which is scavenged from the water column and not produced by ^{234}U decay in the sediment, and assuming a constant ^{230}Th$_{excess}$ flux to the sediment, one can correct the deposition of ^{10}Be for sedimentation rate changes and for lateral sediment redistribution [Francois et al., 2004]. However, because of the half-life of ^{230}Th ($T_{1/2}=75$ ka) this method is limited to the last 400 ka. Age models for older samples can be created from palaeomagnetic or isotopic records. Several studies have already explored the ^{10}Be concentration in marine sediments during the Brunhes-Matuyama field reversal. The bulk ^{10}Be flux to the sediment can then be reconstructed from sedimentation rates, e.g. assigned by a palaeomagnetic age model [Suganuma et al., 2010, 2011].

In other studies, the ^{10}Be input into marine sediments was normalized via the authigenic ^{9}Be [Raisbeck et al., 1985; Henken-Mellies et al., 1990; Carcaillet et al., 2003]. Assuming a stable input of dissolved ^{9}Be to oceans, lakes, or rivers, and a constant galactic cosmic ray flux to the solar system, the ratio of ^{10}Be/^{9}Be in an archive should reflect the changes in production of ^{10}Be caused by solar and geomagnetic variations. At average solar modulation the increase of the ^{10}Be production following the reduction of the

---

[*]δ^{18}O$=\dfrac{\left(\frac{^{18}O}{^{16}O}\right)_{sample}}{\left(\frac{^{18}O}{^{16}O}\right)_{standard}} - 1$

magnetic dipole moment amounts to a factor of two [Masarik and Beer, 1999, 2009]. For solar or geomagnetic events to be recorded in a natural archive the residence time of Be in the environment before entering the archive has to be shorter than the duration of the event, else the signal would be diluted. For example, because of the short residence time of Be in the atmosphere (≈ 1 a, Raisbeck et al. [1981a]) the 11 a solar cycle can be found in annually resolved ice cores [Beer et al., 1990]. Magnetic events occur on time scales of several ka, the average duration was estimated to 7 ka [Clement, 2004]. This is still longer than the maximal residence time of Be reported for single spots in the deep Pacific Ocean (≈ 3 ka, von Blanckenburg and Igel [1999]). Thus, one can expect that the increased production of ^{10}Be during a magnetic excursion or reversal leaves a signal in marine sediments [Christl, 2007]. Such a distinct signature for magnetic events can provide an independent age control of natural archives. Additionally, the authigenic ^{10}Be/^{9}Be ratio can be used to reconstruct past relative palaeomagnetic intensities [Knudsen et al., 2008; Ménabréaz et al., 2011].

The authigenic ^{10}Be/^{9}Be is not limited to the past 400 ka and with the carrier-free method it offers a new approach to investigate a normalized ^{10}Be signature in only one measurement process without need for further isotopic analysis.

5.7.2 Study sites and sample description

Marine sediments from five sites (ODP Sites 769, 983, 1021, 1063, 1090, Shipboard Scientific Party [1990, 1996, 1997, 1998, 1999]) of the Ocean Drilling Program were sampled to search for a ^{10}Be/^{9}Be signature of the Brunhes-Matuyama reversal. Compared to ice cores, sediments have the advantage that they are available over the whole planet and therefore a compilation of sites can be used to explore the global character of the ^{10}Be/^{9}Be signature. The cores are chosen from sites with large depths (2000 m and more) to reduce the terrigenic influence to the sedimentation. However, high sedimentation rates are favourable. They reduce the risk of signal broadening caused by bioturbation [Christl, 2007]. High sedimentation rates of several cm/ka guarantee that signals have been recorded with good time resolution and without having been disturbed too much. Besides, as an important prerequisite for later comparisons, magnetostratigraphic data for all of the five cores are available at the time of the Brunhes-Matuyama field reversal [Oda et al., 2000; Channell and Lehman, 1998; Guyodo et al., 1999; Shipboard Scientific Party, 1998, 1999]. Below, the data are compared to the inclination angles, i.e. the angles between the compass needle and the horizontal plane, recorded at the same site.

The residence time of Be in the ocean and the lock-in depth of the magnetic signal may lead to offsets between the two records of the past magnetic field strength, the ^{10}Be/^{9}Be signal and the magnetization. The lock-in depth of the magnetic signal is induced by a
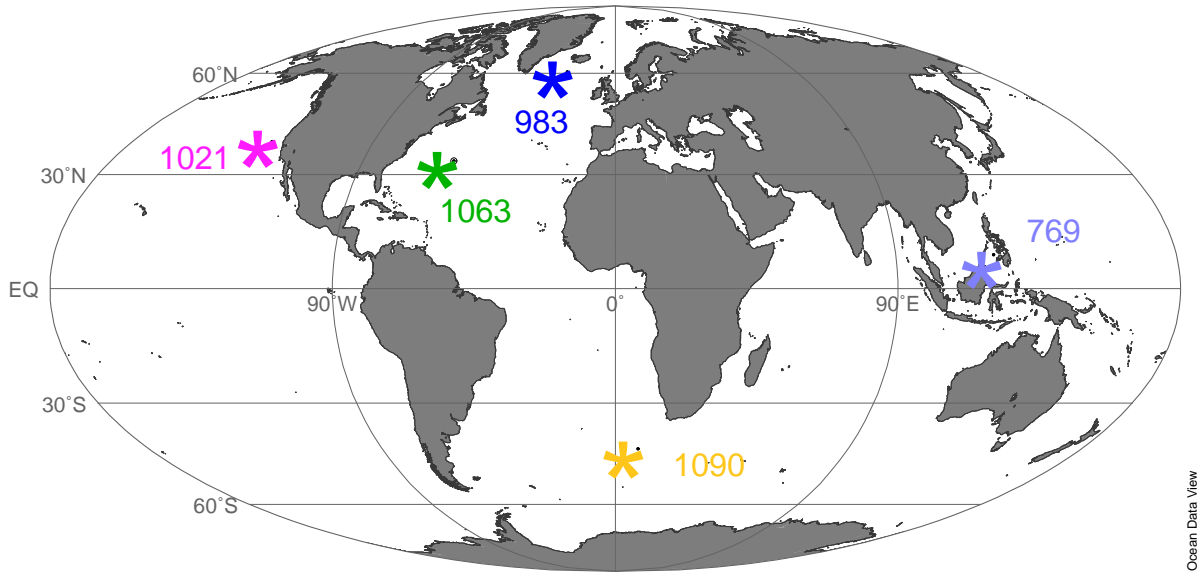
Figure 5.7: ODP Sites chosen for investigating the ^{10}Be/^{9}Be signature of the Brunhes-Matuyama reversal.

post-sedimentary alignment of the magnetic grains in the loose sediment. A long residence time of Be at the studied site (up to ca. 3 ka in the Central Pacific Ocean, von Blanckenburg and Igel [1999]) would further increase the lag between the magnetic and the Be signal.

In total, 78 different samples were prepared from 1 g - 1.5 g marine sediment according to the chemical separation method described in appendix A.1. The targets in the AMS measurement revealed ^{10}Be/^{9}Be ratios above 10^{-8} and currents of 0.15 nA - 1.6 nA.

5.7.3 Age models

In the following, the age models will be described that are used for the comparison of the ^{10}Be/^{9}Be ratios from different sites on one common time scale.

ODP Site 769: 16 samples from Site 769 (hole A, core 7) were examined in a depth range from 59 mbsf* to 65.6 mbsf. According to Oda et al. [2000], the Brunhes-Matuyama reversal at this site is found in a depth of 62.25 mbsf and with an age of (778.9$\pm$1) ka. These calculations are based on a correlation of the planktic δ^{18}O of this site to that of Core MD900963 from Bassinot et al. [1994]. This date is taken as the fixed point, from which the other ages are calculated with the sedimentation rate of (10.1$\pm$0.6) cm/ka that

---

*The unit mbsf stands for "meters below sea floor" and denominates the depth of the sample in the sediment at the respective site and hole.

is reported by Oda et al. [2000]. Age uncertainties of the record are calculated with the errors given above.

ODP Site 983: At Site 983 (hole B, cores 9,10) from the Northern Atlantic Ocean, 16 samples in depths from 79 mbsf to 87 mbsf were prepared and measured. This site has a high sedimentation rate of 11 cm/ka at the time of the reversal. The age model is based on the δ^{18}O control points from Channell and Kleiven [2000] at 722 ka, 753 ka, 773 ka, 790 ka, and 817 ka. The data of inclination vs. age from Channell and Kleiven [2000] shows a start of the reversal at ca. 778 ka. To comply with Channell et al. [2010], where it is reported that the magnetic data show the Brunhes-Matuyama onset at 775.7 ka with the mean at ca. 772.5 ka, an offset of -2.05 ka is applied to the final ages of the Be samples. The inclination data are taken from Channell and Lehman [1998].

ODP Site 1021: 15 samples from Delgada Fan Site 1021 (hole C, core 4) were studied in a depth range from 23 mbsf to 25.2 mbsf. The age model from Guyodo et al. [1999] gives an average sedimentation rate of 3.4 cm/ka for the last 1400 ka, so the samples cover a time span of 65 ka. The inclination data shows the Brunhes-Matuyama field reversal at 24.2 mbsf. The age of the reversal is set to 780 ka following Guyodo et al. [1999].

ODP Site 1063: From the Bermuda Rise Site 1063 (hole B, cores 15 and 16), 15 samples in depths from 134 mbsf to 145 mbsf were prepared. Several age models are available at this site [Grützner et al., 2002; Ferretti et al., 2005; Channell et al., 2012].
The age model presented by Grützner et al. [2002] uses the carbonate percentage of the sediment tuned to orbital parameters of the Earth. However, as pointed out by Keigwin and Jones [1994], ocean circulation changes entail $CaCO_3$ abundance changes making the carbonate percentage age parameter prone to influences of climate and not only of orbital parameters.
A second age model was based on δ^{18}O data [Ferretti et al., 2005] and was taken up by Channell et al. [2012], showing better resolved and more complete magnetic data. In contrast to the above described model, considerably lower sedimentation rates (ca. 7.7 cm/ka) are reported for the time range of the Brunhes-Matuyama reversal. Large variations of the sedimentation rates occur in this depth of the core. So, the assignment of ages to the ^{10}Be/^{9}Be ratios strongly depend on the time points of both age models.
The age model of Channell et al. [2012] is applied for the final presentation of the ^{10}Be/^{9}Be results.

ODP Site 1090: From the South Atlantic Site 1090 (hole D, core 3), 16 samples in depths from 20.5 mbsf to 23 mbsf were analysed. The age model of Venz and Hodell [2002] uses the benthic foraminiferal δ^{18}O signals and correlates them with ODP Site 607. An age of 782.9 ka is assigned to a depth of 21.96 mbsf via three control points in the studied depth range. The sedimentation rate amounts to 3.1 cm/ka for lower depths

and to 7.2 cm/ka for higher depths. The inclination data is taken from the report of the Shipboard Scientific Party [1999].

Table 5.2: Characteristics of the studied ODP Sites.

ODP Site	769	983	1021	1063	1090
longitude	121°17.65'E	23°38.44'W	127°46.98'W	57°36.90'W	8°54.00'E
latitude	8°47.14'N	60°24.21'N	39°5.24'N	33°41.19'N	42°54.82'S
water depth	3645 m	1983 m	4212 m	4583 m	3702 m
age model	$\delta^{18}O$	$\delta^{18}O$	paleomag.	$\delta^{18}O$	$\delta^{18}O$
sed. rate*	10 $\frac{cm}{ka}$	10 $\frac{cm}{ka}$	3.4 $\frac{cm}{ka}$	17 $\frac{cm}{ka}$	2.7 $\frac{cm}{ka}$

* Sedimentation rates are given as average over the total studied period.

5.7.4 Results and interpretation

5.7.4.1 ^{10}Be/^{9}Be ratios and inclination data

The magnetic data and the ^{10}Be/^{9}Be ratios are depicted versus the depth of the sample in the core in the plots shown for the five ODP Sites (Figs. 5.8 - 5.12). Consequently, time elapses from right to left. The ^{10}Be/^{9}Be ratios in each core show a strong signal dynamics of about a factor of two and more between the average and the maximal level. This difference would be expected for the complete absence of the magnetic dipole moment [Masarik and Beer, 1999, 2009]. Initially, the depth distance between the samples in the core had been chosen such that a high resolution was gained during the actual reversal. In most cases, however, a good resolution is only available on the rising slope of the signal, because the maximal ^{10}Be/^{9}Be ratio was recorded at slightly lower depths than suspected. For all five cores, the increase in the ^{10}Be/^{9}Be ratio clearly starts before there is a major change in the inclination or declination signal. The details for the single sites are discussed below.

Sites from the North Atlantic (983, 1063) or the Celebes sea (769) have a larger input from continental erosion and the water there may have a higher concentration of dissolved ^{9}Be, which leads to lower ratios. In contrast, the continental contribution to the Pacific or the Antarctic waters is lower, therefore the ratios at these sites (1021,1090) are higher.

ODP Site 769: Of all studied locations, the Site 769 is closest to the equator. That is why the inclination signature of the reversal is not as distinct as in the other cases. For this location the declination data [Oda et al., 2000] are included in the plot, too.
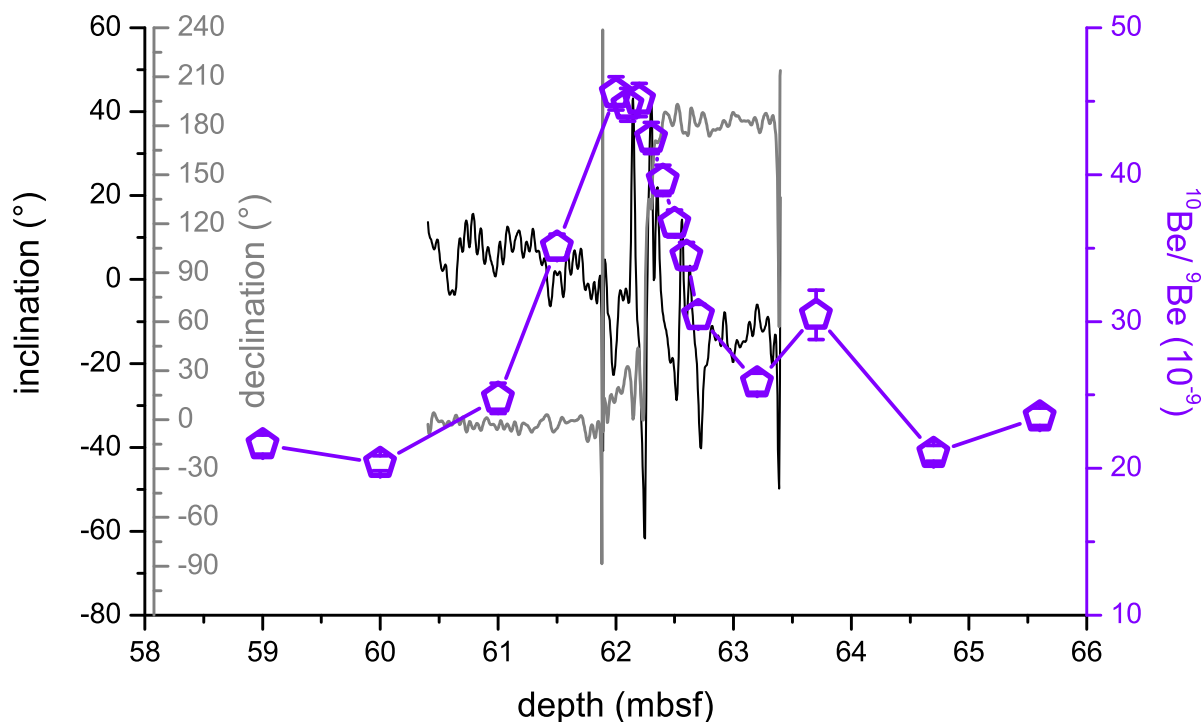
Figure 5.8: Site 769: The ^{10}Be/^{9}Be ratios are depicted against the depth in the core along with declination and inclination data from Oda et al. [2000]. In this and the following graphs, the magnetic data are scaled on the left axis, while the measured ^{10}Be/^{9}Be ratios are coloured and scaled on the right axis.

ODP Site 983: Based on the control points by Channell and Kleiven [2000], an increase in the ^{10}Be/^{9}Be is determined at ca. 785 ka and a double peak at 777 ka-773 ka. An age of 771.5 ka is appointed to the sample with maximal ^{10}Be/^{9}Be ratio if applying the above described offset in order to comply with the newer data of Channell et al. [2010].

ODP Site 1021: Three data points exhibit a very similar maximal ^{10}Be/^{9}Be ratio, resulting in a maximum at 777 ka with the flat peak spanning a period of ca. 6 ka. However, for this Site the age model is fixed by the age appointed to the reversal and thus may have to be shifted if another Brunhes-Matuyama age is established.

ODP Site 1063: The model of Grützner et al. [2002] results in a high sedimentation rate during the Brunhes-Matuyama field reversal (at most 38 cm/ka) and a highly resolved ^{10}Be/^{9}Be ratio record with a width comparable to the 983 record. It gives a very high sedimentation rate of 26 cm/ka leading to a short sampling time range from 770 ka to 810 ka. With this age model, the inclination data of the Shipboard Scientific Party [1998] show the reversal at ca. 783 ka - 781 ka. While the position of the reversal in the ^{10}Be/^{9}Be data also seems to be quite early, the width of the peak is comparable to the records at ODP Site 983 and the EPICA record [Raisbeck et al., 2006].
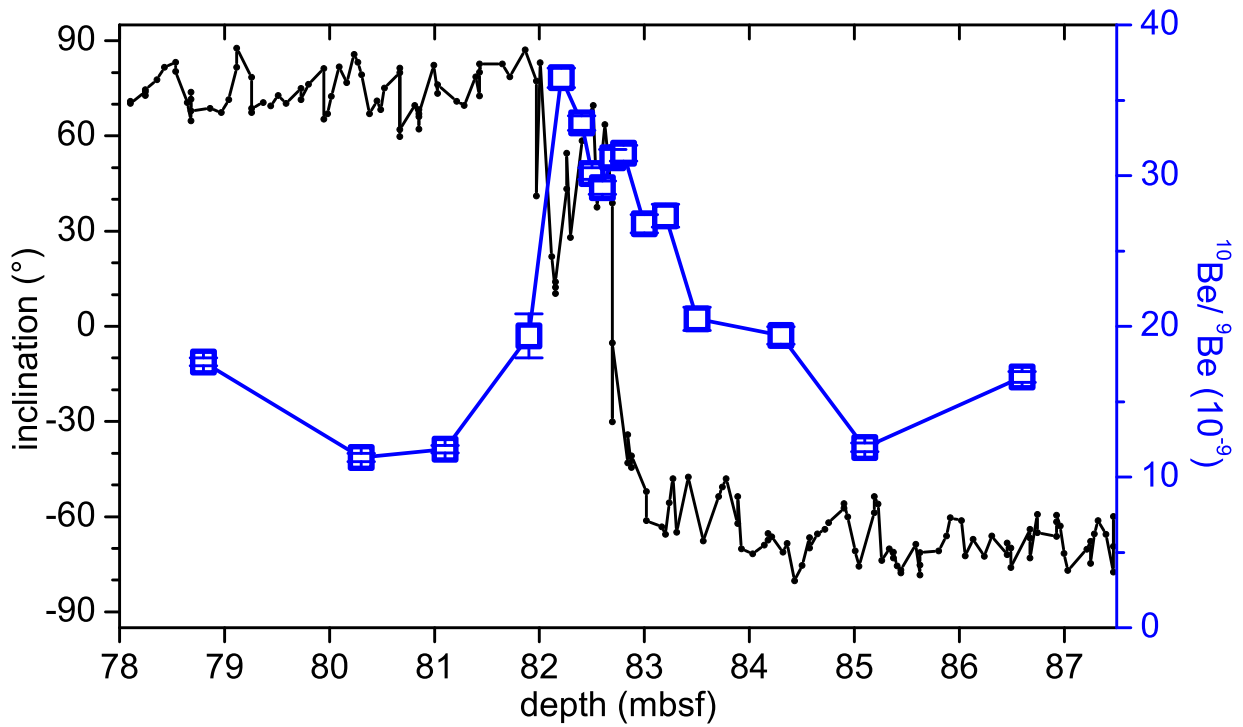
Figure 5.9: Site 983: The ^{10}Be/^{9}Be ratios are depicted along with inclination data from Channell and Lehman [1998].
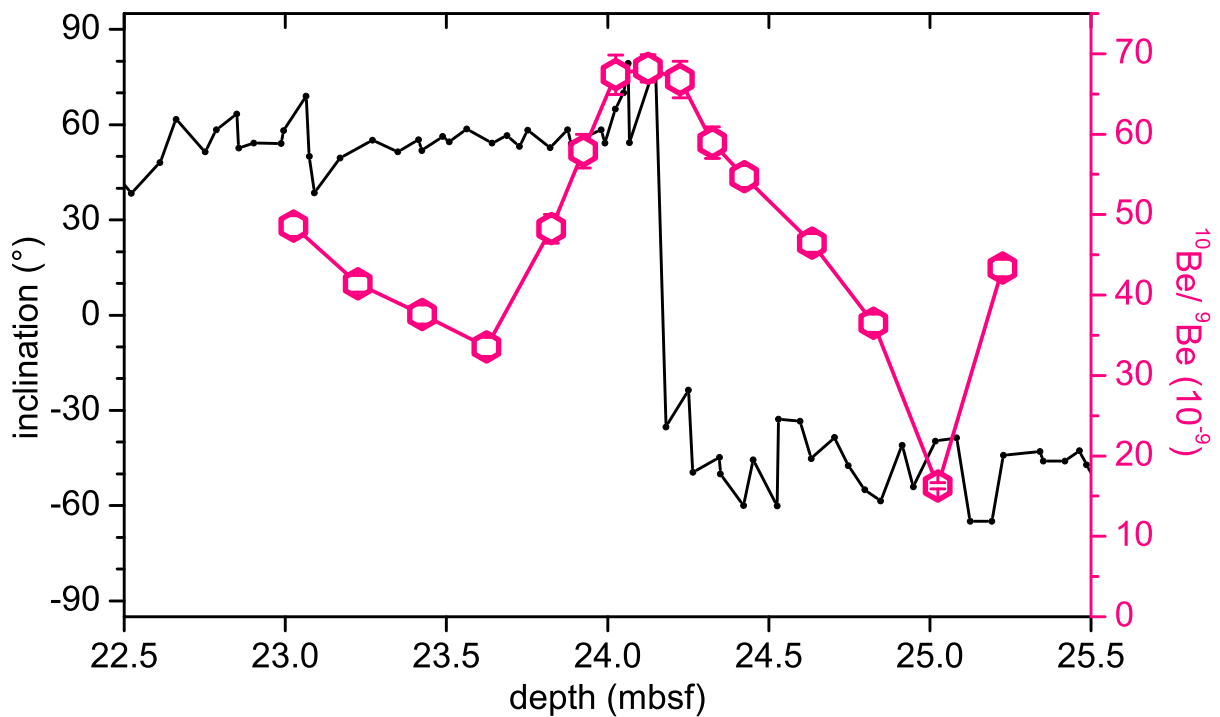
Figure 5.10: Site 1021: The ^{10}Be/^{9}Be ratios are depicted along with inclination data from Guyodo et al. [1999].
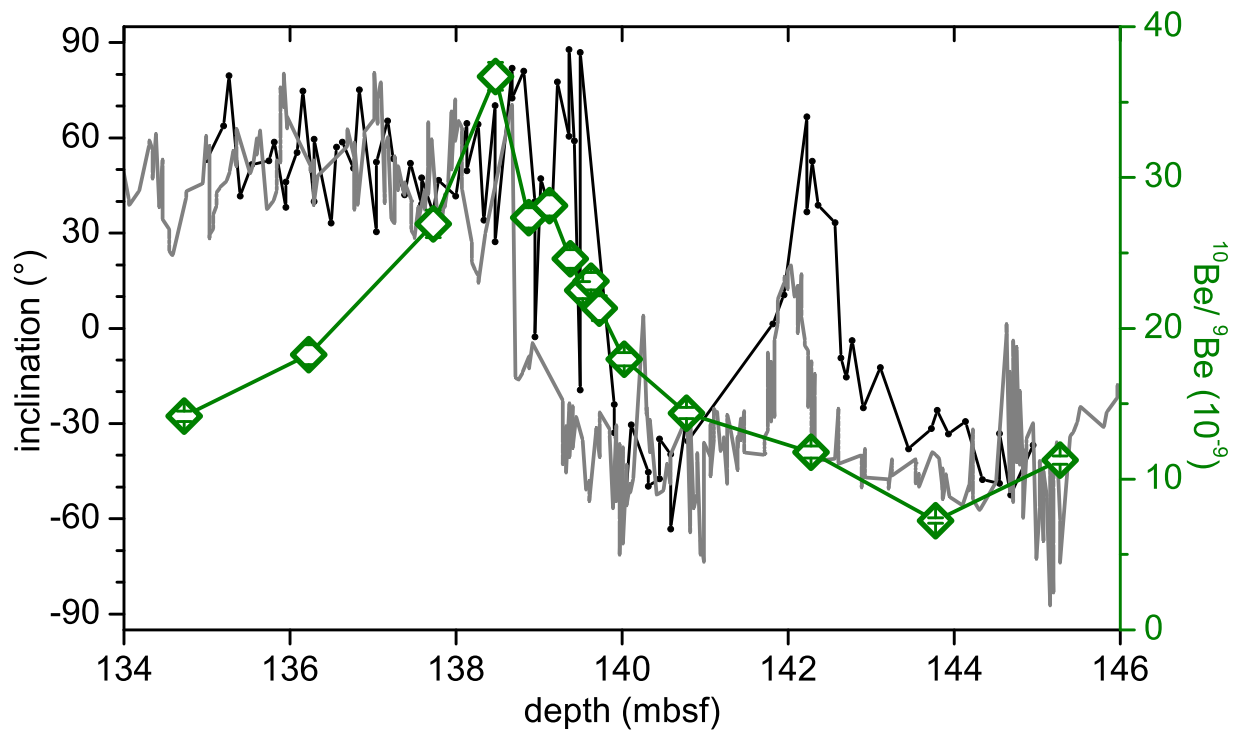
Figure 5.11: Site 1063: The ^{10}Be/^{9}Be ratios are depicted along with inclination data from the report of the Shipboard Scientific Party [1998] and from Channell et al. [2012].
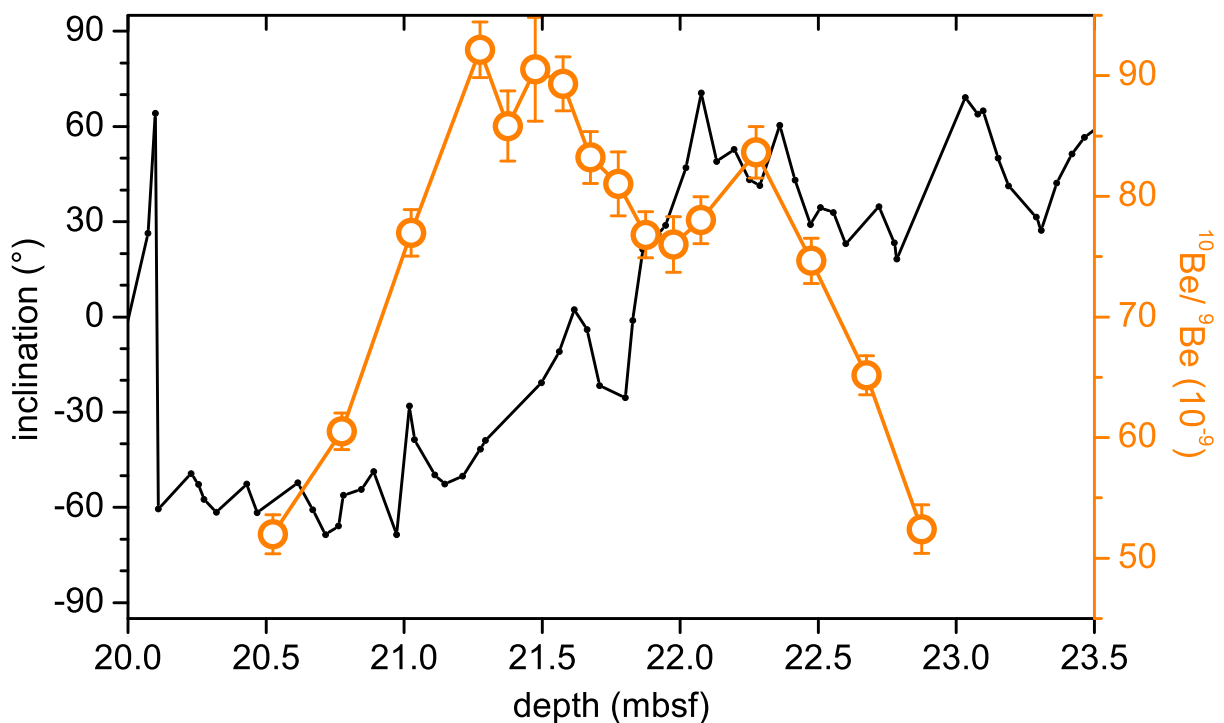
Figure 5.12: Site 1090: The ^{10}Be/^{9}Be ratios are depicted along with inclination data from the report of the Shipboard Scientific Party [1999].

With the lower sedimentation rate resulting from the age model presented by Channell et al. [2012], the ^{10}Be/^{9}Be peak is broadened on the age scale. Its maximal value is attributed to an age of ca. 768 ka. There is an offset of the inclination signal between the two records [Shipboard Scientific Party, 1998; Channell et al., 2012] with the newer record being more consistent with the ^{10}Be/^{9}Be dataset (section 5.7.4.1), i.e. showing the magnetic flip during the increase of the ^{10}Be/^{9}Be ratio and not before.

ODP Site 1090:   Measurements of samples from the opaline- and $CaCO_3$-rich Site 1090 result in the highest ^{10}Be/^{9}Be ratios. The signal is significantly broadened compared to the other study sites. This is most likely caused by the low sedimentation rate present at this location, which makes it prone to bioturbation and other signal diluting effects.

In the following, the results of this study are briefly compared to previous measurements of the authigenic ^{10}Be/^{9}Be ratio at the same Sites or during the Brunhes-Matuyama reversal in other marine sediments. Whenever applicable, corrections for revised standard values are performed and the non-decay-corrected values are given.

A similar relation between authigenic ^{10}Be/^{9}Be and the palaeomagnetic data was observed at Sites 983 and 1063 during the Icelandic Basin excursion [Knudsen et al., 2008]. An explanation would be that the magnetic shield had already been weakened and thus the ^{10}Be production had been increased before there were first signs of a pole flip, which would be recorded in the inclination data. Effects of the archive formation generate the opposite offset: The residence time of Be in the atmosphere and the ocean would cause the ^{10}Be/^{9}Be signature to be recorded at lower depth than the magnetization signal. The previously mentioned post-depositional magnetization, that is if due to the mobility of magnetizable particles the final magnetization is recorded in greater depth and not at the surface, also would produce a contrary time lag. Probably both effects, post-depositional magnetization and reduction of the magnetic field intensity prior to the actual excursion or reversal, concur to produce the observed time lag.

The signal dynamics of the Brunhes-Matuyama reversal (Figs. 5.9 and 5.11) seem to be slightly larger compared to the Icelandic Basin excursion measured by Knudsen et al. [2008] at ODP Sites 983 and 1063. The reported highest and lowest value during the excursion differ by less than a factor of three (983: $55 \cdot 10^{-9} < {}^{10}$Be/^{9}Be$ < 155 \cdot 10^{-9}$; 1063: $80 \cdot 10^{-9} < {}^{10}$Be/^{9}Be$ < 180 \cdot 10^{-9}$) at both locations. However, the absolute values are remarkably high compared to the ratios determined in this study for the same sites (983: $(11.3 \pm 0.3) \cdot 10^{-9} < {}^{10}$Be/^{9}Be$ < (36.5 \pm 0.7) \cdot 10^{-9}$; 1063: $(7.3 \pm 0.2) \cdot 10^{-9} < {}^{10}$Be/^{9}Be$ < (36.7 \pm 0.8) \cdot 10^{-9}$) and cannot be explained by the decay of ^{10}Be since the Brunhes-Matuyama reversal.

Two of the previous studies on the ^{10}Be/^{9}Be signature of the Brunhes-Matuyama field reversal were performed in the vicinity of ODP Site 1090 ((^{10}Be/^{9}Be)$_{max,1090}$=$(92 \pm 2) \cdot 10^{-9}$) and yielded lower but still relatively high ^{10}Be/^{9}Be ratios of ca. $70 \cdot 10^{-9}$ [Raisbeck et al.,

1985] and ca. $60 \cdot 10^{-9}$ [Henken-Mellies et al., 1990]. The study site of Carcaillet et al. [2003] is close to ODP Site 769 in the Celebes Sea ((^{10}Be/^{9}Be)$_{max,769}$=(46±1)·10^{-9}) but much more influenced by Pacific water and thus more comparable to the ODP Site 1021 in the Eastern Pacific ((^{10}Be/^{9}Be)$_{max,1021}$=(68±2)·10^{-9}). This is mirrored by the high maximal ^{10}Be/^{9}Be ratio of ca. $70 \cdot 10^{-9}$ reported by Carcaillet et al. [2003] and the generally high ^{10}Be/^{9}Be ratio at this site, which perfectly matches the values at Site 1021 but not those in the closer Celebes Sea.

5.7.4.2 Decay corrected ^{10}Be/^{9}Be ratios on a common age scale

The depths of the samples can be converted into ages by means of the above discussed age models. The uncertainty of the ^{10}Be half-life is included in the new calculation of the ^{10}Be/^{9}Be ratio uncertainty, although due to its high precision it is only a minor contribution to the overall error. For ODP Site 769 an uncertainty of the age model is available, this age uncertainty is shown in Fig. 5.13. In this case, it contributes to the overall uncertainty of the decay corrected ^{10}Be/^{9}Be ratio but is negligible compared to the measurement uncertainties.

The ^{10}Be/^{9}Be ratio exhibits a maximum around 770 ka - 780 ka at all sites. The signal widths are related to the sedimentation rates at the respective site. Bioturbation smoothes the record of the ^{10}Be/^{9}Be signature. Sites with low sedimentation rates are more easily affected by this and hence their records are broadened.

5.7.4.3 High-resolution Sites 983 and 1063 compared to EPICA record

The North-Atlantic ODP Sites 983 and 1063 exhibit relatively high sedimentation rates and a good temporary resolution of the ^{10}Be/^{9}Be record. These marine sediment ratios are compared with the median ^{10}Be flux recorded in the EPICA Dome C ice core on the EDC3 age scale [Raisbeck et al., 2006; Dreyfus et al., 2008].

The data set from ODP Site 983 has a similar peak width as the ice core record but there is a little offset, which probably can be explained by the uncertainties of the age models for both archives. The delay caused by the Be residence time in the ocean would lead to an offset in the opposite direction. With the age model deduced from Channell et al. [2012], the record from ODP Site 1063 is broader than with the model of Grützner et al. [2002], but the position of the peak is in better accordance with the records of ODP 983 and EPICA. Generally, the ages and general structure of the peaks are very similar: The two marine sediments develop two pre-peaks before the maximal ^{10}Be/^{9}Be ratio is reached. In all three records the signal decreases relatively steeply after reaching the maximal value. From the signature at Sites 983 and 1063 one would infer a younger age of the Brunhes-Matuyama field reversal of ca. 772 ka rather than the established 780 ka, too. This would not only be in accordance with the ^{10}Be ice core record but also with the
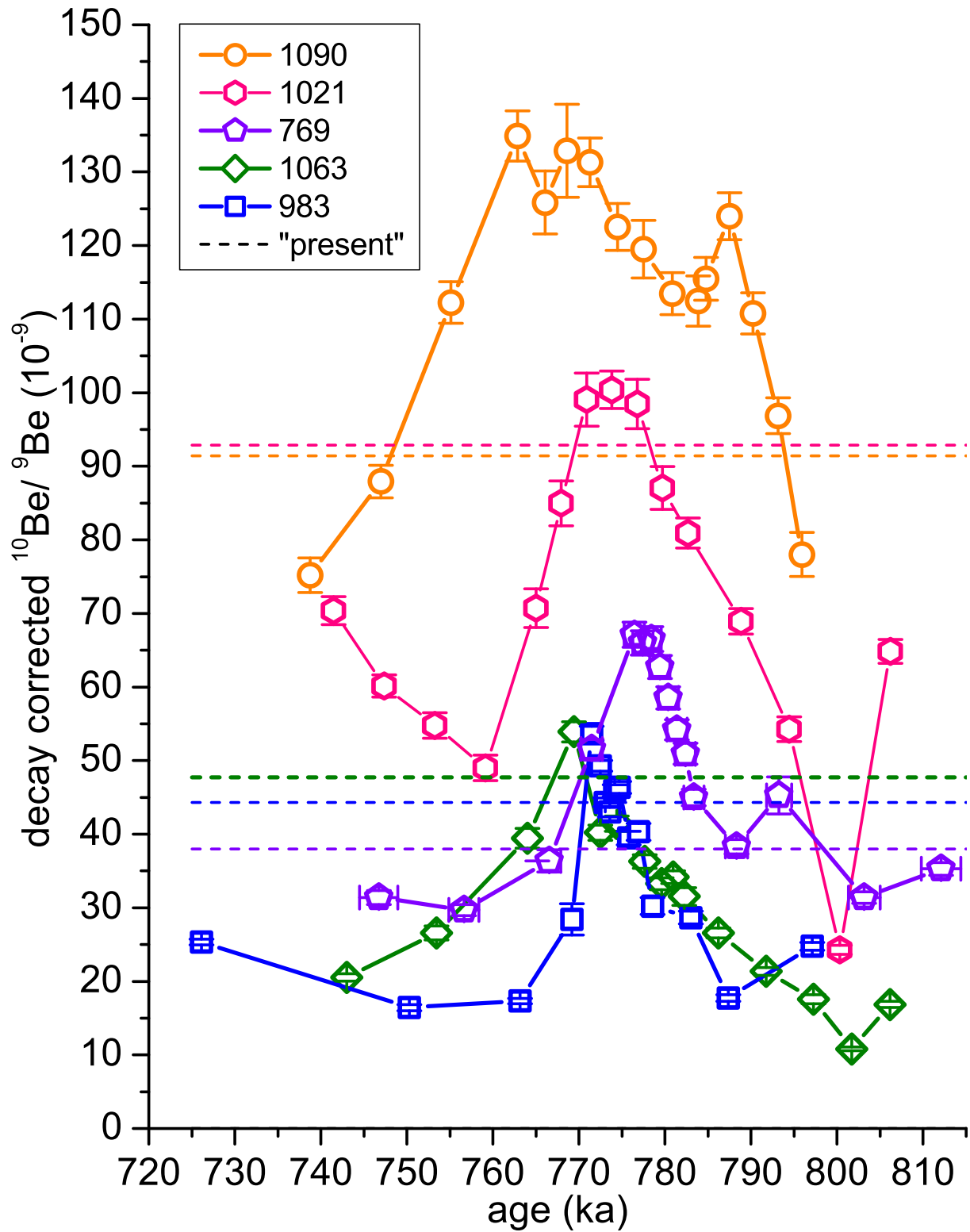
Figure 5.13: The ^{10}Be/^{9}Be ratios are decay corrected for their ages. Present-day seawater values (section 5.7.4.4) derived from manganese crusts at near sites are shown in the corresponding colours.
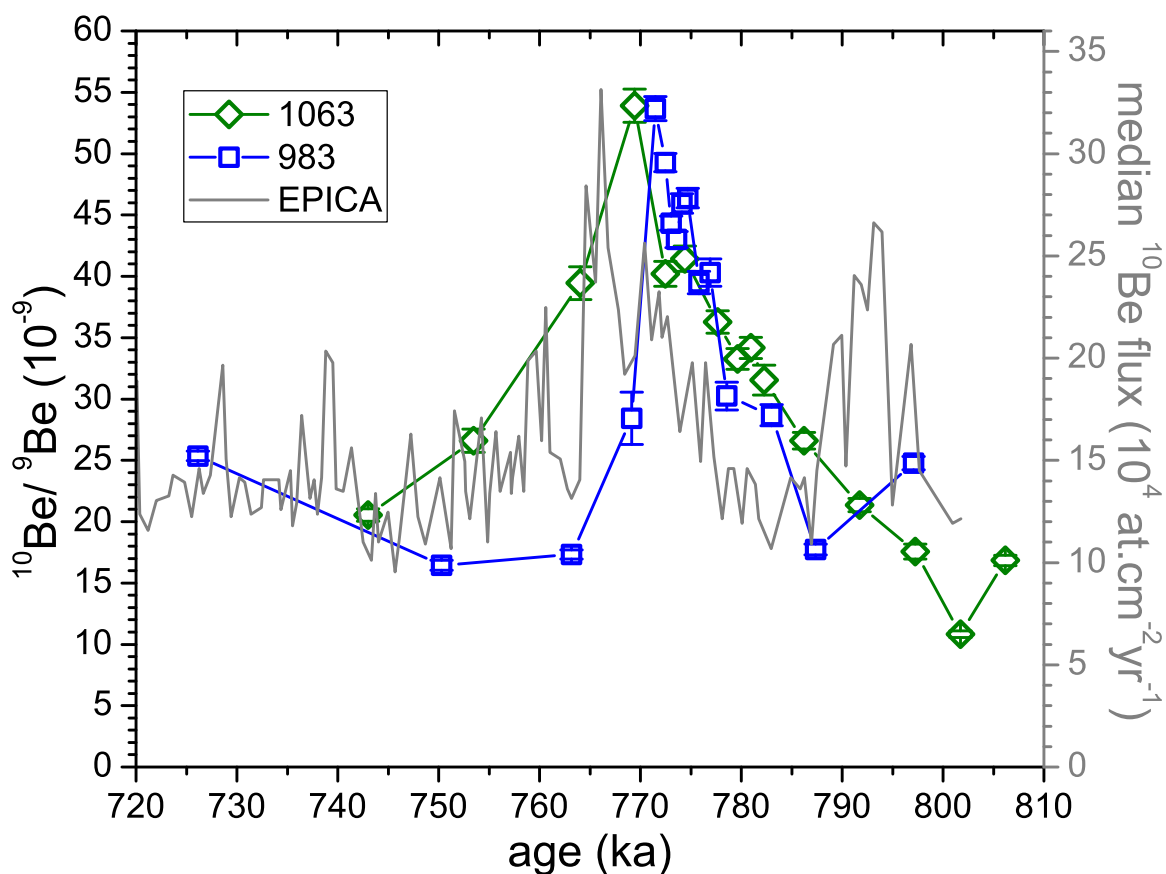
Figure 5.14: Decay corrected ^{10}Be/^{9}Be records from ODP Sites 983 and 1063 (left axis) are compared to the mean ^{10}Be flux (right axis) recorded in the EPICA Dome C ice core.

recent study of Channell et al. [2010] in North Atlantic sediments, which claims an age of 773.1 ka for the reversal.

5.7.4.4 Comparison to recent sea-water ^{10}Be/^{9}Be ratios

The decay corrected values of the ^{10}Be/^{9}Be ratio can be compared to present-day ^{10}Be/^{9}Be ratios measured in deep sea water [Ku et al., 1990] or in the surface layer of ferromanganese crusts [von Blanckenburg et al., 1996b; von Blanckenburg and O'Nions, 1999]. However, because of the low growth rates of few mm/ka, the surface layer of the ferromanganese crusts integrates over a time span of many ka and may correspond to ages of up to 200 ka. Hence, the presented "present-day" ^{10}Be/^{9}Be ratios derived from those crusts are corrected for the ^{10}Be decay. Those ^{10}Be/^{9}Be ratios from literature that are located nearest to the ODP Sites of this work (Fig. 5.7) are chosen for the comparison. At Sites 769 and 1090 in particular, the lower values in the sediment before and after the reversal and the ^{10}Be/^{9}Be ratio in the manganese crust top layer agree very well (Fig. 5.13). At Site 983 the attribution of the closest value is critical. In contrast to all other crusts described in their paper, no further information is given for the data point

south of Greenland (^{10}Be/^{9}Be=39·10^{-9}) in Fig. 1 by von Blanckenburg et al. [1996b]. Thus, here an average value from the Northern Atlantic crusts presented by von Blanckenburg et al. [1996b] and by von Blanckenburg and O'Nions [1999] was calculated to (44.3±5.1)·10^{-9} as present-day ^{10}Be/^{9}Be ratio at Site 983. At Site 1063 the present-day ratio is calculated from a weighted average of the ferromanganese crust data [von Blanckenburg et al., 1996b] and deep-water ratios [Ku et al., 1990]. The present-day ^{10}Be/^{9}Be ratios attributed to Sites 983, 1021 and 1063 are relatively high and only 5-20% lower than the maximal decay-corrected ^{10}Be/^{9}Be ratios during the reversal. Such a difference could be explained by accidentally higher input of ^{9}Be to the ODP Sites during the time of the Brunhes-Matuyama reversal, which could be induced by higher erosion or by different water transport to the ODP Sites compared to the crust positions.

However, the general pattern of ^{9}Be supply to the oceans with higher contributions in the North Atlantic than in the Pacific or Arctic waters has not altered since the Brunhes-Matuyama field reversal. Apart from this, in most cases the ^{10}Be/^{9}Be ratios before and after the event reach values significantly below both the present and the average value. The reversal might be bracketed by periods of more efficient shielding of the cosmic rays and only little ^{10}Be production.

5.7.4.5 Reconstruction of a relative Virtual Dipole Moment

It was shown by Elsasser et al. [1956] that a paleointensity signature can be deduced from ^{14}C production following the formula $P(t) = C \cdot M(t)^{-0.52}$, $P(t)$ being the time-dependent production, $M(t)$ the time-dependent magnetic moment, and $C = P_0 \cdot M_0^{0.52}$ with P_0 as average production and M_0 as average magnetic moment. In the same way as ^{14}C, the decay corrected ^{10}Be/^{9}Be ratios are used as the production proxy P to calculate the relative Virtual Dipole Moment (rVDM) $M(t)/M_0$:

$$\frac{M(t)}{M_0} = \left[\frac{^{10}\text{Be}/^9\text{Be}(t)}{(^{10}\text{Be}/^9\text{Be})_0} \right]^{-1/0.52} \tag{5.1}$$

This is performed for the results from ODP Site 983, which is the best-resolved record during the reversal. The present seawater ratio ((^{10}Be/^{9}Be)$_0$=(44.3±5.1)·10^{-9}, section 5.7.4.4) is taken as average production P_0. Uncertainties are defined by the ^{10}Be/^{9}Be ratio errors, the additional error from P_0 is included. Apart from the good resolution, another reason to choose the ODP Site 983 for the estimation of the rVDM is that from literature [Channell et al., 2004, 2010] relative paleointensity proxies are available for the same location. These data are given in arbitrary units and are compared to the ^{10}Be/^{9}Be derived rVDM in Fig. 5.15. The record of Channell et al. [2010] gives a better resolution but does not cover the full time span of this ^{10}Be/^{9}Be study. Therefore, older data with a worse temporal resolution [Channell et al., 2004] are included, too. The ^{10}Be/^{9}Be based

rVDM very nicely follows the pattern of the relative paleointensity proxies. Again, this confirms that the authigenic $^{10}Be/^{9}Be$ ratio in the sediment is robust against environmental effects such as enhanced Be scavenging and that it provides a proper normalization of the ^{10}Be input to the archive. The amplitude of the $^{10}Be/^{9}Be$ based palaeomagnetic record does not show the full span of the other records. First of all, measuring more samples would have been necessary for better comparability to the more detailed palaeomagnetic records. However, just during the reversal the $^{10}Be/^{9}Be$ derived record might be damped. An attenuation of the signal could be caused by the residence times of Be in atmosphere and ocean and by bioturbation [Christl, 2007].
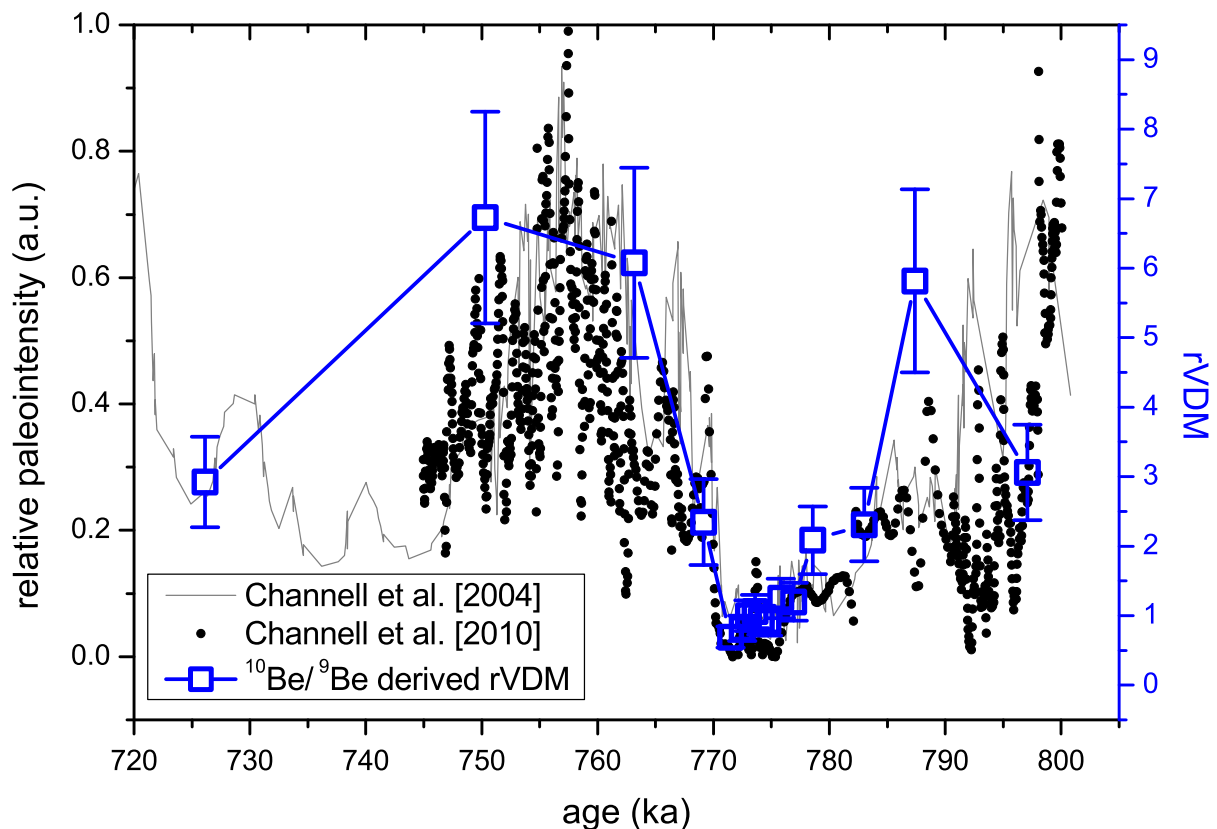
Figure 5.15: Relative paleointensity records [Channell et al., 2004, 2010] are scaled on the left axis and the $^{10}Be/^{9}Be$ derived rVDM from ODP Site 983 (according to equation 5.1) is scaled on the right axis.

The normalization to P_0 is critical for the further reconstruction of the Virtual Axial Dipole Moment, while the general pattern of the record is not influenced by this value if it is calculated according to equation 5.1. The absolute values of the rVDM are only shifted by factors when inserting other ratios than the applied $(^{10}Be/^{9}Be)_0$.

In contrast to the above given equation 5.1, a polynom of fifth order was used by Wagner et al. [2000] to relate the geomagnetic field variations to relative radionuclide production changes. If this polynom is applied for the calculation, the minimal values of the rVDM dur-

ing the reversal are more sensitive to the P_0 normalization than the maximal values before and after. The minimal rVDM according to Wagner et al. [2000] amounts to 0.58 ± 0.16 and the maximal rVDM to 2.99 ± 0.09, utilizing the above discussed $(^{10}Be/^9Be)_0$ ratio. Carcaillet et al. [2003] derived an rVDM from $^{10}Be/^9Be$ measured in the core MD97-2140 from the West Equatorial Pacific with a similar power function approach than the one of Elsasser et al. [1956]. They found an rVDM minimal value of 0.65 and a maximal value of 2.8. In the present calculation for Site 983 according to equation 5.1, the rVDM spans a greater range from 0.69 ± 0.16 to 6.7 ± 1.5. Although the same production signal $(^{10}Be/^9Be)$ and a power function to relate rVDM and production was applied, the rVDM derived from the West Equatorial Pacific core differs significantly from that of Site 983. This difference is mainly generated by the normalization with the above discussed present-day $(^{10}Be/^9Be)_0$. The records could be brought into better accordance by employing a lower average production parameter P_0 than the present-day $(^{10}Be/^9Be)_0$ for Site 983. Regarding the relatively high value of $(^{10}Be/^9Be)_0$ compared to the peak $^{10}Be/^9Be$ ratio during the reversal, it seems realistic that the average $^{10}Be/^9Be$ ratio is actually lower than $(44.3\pm5.1)\cdot10^{-9}$.

5.7.5 Conclusion

An authigenic $^{10}Be/^9Be$ signature of the Brunhes-Matuyama field reversal was measured at five ODP Sites. The observed common global increase of the $^{10}Be/^9Be$ ratio makes it a valuable dating tool. At locations with high sedimentation rates the resolution of the record is even comparable to ice core data. The $^{10}Be/^9Be$ ratio during a geomagnetic event is a distinct time marker that permits the temporal alignment of different archives. The construction of an independent age model derived from the $^{10}Be/^9Be$ ratio would require more data from different depths, so that either by the exponential decay of the $^{10}Be/^9Be$ ratio or from other geomagnetic events additional temporal information could be retrieved.

For a reconstruction of past magnetic field variations in the future more detailed studies of the $^{10}Be/^9Be$ ratio in well dated sediments such as Site 983 may be a good addition to examining the ^{10}Be concentration in ice cores. In marine sediments reaching further back into the past, this method offers a way to extend the time range of studying magnetic field variations beyond the span of 1 Ma that is accessible with ice cores. Additionally, the development of the authigenic $^{10}Be/^9Be$ ratio over longer time scales can provide further insights to long-term changes of the ^9Be input via continental erosion.

A record of the rVDM is derived using the ODP Site 983 data and is compared to paleointensity proxies from the same location. Close-by manganese crusts are used to normalize the ratios during the Brunhes-Matuyama field reversal to a recent $(^{10}Be/^9Be)_0$ ratio. However, to minimize the effect of spatial and temporal variability of the $^{10}Be/^9Be$ ratio,

sediment samples from the studied site over a wider time range would be preferable for this normalization. A robust reconstruction of a Virtual Axial Dipole moment could be conducted with an appropriate average value of the ^{10}Be/^{9}Be ratio for the studied archive.

The wide range of applications of the authigenic ^{10}Be/^{9}Be ratio in marine sediments is demonstrated in this project. The ^{10}Be/^{9}Be variations on a short time scale are related to production changes of ^{10}Be and facilitate the investigation of the past magnetic field. On longer time scales, the ratio can reflect the changes in ^{9}Be input to the oceans from continental erosion.

Chapter 6

Actinides in the environment

6.1 Introduction

The most abundant actinides on Earth are the primordial ^{232}Th, ^{238}U and ^{235}U. Amongst others, the actinides interesting for AMS are ^{236}U, ^{237}Np, and the long-lived Pu isotopes with masses 239, 240, 241 and 244, which all are produced in nuclear reactions with ^{235}U or ^{238}U, as well as ^{231}Pa, which is a decay product in the ^{235}U decay chain. ^{231}Pa was investigated at the Tandy [Christl et al., 2007b] and was applied to reconstruct changes in water mass circulation [Christl et al., 2010a], but also can be measured with common mass-spectrometric methods. However, the interest in actinide analysis with AMS is mainly motivated by their use as tracers and indicators of anthropogenic activity. Not only actinides but anthropogenic radionuclides in general are useful as tracers for transport, mixing, or erosion, which was soon recognized after nuclear fission had been established for military and peaceful employment. An early example is the detection of the ^{51}Cr input from nuclear reactors in river and ocean water [Osterberg et al., 1965]. Major nuclear accidents could be identified by their releases of anthropogenic nuclides, a first example being the measurement of ^{133}Xe in air after the accident at Three Mile Island [Wahlen et al., 1980]. Later anthropogenic contaminations could be quickly recognized via AMS, such as ^{129}I in rainwater after the Chernobyl accident [Paul et al., 1987]. Apart from these regular and accidental releases from nuclear plants the input from reprocessing plants is the third source where nuclear fuel material enters the environment. Again, ^{129}I is a useful tracer and, for example, was applied to model the water transport from the reprocessing plants in La Hague and Sellafield in the North Sea to the Arctic Ocean [Karcher et al., 2012]. One major focus of the first ^{236}U measurements in environmental samples at ETH Zurich was to examine the distribution of this isotope in the same region. The results will be discussed in section 6.3.2. Furthermore, U and Pu were analysed in samples from the Atlantic Ocean. Because of their chemical properties, actinides behave quite differently in the ocean: U forms highly soluble carbonate complexes in the alkaline ocean. This causes

its long residence time in the ocean of more than 300 ka [Dunk et al., 2002] generating a very conservative behaviour during water mass transport. Pu, in contrast, attaches more easily to sinking particles and exhibits a much shorter residence time of ca. 10 a to 30 a [Livingston et al., 2001]. These anthropogenic actinides thus permit investigating different environmental processes, such as water transport or particle scavenging.

The major input for most anthropogenic isotopes stems from the atmospheric nuclear bomb explosions carried out between 1945 and 1980. An example for the detection of actinides is the study on transuranic nuclides in the air filters of the fallout itself [Diamond et al., 1960] and in natural archives [Noshkin et al., 1975]. In this work in particular, the presence of Pu isotopes and their source specific atomic ratios were used to identify contaminations from atmospheric bomb explosions, which is described in section 6.4.2.1.

6.2   Origin and inventories of U, Np, and Pu

6.2.1   Occurrence of important nuclear reactions for AMS actinide formation

Thermal neutrons in nuclear reactors or bombs can be captured by the main U isotopes to form states of ^{236}U and ^{239}U. Most of these capturing processes result in fission of the newly created nucleus and the release of energy. In about one of seven cases, a ^{235}U nucleus being hit by a thermal neutron does not undergo fission ($\sigma(^{235}$U(n,fission)=583 b) but remains as ^{236}U ($\sigma(^{235}$U(n,$\gamma)^{236}$U=98 b). If ^{238}U captures a slow neutron, in most of the cases ^{239}U is formed and decays via β^--decay to the short-lived ^{239}Np, which further decays to ^{239}Pu. More neutrons can be captured on ^{239}Pu and the following Pu isotopes until ^{243}Pu. As this isotope is very short-lived ($T_{1/2}$=5 h), its abundance in the fuel is low and it usually decays to ^{243}Am before another neutron can be captured and ^{244}Pu is created.

^{236}U and ^{239}Pu are found in U ores [Rokop et al., 1972; Seaborg and Perlman, 1948], where they are created by the capture of natural thermal neutrons on ^{235}U and ^{238}U, but their natural abundances are low. By means of the concentrations of neutron produced ^{236}U, ^{239}Pu and ^{36}Cl and of important elements in the rock matrix, the neutron flux in U ores can be modeled [Wilcken et al., 2008]. The neutrons originate either from spontaneous fission of ^{238}U or from secondary reactions after the α-decay of U or Th. More neutrons can be created in (α,n)-reactions with elements of the rock matrix and may be captured by the major U isotopes. The U concentration [U] of the material is related to the neutron flux Φ ([U]) and additionally determines the availability of ^{235}U targets for ^{236}U production. For this reason, in a simple model a higher U concentration would entail an increased ^{236}U/^{238}U ratio. This simple relation is modified by parameters such as the additional neutron contribution from the Th α-decay and the other elements in the material, in

particular concerning their moderating properties and their cross sections for neutron production via (α,n)-reactions and for neutron capture. Furthermore, cosmogenic neutrons might produce ^{236}U at a level $< 10^{-13}$ relative to ^{238}U, if one scales from the estimation of ^{36}Cl production in the Earth's surface layer [Fabryka-Martin, 1988] that happens by the reaction ^{35}Cl(n,γ)^{36}Cl.

Apart from its production via neutron capture on ^{235}U, ^{236}U is created in atomic bomb explosions via fast neutrons in the reaction ^{238}U(n$_{fast}$,3n)^{236}U ($\sigma \approx 0.5$ b for E$_n$=14 MeV). Similarly, ^{237}Np is produced in nuclear bombs via a ^{238}U(n$_{fast}$,2n)^{237}U reaction ($\sigma \approx 1.5$ b for E$_n$=11 MeV) and the following β^--decay of ^{237}U. Also Pu isotopes are formed in the r-process-like environment of a high-yield nuclear device if many neutrons quickly attach to ^{238}U and very neutron rich U isotopes are generated. When these isotopes decay to more stable nuclei, the long-lived ^{239}Pu, ^{240}Pu, ^{241}Pu, ^{242}Pu, ^{244}Pu and even more exotic transuranic isotopes are created.

For most of the anthropogenic actinides the production from nuclear weapons is lower than from nuclear reactors. However, the release from reactor fuel is mainly limited to accidents such as Chernobyl or Fukushima or to the controlled disposal from nuclear reprocessing plants.

In the following, the sources and inventories of anthropogenic U, Np, and Pu are compared. Because Np shows a higher mobility than Pu or Am [Fifield et al., 1997; Thakur and Mulholland, 2012], it is a potentially interesting environmental tracer and is included in this overview although no AMS measurements of this nuclide in environmental samples have yet been performed at ETH Zurich.

6.2.2 ^{236}U and ^{237}Np inventories

The inventory of ^{236}U from global fallout is estimated to 900 kg [Sakaguchi et al., 2009] from the ^{236}U/$^{239+240}$Pu ratios in samples of Japanese soil and applying the total activity of 14.8 PBq for $^{239+240}$Pu in global fallout [Harley, 1980]. The releases of ^{236}U created in nuclear reactors are related to the total release of U and the ^{236}U/^{238}U ratio of the fuel rods. With longer neutron irradiation the ^{236}U/^{238}U ratio increases in the reactor fuel. As ^{236}U acts as a neutron poison in the reactor, its content in the fuel should be minimized. If reprocessed U is employed, however, ^{236}U becomes enriched in the fuel with time, which is illustrated by the releases of La Hague until 1990 (Fig. 6.1). A used nuclear fuel rod exhibits ^{236}U/^{238}U ratios in the range of 10^{-3} [Boulyga and Becker, 2002; Wolf et al., 2005]. Fuel from fresh U ore containing only very little ^{236}U can be admixed to the reprocessed material to lower the ^{236}U fraction to a tolerable degree, which is why the ^{236}U/^{238}U ratio in the discharges is suspected to be not increasing since the early 90s. The reprocessing plants in La Hague at the English Channel and in Sellafield at the Irish Sea have been the main sources of anthropogenic radionuclides to the North
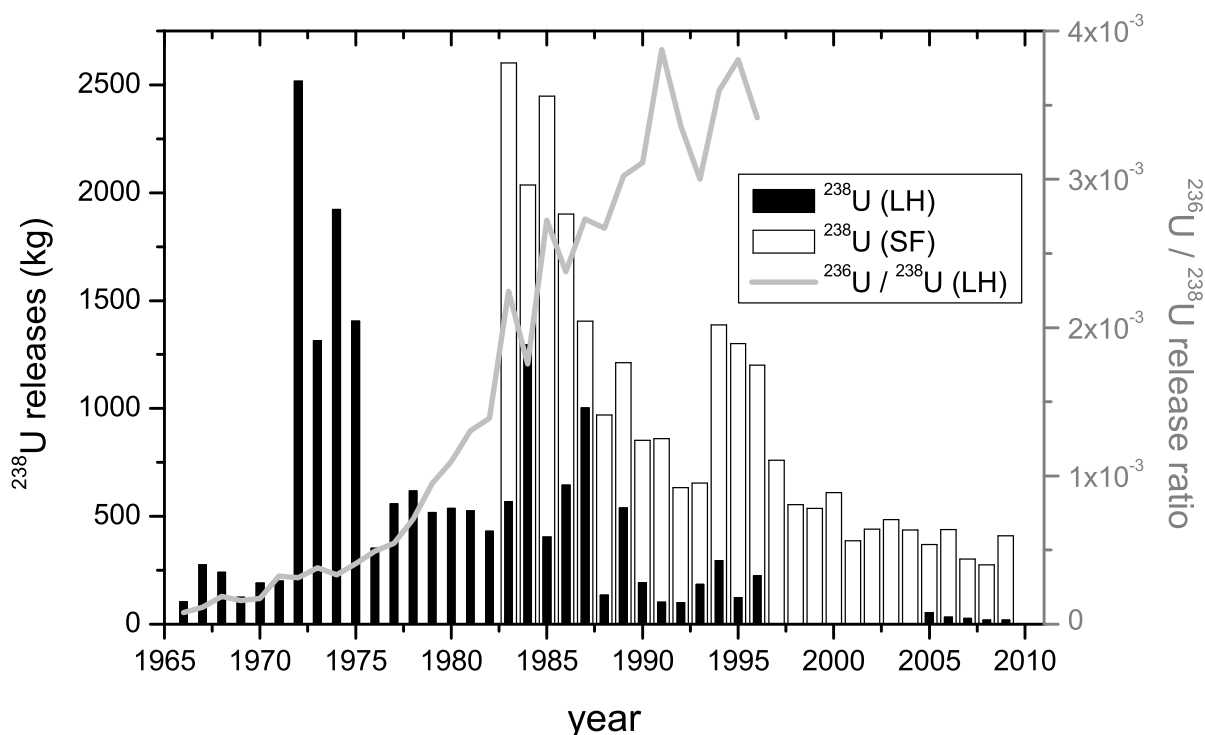
Figure 6.1: The releases of ^{238}U into sea water from the nuclear reprocessing plants Sellafield (SF) and La Hague (LH) decrease with time, while the ^{236}U/^{238}U ratio (scaled on the right axis) reported for La Hague rises [Herrmann, 2010; OSPAR, 2009].

Sea, the Arctic and the Atlantic Ocean. The recent releases from the smaller nuclear fuel fabrication and enrichment plant in Springfields are comparable to the ones reported for La Hague concerning U and Np [OSPAR, 2009]. The input of this plant also is in the Irish Sea and its release is more than one order of magnitude lower than from Sellafield. As the two sources are very close they may not have to be distinguished. To include the Springfields releases in the input function of anthropogenic actinides probably would mean only a small correction to the Sellafield discharges.

^{237}Np release by fallout from atmospheric tests is estimated to ca. 1500 kg [Beasley et al., 1998a]. The reported discharges from Sellafield amount to ca. 250 kg and from La Hague to ca. 150 g [Herrmann, 2010; OSPAR, 2009].

6.2.3 Pu inventory

For better comparability of the strength of the various Pu sources often the combined $^{239+240}$Pu activity is given. However, the ratio between these two isotopes is an important and useful parameter to distinguish the different sources of Pu input and is included in the discussion whenever available. 14.8 PBq $^{239+240}$Pu [Harley, 1980] were introduced into the environment by global fallout. The mean ^{240}Pu/^{239}Pu ratio of global fallout is

0.176±0.014 [Krey et al., 1976; Kelley et al., 1999]. From this global ^{240}Pu/^{239}Pu ratio and from the above mentioned activity for both isotopes an input of ca. 3900 kg ^{239}Pu and 700 kg ^{240}Pu by nuclear weapon explosions is estimated. The global fallout of Pu is not equally distributed. The fallout concentrations in the northern hemisphere are about three to four times larger than in the southern hemisphere [Hardy et al., 1973]. Pu isotope ratios depend on the latitude with slightly depleted abundances of the heavier Pu isotopes in the Southern equatorial region (0°S-30°S) [Kelley et al., 1999]. This is related to the higher fraction of low-yield tests performed in this region. If anomalies in the ^{240}Pu/^{239}Pu can be observed, the heavier Pu isotopes ^{241}Pu and ^{242}Pu are even more affected [Kelley et al., 1999].

Usually, deviations from the global fallout value can be attributed to a local contamination, for example at test sites that are dominated by the tropospheric fallout. At the French test sites Mururoa and Fangataufa atoll [Chiappini et al., 1999; Hrnecek et al., 2005] as well as at the Soviet-Russian test site in Semipalatinsk-21 [Beasley et al., 1998b] the detected ^{240}Pu/^{239}Pu ratios were significantly lower than the global fallout value. On the other hand, higher ^{240}Pu/^{239}Pu ratios were encountered in the region of the Marshall islands, where several weapons with high explosive yield had been tested [Buesseler, 1997; Muramatsu et al., 2001]. Not only nuclear weapon explosions may leave an isotope specific trace, but also the weapon accidents in Palomares or Thule [Mitchell et al., 1997; Chamizo et al., 2006] or nuclear reactor and waste accidents such as in Chernobyl [Muramatsu et al., 2000] and Mayak [Beasley et al., 1998b; Oughton et al., 2000] show significant variations in the ^{240}Pu/^{239}Pu signature compared to the global fallout. In the 2010 accident at the Fukushima Daiichi nuclear plant Pu was released, which could be detected from the high concentration of the short-lived ^{241}Pu in local soil samples [Zheng et al., 2012].

The total $^{239+240}$Pu discharges from Sellafield amount to 613 TBq and from La Hague to 3.5 TBq [Herrmann, 2010; OSPAR, 2009] and are several orders below the global fallout value. Because the ^{240}Pu/^{239}Pu ratio in nuclear fuel strongly depends on the burn-up, it is not uniform in the disposed waste over time. A disentanglement of the two isotopes as in the case of the global fallout therefore is not possible.

6.3   Environmental ^{236}U

6.3.1 ^{236}U in continental waters

Ground water in contact with U rich repositories leaches radionuclides such as ^{36}Cl or ^{236}U, which are created by the neutrons originating from the U radioactivity. These nuclides might act as neutron monitor and indicator of U deposits. Such water from U rich deposits was sampled to test the preparation and the ^{236}U measurement technique.

In the course of a term work [Meister, 2011], water samples from an overflow of the abandoned Menzenschwand U mine in the German Black Forest were taken. According to Hofmann [1989], this deposit formed 300 Ma before present. Previously, this site had been used to investigate the neutron induced ^{36}Cl production [Balderer and Synal, 2004] and a maximum [U] of 14 700 ppm had been estimated as a result. Volumes of 0.5 l and 1 l were analysed for their ^{236}U/^{238}U ratio in order to examine the potential of ^{236}U measurements in ground water and to develop the chemical extraction methods of U from water (appendix A.2). Poor chemical yield and low [U] in the waters caused a relatively high uncertainty for these first natural samples measured for their ^{236}U content at the Tandy setup.

In the new study, a ^{236}U/^{238}U ratio of $(267\pm13)\cdot10^{-12}$ was determined in the overflow water of the mine. This ratio is used to calculate the average [U] via the following equation assuming that production and decay in the ore are in equilibrium. This is fulfilled because the age of the deposit is much larger than the lifetime of ^{236}U.

$$\frac{^{236}\text{U}}{^{238}\text{U}} = \left(\frac{^{235}\text{U}}{^{238}\text{U}}\right)_{\text{nat}} \cdot \sigma\left(^{235}\text{U}(n,\gamma)^{236}\text{U}\right) \cdot \Phi_n\left([\text{U}]\right) \cdot \tau_{236} \tag{6.1}$$

An average host rock [U] of ca. 53 000 ppm is estimated assuming that the neutron production from Th can be neglected and using the neutron flux $\Phi_n\left([\text{U}]\right) = \frac{3.23\cdot[\text{U}]}{4.55\cdot10^{-5}}$ cm^{-2}s^{-1} according to the parameters for Menzenschwand granite given in Balderer and Synal [2004]. This means a disagreement by a factor of more than three compared to the previous study by Balderer and Synal [2004]. It has to be taken into account that the samples of this study were collected in the overflow water of the mine, whereas samples for the previous ^{36}Cl determination had been collected from groundwater in the mine. So, possibly the new samples do not solely represent the ^{236}U/^{238}U ratio of the Menzenschwand ore but are additionally influenced by anthropogenic sources.

At another site, the abandoned coal mine in Riedhof (canton Zurich), two samples were collected from water on the mine floor. Compared to typical coal deposits, this mine is relatively rich in U with a content of 330 ppm [Studer, 2008]. ^{236}U/^{238}U ratios amounted to $(1.57\pm0.11)\cdot10^{-9}$ and $(2.42\pm0.25)\cdot10^{-9}$, respectively, but samples showed only currents of few tens of pA. The low currents point to a very low [U] in the water or a low yield, which had not been checked with ^{233}U at the time of the experiment. These high ^{236}U/^{238}U ratios definitely cannot be ascribed to natural nucleogenic production according to equation 6.1. As the origin of the water in the mine is from precipitation, this rain water might carry anthropogenic ^{236}U, which is dissolved from the above-lying soil layers and causes the high ^{236}U/^{238}U ratios. The U content of the water is low because the water is not ground water continuously leaching the deposit. Thus, also the observed currents were lower than expected.

In Austrian river waters, Srncik et al. [2010] observed high ^{236}U/^{238}U ratios ranging from $5\cdot10^{-9}$ to $5\cdot10^{-5}$. These results confirm the wide-spread contamination of the environment

with ^{236}U. For this reason, the reconstruction of [U] in rock or soil from ^{236}U is not easily possible from water samples.

The method of U extraction from natural water samples could be tested in our first preparations. The first applications on larger scale were carried out in seawater samples and are described in the following.

6.3.2 ^{236}U in the oceans

During the GEOTRACES cruise GA02 of the research vessel Pelagia, six samples were taken at two stations in the western equatorial Atlantic Ocean (marked as GA02-39 and GA02-40 in Fig. 6.2). The following results and calculations are summarized from Christl et al. [2013a]. The depth profile covered the water masses of the local surface water (25 m), the North Atlantic Deep Water (NADW) at 2500 m and a mixture of the NADW with
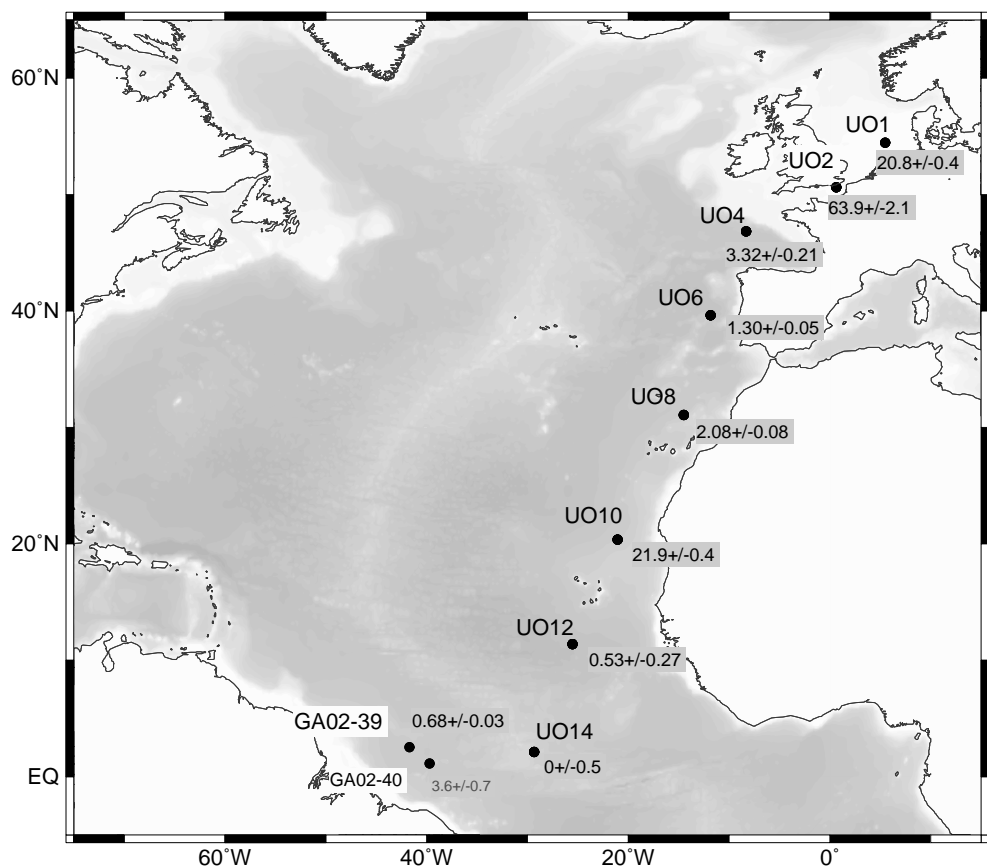
Figure 6.2: Stations of the GEOTRACES cruise 2010 of the Pelagia measured for ^{236}U and sampling locations of the Oden vessel measured for ^{236}U, ^{239}Pu and ^{240}Pu. ^{236}U/^{238}U ratios in the surface water samples are given in units of 10^{-9}. The rather high ratio of the surface sample from station GA02-40 is potentially influenced by a laboratory contamination with ^{236}U.

Antarctic Bottom Water (AABW) at 4250 m. The water masses could be identified using temperature and salinity data. The two stations are ca. 250 km apart from each other and the water masses at the various depths are nearly the same. Station 39 is different from station 40 only at the surface. This might be caused by an influence of Amazon river water to station 39. Surface ^{236}U/^{238}U ratios amount to $(683\pm25)\cdot10^{-12}$ [GA02-39] and $(3567\pm678)\cdot10^{-12}$ [GA02-40]. They clearly show the anthropogenic input from bomb fallout. Because of the extraordinarily high value of the surface sample at station GA02-40, a contamination cannot be excluded, particularly as in the AMS pressing laboratory a contamination with ^{236}U from a high ^{236}U/^{233}U spike still is present. Also in the processing of the samples from the Oden cruise (Fig. 6.2), exceptionally high ^{236}U/^{238}U ratios were encountered in the Atlantic Ocean, which might be caused by the same contamination. As a consequence of this contamination, ^{236}U samples are no longer processed in this laboratory.

The deep samples from the GEOTRACES depth profile exhibit relatively high ratios in the order of 10^{-10}, far above the ratios estimated for natural sources of ^{236}U. The equatorial NADW in 2500 m ($(189\pm6)\cdot10^{-12}$ [GA02-39] and $(191\pm10)\cdot10^{-12}$ [GA02-40]) thus already shows the signal of anthropogenic input from global fallout and reprocessing plants. One can imagine two processes transporting the anthropogenic ^{236}U to these depths. Vertical transport by attachment to sinking particles was ruled out by box model simulations: The vertical particle flux of U necessary to account for the observed ratios would be so strong that it would cause a change of the overall U concentration with depth, which is not observed in the ocean. The second hypothesis is the transport of U as a component of the water mass that is created from North Atlantic surface water and then subducts to form the NADW. The detected values can be explained in a scenario where ^{236}U from global fallout is introduced to a surface mixed layer of 50 m in the North Atlantic, which then contributes to the deep water formation. The nuclear reprocessing plants in Northern Europe only have little influence on the equatorial NADW ratios, because the main input from these plants occurred later than the maximum of the global fallout and the transport of this signal to the site of NADW formation leads to a further delay. The values at 4250 m depth ($(128\pm9)\cdot10^{-12}$ [GA02-39] and $(91\pm5)\cdot10^{-12}$ [GA02-40]) are about a factor of two lower than the ratios in 2500 m depth. This can be ascribed to a mixing of the ^{236}U-carrying NADW water mass with the old AABW that is pre-anthropogenic and has significantly less ^{236}U.

During the same cruise 3 l samples had been taken for ^{129}I analysis, but were prepared for ^{236}U in a collaboration with the Universitat Autònoma de Barcelona (UAB). Amongst others, samples from station 39 were processed and the new results matched the previous determination. This gives the experimental proof that smaller sample volumes are adequate for the extraction of ^{236}U, too, which will facilitate future sampling.

In autumn 2010, the Oden vessel collected surface water samples in the North Sea and in the Atlantic Ocean from depths of 0 m to 10 m. So far, the eight samples north of the equator have been processed and the observed ratios in the Atlantic Ocean range from ca. $0.5 \cdot 10^{-9}$ [UO12] to $22 \cdot 10^{-9}$ [UO10] and cover the range of $^{236}U/^{238}U$ ratios of the surface water samples collected during the GEOTRACES cruise. Contaminations in the laboratory cannot be ruled out as possible reasons of the highly elevated value at station UO10. No possible source of ^{236}U is known in this region. An increase in the North Sea with a $^{236}U/^{238}U$ ratio of $(20.7 \pm 0.4) \cdot 10^{-9}$ is visible. In the English Channel a clear maximum of $(63.9 \pm 2.1) \cdot 10^{-9}$ is determined for the $^{236}U/^{238}U$ ratio. Also the highest value in ^{236}U concentration (Fig. 6.4) of this cruise is observed close to the outlet of La Hague in the English Channel with a further increased value in the central North Sea. The data shows the specific input of ^{236}U in the North Sea region, which will be discussed in the following.

6.3.3 ^{236}U in the North Sea

The contamination of the North Sea originates from disposals of the nuclear fuel reprocessing plants in La Hague and Sellafield. These discharges can be traced with different radionuclides, for example with ^{129}I [Michel et al., 2012], ^3H, ^{90}Sr, ^{137}Cs, and ^{99}Tc [Nies et al., 2009] and are very source specific: At present, for example, ^{99}Tc input is mainly originating from Sellafield, while ^{129}I is mostly introduced by the plant in La Hague. In a collaboration with the German Bundesamt für Seeschifffahrt und Hydrographie (BSH) in Hamburg, 10-20 l surface water samples from the North Sea were measured for their ^{236}U content. The BSH monitors the water in German territorial waters and beyond in annual cruises. 41 samples in total have been analysed from the cruise in 2009, which allows examining the ^{236}U input of the reprocessing plants with a high local resolution (Fig. 6.3). Samples from the cruises in 2010 and 2011 are now available for ^{236}U detection in addition to the measured samples from 2009. Hence, a time resolved study will be possible. Because of the short residence time of water in this region (ca. 1 a), sampling with this time resolution enables to track the annual release variations.

The input from Sellafield follows the flow path of the water along the eastern British coastline after having been transported to the North Sea via the Scottish Coastal Current. Consequently, the Sellafield signal is already more diluted by Atlantic water when entering the North Sea than the La Hague signal, which is directly delivered by the English Channel current. ^{236}U concentration ($160 \cdot 10^6$ at./l) and $^{236}U/^{238}U$ ratios ($20 \cdot 10^{-9}$) show the highest values close to the La Hague outlet. The mixture with the Atlantic inflow from the North results in average values of $10 \cdot 10^{-9}$ for $^{236}U/^{238}U$ and $80 \cdot 10^6$ at./l for the ^{236}U concentration in the central North Sea. The water samples upstream of La Hague are still carrying the signature of Atlantic surface water with relatively low ratios of $6 \cdot 10^{-9}$ and concentrations
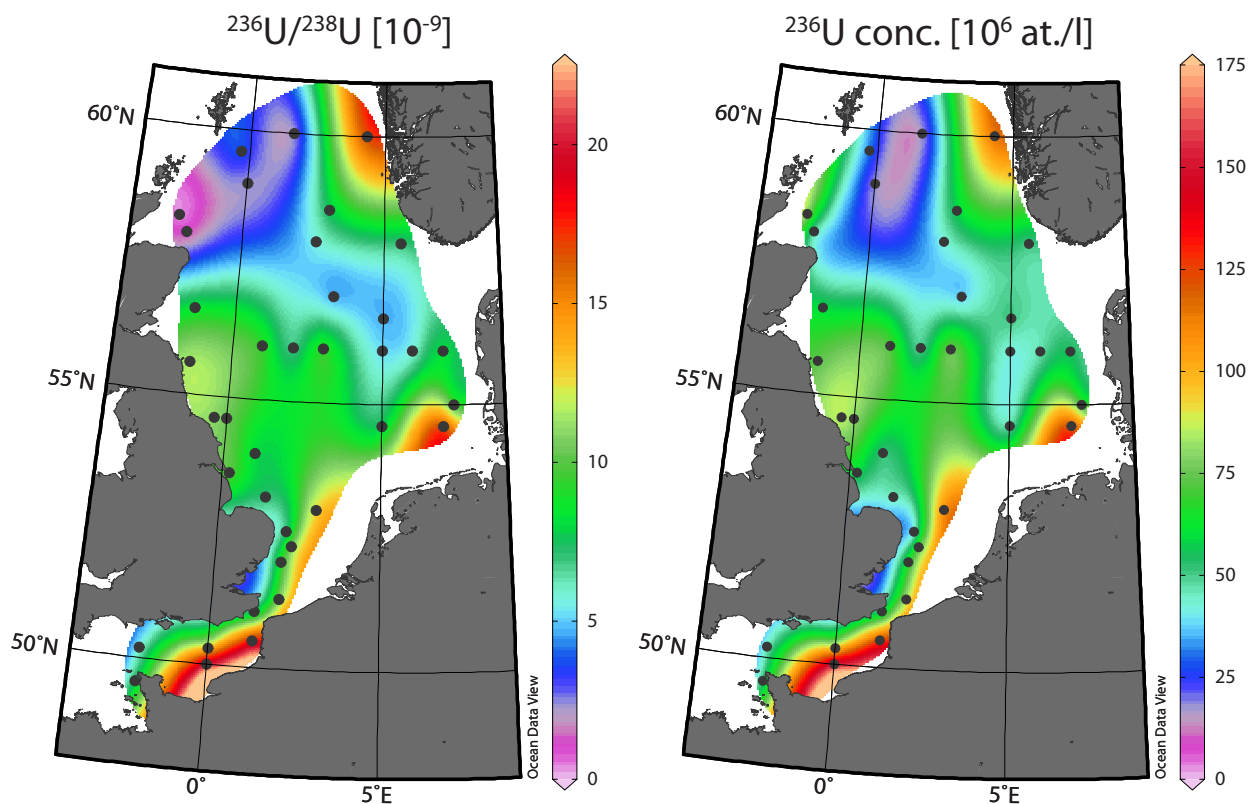
Figure 6.3: Results for the North Sea samples collected during the 2009 Pelagia cruise [Christl et al., 2013a] with ^{236}U/^{238}U ratios in units of 10^{-9} on the left and ^{236}U concentrations in units of 10^6at./l on the right. Sample stations are marked by dots. Interpolations between the stations were calculated by the program ODV [Schlitzer, 2012].

of ca. $50 \cdot 10^6$ at./l. Temporal variability of the releases from La Hague may cause the lower ^{236}U/^{238}U ratios in the English Channel found in this study compared with the maximum value from the Oden cruise (($63.9 \pm 2.1) \cdot 10^{-9}$) observed in this region.

Data for ^{3}H, ^{90}Sr, ^{137}Cs, and $^{239+240}$Pu are available as a result of the routinely performed measurements of radionuclides at BSH in the same water samples. For 2009, ^{129}I was analysed via AMS, but the data is not yet published. These results will make it possible to compare the outputs of the various radionuclides and to identify source-specific release ratios.

6.4 Pu isotopes

6.4.1 Pu in the Ocean

In the samples of the 2010 Oden cruise from the Northern Atlantic, the Pu fraction of the chemical processing for ^{236}U was collected and prepared for AMS measurements [Diebold, 2012]. ^{239}Pu and ^{240}Pu concentrations (Fig. 6.4) and the ^{240}Pu/^{239}Pu ratio were

quantified in the water. The $^{240}Pu/^{239}Pu$ ratios range from 0.140 ± 0.018 to 0.197 ± 0.013 and do not show clear signatures of sources other than the global fallout. A study with better local resolution in the North Sea showed mainly $^{240}Pu/^{239}Pu$ ratios that are increased compared to the global fallout [Bisinger et al., 2010]. Within the 1σ-uncertainties, the two Oden samples from the central North Sea and the English Channel are in agreement with these data.

Also $^{239}Pu/^{236}U$ ratios can be calculated for these samples. They vary from 0.01 to 0.2 and have no local tendency. The ratios reported for Japanese soils, which were applied to calculate the global ^{236}U fallout, have values between 0.21 and 0.25 [Sakaguchi et al., 2009], so our samples seem to be depleted in Pu. This is probably related to the chemical behaviour of the two elements in water described in section 6.1: Whereas U is easily dissolved in water and is still present in this medium from the global fallout, Pu in water readily attaches to particles and is scavenged.

The ^{239}Pu and ^{240}Pu concentrations in North Sea and English Channel are the highest observed on the Oden track. It is noticeable that the values in the North Sea are even higher than in the English Channel. This is just contrary to ^{236}U in this region and points to a remobilisation of Pu from the sediment of the North Sea. The reprocessing plants have reduced their Pu output since the 70s. For this reason, the re-dissolution of particle-bound Pu nowadays becomes an important additional source of this radionuclide [Cook et al., 1997].

Because of the lower concentrations of the Pu isotopes compared to ^{236}U, larger sample volumes have to be prepared to achieve good counting statistics. Furthermore, other mass-spectrometric methods such as ICP-MS can determine Pu isotope ratios and concentrations at the level present in seawater (e.g. Chiappini et al. [1996]).

6.4.2   Coral CaCO$_3$ from Bikini atoll[*]

Many of the American atmospheric nuclear tests between 1946 and 1958 were conducted at the Marshall islands (Enewetak and Bikini atoll). Notably those weapons with a high explosive yield caused a significant local contamination. In general, the explosive yield of a nuclear bomb is connected to the isotopic signature of the dispersed radionuclides: The production of radioactive isotopes strongly depends on the absolute number and the time span of the developing neutron flux and on the amount and distribution of target nuclides in the setup and the environment. Isotopic ratios thus are valuable tools to derive the fraction of radionuclide contribution from different sources or even to reconstruct the initial neutron flux.

In a collaboration with the University Hanover, sediment samples from the Bikini atoll were available for radioisotope analysis. The material was collected in spring 2008 and consists

---

[*]Parts of this chapter are based on Lachner et al. [2010]
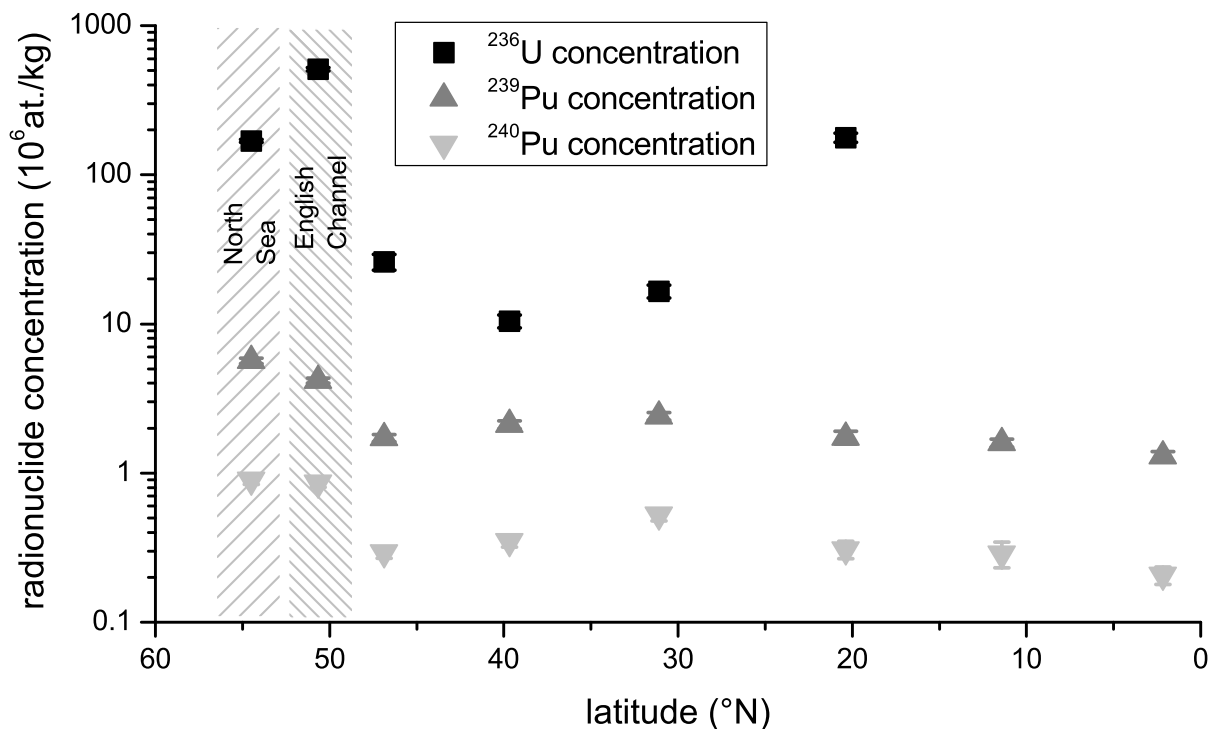
Figure 6.4: Concentrations of ^{236}U, ^{239}Pu and ^{240}Pu in Alantic surface water samples collected during the Oden cruise 2010. ^{236}U values south of 20°N cannot be distinguished from zero and thus are not depicted in this graph.

of coarse grained (mm-size) coral $CaCO_3$. Isotopic ratios and/or concentrations of ^{10}Be, ^{14}C, ^{41}Ca, ^{239}Pu, ^{240}Pu, ^{241}Pu, and ^{244}Pu were detected in these samples (Fig. 6.5). The targets for Pu analysis were prepared at the University Hanover and ^{242}Pu was added as spike, the other samples were prepared at the ETH Zurich.

Four soil specimens were collected on the main Bikini island (BU1, BL5, BL6, BL7), three of them as a depth profile (BL5: 0-2 cm, BL6: 2-7 cm, BL7: 7-15 cm). Another sediment sample (BS8) was taken next to the wreck USS Saratoga at 40 m water depth. This ship sank during the test of the Pu-implosion weapon Baker in 1946, which was the second test at the Bikini atoll. The explosion occurred close to the sampling site, about 25 m above lagoon floor and 25 m below sea surface. The yield of this device (TNT equivalent of 23 kt) was relatively low, which is typical for the early era of nuclear weapons. It detonated underwater and caused a higher contamination of the lagoon floor than its precursor Able, which had been brought to explosion 160 m above sea level [Hawthorne, 1979]. The sediment sample BK9 was obtained from the crater created by the Castle Bravo test (15 Mt) in March 1954 and reused for the Castle Romeo test (11 Mt) one month later [Hawthorne, 1979]. This crater has a diameter of ca. 2 km and the sediment sample was taken from the northeast crater border at 15 m water depth.
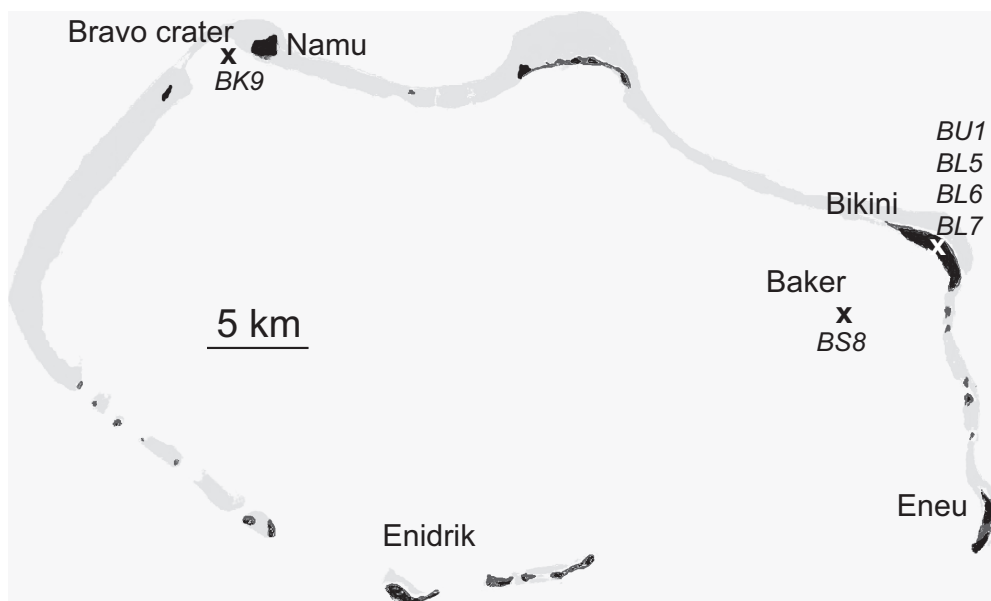
Figure 6.5: Bikini atoll: Sampling sites (**x**) at the Bravo crater (BK9), at the sunken ship Saratoga (BS8) and on Bikini Island (BU1, BL5, BL6, BL7)

6.4.2.1 Pu from local fallout

In many cases, the Pu isotopic composition is useful to identify a specific source of an environmental radioactive contamination. The input of material with a significantly different isotope ratio into a spatially limited region of the environment, e.g. from the Pacific Proving Grounds, was utilized in environmental or oceanographic studies [Kim et al., 2004; Zheng and Yamada, 2005].

In the following, the Pu isotope ratios analysed in the sediment samples from the Bikini atoll are discussed. Uncertainties and upper limits of samples with low counting statistics were estimated according to Feldman and Cousins [1998].

^{240}**Pu/^{239}Pu ratios**

At the Bikini atoll, all samples except one reveal ^{240}Pu/^{239}Pu ratios between 0.263 and 0.323, which is significantly above the global fallout ratio:

The samples from Bikini island (BU1, BL5, BL6, BL7) exhibit the known local fallout ratios of the Bikini atoll, which are dominated by the heavy contamination from the Castle Bravo detonation. In other studies the ^{240}Pu/^{239}Pu ratio of the contaminating fallout from this bomb had been determined to range from 0.302±0.006 to 0.306±0.010 [Muramatsu et al., 2001] and from 0.318±0.033 to 0.338±0.051 [Komura et al., 1984]. The values at the island thereby correspond to the fallout from the Castle Bravo test. In comparison with the ratio measured after the Ivy Mike test (0.363, Diamond et al. [1960]) at Enewetak atoll, the samples from the Bikini island are uniformly lower.

Table 6.1: Pu isotope ratios in samples collected on Bikini atoll, ^{241}Pu/^{239}Pu ratios determined in June 2009; statistical uncertainties of ratios written in italics are calculated according to Feldman and Cousins [1998].

sample	location	^{240}Pu/^{239}Pu	^{241}Pu/^{239}Pu	^{244}Pu/^{239}Pu
BU1	island	0.295±0.034	-	-
BL5	island	0.319±0.026	_0.0062$^{+0.0027}_{-0.0022}$_	_(3.1$^{+5.4}_{-2.0}$)·10^{-4}_
BL6	island	0.323±0.011	0.0023±0.0003	(5.4±1.6)·10^{-4}
BL7	island	0.288±0.006	0.0051±0.0020	(5.7±1.1)·10^{-4}
BS8	lagoon	0.063±0.005	_(7.8$^{+6.1}_{-5.1}$)·10^{-4}_	_< 1.7·10^{-4}_
BK9	crater	0.263±0.003	0.0028±0.0004	(2.5±0.4)·10^{-4}

Sample BS8 from the lagoon floor has a clearly lower ^{240}Pu/^{239}Pu ratio of 0.063. This value is in line with ratios from locations that had input from low yield nuclear tests such as the surface soils at the Enewetak atoll [Muramatsu et al., 2001]. Similarly low ratios are known from the French and Soviet-Russian test sites [Chiappini et al., 1999; Hrnecek et al., 2005; Beasley et al., 1998b] or from contaminations with weapons grade material at Thule and Palomares [Mitchell et al., 1997; Chamizo et al., 2006].

The ^{240}Pu/^{239}Pu ratio in the Bravo crater sediment BK9 is measured to 0.263±0.003. It is above the global fallout value but below the ratio of the material distributed by the Castle Bravo explosion. This suggests a contribution from explosions with a much lower yield than Castle Bravo (15 Mt) and Castle Romeo (11 Mt). Indeed, during the Operation Hardtack in 1958 tests with lower explosive yield (Fir: 1.36 Mt, Sycamore: 92 kt, Aspen: 319 kt, Cedar: 220 kt) were performed at the same site, placed on barges in the middle of the crater [Hawthorne, 1979].

The Pu ratios in the crater and on the island serve as input values for a simple binary mixing model to identify the ^{240}Pu/^{239}Pu ratio of these later tests. About 50% of the Pu fallout found in the crater are attributed to the first two explosions with high neutron flux and high yield (Castle Bravo and Romeo). The remaining 50% originate from later explosions with a ^{240}Pu/^{239}Pu ratio of 0.21. This ratio is closer to the global fallout ratio. In addition, it matches the mean ^{240}Pu/^{239}Pu ratio for the following testing period, which was derived from a dated coral near the crater by Noshkin et al. [1975].

^{244}Pu/^{239}Pu ratio

The ^{244}Pu/^{239}Pu ratio was examined in five samples. Three of those accumulated more than one count during the AMS measurement: Two samples from the island depth profile

(BL6, BL7) and the sample from the Bravo crater (BK9). ^{244}Pu/^{239}Pu ratios at Bikini island range from $2.8 \cdot 10^{-4}$ to $6.2 \cdot 10^{-4}$, which are again, as in the case of the ^{240}Pu/^{239}Pu ratio, significantly lower than the $(11.8 \pm 0.7) \cdot 10^{-4}$ found by Diamond et al. [1960] after the Ivy Mike thermonuclear explosion at Enewetak. Measurements of fallout in Mn nodules from the Pacific [Wallner et al., 2004] also exhibit a higher value of $(1.2 \pm 0.4) \cdot 10^{-3}$. On the other hand, a ^{244}Pu/^{239}Pu ratio of $(5.7 \pm 1.0) \cdot 10^{-5}$ was detected in samples from Austria [Steier et al., 2013] and in the same material a ^{240}Pu/^{239}Pu ratio was determined that matches the global fallout value in the northern hemisphere. Therefore, the value of $(5.7 \pm 1.0) \cdot 10^{-5}$ has to be considered a good estimate for the ^{244}Pu/^{239}Pu ratio from global fallout. From the higher ^{244}Pu/^{239}Pu ratios of the samples in the crater and at the Bikini island the specific influence of explosions with a high neutron flux can be concluded.

Only a single count of ^{244}Pu was detected in the sample BL5 from the surface of the island, which had shown low count rates on the other Pu isotopes, too. Within its large uncertainties, the resulting ratio of $3.1 \cdot 10^{-4}$ is in accordance with the other samples.

The Saratoga sample (BS8) yielded no event, an upper limit of $1.7 \cdot 10^{-4}$ is estimated at 1σ confidence level. This is consistent with the above interpretation that Pu at the Saratoga site carries the isotopic signature of a low yield explosion, but a distinction to the global fallout is not possible.

The trend of a lower abundance of the heavy Pu isotopes in the crater sample compared to the island samples (consistently observed in the ^{240}Pu/^{239}Pu ratio) is observed again, but much more pronounced, in the ^{244}Pu/^{239}Pu ratio. Since large amounts of ^{244}Pu should be predominantly produced in high yield explosions, this again supports the interpretation of a mixture of high- and low-yield explosion fallout at the crater from the various tests carried out at this site.

Above, in a binary mixing model using the ^{240}Pu/^{239}Pu ratios, a 50% contribution of the later low-yield tests was estimated. The uncertainties for the ^{244}Pu/^{239}Pu ratios are much larger but with the values on the island and in the crater also the ^{244}Pu input of the later contributions can be estimated. The resulting input ratio of the following tests, though, is lower than the global fallout value reported by Steier et al. [2013]. Despite their increased ^{240}Pu/^{239}Pu ratio relative to the global average, in the following tests at the same site less ^{244}Pu than expected from global fallout was produced. This points at an overproportional contribution of the few very high-yield explosions to the global fallout of ^{244}Pu.

^{241}Pu/^{239}Pu ratio

To calculate the actual number of ^{241}Pu atoms relative to ^{239}Pu at the time of the explosion, decay corrections have to be applied. Another difficulty in interpreting the results arises from the fact that the tests at Bikini were carried out between 1946 and 1958, a time span of almost one half-life of ^{241}Pu ($T_{1/2}$=14.4 a). The decay correction is adjusted for the individual samples: Concluding from the results for the ^{240}Pu/^{239}Pu ratio, the origin of Pu
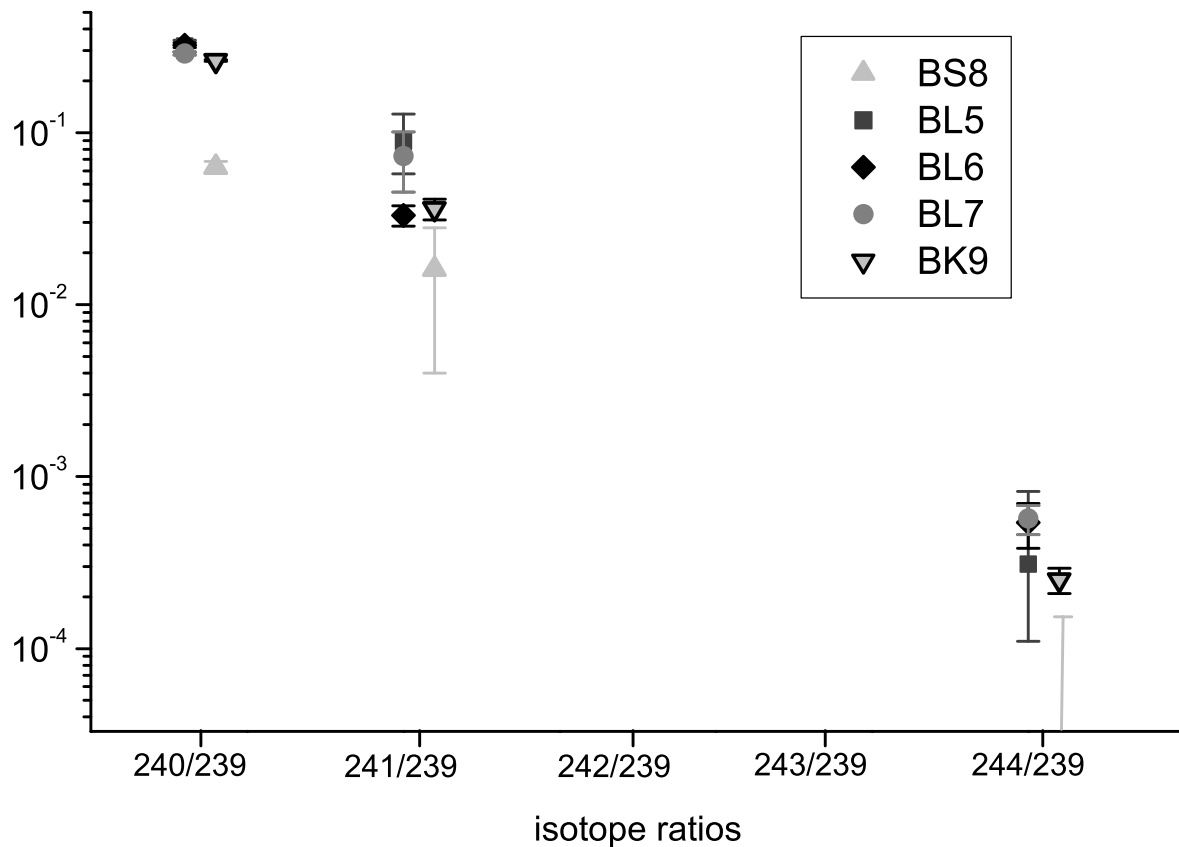
Figure 6.6: Pu isotope ratios from the different sampling locations, the ^{241}Pu/^{239}Pu ratios are decay corrected.

in sample BS8 is attributed to the Baker test in 1946. For the samples from the island the contamination by the Castle Bravo Test in 1954 is supposed to be dominant. As a mixture of material from different input sources between 1954 and 1958 probably occurred in the sample from the crater (BK9), a correction to the year 1956 is applied for this specimen. The corrected ratios fit in the general trend observed for ^{240}Pu and ^{244}Pu. The lagoon sample BS8 has a lower ratio than the sample from the crater (BK9), which in turn shows a lower value than samples from the island (BL5, BL7). However, the samples from the island itself give no concordant picture with respect to the ^{241}Pu/^{239}Pu ratio. Although the uncertainties are large, the sample BL6 differs from BL5 and BL7, while the ratios of the other isotopes are more consistent in these samples. The chemistry was not checked for separation of ^{241}Am. Varying yields in the suppression of this isotope may cause the observed irregularities of the ^{241}Pu/^{239}Pu ratio from the same site.

In summary, from the distribution of Pu isotopes at Bikini atoll the various sources of contamination can be recognized and attributed. Besides the established ^{240}Pu/^{239}Pu ratio, the heavier isotopes such as ^{244}Pu may provide a valuable tool to identify specific sources of Pu input into the environment.

6.4.2.2 ^{41}Ca, ^{14}C, and ^{10}Be production in CaCO$_3$

Other radionuclides (^{10}Be, ^{14}C, ^{41}Ca) were investigated in the samples from Bikini atoll in addition to Pu. The motivation for this experiment and the results are summarized in this section.

Via AMS the activation of materials exposed to nuclear bomb explosions can be determined. From this, the neutron flux Φ [cm^{-2}s^{-1}] or fluence Ψ [cm^{-2}] can be reconstructed and applied for retrospective dosimetry (e.g. Rühm et al. [1995, 2010]; Straume et al. [2003]). CaCO$_3$ contains three isotopes (^{13}C, ^{17}O, ^{40}Ca) that may act as targets for neutron reactions producing the long-lived radioisotopes ^{10}Be ($T_{1/2}$=1.387 Ma, Korschinek et al. [2010]; Chmeleff et al. [2010]), ^{14}C ($T_{1/2}$=5730 a, Godwin [1962]) and ^{41}Ca ($T_{1/2}$=103 ka, Klein et al. [1991]).

Anthropogenic ^{14}C and ^{41}Ca signals [Nydal, 1968; Zerle et al., 1997] are used in studies of atmospheric transport processes. In this context, the locality at Bikini is of specific interest, as the explosion Castle Bravo was one of the few that took place on the surface of a coral island and thus produced and distributed major amounts of ^{41}Ca. The isotope ratios of ^{14}C/^{12}C and ^{41}Ca/^{40}Ca at the Bikini atoll may serve as input parameters for environmental studies. In contrast to ^{14}C and ^{41}Ca, which exhibit clear peaks from atmospheric bomb explosions in corals or ice cores, ^{10}Be from global fallout has not been observed in environmental archives [Beer et al., 1985].

The ^{41}Ca and ^{10}Be measurements were performed at the Tandy, ^{14}C was measured at the 200 kV Radiocarbon facility MICADAS. Elevated concentrations of all studied isotopes are detected in the BK9 sample from the crater of the high yield nuclear explosion Castle Bravo (table 6.2).

Table 6.2: Radionuclide concentrations and ratios on Bikini Island and in the Bravo Crater. The ^{41}Ca/^{40}Ca ratio from Bikini Island is at the level of the corresponding AMS blank sample.

sample	^{10}Be conc.	^{14}C/^{12}C ratio	^{41}Ca/^{40}Ca ratio
crater	(248±14)·10^6 at./g	(28.9±0.004)·10^{-12}	(105.8±2.0)·10^{-12}
island	(41±6)·10^6 at./g	(0.81±0.005)·10^{-12}	*(3.4±0.4)·10^{-12}*

^{41}Ca and ^{14}C concentrations can be estimated from the AMS results under the assumption of a pure target with the stoichiometry of CaCO$_3$. For ^{10}Be the concentration was directly determined in the AMS measurement.

It is assumed that ^{10}Be is predominantly produced via the ^{13}C(n,α)^{10}Be reaction on natural ^{13}C in the CaCO$_3$. Other reactions are not taken into account because possible targets such as ^{10}B and ^{9}Be are not very abundant in CaCO$_3$ and the respective reaction cross sections to create ^{10}Be are less than 10 mb. ^{10}Be is produced as a ternary fission fragment with a relative yield of 4.2·10^{-6} [Vorobyev et al., 1972] corresponding to a ^{10}Be/^{137}Cs ratio

of $6.7 \cdot 10^{-5}$. This fallout source, however, is not included in our considerations, as only the total number of ^{10}Be from this production channel could be calculated but not its input into the sample.

However, for ^{14}C the treatment of its production on a pure $CaCO_3$ target is not adequate, too. Other reaction channels are necessary to reconstruct the observed radionuclide concentrations. The presence of ^{14}N in the biological active part of the coral cannot be neglected and a significant amount of ^{14}C may be generated by the ^{14}N(n,p)^{14}C reaction. Else, the high concentration of ^{14}C cannot be explained.

A simple approach is presented in order to get an idea about the neutron flow that has irradiated the sample BK9. Averaged values for different neutron energy regimes are chosen from the RUSFOND2010 library for nuclear cross sections:

- thermal neutrons (10^{-5} eV $<$ E $<$ 10 eV): σ_{th}

- epithermal neutrons (0.5 eV $<$ E $<$ 100 keV): σ_{epi}

- neutrons from an average fission spectrum (1 keV $<$ E $<$ 20 MeV): σ_{fast}

- neutrons from the ^{2}H-^{3}H fusion reaction (E $=$ 14 MeV): σ_{14}

No neutron spectra for high-yield nuclear devices including fission and fusion stages are published. So, for this case similarities to the known Hiroshima spectrum [White et al., 2005] are assumed, which shows its maximum neutron flux at energies of several hundred keV. Thus, the main fraction of neutrons would be in the energy range of fast neutrons. From the values in table 6.3 limits are estimated for the corresponding neutron fluences Ψ_{th}, Ψ_{epi}, Ψ_{fast}, and Ψ_{14} via this formula:

$$N_{rad} = N_{target} \cdot \sum_i \Psi_i \cdot \sigma_i \tag{6.2}$$

Here, N_{rad} denotes the number of radionuclides produced and N_{target} the number of available targets, both per unit sample size. Some of the energy regimes for the averaged cross sections overlap, but it nevertheless allows deriving some first estimation of the neutron fluence at this site.

The production of ^{10}Be from the ^{13}C(n,α)-reactions is solely sensitive to fast neutrons because it has an energy threshold at 4.1 MeV. Therefore, with this reaction an upper limit for the contribution of 14 MeV neutrons is estimated neglecting that possibly the ternary fission process may have contributed to the observed anthropogenic ^{10}Be. This results in an upper limit of Ψ_{14}=$4 \cdot 10^{13}$ cm^{-2}.

The ^{14}C produced on the targets ^{13}C and ^{17}O is only marginal. The main share of ^{14}C in the sample can be reconstructed assuming a ^{14}N concentration ([N]) in the range of 0.1% to 1%. Locally, corals exhibit [N] of this order, e.g. in the top tissue layer of natural corals

Table 6.3: Averaged cross section data for the relevant neutron reactions provided by the RUS-FOND2010 database.

		$^{40}Ca(n,\gamma)^{41}Ca$	$^{13}C(n,\gamma)^{14}C$	$^{17}O(n,\alpha)^{14}C$	$^{14}N(n,p)^{14}C$	$^{13}C(n,\alpha)^{10}Be$
σ_{th}	[b]	0.408	0.0014	0.235	1.831	0
σ_{epi}	[b]	0.206	$6 \cdot 10^{-4}$	0.106	0.824	0
σ_{fast}	[b]	0.0015	$5 \cdot 10^{-4}$	0.095	0.036	0.0020*
σ_{14}	[b]	$4 \cdot 10^{-4}$	$2 \cdot 10^{-5}$	0.262	0.045	0.075

* Because the threshold energy for the $^{13}C(n,\alpha)^{10}Be$ reaction is 4.1 MeV, this value is not considered in the estimations. It would lead to an overestimation of the produced ^{10}Be.

collected at Nusa Penida (Guam) [N] amounts to 500 ppm in the $CaCO_3$ skeleton and to 1.1% in the overlying coral polyp layer, which is biologically active and has a thickness of 12 mm [Marion et al., 2005].

Because of the high abundance of ^{40}Ca and the high cross section for $^{40}Ca(n,\gamma)^{41}Ca$, reactions creating ^{41}Ca on other targets are disregarded.

To calculate the neutron fluences at lower energies two scenarios are considered: The first is based on the known Hiroshima spectrum. From this spectrum one would infer that neutrons in the thermal range can be neglected, whereas those in the epithermal range (with the additional condition that their energy is lower than 1 keV) are only 1.3% as abundant as the fast neutrons. Using this condition and [N]=0.3%, the measured ^{41}Ca and ^{14}C ratios can be reproduced with values of $\Psi_{epi}=3.25 \cdot 10^{14}$ cm^{-2} and $\Psi_{fast}=2.5 \cdot 10^{16}$ cm^{-2}. In a second scenario it is assumed that the spectrum is already more thermalized when the neutrons interact with the coral. With 5% thermal neutrons and 5% epithermal neutrons, a neutron fluence of $\Psi_{th,epi,fast}=3.3 \cdot 10^{15}$ cm^{-2} and [N]=0.7% in the coral is required to reproduce the results for ^{14}C and ^{41}Ca.

The total number of neutrons necessary to account for the observed ^{41}Ca is very sensitive to the neutron spectrum, because the cross section in the thermal region is 270 times the averaged one in the range of fast neutrons. The ^{14}C production is not that sensitive to the neutron energy. The cross sections of $^{14}N(n,p)^{14}C$ are only a factor of 50 different for thermal and epithermal neutrons. Additionally, for this reaction the number of targets can be adjusted via [N] in this model, which further limits the informative value of the ^{14}C concentration. Still, these examples illustrate that the total number of neutrons and the neutron spectrum are very sensitive parameters in this model of coral irradiation.

Besides the previously presented Pu data, the high concentrations of ^{41}Ca and ^{14}C are clear indicators of high neutron fluences at the Bikini test site. Compared with the natural background, the concentration of ^{10}Be found in the crater is relatively low, which shows that production of ^{10}Be during nuclear bomb testing is only minor and confirms the lack of a ^{10}Be bomb peak observation in natural archives.

Chapter 7

Conclusion and outlook

Several technical and methodic developments helped to broaden the application range of AMS at low energies. Previously, at the Tandy facility measurements of ^{10}Be, ^{129}I, and Pu could be performed competitively compared to larger facilities, routine measurements at smaller systems were limited to ^{14}C. Some modifications of the Tandy system were undertaken. The main improvement was achieved by utilizing He as stripper gas instead of Ar. Charge state yields were enhanced by nearly a factor of three for actinides in the 3^+ state, by ca. 10% for Be^{1+} and by ca. 30% for Al^{2+}. Furthermore, the Be^{2+} yield at lower terminal voltages exhibits a second maximum with values reaching 35%. Future advancements of this setup may follow for ^{10}Be and ^{26}Al if a detection setup with a passive absorber preceding the GIC can be realized. So far, the application of a passive absorber in LE-AMS has been regarded as impossible, but in the case of ^{26}Al it was demonstrated that the detection of ^{26}Al^{2+} and the suppression of ^{13}C^{1+} via an absorber is the most efficient method to measure this isotope at the Tandy facility. In addition, also ^{10}Be-^{10}B separation was accomplished. However, intense ^{10}B beams entering the absorber volume can cause additional background via Rutherford scattering of protons in the SiN entrance window. The installation of an entrance foil containing less H may solve this problem.

Another focus of the technical development was set on the detection of actinides. Some dedicated experiments were necessary to identify the ^{236}U^{3+} background, which eventually turned out to be a combination of surviving 3^+ molecules and scattered ^{235}U^{3+} with the same p/q as ^{236}U^{3+}. The background due to surviving molecules can be eliminated by increasing the stripper areal density at the terminal. The remaining background cannot be fully suppressed but still the setup allows determining ^{236}U/^{238}U ratios greater than $4 \cdot 10^{-12}$, which is sufficient for most environmental samples.

The performance parameters of the current system for Be, Al, and actinides including the first tests of the absorber setup and the test setup for ^{236}U with the time-of-flight detector are summarized in table 7.1.

Besides the implementation of technical advancements, also several projects were started to prove the potential of this facility for a wide range of environmental applica-

Table 7.1: Performance parameters of the Tandy facility. The given detection efficiency (as defined in section 2.2) strongly relies on the tuning and so maximal observed values are presented.

isotope	negative current	terminal voltage	charge state	trans-mission	detection system	detection efficiency	blank level
^{10}Be	4 µA	525 kV	1$^+$	60%	deg/GIC	20%	$< 10^{-15}$
		300 kV	2$^+$	35%	deg/GIC	$\approx 20\%$	$\approx 10^{-15}$
		525 kV	2$^+$	23%	abs/GIC	60%	$\approx 10^{-14}$
^{26}Al	150 nA	480 kV	2$^+$	52%	abs/GIC	58%	$\lesssim 10^{-14}$
		500 kV	3$^+$	15%	GIC	90%	$\lesssim 10^{-14}$
^{236}U	100 nA	320 kV	3$^+$	35%	GIC	80%	$4 \cdot 10^{-12}$
					TOF	30%	$\lesssim 10^{-12}$
^{237}Np Pu	-	320 kV	3$^+$	$\approx 35\%$	GIC	80%	$\lesssim 0.3$ fg < 0.5 fg

tions. These applied projects benefitted a lot from the physical novelties: Only with the increased sensitivity and selectivity of the Tandy setup measurements of a large number of samples for ^{10}Be and actinides could be easily executed.

The carrier-free ^{10}Be/^{9}Be AMS technique was established by conducting comparison studies with the conventional method in samples from the Arctic Ocean and from fluvial terraces. The applied chemical processing works well and is reproducible for ocean sediments, provided that $CaCO_3$ is not the major part of the sample. Terrestrial samples are more problematic; particularly in $CaCO_3$-rich samples the reproducibility of the preparation has to be improved. However, in the terrestrial and the oceanic environment the dating of the sediment via the authigenic ^{10}Be/^{9}Be can give reasonable results. At five sites around the globe, marine drill cores were examined in order to extract a common ^{10}Be/^{9}Be signature of the Brunhes-Matuyama field reversal. Increased production of ^{10}Be during the pole-flip could be derived frome the distinct ^{10}Be/^{9}Be peaks detected at all sites. The North-Atlantic cores ODP 983 and 1063 with high sedimentation rates proved to be especially valuable for the comparison with ice core records or for the reconstruction of geomagnetic variations because of their detailed recording of past ^{10}Be/^{9}Be changes. It was demonstrated that the carrier-free ^{10}Be/^{9}Be determination is an alternative to conventional ^{10}Be measurements. It is especially attractive when other normalization techniques for the flux of ^{10}Be to the sediment fail, e.g. for old sediments.

The occurrence of actinides was investigated in water samples and in sediments. The processing of ocean water for U analysis started from 20 l samples, but this volume could

be continuously reduced to currently 3 l. However, if additionally Pu data should be generated, larger volumes (ca. 10 l) are still necessary because of the low abundance of Pu in ocean water. On the other hand, the first tests of a parallel extraction of both elements from the same sample were successful. This new method could reduce the overall amount of material required for actinide measurements. ^{236}U was probed in the North Sea and in the Atlantic Ocean. Input from the reprocessing plant in La Hague could be identified in the North Sea, whereas the Atlantic Ocean is still dominated by the global fallout. Downward transport of North Atlantic water masses can explain the high ^{236}U concentrations in 2500 m depth at equatorial latitudes. A currently active ^{236}U study on a larger number of samples provides a better local resolution of this area and strengthens this interpretation. These projects demonstrate that this nuclide is becoming a very interesting new tracer for oceanic water transport. In the coming years, its abundance in the various world oceans will be studied in several projects. The reduction of the required sample volume already achieved will help to establish this nuclide as an easily accessible tracer. The stability of the chemical procedure still has to be improved; with the measurement efficiency available at the Tandy and an optimal chemical yield even water samples of only 1 l should suffice. If an additional separation of Pu and Np in an efficient extraction from ocean water can be provided, the different environmental behaviour of these three actinide elements might turn out to be of further use. In any case, the quantification of the various input processes (global and local fallout, reprocessing plants, reactor accidents, natural sources) for ^{236}U and also for the other anthropogenic actinides requires more work.

The next aim concerning the technical progress of LE-AMS is to develop a facility with a terminal voltage of 300 kV that is capable of detecting ^{10}Be, ^{14}C, ^{26}Al, ^{129}I and actinides. The reduction of such a system's dimensions compared to the Tandy is not the major advantage, as the size of the magnets and the ESA is not reduced. So, despite the fact that the required terminal voltage is only half the maximum value available with the Tandy, the system would not be much more compact. It is rather the simplification of the accelerator stage employing a power supply for the generation of the terminal voltage instead of the pelletron system and the fact that SF_6 protective gas is no longer required that would raise the attractiveness of such a multi-isotope system also for non-physics laboratories.

Appendix A

Chemical methods

A.1   Processing of carrier-free ^{10}Be/^{9}Be samples

The procedure of leaching the authigenic Be from marine or fluvial sediment samples for carrier-free ^{10}Be/^{9}Be measurements is adapted from [Gutjahr et al., 2007], where it was developed for the extraction of trace metals such as Nd from authigenic Fe-Mn-oxyhydroxide coatings. About 1 g of sediment is first leached in 40 ml acetate buffer (pH 4.66) for 2 h to dissolve the carbonate fraction. After centrifugation and removal of the supernatant, the Be fraction is extracted from the sample in a second leaching: During another 2 h of shaking, the seawater-derived ferromanganese coatings are dissolved in 40 ml of 0.05 M* hydroxylamine-hydrochloride in 15% acetic acid, buffered to pH 4 with NaOH. After the second centrifugation, the supernatant is evaporated and processed further.

he sample is repeatedly redissolved and evaporated using HNO$_3$ and HCl to remove organic materials. Finally, it is dissolved in ca. 5 ml 6 M HCl. In this form the sample is loaded onto a column containing 2 ml resin 1x8 (100-200 mesh, manufactured by BioRad AG or Eichrom), where the Fe is separated. In the preparation of this step, the resin is first rinsed with 10 ml MilliQ water, cleaned with 10 ml 0.3 M HCl and conditioned with 6 ml 6 M HCl. When the sample is loaded onto the column, the Be fraction is collected immediately. Afterwards, the column is rinsed with another 5 ml 6 M HCl, which also is collected and combined with the Be fraction for further processing.

The material is then evaporated and redissolved in ca. 10 ml 0.4 M oxalic acid. This step may be critical if the sediment carried large amounts of CaCO$_3$, because Ca will precipitate as Calciumoxalate and this removes oxalic acid from the solution and lowers its molarity. Thus, the consistency of the solution would not be well defined when being loaded onto the next column. Therefore, in such a case after a centrifugation the supernatant is

---

*The molarity M denominates the amount of constituent per volume: 1 M = 1 mol/l

again evaporated and redissolved in 5-15 ml oxalic acid. Otherwise the original solution is processed.

The next purification step is carried out on 1 ml columns of BioRad AG50x8 (200-400 mesh) [von Blanckenburg et al., 1996a]. The resin is cleaned with 6 ml 5 M HNO$_3$ and rinsed with 8 ml MilliQ water. Further, the resin is conditioned with 8 ml 0.4 M oxalic acid. The sample is loaded in a volume of 5-15 ml of the same solution. 15 ml of this solution is used to wash the sample down and to remove cations such as Fe, Al and Ti. After rinsing with MilliQ water, 6 ml of 0.5 M HNO$_3$ is used to elute Na. Finally, the Be fraction is collected in 12 ml 1 M HNO$_3$.

This step is followed by a coprecipitation with 0.5-1 mg Fe, which is cleaned in advance using a BioRad AG1x8 column to avoid any introduction of ^{9}Be in this step. The sample is dried at 80°C and afterwards oxidized at 650°C in a crucible for 1-2 h. After mixing with ca. 4 mg Nb powder (325 mesh) the material is pressed into an aceton cleaned Ti cathode.

For the treatment of sediment samples the hydroxylammonium chloride, acetic acid and sodium hydroxide have pro analysi purity, all other chemicals are used at suprapure level.

1g sediment

A) carbonate removal
leach with 40 ml acetic buffer solution (pH4.6)
centrifuge & decant supernatant

process
residual

B) authigenic fraction
leach with 45 ml HH in 15% acetic ac. (pH4)
centrifuge & transfer supernatant

discharge supernatant

dry on hotplate
convert into chloride form
redissolve in 5ml 6 M HCl

C) column I: Fe separation

4) load sample

3) 10 ml 6M HCl conditioning
2) 10 ml 0.3M HCl cleaning
1) 10 ml MQ water rinsing

5) elute with 5 ml 6M HCL

2ml resin: Biorad AG or Eichrom: 1x8 (100-200 mesh)

collect fractions 4 + 5

D) Ca removal
dry on hotplate
redissolve in 5-15 ml 0.4M oxalic acid
centrifuge & transfer supernatant

E) column II: Al separation

4) load sample

3) 8 ml 0.4 M ox. ac. conditioning
2) 8 ml MQ water rinsing
1) 6ml 5M HNO_3 cleaning

5) rinse with 15 ml 0.4M ox. ac.
6) rinse with 6 ml 0.5M HNO_3
7) elute with 12 ml 1M HNO_3

1ml resin: Biorad AG: 50x8 (200-400 mesh)

collect fraction 7

F) target preparation
Fe coprecipitation (0.5-1mg Fe, NH_4OH, pH10)
decant supernatant
wash with pH8 MQ water, decant supernatant
dry at 80°C (in centrifuge tube or transfer to quartz crucible)
oxidize at 650°C in quartz
mix with 4 mg Nb (325 mesh)
press into Ti cathode holder

A.2 Chemical separation of U and Pu from environmental samples

A description of the parallel chemical extraction of U and Pu from water samples is given in Diebold [2012]. The procedure is set together by coprecipitations of the actinides with $Fe(OH)_2$ to reduce the sample volume and following purification and separation of the elements using UTEVA resin. This is a resin especially designed for separation of actinides and its main features are described in Horwitz et al. [1992]. The utilized chemicals are at suprapure level in order not to introduce the desired radioisotopes during the chemical procedure. The important steps are described below:

The amount of sample has to be specified, which is usually done gravimetrically. If the sample is to be stored, it is acidified with HNO_3 to prevent adhesion of the desired nuclides to the container walls. The preparation starts with the addition of the spike material, ^{233}U and/or ^{242}Pu. Adding a known amount of these isotopes and later counting them in a sequence with ^{236}U or the other Pu isotopes allows quantifying the overall yield of chemical preparation and AMS measurement and the concentration of the radionuclides in the original sample volume. The amount of the added spike should be large enough that only little measurement time has to be employed in order to achieve good counting statistics. On the other hand, spikes may not be totally clean and may even carry a fraction of the desired isotopes of the order of 10^{-3}, e.g. the ^{240}Pu contamination in the standard dilution series presented in Fig. 4.9. Thus, the amount of ^{233}U and/or ^{242}Pu spike has to be adjusted so that neither is the uncertainty of the determination significantly increased due to insufficient statistics nor are low samples contaminated with the isotopes of interest. Of course, the added spike nuclides must not be present in the initial sample. Neither ^{233}U nor ^{242}Pu have been emitted in major amounts by anthropogenic activities and thus are appropriate spike isotopes. Few (typically five) pg of the spike nuclide are sufficent. The spike solution has a known concentration (^{233}U: (91.26 ± 0.14) pg/g; ^{242}Pu: (96.0 ± 2.4) pg/g) and the amount of spike added is determined gravimetrically on a scales with sub-mg precision. A fully-processed blank is prepared in parallel to the samples in order to monitor contaminations employing the same amount of spike and Fe solution as for the samples.

Spike and sample are mixed by stirring the solution with a glass rod. Afterwards, the sample is left for ca. 2 h in which spike and sample can equilibrate. This is critical as the existence of spike and desired isotopes in different valence states would impair the further preparation. Depending on the sample volume 300-500 mg Fe dissolved in HNO_3 is added and mixed with the sample. The Fe solution is self-prepared by dissolving Fe in HNO_3 and cleaning it on a UTEVA column in the same way as described below for the separation of U. Increasing the pH above 8 by adding ammonia solution causes $Fe(OH)_2$ to precipitate in macromolecules, which also carry the desired U and Pu. The supernatant is discarded.

This step is repeated until a precipitate volume of 250 ml is reached. Then the sample is centrifuged and the centrifugate is redissolved in aqua regia, dried again and dissolved in 20 ml 5 M HNO_3. This step destroys organic material and prepares the sample for the following step on the column. The column is filled with 2 ml UTEVA resin which is cleaned using MilliQ water and 5 M HNO_3 prior to the purification of the sample. Tests were performed employing volumes of 1 ml and 2 ml resin, but no significant differences were observed. The sample solution is loaded onto the column and U(VI) and Pu(IV) are retained at this molarity of HNO_3. A washing step with 6 ml 3 M HNO_3 removes the traces of Fe and matrix elements still present on the column. Subsequently, a reduction step is required to selectively extract Pu and leave U on the column. 4 ml of 0.2 M oxalic acid in 2 M HNO_3 are used to coordinate Pu, which is washed out and collected [Goodall and Lythgoe, 1999]. In this step, also Np is cleared from the resin and it thus serves as a suppression of the potentially present isobar [236]Np. Finally, 32 ml 0.5 M HCl is poured over the resin and the eluant containing the U fraction is collected. The available U and Pu solutions are very clear. 0.5 mg to 1 mg Fe are added from the previously used Fe solution and a final precipitation is carried out. The material is washed with pH 8 water in order to remove acid and major amounts of ammonia still present in the precipitate. The Fe containing U or Pu is transferred into a quartz crucible and dried on a hotplate. The sample is finally oxidized at 650° for 2 h. The material is mixed with Nb powder and pressed into a Ti cathode.

Unfortunately, even in large scale preparation series of similar samples so far the overall yield has been unstable and ranged from $1 \cdot 10^{-5}$ to $1 \cdot 10^{-4}$. Varying behaviour of the samples was mainly observed during the column purification step; the flow times fluctuated especially strongly. It still has to be settled if this is sample or resin related.

water sample + spikes (^{233}U, ^{242}Pu, each ca. 5 pg)

A) Fe coprecipitation
acidify sample with HNO_3 (pH<4)
add 0.3-0.5g Fe and let equilibrate for some hours

add NH_4OH until pH10 is reached
wait for $Fe(OH)_3$ to precipitate
discard supernatant and collect precipitate
continue processing in smaller volume

volume > 250 ml

redissolve with HNO_3

volume < 250 ml

centrifuge, discard supernatant
redissolve precipitate in Aqua Regia & dry on hot plate
convert into nitric form & dry on hot plate
redissolve in 20 ml 5 M HNO_3

B) column UTEVA: Fe separation

3) load sample

2) 20 ml 5 M HNO_3 conditioning
1) 20 ml MQ water rinsing

4) rinse with 6 ml 3 M HNO_3
5) elute Pu & Np with 4 ml 0.2 M ox. ac. in 2M HNO_3
6) elute U with 32 ml 0.5 M HCl

2ml resin: UTEVA (100-150µm)

collect fraction 5 for Pu   collect fraction 6 for U

C) target preparation
Fe coprecipitation (1 mg Fe, NH_4OH, pH10)
decant supernatant
wash with pH8 MQ water, decant supernatant
dry at 80°C (in centrifuge tube or transfer to quartz crucible)
oxidize at 650°C in quartz
mix with 3 mg Nb (325 mesh)
press into cathode holder

References

Adler, R. E., Polyak, L., Ortiz, J. D., Kaufman, D. S., Channell, J. E. T., Xuan, C., Grottoli, A. G., Sellén, E., and Crawford, K. A. (2009). Sediment record from the western Arctic Ocean with an improved Late Quaternary age resolution: HOTRAX core HLY0503-8JPC, Mendeleev Ridge. *Global Planet. Change*, 68(1-2):18–29.

Alfimov, V. and Synal, H.-A. (2010). ^{129}I AMS at 0.5 MV tandem accelerator. *Nucl. Instrum. Meth. B*, 268(7-8):769–772.

Anders, E. and Grevesse, N. (1989). Abundances of the elements: Meteoritic and solar. *Geochim. Cosmochim. Ac.*, 53(1):197–214.

Anderson, E. C. and Libby, W. F. (1951). World-Wide Distribution of Natural Radiocarbon. *Phys. Rev.*, 81:64–69.

Anderson, R. F., Lao, Y., Broecker, W. S., Trumbore, S. E., Hofmann, H. J., and Wolfli, W. (1990). Boundary scavenging in the Pacific Ocean: a comparison of ^{10}Be and ^{231}Pa. *Earth Planet. Sc. Lett.*, 96(3-4):287–304.

Anthony, J. M., Beavers, R. L., Bennett, T. J., Matteson, S., Marble, D. K., Weathers, D. L., McDaniel, F. D., and Duggan, J. L. (1991). Materials characterization using accelerator mass spectrometry. *Nucl. Instrum. Meth. B*, 56-57(Part 2):873–876.

Arazi, A., Faestermann, T., Fernández Niello, J. O., Frischke, D., Knie, K., Korschinek, G., Maier, H. J., Richter, E., Rugel, G., and Wallner, A. (2004). Magnesium suppression for ^{26}Al measurements using AlO$^-$ ions. *Nucl. Instrum. Meth. B*, 223-224:259–262.

Arnold, J. R. (1956). Beryllium-10 Produced by Cosmic Rays. *Science*, 124(3222):584–585.

Auer, M., Kutschera, W., Priller, A., Wagenbach, D., Wallner, A., and Wild, E. (2007). Measurement of ^{26}Al for atmospheric and climate research and the potential of ^{26}Al/^{10}Be ratios. *Nucl. Instrum. Meth. B*, 259(1):595–599.

Bach, G. G. and Livesey, D. J. (1955). The cross section for the reaction B-10(P,A)Be-7 at proton energies below 200-KeV. *Philos. Mag.*, 46:824.

Backman, J., Jakobsson, M., Frank, M., Sangiorgi, F., Brinkhuis, H., Stickley, C., O'Regan, M., Løvlie, R., Pälike, H., Spofforth, D., Gattacecca, J., Moran, K., King, J., and Heil, C. (2009). Age model and core-seismic integration for the Cenozoic Arctic Coring Expedition sediments from the Lomonosov Ridge. *Paleoceanography*, 23:PA1S03.

Bada, J. L. and Schroeder, R. A. (1975). Amino acid racemization reactions and their geochemical implications. *Naturwissenschaften*, 62:71–79.

Balderer, W. and Synal, H.-A. (2004). Tracing groundwater from uranium rich environments by ^{36}Cl isotope method: possibilities for natural analogue studies. *Nucl. Instrum. Meth. B*, 223-224:471–478.

Bassinot, F. C., Labeyrie, L. D., Vincent, E., Quidelleur, X., Shackleton, N. J., and Lancelot, Y. (1994). The astronomical theory of climate and the age of the Brunhes-Matuyama magnetic reversal. *Earth Planet. Sc. Lett.*, 126(1-3):91–108.

Baumgartner, S., Beer, J., Masarik, J., Wagner, G., Meynadier, L., and Synal, H.-A. (1998). Geomagnetic Modulation of the ^{36}Cl Flux in the GRIP Ice Core, Greenland. *Science*, 279(5355):1330–1332.

Baumgartner, S., Beer, J., Suter, M., Dittrich-Hannen, B., Synal, H.-A., Kubik, P. W., Hammer, C., and Johnsen, S. (1997). Chlorine-36 fallout in the Summit Greenland Ice Core Project ice core. *J. Geophys. Res.*, 102(C12):26,659–26,662.

Beasley, T. M., Kelley, J. M., Maiti, T. C., and Bond, L. A. (1998a). ^{237}Np/^{239}Pu atom ratios in integrated global fallout: a reassessment of the production of ^{237}Np. *J. Environ. Radioactiv.*, 38(2):133–146.

Beasley, T. M., Kelley, J. M., Orlandini, K. A., Bond, L. A., Aarkrog, A., Trapeznikov, A. P., and Pozolotina, V. N. (1998b). Isotopic Pu, U, and Np Signatures in Soils from Semipalatinsk-21, Kazakh Republic and the Southern Urals, Russia. *J. Environ. Radioactiv.*, 39(2):215–230.

Beck, J. W., Richards, D. A., Edwards, R. L., Silverman, B. W., Smart, P. L., Donahue, D. J., Hererra-Osterheld, S., Burr, G. S., Calsoyas, L., Jull, A. J. T., and Biddulph, D. (2001). Extremely Large Variations of Atmospheric ^{14}C Concentration During the Last Glacial Period. *Science*, 292(5526):2453–2458.

Beer, J., Andrée, M., Oeschger, H., Stauffer, B., Balzer, R., Bonani, G., Stoller, C., Suter, M., Wölfli, W., and Finkel, R. C. (1985). Greenland ice core: geophysics, geochemistry, and the environment. In Langway, C. C., Oeschger, H., and Dansgaard, W., editors, *Greenland ice core: geophysics, geochemistry, and the environment*, pages 66–70. American Geophysical Union, Washington, D.C.

Beer, J., Blinov, A., Bonani, G., Finkel, R. C., Hofmann, H. J., Lehmann, B., Oeschger, H., Sigg, A., Schwander, J., Staffelbach, T., Stauffer, B., Suter, M., and Wölfli, W. (1990). Use of ^{10}Be in polar ice to trace the 11-year cycle of solar activity. *Nature*, 347:164–166.

Beer, J., Siegenthaler, U., Bonani, G., Finkel, R. C., Oeschger, H., Suter, M., and Wölfli, W. (1988). Information on past solar activity and geomagnetism from ^{10}Be in the Camp Century ice core. *Nature*, 331:675–679.

Bennett, C. L., Beukens, R. P., Clover, M. R., Elmore, D., Gove, H. E., Kilius, L., Litherland, A. E., and Purser, K. H. (1978). Radiocarbon Dating with Electrostatic Accelerators: Dating of Milligram Samples. *Science*, 201(4353):345–347.

Bennett, C. L., Beukens, R. P., Clover, M. R., Gove, H. E., Liebert, R. B., Litherland, A. E., Purser, K. H., and Sondheim, W. E. (1977). Radiocarbon Dating Using Electrostatic Accelerators: Negative Ions Provide the Key. *Science*, 198(4316):508–510.

Berkovits, D., Feldstein, H., Ghelberg, S., Hershkowitz, A., Navon, E., and Paul, M. (2000). ^{236}U in uranium minerals and standards. *Nucl. Instrum. Meth. B*, 172(1-4):372–376.

Bisinger, T., Hippler, S., Michel, R., Wacker, L., and Synal, H.-A. (2010). Determination of plutonium from different sources in environmental samples using alpha-spectrometry and AMS. *Nucl. Instrum. Meth. B*, 268(7-8):1269–1272.

Boulyga, S. F. (2011). Mass spectrometric analysis of long-lived radionuclides in bio-assays. *Int. J. Mass Spectrom.*, 307(1-3):200–210.

Boulyga, S. F. and Becker, J. S. (2002). Isotopic analysis of uranium and plutonium using ICP-MS and estimation of burn-up of spent uranium in contaminated environmental samples. *J. Anal. At. Spectrom.*, 17:1143–1147.

Bourlès, D., Raisbeck, G. M., and Yiou, F. (1989). ^{10}Be and ^{9}Be in marine sediments and their potential for dating. *Geochim. Cosmochim. Ac.*, 53(2):443–452.

Bourlès, D. L., Brown, E. T., German, C. R., Measures, C. I., Edmond, J. M., Raisbeck, G. M., and Yiou, F. (1994). Examination of hydrothermal influences on oceanic beryllium using fluids, plume particles and sediments from the TAG hydrothermal field. *Earth Planet. Sc. Lett.*, 122(1-2):143–157.

Brown, E. T., Edmond, J. M., Raisbeck, G. M., Bourlès, D. L., Yiou, F., and Measures, C. I. (1992a). Beryllium isotope geochemistry in tropical river basins. *Geochim. Cosmochim. Ac.*, 56(4):1607–1624.

Brown, E. T., Measures, C. I., Edmond, J. M., Bourlès, D. L., Raisbeck, G. M., and Yiou, F. (1992b). Continental inputs of beryllium to the oceans. *Earth Planet. Sc. Lett.*, 114(1):101–111.

Brown, T. A., Marchetti, A. A., Martinelli, R. E., Cox, C. C., Knezovich, J. P., and Hamilton, T. F. (2004). Actinide measurements by accelerator mass spectrometry at Lawrence Livermore National Laboratory. *Nucl. Instrum. Meth. B*, 223-224:788–795.

Buesseler, K. O. (1997). The Isotopic Signature of Fallout Plutonium in the North Pacific. *J. Environ. Rad.*, 36(1):69–83.

Burcham, W. E. and Freeman, J. M. (1950). The emission of short-range alpha particles from light elements under proton bombardment. II. Further observations on the reaction ^{10}B(p,α)^{7}Be. *Philos. Mag.*, 41:337.

Carcaillet, J., Bourlès, D. L., Thouveny, N., and Arnold, M. (2004). A high resolution authigenic ^{10}Be/^{9}Be record of geomagnetic moment variations over the last 300 ka from sedimentary cores of the Portuguese margin. *Earth Planet. Sc. Lett.*, 219(3-4):397–412.

Carcaillet, J. T., Thouveny, N., and Bourlès, D. L. (2003). Geomagnetic moment instability between 0.6 and 1.3 Ma from cosmonuclide evidence. *Geophys. Res. Lett.*, 30(15):1792.

Chamizo, E., Enamorado, S. M., García-León, M., Suter, M., and Wacker, L. (2008). Plutonium measurements on the 1 MV AMS system at the Centro Nacional de Aceleradores (CNA). *Nucl. Instrum. Meth. B*, 266(22):4948–4954.

Chamizo, E., García-León, M., Synal, H.-A., Suter, M., and Wacker, L. (2006). Determination of the ^{240}Pu/^{239}Pu atomic ratio in soils from Palomares (Spain) by low-energy accelerator mass spectrometry. *Nucl. Instrum. Meth. B*, 249(1-2):768–771.

Channell, J. E. T., Curtis, J. H., and Flower, B. P. (2004). The Matuyama-Brunhes boundary interval (500-900 ka) in North Atlantic drift sediments. *Geophys. J. Int.*, 158:489–505.

Channell, J. E. T., Hodell, D. A., and Curtis, J. H. (2012). ODP Site 1063 (Bermuda Rise) revisited: Oxygen isotopes, excursions and paleointensity in the Brunhes Chron. *Geochem. Geophys. Geosyst.*, 13:Q02001.

Channell, J. E. T., Hodell, D. A., Singer, B. S., and Xuan, C. (2010). Reconciling astrochronological and ^{40}Ar/^{39}Ar ages for the Matuyama-Brunhes boundary and late Matuyama Chron. *Geochem. Geophys. Geosyst.*, 11:Q0AA12.

Channell, J. E. T. and Kleiven, H. F. (2000). Geomagnetic palaeointensities and astrochronological ages for the Matuyama-Brunhes boundary and the boundaries of the Jaramillo Subchron: palaeomagnetic and oxygen isotope records from ODP Site 983. *Phil. Trans. R. Soc. Lond. A*, 358:1027–1047.

Channell, J. E. T. and Lehman, B. (1998). Magnetic Stratigraphy of North Atlantic Sites 980-984. In Raymo, M. E., Jansen, E., and D., H. T., editors, *Proc. ODP, Sci. Results, 162*, pages 113–130. College Station, TX (Ocean Drilling Program).

Chase, Z., Anderson, R. F., Fleisher, M. Q., and Kubik, P. W. (2003). Scavenging of ^{230}Th, ^{231}Pa and ^{10}Be in the Southern Ocean (SW Pacific sector): the importance of particle flux, particle composition and advection. *Deep Sea Research Part II: Topical Studies in Oceanography*, 50(3-4):739–768.

Chiappini, R., Pointurier, F., Millies-Lacroix, J., Lepetit, G., and Hemet, P. (1999). ^{240}Pu/^{239}Pu isotopic ratios and $^{239+240}$Pu total measurements in surface and deep waters around Mururoa and Fangataufa atolls compared with Rangiroa atoll (French Polynesia). *Sci. Total Environ.*, 237-238:269–276.

Chiappini, R., Taillade, J.-M., and Brébion, S. (1996). Development of a high-sensitivity inductively coupled plasma mass spectrometer for actinide measurement in the femtogram range. *J. Anal. At. Spectrom.*, 11:497–503.

Child, D. P., Hotchkis, M. A. C., Whittle, K., and Zorko, B. (2010). Ionisation efficiency improvements for AMS measurement of actinides. *Nucl. Instrum. Meth. B*, 268(7-8):820–823.

Chmeleff, J., von Blanckenburg, F., Kossert, K., and Jakob, D. (2010). Determination of the ^{10}Be half-life by multicollector ICP-MS and liquid scintillation counting. *Nucl. Instrum. Meth. B*, 268(2):192–199.

Christl, M. (2007). Sensitivity and response of beryllium-10 in marine sediments to rapid production changes (geomagnetic events): A box model study. *Geochem. Geophys. Geosyst.*, 8:Q09015.

Christl, M. and Kubik, P. W. (2013). New Be-cathode preparation method for the ETH 6 MV Tandem. *Nucl. Instrum. Meth. B*, 294:199–202.

Christl, M., Lachner, J., Vockenhuber, C., Goroncy, I., Herrmann, J., and Synal, H.-A. (2013a). First data of Uranium-236 in the North Sea. *Nucl. Instrum. Meth. B*, 294:530–536.

Christl, M., Lippold, J., Hofmann, A., Wacker, L., Lahaye, Y., and Synal, H.-A. (2010a). ^{231}Pa/^{230}Th: A proxy for upwelling off the coast of West Africa. *Nucl. Instrum. Meth. B*, 268(7-8):1159–1162.

Christl, M., Lippold, J., Steinhilber, F., Bernsdorff, F., and Mangini, A. (2010b). Reconstruction of global ^{10}Be production over the past 250 ka from highly accumulating Atlantic drift sediments. *Quaternary Sci. Rev.*, 29(19-20):2663–2672.

Christl, M., Maden, C., Kubik, P. W., Müller, A. M., Ivy-Ochs, S., Suter, M., and Synal, H.-A. (2010c). Carrier-free measurements of natural ^{10}Be/^{9}Be ratios at low energies. *Nucl. Instrum. Meth. B*, 268(7-8):726–729.

Christl, M., Mangini, A., and Kubik, P. (2007a). Highly resolved Beryllium-10 record from ODP Site 1089 - A global signal? *Earth Planet. Sc. Lett.*, 257(1-2):245–258.

Christl, M., Vockenhuber, C., Kubik, P. W., Wacker, L., Lachner, J., Alfimov, V., and Synal, H.-A. (2013b). The ETH Zurich AMS facilities: Performance parameters and reference materials. *Nucl. Instrum. Meth. B*, 294:29–38.

Christl, M., Wacker, L., Lippold, J., Synal, H.-A., and Suter, M. (2007b). Protactinium-231: A new radionuclide for AMS. *Nucl. Instrum. Meth. B*, 262(2):379–384.

Clement, B. M. (2004). Dependence of the duration of geomagnetic polarity reversals on site latitude. *Nature*, 428:637–640.

Cook, G. T., MacKenzie, A. B., McDonald, P., and Jones, S. R. (1997). Remobilization of Sellafield-derived radionuclides and transport from the north-east Irish Sea. *J. Environ. Radioactiv.*, 35(3):227–241.

Dai, X., Christl, M., Kramer-Tremblay, S., and Synal, H.-A. (2012). Ultra-trace determination of plutonium in urine samples using a compact accelerator mass spectrometry system operating at 300 kV. *J. Anal. At. Spectrom.*, 27:126–130.

Darby, D. A., Jakobsson, M., and Polyak, L. (2005). Icebreaker expedition collects key Arctic seafloor and ice data. *Eos transactions, AGU*, 82(52):549–556.

De Cesare, M., Fifield, L. K., Sabbarese, C., Tims, S. G., De Cesare, N., D'Onofrio, A., D'Arco, A., Esposito, A. M., Petraglia, A., Roca, V., and Terrasi, F. (2013). Actinides AMS at CIRCE and ^{236}U and Pu measurements of structural and environmental samples from in and around a mothballed nuclear power plant. *Nucl. Instrum. Meth. B*, 294:152–159.

Diamond, H., Fields, P. R., Stevens, C. S., Studier, M. H., Fried, S. M., Inghram, M. G., Hess, D. C., Pyle, G. L., Mech, J. F., Manning, W. M., Ghiorso, A., Thompson, S. G., Higgins, G. H., Seaborg, G. T., Browne, C. I., Smith, H. L., and Spence, R. W. (1960). Heavy Isotope Abundances in Mike Thermonuclear Device. *Phys. Rev.*, 119:2000–2004.

Diebold, A. (2012). Measurement of Uranium and Plutonium in Seawater Samples by AMS. Term paper, ETH Zürich.

Dreyfus, G. B., Raisbeck, G. M., Parrenin, F., Jouzel, J., Guyodo, Y., Nomade, S., and Mazaud, A. (2008). An ice core perspective on the age of the Matuyama-Brunhes boundary. *Earth Planet. Sc. Lett.*, 274(1-2):151–156.

Dunk, R. M., Mills, R. A., and Jenkins, W. J. (2002). A reevaluation of the oceanic uranium budget for the Holocene. *Chem. Geol.*, 190(1-4):45–67.

Elmore, D., Fulton, B. R., Clover, M. R., Marsden, J. R., Gove, H. E., Naylor, H., Purser, K. H., Kilius, L. R., Beukens, R. P., and Litherland, A. E. (1979). Analysis of ^{36}Cl in environmental water samples using an electrostatic accelerator. *Nature*, 277:22–25.

Elmore, D., Gove, H. E., Ferraro, R., Kilius, L. R., Lee, H. W., Chang, K. H., Beukens, R. P., Litherland, A. E., Russo, C. J., Purser, K. H., Murrell, M. T., and Finkel, R. C. (1980). Determination of ^{129}I using tandem accelerator mass spectrometry. *Nature*, 286:138–140.

Elsasser, W., Ney, E. P., and Winckler, J. R. (1956). Cosmic-ray intensity and geomagnetism. *Nature*, 178:1226–1227.

Elsasser, W. M. (1946). Induction Effects in Terrestrial Magnetism Part I. Theory. *Phys. Rev.*, 69:106–116.

Fabryka-Martin, J. T. (1988). *Production of radionuclides in the earth and their hydrogeologic significance, with emphasis on chlorine-36 and iodine-129*. PhD thesis, University of Arizona.

Feldman, G. J. and Cousins, R. D. (1998). Unified approach to the classical statistical analysis of small signals. *Phys. Rev. D*, 57:3873–3889.

Ferretti, P., Shackleton, N. J., Rio, D., and Hall, M. A. (2005). Early-Middle Pleistocene deep circulation in the western subtropical Atlantic: southern hemisphere modulation of the North Atlantic Ocean. In Head, M. and Gibbard, P., editors, *Early-Middle Pleistocene Transitions: The Land-Ocean Evidence*, volume 247, pages 131–145. Geological Society, London, Special Publications.

Field, C. V., Schmidt, G. A., Koch, D., and Salyk, C. (2006). Modeling production and climate-related impacts on ^{10}Be concentration in ice cores. *J. Geophys. Res.*, 111:D15107.

Fifield, L. K., Clacher, A. P., Morris, K., King, S. J., Cresswell, R. G., Day, J. P., and Livens, F. R. (1997). Accelerator mass spectrometry of the planetary elements. *Nucl. Instrum. Meth. B*, 123(1-4):400–404.

Fifield, L. K., Cresswell, R. G., di Tada, M. L., Ophel, T. R., Day, J. P., Clacher, A. P., King, S. J., and Priest, N. D. (1996). Accelerator mass spectrometry of plutonium isotopes. *Nucl. Instrum. Meth. B*, 117(3):295–303.

Fifield, L. K., Synal, H.-A., and Suter, M. (2004). Accelerator mass spectrometry of plutonium at 300 kV. *Nucl. Instrum. Meth. B*, 223-224:802–806.

Fifield, L. K., Tims, S. G., Fujioka, T., Hoo, W. T., and Everett, S. E. (2010). Accelerator mass spectrometry with the 14UD accelerator at the Australian National University. *Nucl. Instrum. Meth. B*, 268(7-8):858–862.

Fifield, L. K., Tims, S. G., Gladkis, L. G., and Morton, C. R. (2007). ^{26}Al measurements with ^{10}Be counting statistics. *Nucl. Instrum. Meth. B*, 259(1):178–183.

Fifield, L. K., Tims, S. G., Stone, J. O., Argento, D. C., and De Cesare, M. (2013). Ultra-sensitive measurements of ^{36}Cl and ^{236}U at the Australian National University. *Nucl. Instrum. Meth. B*, 294:126–131.

Fink, D., Klein, J., Middleton, R., Vogt, S., and Herzog, G. F. (1991). ^{41}Ca in iron falls, Grant and Estherville: production rates and related exposure age calculations. *Earth Planet. Sc. Lett.*, 107(1):115–128.

Fink, D., Meirav, O., Paul, M., Ernst, H., Henning, W., Kutschera, W., Kaim, R., Kaufman, A., and Magaritz, M. (1984). Accelerator mass spectrometry at the rehovot pelletron tandem: Measurements of abundances of cosmogenic radioisotopes and future prospects. *Nucl. Instrum. Meth. B*, 5(2):123–128.

Francois, R., Frank, M., Rutgers van der Loeff, M. M., and Bacon, M. P. (2004). ^{230}Th normalization: An essential tool for interpreting sedimentary fluxes during the late Quaternary. *Paleoceanography*, 19:PA1018.

Frank, M., Backman, J., Jakobsson, M., Moran, K., O'Regan, M., King, J., Haley, B. A., Kubik, P. W., and Garbe-Schönberg, D. (2008). Beryllium isotopes in central Arctic Ocean sediments over the past 12.3 million years: Stratigraphic and paleoclimatic implications. *Paleoceanography*, 23:PA1S02.

Frank, M., Porcelli, D., Andersson, P., Baskaran, M., Björk, G., Kubik, P. W., Hattendorf, B., and Günther, D. (2009). The dissolved Beryllium isotope composition of the Arctic Ocean. *Geochim. Cosmochim. Ac.*, 73(20):6114–6133.

Frank, M., Schwarz, B., Baumann, S., Kubik, P. W., Suter, M., and Mangini, A. (1997). A 200 kyr record of cosmogenic radionuclide production rate and geomagnetic field intensity from ^{10}Be in globally stacked deep-sea sediments. *Earth Planet. Sc. Lett.*, 149:121–129.

Franzreb, K., Hrušák, J., Alikhani, M. E., Lörinčík, J., R. C. Sobers, J., and Williams, P. (2004). Gas-phase diatomic trications of Se_2^{3+}, Te_2^{3+}, and LaF^{3+}. *J. Chem. Phys.*, 121(24):12293–12302.

Glatzmaier, G. A., Coe, R. S., Hongre, L., and Roberts, P. H. (1999). The role of the Earth's mantle in controlling the frequency of geomagnetic reversals. *Nature*, 401:885–890.

Godwin, H. (1962). Half-life of radiocarbon. *Nature*, 195:984.

Goel, P. S., Kharkar, D. P., Lal, D., Narsappaya, N., Peters, B., and Yatirajam, V. (1957). The beryllium-10 concentration in deep-sea sediments. *Deep Sea Research (1953)*, 4:202–210.

Goodall, P. and Lythgoe, C. (1999). Rapid separation of uranium and plutonium by extraction chromatography for determination by thermal ionisation mass spectrometry. *Analyst*, 124:263–269.

Grajcar, M. (2005). *New concepts of ^{10}Be Accelerator Mass Spectrometry at low energies*. PhD thesis, ETH Zürich. Diss. ETH Nr. 16249.

Grajcar, M., Döbeli, M., Kubik, P. W., Maden, C., Suter, M., and Synal, H.-A. (2004). ^{10}Be measurements with terminal voltages below 1 MV. *Nucl. Instrum. Meth. B*, 223-224:190–194.

Grajcar, M., Döbeli, M., Kubik, P. W., Synal, H.-A., Wacker, L., and Suter, M. (2007). New concepts of ^{10}Be AMS at low energies. *Nucl. Instrum. Meth. B*, 259(1):173–177.

Granger, D. E. and Muzikar, P. F. (2001). Dating sediment burial with in situ-produced cosmogenic nuclides: theory, techniques, and limitations. *Earth Planet. Sc. Lett.*, 188(1-2):269–281.

Grützner, J., Giosan, L., Franz, S. O., Tiedemann, R., Cortijo, E., Chaisson, W. P., Flood, R. D., Hagen, S., Keigwin, L. D., Poli, S., Rio, D., and Williams, T. (2002). Astronomical age models for Pleistocene drift sediments from the western North Atlantic (ODP Sites 1055-1063). *Mar. Geol.*, 189(1-2):5–23.

Gutjahr, M., Frank, M., Stirling, C. H., Klemm, V., van de Flierdt, T., and Halliday, A. N. (2007). Reliable extraction of a deepwater trace metal isotope signal from Fe-Mn oxyhydroxide coatings of marine sediments. *Chem. Geol.*, 242(3-4):351–370.

Guyodo, Y., Richter, C., and Valet, J.-P. (1999). Paleointensity record from Pleistocene sediments (1.4-0 Ma) off the California Margin. *J. Geophys. Res.*, 104(B10):22953–22964.

Hardy, E. P., Krey, P. W., and Volchok, H. L. (1973). Global Inventory and Distribution of Fallout Plutonium. *Nature*, 141:444–445.

Harley, J. H. (1980). Plutonium in the environment - a review. *J. Radiat. Res.*, 21(1):83–104.

Hawthorne, H. A. (1979). *Compilation of local fallout data from test detonations 1945-1962 extracted from DASA 1251, Volume II - Oceanic U.S. tests*.

Heikkilä, U. (2007). *Modeling of the atmospheric transport of the cosmogenic radionuclides ^{10}Be and ^{7}Be using the ECHAM5-HAM General Circulation Model*. PhD thesis, ETH Zürich. Diss. ETH. Nr. 17516.

Henken-Mellies, W. U., Beer, J., Heller, F., Hsü, K. J., Shen, C., Bonani, G., Hofmann, H. J., Suter, M., and Wölfli, W. (1990). ^{10}Be and ^{9}Be in South Atlantic DSDP Site 519: Relation to geomagnetic reversals and to sediment composition. *Earth Planet. Sc. Lett.*, 98(3-4):267–276.

Herrmann, J. (2010). personal communication.

Hevesy, G. V. and Paneth, F. (1913). Die Löslichkeit des Bleisulfids und Bleichromats. *Z. anorg. Chem.*, 82(1):323–328.

Hofmann, B. (1989). *Genese, Alteration, und rezentes Fliess-System der Uranlagerstätte Krunkelbach (Menzenschwand, Südschwarzwald)*. PhD thesis, Universität Bern. Nagra, Technischer Bericht 88-30.

Hofmann, C. (2010). Background analysis for AMS of ^{236}U at the ETH Tandy facility using time-of-flight detectors. Term paper, ETH Zürich.

Holden, N. E. (1989). Total and spontaneous fission half-lives for uranium, plutonium, americium and curium nuclides. *Pure Appl. Chem.*, 61(8):1483–1504.

Horwitz, E. P., Dietz, M. L., Chiarizia, R., Diamond, H., Essling, A. M., and Graczyk, D. (1992). Separation and preconcentration of uranium from acidic media by extraction chromatography. *Anal. Chim. Acta*, 266(1):25–37.

Hotchkis, M. A. C., Child, D., Fink, D., Jacobsen, G. E., Lee, P. J., Mino, N., Smith, A. M., and Tuniz, C. (2000). Measurement of ^{236}U in environmental media. *Nucl. Instrum. Meth. B*, 172(1-4):659–665.

Hrnecek, E., Steier, P., and Wallner, A. (2005). Determination of plutonium in environmental samples by AMS and alpha spectrometry. *Appl. Radiat. Isot.*, 63(5-6):633–638.

Hughen, K., Lehman, S., Southon, J., Overpeck, J., Marchal, O., Herring, C., and Turnbull, J. (2004). ^{14}C Activity and Global Carbon Cycle Changes over the Past 50,000 Years. *Science*, 303(5655):202–207.

Hunt, A. L., Petrucci, G. A., Bierman, P. R., and Finkel, R. C. (2006). Metal matrices to optimize ion beam currents for accelerator mass spectrometry. *Nucl. Instrum. Meth. B*, 243(1):216–222.

Hvelplund, P., Lægsgaard, E., and Horsdal Pedersen, E. (1972). Equilibrium charge distributions of light ions in helium, measured with a position-sensitive open electron multiplier. *Nucl. Instrum. Meth.*, 101(3):497–502.

Jacob, S. (2001). *Beschleunigermassenspektrometrie (AMS) von ^{14}C bei tiefen Energien*. PhD thesis, ETH Zürich. Diss. ETH. Nr. 14071.

Karcher, M., Smith, J. N., Kauker, F., Gerdes, R., and Smethie Jr., W. M. (2012). Recent changes in Arctic Ocean circulation revealed by iodine-129 observations and modeling. *J. Geophys. Res.*, 117:C08007.

Kaufman, D. S., Polyak, L., Adler, R., Channell, J. E. T., and Xuan, C. (2008). Dating late Quaternary planktonic foraminifer Neogloboquadrina pachyderma from the Arctic Ocean using amino acid racemization. *Paleoceanography*, 23:PA3224.

Keigwin, L. D. and Jones, G. A. (1994). Western North Atlantic evidence for millennial-scale changes in ocean circulation and climate. *J. Geophys. Res.*, 99(C6):12397–12410.

Keith-Roach, M. J., Day, J. P., Fifield, L. K., and Livens, F. R. (2001). Measurement of Np in environmental water samples by accelerator mass spectrometry. *Analyst*, 126:58–61.

Kelley, J. M., Bond, L. A., and Beasley, T. M. (1999). Global distribution of Pu isotopes and ^{237}Np. *Sci. Total Environ.*, 237-238:483–500.

Kilius, L. R., Beukens, R. P., Chang, K. H., Lee, H. W., Litherland, A. E., Elmore, D., Ferraro, R., and Gove, H. E. (1979). Separation of ^{26}Al and ^{26}Mg isobars by negative ion mass spectrometry. *Nature*, 282:488–489.

Kim, C. K., Kim, C. S., Chang, B. U., Choi, S. W., Chung, C. S., Hong, G. H., Hirose, K., and Igarashi, Y. (2004). Plutonium isotopes in seas around the Korean Peninsula. *Sci. Total Environ.*, 318(1-3):197–209.

Klein, J., Fink, D., Middleton, R., Nishiizumi, K., and Arnold, J. (1991). Determination of the half-life of ^{41}Ca from measurements of Antarctic meteorites. *Earth Planet. Sc. Lett.*, 103(1-4):79–83.

Klein, J., Middleton, R., and Tang, H. (1982). Modifications of an FN tandem for quantitative ^{10}Be measurement. *Nucl. Instrum. Methods*, 193(3):601–616.

Knudsen, M. F., Henderson, G. M., Frank, M., Mac Niocaill, C., and Kubik, P. W. (2008). In-phase anomalies in Beryllium-10 production and palaeomagnetic field behaviour during the Iceland Basin geomagnetic excursion. *Earth Planet. Sc. Lett.*, 265(3-4):588–599.

Komura, K., Sakanoue, M., and Yamamoto, M. (1984). Determination of ^{240}Pu/^{239}Pu ratio in environmental samples based on the measurement of Lx/α-ray activity ratio. *Health Phys.*, 46(6):1213–1219.

Korschinek, G., Bergmaier, A., Faestermann, T., Gerstmann, U. C., Knie, K., Rugel, G., Wallner, A., Dillmann, I., Dollinger, G., Lierse von Gostomski, C., Kossert, K., Maiti, M., Poutivtsev, M., and Remmert, A. (2010). A new value for the half-life of ^{10}Be by Heavy-Ion Elastic Recoil Detection and liquid scintillation counting. *Nucl. Instrum. Meth. B*, 268(2):187–191.

Kottler, C. (2005). *Dünnschichtanalyse mittels Vorwärtsstreuung bei tiefer Energie*. PhD thesis, ETH Zürich. Diss. ETH. Nr. 16079.

Krey, P. W., Hardy, E. P., Pachucki, C., Rourke, F., Coluzza, J., and Benson, W. K. (1976). Mass isotopic composition of global fall-out plutonium in soil. Transuranium nuclides in the environment. *IAEA-SM-199/39, Vienna*, 46(6):671–678.

Ku, T. L., Kusakabe, M., Measures, C. I., Southon, J. R., Cusimano, G., Vogel, J. S., Nelson, D. E., and Nakaya, S. (1990). Beryllium isotope distribution in the western North Atlantic: a comparison to the Pacific. *Deep Sea Res.*, 37(5):795–808.

Kubik, P. W. and Christl, M. (2010). ^{10}Be and ^{26}Al measurements at the Zurich 6 MV Tandem AMS facility. *Nucl. Instrum. Meth. B*, 268(7-8):880–883.

Kumar, P., Korschinek, G., Chopra, S., Faestermann, T., Ludwig, P., Rugel, G., Seiler, D., Wallner, A., Ojha, S., Gargari, S., Joshi, R., and Kanjilal, D. (2011). Charge state distribution studies of SrF_3, MnF_3 and CaF_3 molecules using single and double stripping in a Tandem accelerator. *Nucl. Instrum. Meth. B*, 269(18):1986–1991.

Kusakabe, M., Ku, T. L., Southon, J. R., Liu, S., Vogel, J. S., Nelson, D. E., Nakaya, S., and Cusimano, G. L. (1991). Be isotopes in rivers/estuaries and their oceanic budgets. *Earth Planet. Sc. Lett.*, 102(3-4):265–276.

Kusakabe, M., Ku, T.-L., Southon, J. R., and Measures, C. I. (1990). Beryllium isotopes in the ocean. *Geochem. J.*, 24:263–272.

Kutschera, W. (2005). Progress in isotope analysis at ultra-trace level by AMS. *Int. J. Mass Spectrom.*, 242(2-3):145–160.

Lachner, J., Christl, M., Bisinger, T., Michel, R., and Synal, H.-A. (2010). Isotopic signature of plutonium at Bikini atoll. *Appl. Radiat. Isotopes*, 68(6):979–983.

Lachner, J., Christl, M., Synal, H.-A., Frank, M., and Jakobsson, M. (2013a). Carrier free ^{10}Be/^{9}Be measurements with low-energy AMS: Determination of sedimentation rates in the Arctic Ocean. *Nucl. Instrum. Meth. B*, 294:67–71.

Lachner, J., Christl, M., Vockenhuber, C., and Synal, H.-A. (2013b). Detection of UH^{3+} and ThH^{3+} molecules and ^{236}U background studies with low-energy AMS. *Nucl. Instrum. Meth. B*, 294:364–368.

Lachner, J., Christl, M., Vockenhuber, C., Synal, H.-A., Cao-Dolg, X., and Dolg, M. (2012a). Existence of triply charged actinide-hydride molecules. *Phys. Rev. A*, 85:022717.

Lachner, J., Dillmann, I., Faestermann, T., Korschinek, G., Poutivtsev, M., Rugel, G., Lierse von Gostomski, C., Türler, A., and Gerstmann, U. (2012b). Attempt to detect primordial ^{244}Pu on Earth. *Phys. Rev. C*, 85:015801.

Lal, D. and Peters, B. (1967). Cosmic ray produced radioactivity on the Earth. In Flugge, S., editor, *Handbuch der Physik*, volume 4612, pages 551–612.

Lebatard, A.-E., Bourlès, D. L., Braucher, R., Arnold, M., Duringer, P., Jolivet, M., Moussa, A., Deschamps, P., Roquin, C., Carcaillet, J., Schuster, M., Lihoreau, F., Likius, A., Mackaye, H. T., Vignaud, P., and Brunet, M. (2010). Application of the authigenic ^{10}Be/^{9}Be dating method to continental sediments: Reconstruction of the Mio-Pleistocene sedimentary sequence in the early hominid fossiliferous areas of the northern Chad Basin. *Earth Planet. Sc. Lett.*, 297(1-2):57–70.

Lebatard, A.-E., Bourlès, D. L., Duringer, P., Jolivet, M., Braucher, R., Carcaillet, J., Schuster, M., Arnaud, N., Monié, P., Lihoreau, F., Likius, A., Mackaye, H. T., Vignaud, P., and Brunet, M. (2008). Cosmogenic nuclide dating of Sahelanthropus tchadensis and Australopithecus bahrelghazali: Mio-Pliocene hominids from Chad. *P. Natl. Acad. Sci. USA*, 105(9):3226–3231.

Lee, H. W., Galindo-Uribarri, A., Chang, K. H., Kilius, L. R., and Litherland, A. E. (1984). The ^{12}CH$_2^{2+}$ molecule and radiocarbon dating by accelerator mass spectrometry. *Nucl. Instrum. Meth. B*, 5(2):208–210.

León Vintró, L., Mitchell, P. I., Condren, O. M., Moran, M., Vives i Batlle, J., and Sánchez-Cabeza, J. A. (1996). Determination of the ^{240}Pu/^{239}Pu atom ratio in low activity environmental samples by alpha spectrometry and spectral deconvolution. *Nucl. Instrum. Meth. A*, 369(2-3):597–602.

Livingston, H. D., Povinec, P. P., Ito, T., and Togawa, O. (2001). The behaviour of plutonium in the Pacific Ocean. In Kudo, A., editor, *Plutonium in the Environment Proceedings of the Second International Symposium*, volume 1 of *Radioactivity in the Environment*, pages 267–292. Elsevier.

Lund, S., Stoner, J. S., Channell, J. E. T., and Acton, G. (2006). A summary of Brunhes paleomagnetic field variability recorded in Ocean Drilling Program cores. *Phys. Earth. Planet. In.*, 156(3-4):194–204.

Maden, C., Döbeli, M., Kubik, P. W., Frank, M., and Suter, M. (2004). Measurement of carrier-free ^{10}Be samples with AMS: the method and its potential. *Nucl. Instrum. Meth. B*, 223-224:247–252.

Mangini, A., Segl, M., Bonani, G., Hofmann, H. J., Morenzoni, E., Nessi, M., Suter, M., Wölfli, W., and Turekian, K. K. (1984). Mass-spectrometric ^{10}Be dating of deep-sea sediments applying the Zürich tandem accelerator. *Nucl. Instrum. Meth. B*, 5(2):353–358.

Marion, G. S., Dunbar, R. B., Mucciarone, D. A., Kremer, J. N., Lansing, J. S., and Arthawiguna, A. (2005). Coral skeletal d^{15}N reveals isotopic traces of an agricultural revolution. *Mar. Pollut. Bull.*, 50:931–944.

Masarik, J. and Beer, J. (1999). Simulation of particle fluxes and cosmogenic nuclide production in the Earth's atmosphere. *J. Geophys. Res.*, 104(D10):12099–12111.

Masarik, J. and Beer, J. (2009). An updated simulation of particle fluxes and cosmogenic nuclide production in the Earth's atmosphere. *J. Geophys. Res.*, 114:D11103.

Maxeiner, S. (2012). Kohlenstoffstripping in Helium bei 45 keV. Master's thesis, ETH Zürich.

McHargue, L. R. and Damon, P. E. (1991). The Global Beryllium-10 Cycle. *Rev. Geophys.*, 29(2):141–158.

McHargue, L. T., Damon, P. E., and Donahue, D. J. (1995). Enhanced cosmic-ray production of ^{10}Be coincident with the Mono Lake and Laschamp geomagnetic excursions. *Geophys. Res. Lett.*, 22(5):659–662.

Measures, C. I. and Edmond, J. M. (1982). Beryllium in the water column of the central North Pacific. *Nature*, 297:51–53.

Measures, C. I. and Edmond, J. M. (1983). The geochemical cycle of ^{9}Be: a reconnaissance. *Earth Planet. Sc. Lett.*, 66:101–110.

Measures, C. I., Ku, T. L., Luo, S., Southon, J. R., Xu, X., and Kusakabe, M. (1996). The distribution of ^{10}Be and ^{9}Be in the South Atlantic. *Deep Sea Res. Pt. I*, 43(7):987–1009.

Meister, D. (2011). ^{236}U/^{238}U am TANDY - Erste Ergebnisse. Term paper, ETH Zürich.

Ménabréaz, L., Thouveny, N., Bourlès, D., Deschamps, P., Hamelin, B., and Demory, F. (2011). The Laschamp geomagnetic dipole low expressed as a cosmogenic ^{10}Be atmospheric overproduction at ∼41 ka. *Earth Planet. Sc. Lett.*, 312(3-4).

Merrill, J. R., Lyden, E. F. X., Honda, M., and Arnold, J. R. (1960). The sedimentary geochemistry of the beryllium isotopes. *Geochim. Cosmochim. Ac.*, 18:108–129.

Michel, R., Daraoui, A., Gorny, M., Jakob, D., Sachse, R., Tosch, L., Nies, H., Goroncy, I., Herrmann, J., Synal, H.-A., Stocker, M., and Alfimov, V. (2012). Iodine-129 and iodine-127 in European seawaters and in precipitation from Northern Germany. *Sci. Total Environ.*, 419:151–169.

Mitchell, P. I., León Vintró, L., Dahlgaard, H., Gascó, C., and Sánchez-Cabeza, J. A. (1997). Perturbation in the ^{240}Pu/^{239}Pu global fallout ratio in local sediments following the nuclear accidents at Thule (Greenland) and Palomares (Spain). *Sci. Total Environ.*, 202(1-3):147–153.

Moak, C. D., Lutz, H. O., Bridwell, L. B., Northcliffe, L. C., and Datz, S. (1967). Evidence of Shell Effects and the Approach to Equilibrium in the Charge-State Distributions for 15-160 MeV ^{79}Br and ^{127}I Ions in Carbon. *Phys. Rev. Lett.*, 18:41–43.

Monaghan, M. C., Krishnaswami, S., and Thomas, J. H. (1983). ^{10}Be concentrations and the long-term fate of particle-reactive nuclides in five soil profiles from California. *Earth Planet. Sc. Lett.*, 65(1):51–60.

Müller, A. (2009). *Entwicklung von universellen AMS Anlagen bei tiefen Energien*. PhD thesis, ETH Zürich. Diss. ETH Nr. 18393.

Müller, A. M., Christl, M., Döbeli, M., Kubik, P. W., Suter, M., and Synal, H.-A. (2010a). Boron suppression with a gas ionization chamber at very low energies (E< 1MeV). *Nucl. Instrum. Meth. B*, 268(7-8):843–846.

Müller, A. M., Christl, M., Lachner, J., Suter, M., and Synal, H.-A. (2010b). Competitive ^{10}Be measurements below 1 MeV with the upgraded ETH-TANDY AMS facility. *Nucl. Instrum. Meth. B*, 268(17-18):2801–2807.

Müller, A. M., Döbeli, M., Suter, M., and Synal, H.-A. (2012). Performance of the ETH gas ionization chamber at low energy. *Nucl. Instrum. Meth. B*, 287:94–102.

Muller, R. A. (1977). Radioisotope Dating with a Cyclotron. *Science*, 196(4289):489–494.

Muller, R. A., Stephenson, E. J., and Mast, T. S. (1978). Radioisotope Dating with an Accelerator: A Blind Measurement. *Science*, 201(4353):347–348.

Muramatsu, Y., Hamilton, T., Uchida, S., Tagami, K., Yoshida, S., and Robison, W. (2001). Measurement of ^{240}Pu/^{239}Pu isotopic ratios in soils from the Marshall Islands using ICP-MS. *Sci. Total Environ.*, 278(1-3):151–159.

Muramatsu, Y., Rühm, W., Yoshida, S., Tagami, K., Uchida, S., and Wirth, E. (2000). Concentrations of ^{239}Pu and ^{240}Pu and Their Isotopic Ratios Determined by ICP-MS in Soils Collected from the Chernobyl 30-km Zone. *Environ. Sci. Technol.*, 34(14):2913–2917.

Muscheler, R., Beer, J., Kubik, P. W., and Synal, H.-A. (2005). Geomagnetic field intensity during the last 60,000 years based on ^{10}Be and ^{36}Cl from the Summit ice cores and ^{14}C. *Quaternary Sci. Rev.*, 24(16-17):1849–1860.

Nelson, D. E., Korteling, R. G., and Stott, W. R. (1977). Carbon-14: Direct Detection at Natural Concentrations. *Science*, 198(4316):507–508.

Nies, H., Goroncy, I., Herrmann, J., Michel, R., Daraoui, A., Gorny, M., Jakob, D., Sachse, R., and Tosch, L. (2009). *Kartierung von Tc-99, I-129 und I-127 im Oberflächenwasser der Nordsee*.

Noshkin, V. E., Wong, K. M., Eagle, R. J., and Gatrousis, C. (1975). Transuranics and other radionuclides in Bikini lagoon: Concentration data retrieved from aged coral sections. *Limnol. Oceanogr.*, 20(5):729–742.

Not, C. and Hillaire-Marcel, C. (2010). Time constraints from ^{230}Th and ^{231}Pa data in late Quaternary, low sedimentation rate sequences from the Arctic Ocean: an example from the northern Mendeleev Ridge. *Quaternary Sci. Rev.*, 29(25-26):3665–3675.

Nydal, R. (1968). Further Investigation on the Transfer of Radiocarbon in Nature. *J. Geophys. Res.*, 73(12):3617–3635.

Oda, H., Shibuya, H., and Hsu, V. (2000). Palaeomagnetic records of the Brunhes/Matuyama polarity transition from ODP Leg 124 (Celebes and Sulu seas). *Geophys. J. Int.*, 142(2):319–338.

OSPAR (2009). Ospar commission work areas/radioactive substances/publications, publication no.: 543/2011.

Osterberg, C., Cutshall, N., and Cronin, J. (1965). Chromium-51 as a Radioactive Tracer of Columbia River Water at Sea. *Science*, 150(3703):1585–1587.

Oughton, D. H., Fifield, L. K., Day, J. P., Cresswell, R. C., Skipperud, L., Di Tada, M. L., Salbu, B., Strand, P., Drozcho, E., and Mokrov, Y. (2000). Plutonium from Mayak: Measurement of Isotope Ratios and Activities Using Accelerator Mass Spectrometry. *Environ. Sci. Tech.*, 34(10):1938–1945.

Paul, M., Fink, D., Hollos, G., Kaufman, A., Kutschera, W., and Magaritz, M. (1987). Measurement of ^{129}I concentrations in the environment after the Chernobyl reactor accident. *Nucl. Instrum. Meth. B*, 29(1-2):341–345.

Pavich, M. J., Brown, L., Harden, J., Klein, J., and Middleton, R. (1986). ^{10}Be distribution in soils from Merced River terraces, California. *Geochim. Cosmochim. Ac.*, 50(8):1727–1735.

Pétrélis, F., Besse, J., and Valet, J.-P. (2011). Plate tectonics may control geomagnetic reversal frequency. *Geophys. Res. Lett.*, 38:L19303.

Polyak, L., Bischof, J., Ortiz, J. D., Darby, D. A., Channell, J. E. T., Xuan, C., Kaufman, D. S., Løvlie, R., Schneider, D. A., Eberl, D. D., Adler, R. E., and Council, E. A. (2009). Late Quaternary stratigraphy and sedimentation patterns in the western Arctic Ocean. *Global Planet. Change*, 68(1-2):5–17.

Priller, A., Auer, M., Golser, R., Herschmann, A., Kutschera, W., Lukas, J., Steier, P., and Wallner, A. (2007). Ion source refinement at VERA. *Nucl. Instrum. Meth. B*, 259(1):94–99.

Purser, K. H., Litherland, A. E., and Rucklidge, J. C. (1979). Secondary Ion Mass Spectrometry at Close to Single-atom Concentration Using DC Accelerators. *Surf. Interface Anal.*, 1(1):12–19.

Qiao, J., Hou, X., Roos, P., and Miró, M. (2011). Reliable determination of ^{237}Np in environmental solid samples using ^{242}Pu as a potential tracer. *Talanta*, 84(2):494–500.

Raisbeck, G. M., Yiou, F., Bourles, D., Lestringuez, J., and Deboffle, D. (1984). Measurement of ^{10}Be with a tandetron accelerator operating at 2 MV. *Nucl. Instrum. Meth. B*, 5(2):175–178.

Raisbeck, G. M., Yiou, F., Cattani, O., and Jouzel, J. (1985). Evidence for an increase in cosmogenic ^{10}Be during a geomagnetic reversal. *Nature*, 315:315–317.

Raisbeck, G. M., Yiou, F., Cattani, O., and Jouzel, J. (2006). ^{10}Be evidence for the Matuyama-Brunhes geomagnetic reversal in the EPICA Dome C ice core. *Nature*, 444:82–84.

Raisbeck, G. M., Yiou, F., Fruneau, M., Lieuvin, M., and Loiseaux, J. (1978a). Measurement of ^{10}Be in 1,000- and 5,000-year-old Antarctic ice. *Nature*, 275:731–733.

Raisbeck, G. M., Yiou, F., Fruneau, M., and Loiseaux, J. M. (1978b). Beryllium-10 Mass Spectrometry with a Cyclotron. *Science*, 202(4364):215–217.

Raisbeck, G. M., Yiou, F., Fruneau, M., Loiseaux, J. M., Lieuvin, M., and Ravel, J. C. (1981a). Cosmogenic ^{10}Be/^{7}Be as a probe of atmospheric transport processes. *Geophys. Res. Lett.*, 8:1015–1018.

Raisbeck, G. M., Yiou, F., Fruneau, M., Loiseaux, J. M., Lieuvin, M., Ravel, J. C., and Lorius, C. (1981b). Cosmogenic ^{10}Be concentrations in Antarctic ice during the past 30,000 years. *Nature*, 292:825–826.

Raisbeck, G. M., Yiou, F., Fruneau, M., Loiseaux, J. M., Lieuvin, M., Ravel, J. C., Reyss, J. M., and Guichard, F. (1980). ^{10}Be concentration and residence time in the deep ocean. *Earth Planet. Sc. Lett.*, 51(2):275–278.

Rokop, D. J., Metta, D. N., and Stevens, C. M. (1972). ^{236}U/^{238}U measurements in three terrestrial minerals and one processed ore. *Int. J. Mass Spectrom.*, 8(4):259–264.

Rühm, W., Kato, K., Korschinek, G., Morinaga, H., and Nolte, E. (1995). Neutron spectrum and yield of the Hiroshima A-bomb deduced from radionuclide measurements at one location. *Int. J. Radiat. Biol.*, 68(1):97–103.

Rühm, W., Wallner, A., Cullings, H., Egbert, S. D., El-Faramawy, N., Faestermann, T., Kaul, D., Knie, K., Korschinek, G., Nakamura, N., Roberts, J., and Rugel, G. (2010). ^{41}Ca in tooth enamel. Part II: A means for retrospective biological neutron dosimetry in atomic bomb survivors. *Radiat. Res.*, 174:146–154.

Ryding, G., Wittkower, A., Nussbaum, G. H., Saxman, A. C., Bastide, R., Kessel, Q., and Rose, P. H. (1970). Equilibrium Charge Fractions of Aluminum Ions in Nitrogen from 0.4 to 4.0 MeV. *Phys. Rev. A*, 1:1081–1082.

Sakaguchi, A., Kawai, K., Steier, P., Quinto, F., Mino, K., Tomita, J., Hoshi, M., Whitehead, N., and Yamamoto, M. (2009). First results on ^{236}U levels in global fallout. *Sci. Total Environ.*, 407(14):4238–4242.

Schlitzer, R. (2012). Ocean Data View. http://odv.awi.de.

Schulze-König, T., Maden, C., Denk, E., Freeman, S. P. H. T., Stocker, M., Suter, M., Synal, H.-A., and Walczyk, T. (2010). Comparison of ^{41}Ca analysis on 0.5 MV and 5 MV-AMS systems. *Nucl. Instrum. Meth. B*, 268(7-8):752–755.

Schulze-König, T., Seiler, M., Suter, M., Wacker, L., and Synal, H.-A. (2011). The dissociation of ^{13}CH and ^{12}CH$_2$ molecules in He and N$_2$ at beam energies of 80-250 keV and possible implications for radiocarbon mass spectrometry. *Nucl. Instrum. Meth. B*, 269(1):34–39.

Seaborg, G. T. and Perlman, M. L. (1948). Search for Elements 94 and 93 in Nature. Presence of 94^{239} in Pitchblende. *J. Am. Chem. Soc.*, 70(4):1571–1573.

Segl, M., Mangini, A., Bonani, G., Hofmann, H. J., Nessi, M., Suter, M., Wölfli, W., Friedrich, G., Plüger, W. L., Wiechowski, A., and Beer, J. (1984). [10]Be-dating of a manganese crust from Central North Pacific and implications for ocean palaeocirculation. *Nature*, 309:540–543.

Sellén, E., Jakobsson, M., Frank, M., and Kubik, P. W. (2009). Pleistocene variations of beryllium isotopes in central Arctic Ocean sediment cores. *Global Planet. Change*, 68(1-2):38–47.

Shen, G., Gao, X., Gao, B., and Granger, D. E. (2009). Age of Zhoukoudian Homo erectus determined with [26]Al/[10]Be burial dating. *Nature*, 458:198–200.

Shima, K., Kuno, N., Yamanouchi, M., and Tawara, H. (1992). Equilibrium charge fractions of ions of Z = 4-92 emerging from a carbon foil. *Atomic Data and Nuclear Data Tables*, 51(2):173–241.

Shipboard Scientific Party (1990). Site 769. In Rangin, C., Silver, E., von Breymann, M. X., et al., editor, *Proc. ODP, Init. Repts., 124*, pages 299–342. College Station, TX (Ocean Drilling Program).

Shipboard Scientific Party (1996). Site 983. In Jansen, E., Raymo, M. E., Blum, P., et al., editor, *Proc. ODP, Init. Repts., 162*, pages 139–167. College Station, TX (Ocean Drilling Program).

Shipboard Scientific Party (1997). Site 1021. In Lyle, M., Koizumi, I., Richter, C., et al., editor, *Proc. ODP, Init. Repts., 167*, pages 431–459. College Station, TX (Ocean Drilling Program).

Shipboard Scientific Party (1998). Bermuda rise and sohm abyssal plain, sites 1063 and 1064. In Keigwin, L. D., Rio, D., Acton, G. D., et al., editor, *Proc. ODP, Init. Repts., 172*, pages 251–308. College Station, TX (Ocean Drilling Program).

Shipboard Scientific Party (1999). Site 1090. In Gersonde, R., Hodell, D. A., Blum, P., et al., editor, *Proc. ODP, Init. Repts., 177*, pages 1–101. College Station, TX (Ocean Drilling Program).

Simion (2010). *Scientific Instrument Services, 1027 Old York Road, Ringoes, NJ 08551-1054, USA*.

Southon, J. and Santos, G. M. (2007). Life with MC-SNICS. Part II: Further ion source development at the Keck carbon cycle AMS facility. *Nucl. Instrum. Meth. B*, 259(1):88–93.

Spassov, N., Geraads, D., Hristova, L., Markov, G. N., Merceron, G., Tzankov, T., Stoyanov, K., Böhme, M., and Dimitrova, A. (2012). A hominid tooth from Bulgaria: The last pre-human hominid of continental Europe. *J. Hum. Evol.*, 62:138–145.

Srncik, M., Steier, P., and Wallner, G. (2010). Determination of the isotopic ratio [236]U/[238]U in Austrian water samples. *Nucl. Instrum. Meth. B*, 268(7-8):1146–1149.

Steier, P., Bichler, M., Fifield, L. K., Golser, R., Kutschera, W., Priller, A., Quinto, F., Richter, S., Srncik, M., Terrasi, P., Wacker, L., Wallner, A., Wallner, G., Wilcken, K. M., and Wild, E. M. (2008). Natural and anthropogenic [236]U in environmental samples. *Nucl. Instrum. Meth. B*, 266(10):2246–2250.

Steier, P., Hrnecek, E., Priller, A., Quinto, F., Srncik, M., Wallner, A., Wallner, G., and Winkler, S. (2013). AMS of the Minor Plutonium Isotopes. *Nucl. Instrum. Meth. B*, 294:160–164.

Steinhilber, F., Abreu, J. A., Beer, J., Brunner, I., Christl, M., Fischer, H., Heikkilä, U., Kubik, P. W., Mann, M., McCracken, K. G., Miller, H., Miyahara, H., Oerter, H., and Wilhelms, F. (2012). 9,400 years of cosmic radiation and solar activity from ice cores and tree rings. *P. Natl. Acad. Sci. USA*, 109(16):5967–5971.

Stocker, M., Bertschinger, R., Döbeli, M., Grajcar, M., Jacob, S., Scheer, J., Suter, M., and Synal, H.-A. (2004). Status of the PSI/ETH compact AMS facility. *Nucl. Instrum. Meth. B*, 223-224:104–108.

Stocker, M., Döbeli, M., Grajcar, M., Suter, M., Synal, H.-A., and Wacker, L. (2005). A universal and competitive compact AMS facility. *Nucl. Instrum. Meth. B*, 240(1-2):483–489.

Stocker, M. G. (2006). *AMS bei tiefen Energien*. PhD thesis, ETH Zürich. Diss. ETH. Nr. 16787.

Straume, T., Rugel, G., Marchetti, A. A., Rühm, W., Korschinek, G., McAninch, J. E., Carroll, K., Egbert, S., Faestermann, T., Knie, K., Martinelli, R., Wallner, A., and Wallner, C. (2003). Measuring fast neutrons in Hiroshima at distances relevant to atomic-bomb survivors. *Nature*, 424:539–542.

Studer, A. (2008). Trace elements in miocene subbituminous coals from the swiss molasse basin with special attention to uranium and its mode of occurrence. Master's thesis, ETH Zürich.

Stuiver, M., Quay, P. D., and Ostlund, H. G. (1983). Abyssal Water Carbon-14 Distribution and the Age of the World Oceans. *Science*, 219(4586):849–851.

Suganuma, Y., Okuno, J., Heslop, D., Roberts, A. P., Yamazaki, T., and Yokoyama, Y. (2011). Post-depositional remanent magnetization lock-in for marine sediments deduced from ^{10}Be and paleomagnetic records through the Matuyama-Brunhes boundary. *Earth Planet. Sc. Lett.*, 311(1-2):39–52.

Suganuma, Y., Yokoyama, Y., Yamazaki, T., Kawamura, K., Horng, C.-S., and Matsuzaki, H. (2010). ^{10}Be evidence for delayed acquisition of remanent magnetization in marine sediments: Implication for a new age for the Matuyama-Brunhes boundary. *Earth Planet. Sc. Lett.*, 296(3-4):443–450.

Sun, G., Döbeli, M., Müller, A. M., Stocker, M., Suter, M., and Wacker, L. (2007). Energy loss and straggling of heavy ions in silicon nitride in the low MeV energy range. *Nucl. Instrum. Meth. B*, 256(2):586–590.

Suter, M. (1998). A new generation of small facilities for accelerator mass spectrometry. *Nucl. Instrum. Meth. B*, 139(1-4):150–157.

Suter, M., Huber, R., Jacob, S. A. W., Synal, H.-A., and Schroeder, J. B. (1999). A new small accelerator for radiocarbon dating. *AIP Conf. Proc.*, 475(1):665–667.

Suter, M., Jacob, S., and Synal, H. A. (1997). AMS of ^{14}C at low energies. *Nucl. Instrum. Meth. B*, 123(1-4):148–152.

Synal, H.-A., Jacob, S., and Suter, M. (2000a). New concepts for radiocarbon detection systems. *Nucl. Instrum. Meth. B*, 161-163:29–36.

Synal, H.-A., Jacob, S., and Suter, M. (2000b). The PSI/ETH small radiocarbon dating system. *Nucl. Instrum. Meth. B*, 172(1-4):1–7.

Synal, H.-A., Schulze-König, T., Seiler, M., Suter, M., and Wacker, L. (2013). Mass spectrometric detection of radiocarbon for dating applications. *Nucl. Instrum. Meth. B*, 294:349–352.

Synal, H.-A., Stocker, M., and Suter, M. (2007). MICADAS: A new compact radiocarbon AMS system. *Nucl. Instrum. Meth. B*, 259(1):7–13.

Szabó, J., Csikai, J., and Várnagy, M. (1972). Low-energy cross sections for ^{10}B(p,α)^{7}Be. *Nucl. Phys. A*, 195(2):527–533.

Taylor, D. M. (1989). The biodistribution and toxicity of plutonium, americium and neptunium. *Sci. Total Environ.*, 83(3):217–225.

Taylor, S. R. (1964). Abundance of chemical elements in the continental crust: a new table. *Geochim. Cosmochim. Ac.*, 28(8):1273–1285.

Thakur, P. and Mulholland, G. P. (2012). Determination of ^{237}Np in environmental and nuclear samples: A review of the analytical method. *Appl. Radiat. Isot.*, 70(8):1747–1778.

Turekian, K. K., Cochran, J. K., Krishnaswami, S., Lanford, W. A., Parker, P. D., and Bauer, K. A. (1979). The measurement of ^{10}Be in manganese nodules using a tandem Van De Graaff accelerator. *Geophys. Res. Lett.*, 6(5):417–420.

Venz, K. A. and Hodell, D. A. (2002). New evidence for changes in Plio-Pleistocene deep water circulation from Southern Ocean ODP Leg 177 Site 1090. *Palaeogeogr. Palaeocl.*, 182(3-4):197–220.

Vockenhuber, C., Alfimov, V., Christl, M., Lachner, J., Schulze-König, T., Suter, M., and Synal, H.-A. (2013). The potential of He stripping in heavy ion AMS. *Nucl. Instrum. Meth. B*, 294:382–386.

Vockenhuber, C., Bergmaier, A., Faestermann, T., Knie, K., Korschinek, G., Kutschera, W., Rugel, G., Steier, P., Vorderwinkler, K., and Wallner, A. (2007). Development of isobar separation for ^{182}Hf AMS measurements of astrophysical interest. *Nucl. Instrum. Meth. B*, 259(1):250–255.

Vockenhuber, C., Christl, M., Hofmann, C., Lachner, J., Müller, A. M., and Synal, H.-A. (2011). Accelerator mass spectrometry of ^{236}U at low energies. *Nucl. Instrum. Meth. B*, 269(24):3199–3203.

von Blanckenburg, F., Belshaw, N. S., and O'Nions, R. K. (1996a). Separation of ^{9}Be and cosmogenic ^{10}Be from environmental materials and SIMS isotope dilution analysis. *Chem. Geol.*, 129(1-2):93–99.

von Blanckenburg, F., Bouchez, J., and Wittmann, H. (2012). Earth surface erosion and weathering from the ^{10}Be(meteoric)/^{9}Be ratio. *Earth Planet. Sc. Lett.*, 351-352:295–305.

von Blanckenburg, F. and Igel, H. (1999). Lateral mixing and advection of reactive isotope tracers in ocean basins: observations and mechanisms. *Earth Planet. Sc. Lett.*, 169(1-2):113–128.

von Blanckenburg, F. and O'Nions, R. K. (1999). Response of beryllium and radiogenic isotope ratios in Northern Atlantic Deep Water to the onset of northern hemisphere glaciation. *Earth Planet. Sc. Lett.*, 167(3-4):175–182.

von Blanckenburg, F., O'Nions, R. K., Belshaw, N. S., Gibb, A., and Hein, J. R. (1996b). Global distribution of beryllium isotopes in deep ocean water as derived from Fe-Mn crusts. *Earth Planet. Sc. Lett.*, 141(1-4):213–226.

Vorobyev, A. A., Seleverstov, D. M., Grachov, V. T., Kondurov, I. A., Nikitin, A. M., Smirnov, N. N., and Zalite, Y. K. (1972). Light Nuclei from 235U Neutron Fission. *Phys. Lett.*, 40B:102–104.

Wacker, L., Chamizo, E., Fifield, L. K., Stocker, M., Suter, M., and Synal, H. A. (2005). Measurement of actinides on a compact AMS system working at 300 kV. *Nucl. Instrum. Meth. B*, 240(1-2):452–457.

Wagner, G., Masarik, J., Beer, J., Baumgartner, S., Imboden, D., Kubik, P. W., Synal, H.-A., and Suter, M. (2000). Reconstruction of the geomagnetic field between 20 and 60 kyr BP from cosmogenic radionuclides in the GRIP ice core. *Nucl. Instrum. Meth. B*, 172(1-4):597–604.

Wahlen, M., Kunz, C. O., Matuszek, J. M., Mahoney, W. E., and Thompson, R. C. (1980). Radioactive Plume from the Three Mile Island Accident: Xenon-133 in Air at a Distance of 375 Kilometers. *Science*, 207(4431):639–640.

Wallner, A., Ikeda, Y., Kutschera, W., Priller, A., Steier, P., Vonach, H., and Wild, E. (2000). Precision and accuracy of ^{26}Al measurements at VERA. *Nucl. Instrum. Meth. B*, 172(1-4):382–387.

Wallner, C., Faestermann, T., Gerstmann, U., Knie, K., Korschinek, G., Lierse, C., and Rugel, G. (2004). Supernova produced and anthropogenic ^{244}Pu in deep sea manganese encrustations. *New Astron. Rev.*, 48(1-4):145–150.

Wang, L., Ku, T. L., Luo, S., Southon, J. R., and Kusakabe, M. (1996). ^{26}Al-^{10}Be systematics in deep-sea sediments. *Geochim. Cosmochim. Ac.*, 60(1):109–119.

Weathers, D. L., McDaniel, F. D., Matteson, S., Duggan, J. L., Anthony, J. M., and Douglas, M. A. (1991). Triply-ionized B$_2$ molecules from a tandem accelerator. *Nucl. Instrum. Meth. B*, 56-57(Part 2):889–892.

White, S. W., Whalen, P. P., and Heath, A. R. (2005). Source term evaluations. In Young, R. W. and Kerr, G. D., editors, *Reassessment of the Atomic Bomb Radiation Dosimetry for Hiroshima and Nagasaki - Dosimetry System 2002*, pages 62–79. Radiation Effects Research Foundation, Hiroshima.

Wilcken, K. M., Fifield, L. K., Barrows, T. T., Tims, S. G., and Gladkis, L. G. (2008). Nucleogenic ^{36}Cl, ^{236}U and ^{239}Pu in uranium ores. *Nucl. Instrum. Meth. B*, 266(16):3614–3624.

Willenbring, J. K. and von Blanckenburg, F. (2010). Meteoric cosmogenic Beryllium-10 adsorbed to river sediment and soil: Applications for Earth-surface dynamics. *Earth-Sci. Rev.*, 98(1-2):105–122.

Winkler, S., Fifield, L. K., Tims, S. G., and Morton, C. R. (2007). Improving the detection limit for ^{182}Hf. *Nucl. Instrum. Meth. B*, 259(1):256–259.

Wittkower, A. B. and Betz, H. D. (1973a). Equilibrium Charge-State Distributions of 2-15-MeV Tantalum and Uranium Ions Stripped in Gases and Solids. *Phys. Rev. A*, 7:159–167.

Wittkower, A. B. and Betz, H. D. (1973b). Equilibrium-charge-state distributions of energetic ions (z > 2) in gaseous and solid media. *Atomic Data*, 5(2):113–166.

Wittmann, H., von Blanckenburg, F., Bouchez, J., Dannhaus, N., Naumann, R., Christl, M., and Gaillardet, J. (2012). The dependence of meteoric ^{10}Be concentrations on particle size in Amazon River bed sediment and the extraction of reactive ^{10}Be/^{9}Be ratios. *Chem. Geol.*, 318-319:126–138.

Wolf, S. F., Bowers, D. L., and Cunnane, J. C. (2005). Analysis of high burnup spent nuclear fuel by ICP-MS. *J. Radioanal. Nucl. Chem.*, 263:581–586.

Yiou, F., Raisbeck, G. M., Baumgartner, S., Beer, J., Hammer, C., Johnsen, S., Jouzels, J., Kubik, P. W., Lestringuez, J., Stiévenards, M., Suter, M., and Yiou, P. (1997). Beryllium-10 in the Greenland Ice Core Project ice core at Summit, Greenland. *J. Geophys. Res.*, 102(C12):26,783–26,794.

Young, J. A. and Silker, W. B. (1980). Aerosol deposition velocities on the Pacific and Atlantic oceans calculated from ^{7}Be measurements. *Earth Planet. Sc. Lett.*, 50:92–104.

Zerle, L., Faestermann, T., Knie, K., Korschinek, G., and Nolte, E. (1997). The ^{41}Ca bomb pulse and atmospheric transport of radionuclides. *J. Geophys. Res.*, 102(D16):19517–19527.

Zhao, X.-L., Kieser, W. E., Dai, X., Priest, N. D., Kramer-Tremblay, S., Eliades, J., and Litherland, A. E. (2013). Preliminary studies of Pu measurement by AMS using PuF$_4^-$. *Nucl. Instrum. Meth. B*, 294:356–360.

Zhao, X.-L., Kilius, L. R., Litherland, A. E., and Beasley, T. (1997). AMS measurement of environmental U-236 Preliminary results and perspectives. *Nucl. Instrum. Meth. B*, 126(1-4):297–300.

Zhao, X.-L., Litherland, A. E., Doupé, J. P., and Kieser, W. E. (2004). The potential for AMS analysis of ^{10}Be using BeF$^-$. *Nucl. Instrum. Meth. B*, 223-224:199–204.

Zhao, X.-L., Nadeau, M.-J., Kilius, L. R., and Litherland, A. E. (1994). The first detection of naturally-occurring ^{236}U with accelerator mass spectrometry. *Nucl. Instrum. Meth. B*, 92(1-4):249–253.

Zheng, J., Tagami, K., Watanabe, Y., Uchida, S., Aono, T., Ishii, N., Yoshida, S., Kubota, Y., Fuma, S., and Ihara, S. (2012). Isotopic evidence of plutonium release into the environment from the Fukushima DNPP accident. *Scientific Reports*, 2:304.

Zheng, J. and Yamada, M. (2005). Vertical distributions of $^{239+240}$Pu activities and ^{240}Pu/^{239}Pu atom ratios in sediment cores: implications for the sources of Pu in the Japan Sea. *Sci. Total Environ.*, 340(1-3):199–211.

Ziegler, J., Biersack, J., and Littmark, U. (1985). The stopping and range of ions in solids. Pergamon Press.

Ziegler, J., Biersack, J., and Ziegler, M. (2008). SRIM - The Stopping and Range of Ions in Matter. SRIM Co.

Danke!

Curriculum vitae

Persönliche Daten

Anschrift: Johannes Lachner
                    Magdalenenstrasse 21
                    8050 Zürich
                    Schweiz

E-Mail: lachner@phys.ethz.ch

Geboren: 7.6.1983 in Landshut

Nationalität: deutsch

Ausbildung und Arbeitsstellen

1989-1993:   Grundschule Bruckberg

1993-2002:   Hans-Carossa-Gymnasium in Landshut, Abschluss mit dem Abitur

2002-2003:   Zivildienst im Kinderheim St. Vinzenz in Landshut

09/2003-09/2008:   Physikstudium an der TU München, Abschluss mit dem Diplom
                    Diplomarbeit zum Thema "Suche nach primordialen Radionukliden
                    mittels Beschleunigermassenspektrometrie"

09/2005-12/2008:   Übungsgruppenleitung für die Vorlesungen Mathematik für Chemiker,
                    Quantenmechanik für Chemiker und Experimentalphysik III & IV

10/2008-12/2008:   Wissenschaftlicher Mitarbeiter am Exzellenzcluster "Origin and
                    Structure of the Universe" der TU München

seit 2009:   Promotion am Labor für Ionenstrahlphysik (ETH Zürich) zum
                    Thema "Environmental applications of low-energy Accelerator Mass
                    Spectrometry", Übungsgruppenleitung für die Vorlesungen Kern-
                    & Teilchenphysik und Experimentalphysik I sowie Betreuung von
                    physikalischen Laborpraktika